Wigeon

Multi-Disciplinary Design and Optimisation of a Long-Range eVTOL Aircraft

Design Synthesis Exercise
Final Report
Group 06 - Spring 2021

TU Delft

This page has been intentionally left blank.

Wigeon

Multi-Disciplinary Design and Optimisation of a Long-Range eVTOL Aircraft

Group 06 - Spring 2021

Student Name	Student Number
Alba Maestre, Javier	4844009
Beyne, Egon	4797957
Buszek, Michael	4773934
Cuadrat-Grzybowski, Miguel	4838726
Montoya Santamaría, Alejandro	4789946
Poliakov, Nikita	4804236
Prud'homme van Reine, Koen	4878965
Salvador López, Noah	4882512
Schoser, Jakob	4843754
Wadia, Kaizad	4789849

Tutor: Saullo Giovani Pereira Castro
Coaches: Davide Biagini and Ali Nokhbatolfoghahai
Teaching Assistant: Paula Meseguer Berroy

Institution: Delft University of Technology
Place: Faculty of Aerospace Engineering, Delft

Submission Date: Tuesday 29th June, 2021

TU Delft

Preface

We are a group of 10 undergraduate students studying aerospace engineering at the Delft University of Technology, the Netherlands, completing the final project for the bachelor's degree, otherwise known as the Design Synthesis Exercise. However, we present this report to you not just as future aerospace engineers, but as enthusiasts of the revolution of urban air mobility and electric vertical takeoff and landing vehicles in particular. It goes without saying that the concept is not entirely novel, people have wanted their own flying vehicle for decades. The earliest examples of this that most of us experienced during our childhood were the flying cars in the 1980s science fiction movie Back to the Future II. Since then, we have managed to come far and are honoured to be a part of a growing field that while new, is continuously evolving. With this in mind, we are proud to present the product of research, programming, design and reporting over ten weeks of the Design Synthesis Exercise.

For this, we would like to thank our tutor Dr. Saullo Giovani Pereira Castro, our coaches Davide Biagini and Dr. Ali Nokhbatolfoghahai, and our teaching assistant, Paula Meseguer Berroy, who have been relentlessly supportive throughout the project. Moreover, we are indebted to many of the experts who gave their guidance at different stages in the exercise. This includes Prof. Damiano Casalino, Yunusi Fuerkaiti, Dr. Wouter van der Velden and Dr. Francesco Avallone for their immense help and support in aeroacoustics, Dr. Daniele Ragni for his advice on noise analysis, Dr. Tomas Sinnige for his insight on propellers, and Dr. Jianning Dong for his help with electrical engines. We are also sincerely grateful to Prof. Georg Eitelberg for his advice on experimental methods and propulsion integration, Robert Nederlof for his guidance on propeller-wing interaction, Dr. Christos Kassapoglou for the help on crashworthy design, Dr. Marilena Pavel, Dr. Erik-Jan van Kampen and Mr. Ismael Matamoros for their knowledge on control and Ir. Jos Sinke who gave invaluable advice detailing the production plan for the vehicle. We also want to thank Eddy van den Bos and Daniel Atherstone for their help and advice with the creation of CAD models.

With that said, we would also like to thank you, the reader, for being a part of this evergrowing world; our world, that could never have existed without the interest of individuals such as yourself.

> When once you have tasted flight, you will forever walk the Earth with your eyes turned skyward, for there you have been, and there you will always long to return.
>
> *Leonardo da Vinci*

Summary

The issue of adequate transportation is widespread. Not only are many modes of transportation expensive, but they often require dedicated infrastructure and are prone to traffic and congestion. In an attempt to attenuate this costly problem, an electrical Vertical Takeoff and Landing (eVTOL) aircraft concept, the Wigeon, is proposed after a trade off of three such concepts. The purpose of the project is to provide sustainable, personal aerial transportation for inter-city travel that is competitive with the current transportation methods while requiring minimal infrastructure. In order to accomplish this goal, a multidisciplinary design approach was conducted.

In order to focus the design on a single idea, three possible configurations were analysed and put into a trade-off. It was found that the tandem configuration was least complex, cheapest and safest with regards to one engine inoperative condition. All configurations analysed carried 4 passengers and 1 pilot.

During the market analysis, primarily focused on central Europe, it was decided that the Wigeon should target daily commuters and short overnight trips, as these account up to 80% of regional travels and are mostly within 300 km, the target range of mission. Moreover, increasing the range by another 50 km allowed for an increase in customer base by 36%. The cost and price of one unit was estimated to be roughly 940 thousand euros and 1.8 million euros respectively, leading to the break-even point at 152 units.

The technical design phase began with an aerodynamic analysis. The wing planform was defined with the selected airfoil being NACA 44017 for both wings, a sweep quarter-chord angle of 0 deg and a taper ratio of 0.45. The wing performance was evaluated along with the tips which were all modelled with lifting line theory. Then the propeller wing interaction was determined, along with the drag polar which permitted the modelling of the transition to horizontal flight, showing that the latter assists in the reduction of the surface area. Moreover, given the span limits of the aircraft, it was decided to include blended winglets, with a total height of 0.4 m improving the aerodynamic efficiency of the Wigeon. The validation of the model was finally conducted using CFD shown to be in high agreement with the implemented models.

The propulsion and power subsystem design for the Wigeon project consisted in the design of propellers to maximise efficiency and ensure that the wide variety of needed thrust levels can be achieved. The selected number of engines was 12 (3 per half wing), ensuring sufficient redundancy and ground clearance. To avoid problems with wing positioning and rotation, it was decided to leave a clearance of 0.3 m between the propeller tip and the fuselage and other propellers. With the latter, the final radius of each propeller was 0.5029 m, based on blade element momentum theory (BEM). The thrust values were: 158 N, 2502 N and 3745 N for cruise, hover and full thrust respectively. The final stage was to estimate to size the power system and estimate noise which was found to be: 74.85 dB at a 100 m distance. The battery estimations yielded a value of 886.2 kg and a powertrain mass of 502.6 kg for a total of 16483 cells.

The design is consolidated with a flight performance analysis which detailed the performance related aspects of the vehicles. This began with a simulation of the Wigeon during transition from stand-still to cruise and vice versa. This proved the ability of the aircraft to perform these manoeuvres and showed that accelerations did not exceed 0.2 g. Next, an energy estimation of a 300 km mission, including 15 minutes of loiter was performed. Furthermore, a performance evaluation of the rate of climb in cruise and vertical configuration was done, along with a payload-range diagram. This was concluded with a sensitivity study for different parts of the model, as well as the validation of the models used. It was found that the Wigeon cruises most efficiently at 72.2 m/s. At this speed, it has a range of 400 km, and can loiter for 15 minutes. This high range resulted from a 10 % contingency applied to the MTOM to size all systems.

Continuing with stability and control, in which the criteria for stability and control were defined for both flight conditions hover and cruise. The wings were sized and positioned at the front and the very rear of the vehicle in order to ensure optimal control authority at stall and positive stability margin at cruise. The optimal size for stability is determined to be uneven, although this was not selected. The landing gears were

then positioned to not be below passengers and sized to have a height of 0.6624 m and a track width of 1.850 m. The vertical tail and rudder sizing followed to ensure lateral controllability (for an OEI condition) and stability which lead it to be 1.503 m tall. In terms of pitch and roll controllability, an elevon was sized in order to provide sufficient positive pitching moment at stall and ensure a roll rate specified by regulations. The elevon's chord ratio was found to be 0.25 with a span ratio of 0.868, with the aileron placed at 47.03% of half-wing span.

The aircraft's dynamic behaviour was analysed using a combined method of derived analytical equations and semi-empirical relations in order to compute the stability and control derivatives. A special design consideration was given to the unstable Dutch Roll and Spiral modes for lateral motion which led to a necessary dihedral of the wings of –0.5 deg and –4.0 deg for the forward and rear wings respectively. The stability and control design ends showing how to improve the damping of the longitudinal dynamics and ensure lateral stability with a feedback loop controller.

The structural design began with an a flight envelope where a maximum load factor during a cruise gust was discovered, equation to 3.4. The structure thereafter is designed for an ultimate load factor of 5.1. The wingbox was primarily designed against buckling and yielding using the Von Mises failure criterion. The wingbox resulted in 1.3 mm skin and 18.7 mm vertical spars, placed at 0.15% and 0.75% of the chord, caused by large vertical shear forces. With an addition of only 3 stringers, the buckling could be fully prevented. Fatigue and aeroelasticity effects were also taken into account, with fatigue mainly focusing on the lug design and aeroelasticity focusing on flutter, leading to a design of a propeller support with stiffness of 3875 kN/m and a lug that is safe-life for 46,000 flights. Crash-worthiness was thoroughly analysed, deeming the aircraft safe after an optimised landing gear design as well as the energy absorbing honeycomb structure made out of aramid composite that was introduced. The Maximum Take-Off Mass was estimated to be 2.8 tons after a Class II weight estimation iteration. The structure is almost entirely made out Aluminium 2024-T3 and Aluminium 7075-T6, further aiding sustainability and ease of manufacturing.

The final design outlined the integrated design program which was used to come up with a convergent design, the specifications of which can be found below. Next, an local optimisation with respect to energy consumption was performed using this program. The result was an aircraft with an MTOM of 2125 kg, a cruise speed of 65 m/s and an energy consumption of 159 kWh for a 300 km mission including 15 minutes of loiter. This is the result of a purely numerical simulation, and should still be analysed further in a later design stage. This is followed by the sustainability approach taken. There, the three pillars of sustainability (social, environmental and economic) were used to plan efforts towards obtaining a sustainable design.

Lastly, the compliance of the final design to the requirements that were previously set was assessed, showing that most of the requirements were respected with a small number that will be investigated in the future. With all the aforementioned, the final values of the design can be found in the table below.

Final design parameters of Wigeon

Parameter	**Value**	**Parameter**	**Value**
MTOM [kg]	2790.1	Wing span [m]	8.2
OEM [kg]	1428.9	Total wing area [m^2]	19.8
Range [km]	400	Fuselage length [m]	7.3
Cruise speed [m/s]	72.2	Lift to Drag ratio [-]	16.3
Stall speed [m/s]	40	No. of engines [-]	12
Battery capacity [kWh]	301.1	Maximum Thrust [kN]	34.3
Battery recharge time [min]	25	Payload mass [kg]	440
No. passengers and pilot [-]	5	Cost [€]	938 700

Contents

Nomenclature **vii**

1 Introduction **1**

2 Configuration & Layout **2**

2.1 Trade-off . . . 2

2.2 Final Configuration . . . 2

3 Market Analysis **4**

3.1 Target Industries . . . 4

3.2 Market Calibration . . . 5

3.3 Competition Analysis . . . 8

4 Financial Plan **10**

4.1 Unit Cost Analysis . . . 10

4.2 Direct Operational Cost . . . 11

4.3 Return on Investment . . . 12

4.4 Future Development of the Project . . . 14

5 Functional Analysis **17**

5.1 Functional Breakdown Structure . . . 17

5.2 Functional Flow Block Diagram . . . 17

6 Technical Risk Analysis **20**

6.1 Risk Assessment & Identification . . . 20

6.2 Risk Prevention and Mitigation . . . 22

7 Aerodynamic Design **25**

7.1 Wing Configuration and Planform . . . 25

7.2 Airfoil Selection . . . 26

7.3 Wing Performance . . . 27

7.4 Drag Polar . . . 32

7.5 Aerodynamics Model for Transition . . . 34

7.6 CFD Analysis . . . 35

7.7 Sensitivity Analysis . . . 36

7.8 Verification and Validation . . . 38

8 Propulsion **40**

8.1 Propeller Positioning and Sizing . . . 40

8.2 Design of the Propeller Blades . . . 41
8.3 Analysis of the Blades in Off-Design Conditions . . . 45
8.4 Final Propeller Design and Performance Parameters . . . 47
8.5 Noise Analysis . . . 48
8.6 Sensitivity Analysis . . . 49
8.7 Verification and Validation . . . 50
8.8 Future Recommendations . . . 51
9 Power **52**
9.1 Energy Storage Method Selection . . . 52
9.2 Battery Information and Characteristic Values . . . 52
9.3 Power Budget . . . 53
9.4 Battery Sizing . . . 54
9.5 Remaining Powertrain Characteristics . . . 54
9.6 Battery Configuration . . . 54
9.7 Compliance with Requirements . . . 55
9.8 Sensitivity Analysis . . . 56
9.9 Verification and Validation . . . 56
9.10 Future Recommendations . . . 56
9.11 Aircraft System Characteristics . . . 57
10 Flight Performance **58**
10.1 Energy Estimation . . . 58
10.2 Performance Evaluation . . . 62
10.3 Sensitivity Study . . . 63
10.4 Verification and Validation . . . 64
11 Stability and Control **67**
11.1 Criteria for Stability and Controllability . . . 67
11.2 Design for Stability and Controllability . . . 70
11.3 Dynamic Analysis . . . 79
11.4 Controller Design . . . 88
11.5 Compliance with Requirements . . . 91
11.6 Verification and Validation . . . 92
12 Structures & Materials **94**
12.1 Load Identification . . . 94
12.2 Wingbox Design . . . 95

12.3 Fuselage Design 99
12.4 Material Selection 102
12.5 Design Against Fatigue 104
12.6 Corrosion 106
12.7 Crashworthiness 107
12.8 Aeroelasticity 110
12.9 Component Weight Estimation 113
12.10Verification & Validation 115
13 Integration and Optimisation **117**
13.1 Integration 117
13.2 Optimisation 117
13.3 Three View Drawings 119
14 Resource Allocation and Budget Breakdown **121**
15 Sustainability Approach **122**
15.1 The 3 Pillars 122
15.2 Lean Manufacturing 122
15.3 Influences on Design 122
16 Production Plan **125**
16.1 Manufacturing Methods 125
16.2 Assembly 126
17 Operations and Logistics **128**
17.1 Detailed Description 128
17.2 RAMS 129
18 Requirements Compliance **131**
18.1 Compliance with the Mass Requirement 131
18.2 Change in Requirements 131
18.3 Recommendations on Unverified Requirements 132
19 Conclusion & Recommendations **134**
19.1 Conclusion 134
19.2 Recommendations 135
References **139**

Nomenclature

Abbreviations

Abbreviation	Definition
ac	Aerodynamic Centre
ACAI	Available Control Authority Index
ADT	Actuator Disk Theory
BC	Boundary Condition
BEM	Blade Element Momentum Theory
CAD	Computer Aided Design
CAGR	Compounded Annual Growth Rate
CapEx	Capital Expenditure
CFD	Computational Fluid Dynamics
CG	Centre of Gravity
DoD	Depth of Discharge
DSE	Design Synthesis Exercise
EASA	European Union Aviation Safety Agency
EOLC	Fraction of capacitance of battery retained at end of life
eVTOL	Electrical Vertical Take-Off and Landing
FBD	Free-body diagram
FAA	Federal Aviation Administration
GA	General Aviation
ICAO	International Civil Aviation Organization
IRR	Internal Rate of Return
ISA	International Standard Atmosphere
KTAS	True Airspeed expressed in knots [kts]
MTOM	Maximum Take-Off Mass
NPV	Net Present Value
OEI	One Engine Inoperative
OEM	Operating Empty Mass
RAMS	Reliability, Availability, Maintainability, and Safety
RANS	Reynolds-Averaged Navier-Stokes
ROI	Return on Investment
Sdr	Specific turbulence Dissipation Rate
SST	Shear Stress Transport
TPM	Technical Performance Management
VTOL	Vertical Take-off and Landing
V&V	Verification and validation

Symbols

Symbol	Definition	Unit
a	Axial interference factor	[-]
a′	Rotational interference factor	[-]
A_{prop}	Propeller area	[m^2]
AR	Aspect ratio	[-]
b	Wing span	[m]
B	Number of blades of the propeller	[-]
$\bar{c}$	Wing chord	[m]
c_{fp}	Fuselage-propeller clearance	[m]
c_{pp}	Propeller-propeller clearance	[m]
C	Cost	[$] or [€]
C_d	Drag coefficient of the airfoil	[-]
C_D	Drag coefficient of the wing	[-]
C_l	Lift coefficient of the airfoil	[-]
C_L	Lift coefficient of the wing	[-]
C_{L_α}	Lift gradient	[rad^{-1}]
C_m	Pitch moment coefficient	[-]
C_n	Yaw moment coefficient	[-]
C_X	Forward force coefficient	[-]
C_Y	Side-force coefficient	[-]
C_Z	Down-force coefficient	[-]
C	Capacity	[Ah]
D	Drag	[N]
e	Oswald efficiency factor	[-]
E	Energy	[J] or [Wh]
E_{sp}	Specific energy	[Wh/kg]
E_{vol}	Volumetric energy density	[Wh/l]
G	Non-dimensional Circulation	[-]
G_p	Gap	[m]
h	Altitude	[m]
J	Advance ratio	[-]
K	Maximum thrust per engine in hover	[N]
k_μ	Ratio of reactive torque to thrust	[-]
L	Lift	[N]
$\mathcal{L}$	Aerodynamic roll moment	[Nm]
M	Aerodynamic pitch moment	[Nm]
n	Load factor	[-]
n	Propeller rotational speed	[rps]
N	Aerodynamic yaw moment	[Nm]
$\dot{m}$	Mass flow	[kg/s]
p	Roll rate	[rad/s]
P	Power	[W]
P_{den}	Power Density	[W/kg]
q	Pitch rate	[rad/s]
q_∞	Freestream dynamic pressure	[Pa]
r	Yaw rate	[rad/s]
r	Local radius of the propeller blade	[m]
R	Propeller radius	[m]
S	Wing surface area	[m^2]
S_t	Stagger	[m]
t	Time	[s]
T	Thrust	[N]
v	volume	[m^3]
V	Velocity	[m/s]
V	Voltage	[V]
W	Weight	[kg]
y^+	Dimensionless wall distance	[-]
α	Angle of attack	[deg]
β	Sideslip angle	[rad]
β	Blade pitch angle	[rad]
Γ	Circulation	[m^2/s]
δ	Control surface deflection	[rad]
ϵ	Downwash angle	[rad]
ε	Drag-to-lift ratio	[-]
η	Efficiency	[-]
θ	Pitch angle	[rad]
λ	Taper ratio	[-]
Λ	Sweep angle	[rad]
μ	Dynamic viscosity	[N·s/m^2]
ξ	Non dimensional propeller radius	[-]
ρ	Density	[kg/m^3]
σ	Stress	[MPa]
ϕ	Roll angle	[rad]
ϕ	Local flow angle in the blade	[rad]
ψ	Yaw angle	[rad]
ψ_{TO}	Turn-over angle	[rad]
Ω	Propeller rotational speed	[rad/s]

1 Introduction

The widespread interest of electrical Vertical Takeoff and Landing (eVTOL) vehicles has accrued ample momentum over the years to spark a new flying revolution. A revolution in which man can fly whenever he pleases, like the Wigeon, a carefree and aerial duck that possesses the capability to vertically take off. However, several technological and socioeconomic obstacles lie before the widespread adoption of urban air mobility vehicles such as eVTOLs. In order to bridge some of these gaps, a multidisciplinary design of one such concept (colloquially referred to as Wigeon) is conducted and the results presented in this report.

The aim of this report is to present a multidisciplinary preliminary design of an electrical vertical takeoff and landing (eVTOL) aircraft and to evaluate the compliance of the design to the requirements outlined in the baseline stage of the design. In order for this to be realised, the vehicle was divided into subsystems that were each modelled by their corresponding discipline, and the models were validated. These disciplines were the aerodynamics, stability and control, structures and performance, each of which modelled the phenomena that their respective subsystem encounters. This was coupled with the foresight of other non technical aspects such as sustainability and risk analysis as well as evaluation of the aircraft's operations and logistics. Lastly, the adherence of the designed aircraft to the requirements is evaluated and discussed.

The report is outlined as follows. In Chapters 2 to 14 the non technical aspects of the design are introduced and discussed. These are followed by the technical design of the aircraft in Chapters 7 to 10. In each technical chapter, first the requirements and necessary analyses are declared. Thereafter the analyses are conducted and the compliance to requirements assessed. Lastly, the methods used are verified and validated. Then, the non technical aspects of the design that pertain to flight, operations and sustainability are explicated in Chapters 13 to 17. Finally, the compliance of the design is presented in Chapter 18 with which the report is concluded in Chapter 19.

2 Configuration & Layout

In this chapter the trade off previously conducted between the three configurations is described, along with a preliminary design of the final chosen configuration.

2.1. Trade-off

Previously, a trade-off was conducted in order to select a configuration out of three options. To do so, a multidisciplinary approach to analyse the strengths and weaknesses of each of the three concepts, in sufficient depth, was necessary. Through the process of analysing the different options, a better defined configuration and layout had to be chosen for each of the three concepts. All the concepts have some aspects in common such as the fuselage layout, which is presented in Section 2.2. As can be observed a 1-2-2 seat configuration is chosen for passenger comfort, with large cargo located at the back to minimise the cross-section. Furthermore, solid state batteries were chosen for all the different configurations as the energy source, as it was deemed to be an aspect independent of the configuration.

Finally, by analysing and simulating the flight performance during cruise, transition and hover for the configuration, as well as computing the critical loading cases that the eVTOL will encounter during service, it was possible to compute a class II weight estimation for the aircraft, which yielded a Maximum Take-Off Mass of 1867.7 kg and an Operational Empty Mass of 1307 kg.

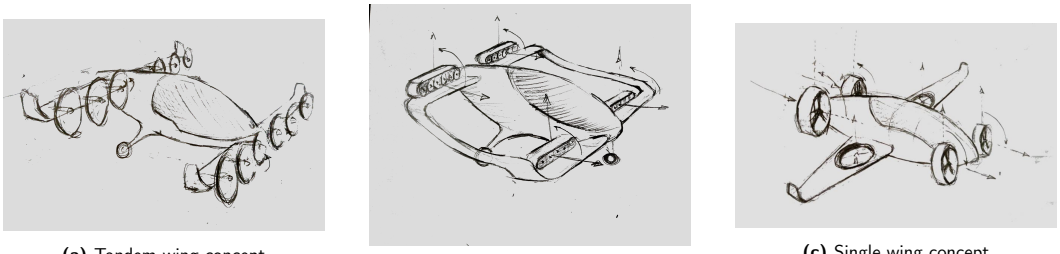

(a) Tandem wing concept

(b) Box wing concept

(c) Single wing concept

Figure 2.1: Drawings of all three proposed concepts

2.2. Final Configuration

After the trade-off, the best overall configuration out of the three was the tandem configuration, for which a conceptual drawing is shown in Figure 2.1a. This concept uses leading edge open propellers for propulsion, providing a higher air velocity over the wing. In order to achieve vertical take-off and landing, a system will be designed to allow the entire wing to rotate about its spanwise axis. By doing this, the downwash of the propellers will not hit the top surface of the wing when taking-off or landing vertically. A total of 12 engines will be used with a propeller area of 0.47 m^2 per engine. Regarding the wing planform, both wings were chosen to be identical, as according to literature, for a tandem configuration, having equal span wings reduces induced drag [114]. For lateral stability, it was found that a vertical tail is needed. The two front landing gears are placed below and to the sides of the pilot and the two rear ones are just behind the passenger cabin. These landing gears, together with the possibility to tilt the wings to direct the thrust, make the aircraft compliant with requirement VTOL-GND-3, which requires the aircraft to taxi autonomously. Due to the small width of the fuselage, in order for the turnover requirement for stability on ground to be met, the landing gear must stick outside to the sides of the fuselage, this is explained in more detail in Section 11.2.3. The layout of the cabin is displayed in Figure 2.2 with the aid of technical drawings of the fuselage including the wings for reference.

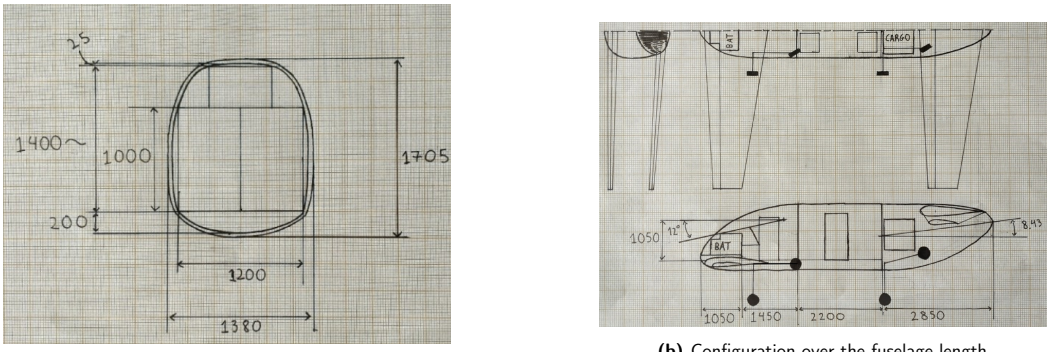

(a) Fuselage cross section

(b) Configuration over the fuselage length

Figure 2.2: Fuselage cabin configuration

For sizing the fuselage, the smallest diameter as possible was used while ensuring passenger comfort. The sizing procedure is that found in [126], in which it is stated that a 10% larger fuselage can result in up to a 3% increase in total drag. The fuselage is the largest contributor to parasitic drag, therefore making it crucial to have it be as small as possible. The slightly rectangular fuselage was made as it is not pressurised and therefore does not carry loads, although straight edges are avoided in order to minimise the occurrence of cracks that may nucleate due to large stress concentrations [126]. The tail cone upsweep angle was made in order to minimise drag but still ensuring that the back wing can still be placed at a considerable vertical distance from the front wing to minimise interaction between the wings. This fuselage is a closed volume, which makes the aircraft compliant with VTOL-SOC-1 and VTOL-STK-15. Only one Type I door is implemented as this is a relatively small aircraft which negates the use of multiple doors which only add extra stress concentrations due to their openings [126]. A type II door also has to be placed for the pilot, since the cockpit is separate from the passenger cabin. This makes the aircraft compliant with the requirement VTOL-SAF-1 about emergency exits. Lastly, it is worth mentioning that the cockpit dimensions are sized such that all controls are accessible for a single pilot, thus complying with VTOL-CTL-1.

The seating configuration will be include pilot in the front, coupled with two rows of two seats of passengers. It can be seen that due to the width of the fuselage, each seat will occupy 0.5 m of width, with a 10 cm armrest in the middle for passenger comfort. This will also allow the gap to contain a storage location for safety equipment, which will leave room under the seat for extra leg space for passengers sitting behind. Lengthwise, it is evident that there is 2.2 metres of cabin space for the passengers, which means that the seat pitch is approximately 1 metres, a typical value for the business class in medium range aircraft [126] (with the two aftmost passengers being against the back wall, and the front two against the front wall). This ensures maximum comfort and complies with requirements VTOL-STK-19, VTOL-STK-20 on cabin design, thus meaning that also VTOL-PLD-5 and VTOL-PLD-6 and all their sub requirements are surpassed.

It is noticeable that in this report two nominal constituents of technical reports are not included: the hardware and software block diagrams, the electrical block diagram and the data handling block diagram. However, the inclusion of these diagrams are considered superfluous due to the flight control systems not being precisely modelled since this is a preliminary multidisciplinary design. Usually, the control and communications systems are designed and implemented in the more detailed phase in the design. Moreover, they are made during the final stage of the design, as they require several considerations of a detailed design to already be conducted, which makes this task more difficult to perform on a vehicle that has not ever been produced or even designed. All of the above serve as reasons as to why the previously mentioned diagrams are not included in this report. This has been agreed with by the tutor and OSCCs.

3 Market Analysis

This chapter deals with a market analysis investigating the feasibility of selling eVTOLs in the market. Section 3.1 lists the potential markets to be explored where eVTOLs could be sold. Then, in Section 3.2, the market share for the proposed eVTOL product is estimated in terms of monetary value and number of units. Section 3.3 details the competitors and challengers present in the eVTOL industry. Due to limited resources, time and manpower, this analysis was constructed through the use of already existing articles and reports from key players in the aerospace industry.

3.1. Target Industries

The very first step of a market analysis for this eVTOL product is to identify all the potential industries where the use and purchase of VTOL units could have a large impact. These include but are not limited to:

- Government and military industry.
- Emergency services: police, firefighters, ambulance and natural disaster response officers.
- Commercial transport.
- Logistics and cargo transport: aerial warehousing and delivery.
- Entertainment, leisure and media.
- Construction and building maintenance.
- Private use.

The team prioritised those industries that are deemed as the most relevant to the type of product to be developed. In this case, the emergence of long range eVTOL aircraft will screen the markets for commercial transport, entertainment and private use. This idea is reinforced by the observed trends during the 2010s decade where the desire and need to adopt Urban Air Mobility (UAM) systems have increased to the point where 1.3 billion US dollars have already been invested in 2021 and is currently rising [1]. If the product is focused on this industries we can identify a number of stakeholders:

- Passengers: they are the customers of the product
- Pilots: they are needed to operate the aircraft.
- Citizens: the noise created by the aircraft could disturb citizens.
- Government: They set the regulations that the aircraft has to follow.
- Competitors and manufacturers: the eVTOL is a substitute of a number of current means of transport like helicopters.
- Public transport: the eVTOL could be a future alternative to trains and buses.
- Car manufacturers: the eVTOL could be a future alternative to travelling by car in order to avoid traffic congestion.
- Energy source provider: whether it is batteries, fuel cells, hydrogen, etc. Success of the eVTOL will result in good marketing for the provider.

One of the main requirements of the Wigeon developed by this team defines a maximum range of at least 300 km, which one can attribute to intercity travel when targeting potential travellers. Figure 3.1 illustrates different travel options within UAM mainly differing in the distance to be covered. The Wigeon will be designed to accomplish this 300 km range, but this does not exclude the fact that the same product can be used for intracity and smaller distance travelling; and in the same way, this does not exclude that this team's eVTOL product can be used outside commercial and private transport.

In 2014, the German-based Institute for Mobility Research (IFMO) [99] published a study in which the current trends and future perspectives of long distance mobility were analysed. Table 3.1 collects the results

[1] URL http://interactive.aviationtoday.com/avionicsmagazine/february-march-2021/evtol-investments-will-continue-billion-dollar-trend-in-2021/ [cited 29/06/2021]

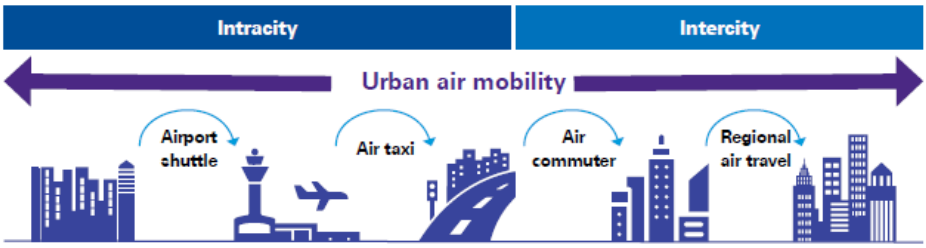

Figure 3.1: Emergence of a new mobility option [77].

of an investigation in current travel demand of German people. It can be observed that a large percentage of both the number of trips and the average travel distance correspond to around 300 km long intercity journeys, which suggests that the implementing this team's eVTOL product could achieve a high penetration rate in the market segment around commuters, tourists, business and personal trips. It is reasonable to extrapolate this observation to the whole of Europe and European population since Germany is one of the main economies of the European region. Additionally, IFMO state that demographic and spatial development, together with economic evolution and the rise of new technologies are major drivers affecting long distance mobility, increasing the need of more aerial transportation methods. This is supported by a study performed by Airbus in 2019, where it is expected that passenger traffic will grow by 4.3 % and approximately 39 000 new aircraft will be delivered by 2038 [4].

Table 3.1: Number of trips per person and average distance travelled per trip [99].

Segment	Number of trips per person	Average travel distance [km]
Holiday trips (5+ days)	1.0	1 600
Short holiday trips (2-4 days)	1.2	410
Other personal overnight trips	0.3	410
Personal day trips	6.0	200
Overnight business trips	1.2	500
Business day trips	1.2	150
Long-distance everyday personal trips, commuting and business trips	5.0	150

Therefore, the customers to target are the segment of people living among the largest metropolitan settlements with a potential desire to mobilise through urban, suburban, regional and rural areas. Another lucrative segment include those people with a higher income per capita who wish to spend more attempting to evade today's urban mobility problems more comfortably and spanning the same kind of cities.

Market feasibility for such a project can be broken down to consumer demand, operations, infrastructure and timing of all industries involved with aerospace products. All these factors point to the United States and European regions, as well as Asia's largest cities, which offer the best possibilities in terms of eVTOL implementation within society. Thus, these two regions would become the main geographical targets to consider and approach. As a result, the market study performed in this report will exclusively focus on selling eVTOL products within the identified potential markets. The financial and business plans will be built accordingly to ensure success of this promising project.

3.2. Market Calibration

The race to dominate urban skies has prompted many key players from the aerospace industry to understand the feasibility of developing projects related to Urban Air Mobility. As a result, many market analyses and studies have been recently published by a range of consultancy firms. For example, the firm BIS Research projects that by 2035, the VTOL market will reach 1.9 billion US dollars [15]. On the other hand, NASA hired both McKinsey & Company and Crown Consulting firms constructing parallel analyses. McKinsey believe that market size for Air Taxis (short distance UAM) will reach as high as 500 billion US dollars [78]. Other studies performed by IDTechEx [59] and Deloitte [41] predict that the global market will rise as much as 14.7 and 17.7 billion US dollars by 2040. Moreover, Reports and Data [103] collected that the market size will reach 7.9 billion US dollars by 2030. While these notorious firms present a significant range in their estimations, one can be certain that the market potential of Urban Air Mobility is only going increase from this point onward and become hugely profitable. Based on these reports, the team has established that the

market size for eVTOLs within commercial transport and private use is highly likely to be around 15 billion US dollars by the year 2040.

Next, in order to determine the market size in terms of aircraft unit, the retail price for a single eVTOL must be estimated. To do so, a comparison with direct competitors was carried and explained later in Section 3.3. In essence, the average price of a helicopter was deemed to be 1.8 million US dollars. Early estimations for eVTOL aircraft suggest that the price of a two-seater aircraft will be as high as 1.5 million US dollars, while for its four-seater airliner counterpart can cost up to 3.5 million US dollars. These insights were estimated by Trascend's chief operating officer [2], who also estimated a price of 6 million US dollars for an executive version of an eVTOL aircraft. However, production costs will be reduced as time progresses due to the evolution of necessary infrastructure, evolution in materials with better properties and manufacturing methods. Sale patterns and cost reduction are illustrated in different stages in Figure 3.2. It can be deduced how helicopters currently lie towards the later stages of decline, creating a gap that can be replaced with the emerging market of eVTOLs. Since eVTOLs are still in development and targeting year frames between 2025 and 2040, it is reasonable to suggest that the eVTOL market currently lies the introduction phase and that it will eventually reach the start of the growth phase by 2035. Multiple studies provide evidence of this, where the Compounded Annual Growth Rate (CAGR) is estimated to have a value of 11.1 % between 2021 and 2026 [125] and 13,75 % between the years 2025 and 2035 [15, 14]. As a result, the team forecasts that the initial price for an eVTOL unit can be estimated to lie around 3 million US dollars with the long-term objective of reducing the price down to 1.5 million US dollars.

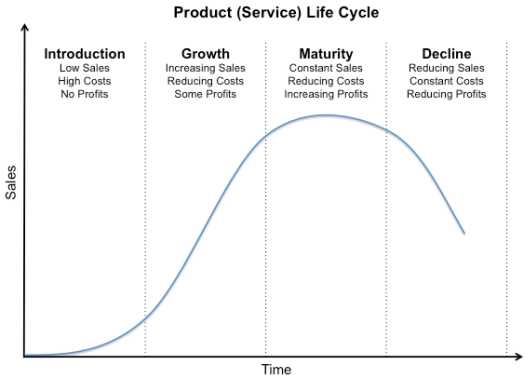

Figure 3.2: Product Life Cycle [19].

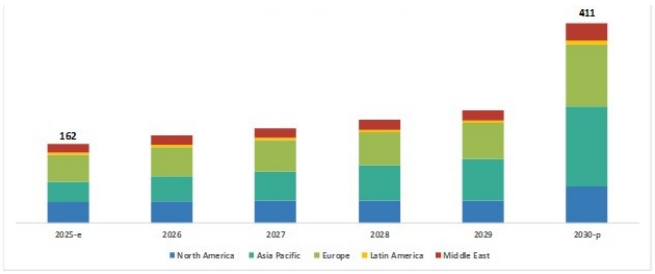

Figure 3.3: eVTOL aircraft market size by region (USD million) [73].

The market size as a number of eVTOL units follows from a simple computation dividing the monetary value of the market size by the expected price for a single unit. This yields an estimation of 5 000 eVTOL units to be produced and sold only in 2040. The market share that could be achieved by this team's eVTOL was divided by region. To do a unit breakdown estimation, the team relied on the current helicopter market where there exist 26 500 civil helicopters worldwide [52] from which a maximum of 15 000 are registered in the US [3]. Nonetheless, KPMG claim that the North American and European markets will have similar size, but emphasise how the Asia-Pacific and middle east regions will prominently dominate the intracity scene rather than intercity travel [77]. On the other hand, in the analysis performed by Markets and Markets [73, 74], it is claimed that Asia-Pacific will have the largest and fastest growing eVTOL market by 2030, where major players like Chinese company Ehang are set to take large market shares. As a result, the team crafted a regional market breakdown, with estimations based on the region's readiness to adopt necessary infrastructure, legislation and regulation, in combination with the presence of large potential markets. The estimations are collected in Table 3.2.

Due to the extensive competition and the threat of important players, one cannot expect to achieve a large market share over the entire globe. Instead, the team has set regional targets to capitalise on the forseen market opportunities. As a result, the team aims to achieve a medium market share of 8 % in Europe which translates in 140 eVTOLs production and sale rate per year in 2040 and a low 2 % market share, or 60 eVTOL units, for North America and Asia-Pacific. The team also expects to take a market share of 2% for

[2] URL https://robbreport.com/motors/aviation/vtol-new-type-of-helicopter-2906415/ [cited 29/06/2021]
[3] URL https://www.grandviewresearch.com/industry-analysis/commercial-helicopters-market [cited 29/06/2021]

the rest of the world whose markets have not been prioritised, therefore selling an additional 5 aircraft. In total, the team should achieve producing and selling around 205 eVTOL units per year in 2040 (again shown in Table 3.2), excluding those units effectively sold to be used outside commercial and personal transport. The team deems appropriate to focus on Europe during the early stages of production for a number of reasons, including the upcoming European Union climate-neutral policies and legislation together with the increasing number of manufacturing bases for these advanced aircraft. On the other hand, the team believes that expanding to the North American and Asia-Pacific markets should be done slowly and is to be tackled on a second stage after a solid core of sales in Europe. The team anticipates that selling some units in these markets will help with branding, but shall not be high enough as to hinder production capabilities. Other markets like the Chinese are very prone to set up their own firms with solutions similar to existing products, as observed within computer, vehicle, aircraft and other high-tech industries.

Table 3.2: eVTOL 2040 market breakdown and sales expectation per region.

Region	% Market size	Projected Total Number of Aircraft	Expected Number of Sales
NA	30	1500	30
EU	35	1750	140
Asia-Pacific	30	1500	30
Rest of World	5	250	5

205 eVTOL units per year seems to be a feasible objective, based on a report for the design of a eVTOL, which claims that producing below 450 units is not economically feasible due to the high RDT&E costs per aircraft [131]. The team aims to produce and sell 205 eVTOLs only in 2040, meaning that a much higher number will be produced and sold over the entire project lifespan. For example, assuming a total production of 1000 eVTOLs over a 5 year span yields a value of 200 eVTOL units, which is very close to the 205 units estimated based on the suggested market shares.

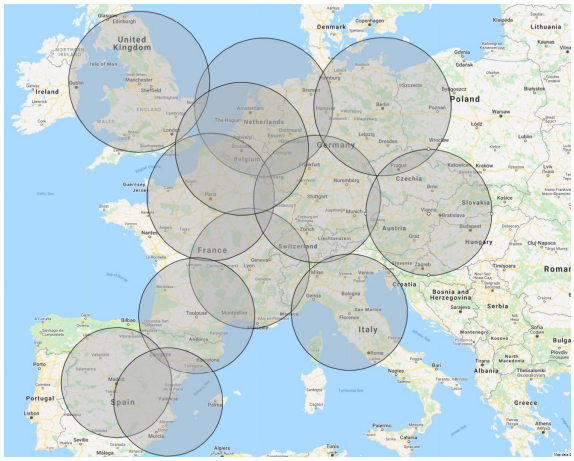

Figure 3.4: European map with 300 km radii circumferences around selected cities.

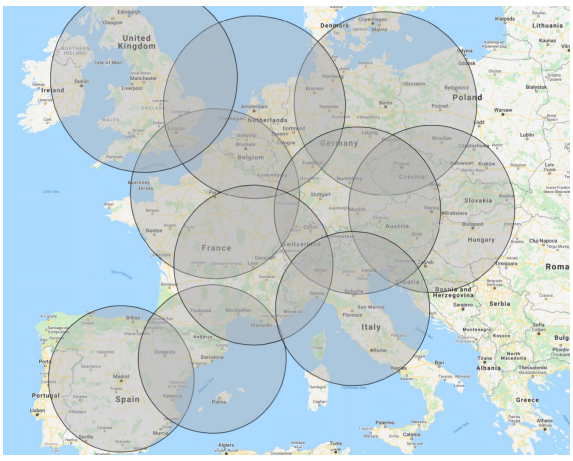

Figure 3.5: European map with 400 km radii circumferences around selected cities.

This should be achievable by crafting a financial plan in which the team first focuses on selling in Europe and then expands to the rest of the world. To verify this, the team compared how eVTOL travelling would perform against other intercity means of transport. It is estimated that by 2040, 42 pairs of North American cities will run eVTOL routes [55]. Figure 3.4 illustrates 300 km radii circumferences around selected major European cities, from which it can be clearly observed that most major cities can be connected with direct eVTOL flights or through a connection in a secondary city. It is an example of how wide can this type of aircraft cover long mobility needs while offering a decrease in traffic congestion, traffic accidents, transport time, pollution and reducing the strain in already existing public transport networks.

It is also worth noting that from Figure 3.5 it can be noticed that by increasing the range by 50 or 100 km the travel options could be significantly expanded, for instance, Paris - London , Florence - Naples and Madrid - Bilbao would be possible. Due to this, it is expected that the number of customers when increasing the range would also increase significantly, and thus the market share and the number of units sold of the

Wigeon would increase. It must also be added that as shown in Figure 3.7, no eVTOL has a range above 300 km, hence all customers that want to travel over 300 km thorugh an eVTOL would have to fly with the Wigeon. To estimate the increase in units produced and market size we can use the increase in covered area. If we assume that cities and therefore population are spread homogeneously, the number of trips available by increasing the range can be assumed to increase proportionally to the area covered by the eVTOL, which is proportional to the range squared. Assuming the evenly spread population would not be a valid assumption for smaller scales, since the population density is greater near city centres. However, in scales above 50 km this is no longer significant [30]. Based on this principle the number of customers for the eVTOL would increase 36 % for a 50 km increase and 78 % for a 100 km increase. This would mean selling 279 units or 365 units for 50 and 100 km increases respectively in 2040 instead of the predicted 205. However, in reality, the product would become more expensive and customers could choose to use a different travel method, or perhaps to break the trip in two halves which would lower this increase in market size.

This transit network would only become a reality with the governmental support to develop the necessary infrastructure. The concept of vertiports has gained strength lately in the scene thanks to its characteristics. A vertiport is designed to act as a modular hub for eVTOLs. Its design offers flexibility and takes much less space than an airport facility. Its price ranges from 1.5 million US dollars for a small 2-parking vertiport to 15 million for a larger 8-spot vertiport. Vertiports offer numerous important advantages over regular airports, such as the amount of space used and a lower cost per traveller. A SWOT analysis was also conducted to identify the strengths and weaknesses of the project focusing on the market, it is shown in Figure 3.6.

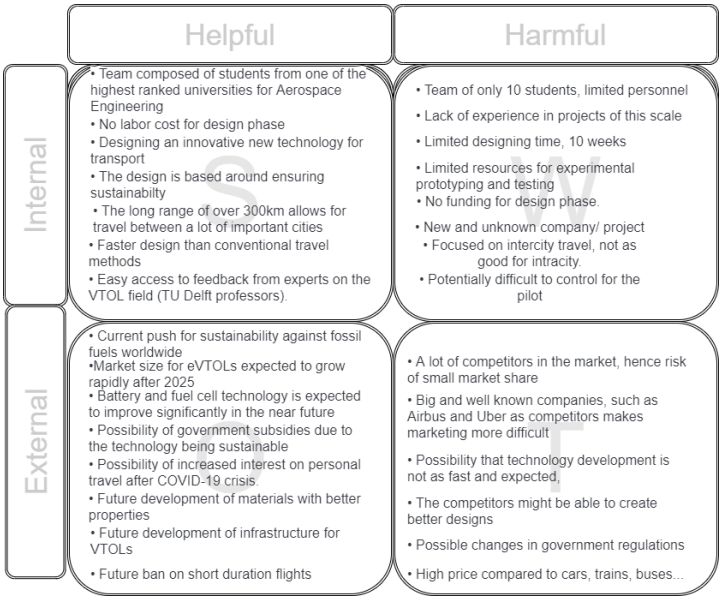

Figure 3.6: SWOT analysis for the project regarding market competitiveness.

3.3. Competition Analysis

The competition for the Wigeon aircraft being developed can be divided into two main categories, direct, and indirect competition. Indirect competitors are any type of method that can transport people from one city to another, regardless of the method. This would include trains, buses, commercial transport aircraft, cars, boats, etc. More of this type of competition could appear in the future with new technologies such as the Hyperloop. However, the method of accomplishing the transportation differs largely from the method for a eVTOL. The main characteristics that separate these aircraft from the previously mentioned methods are that eVTOLs offer personal transportation, and that they transport through the air. Given this, the currently existing direct competitors for eVTOLs are other VTOLs, business jets, and mainly helicopters. Helicopters also share with eVTOLs the capacity of landing and taking off vertically, and also a more similar range and speed. The common range of values for these parameters are shown in Table 3.3 below and compared to the parameters given in the project description. Thus helicopters are the most direct competitors for eVTOLs.

Two helicopter models which can be considered to have very similar missions to the eVTOL and thus are direct substitutes are the Robinson R44 and the Airbus H125. These vehicles can both carry 4 passengers at approximately 240 km/h for distances of 450 and 540 km respectively [4] [5]. It must be noticed that despite the eVTOL having a clearly inferior range, there are 3 main factors that give advantages to eVTOLs and

[4]URL https://www.airbus.com/helicopters/civil-helicopters.html [cited 29/04/2021]
[5]URL https://www.aircraftcostcalculator.com/AircraftOperatingCosts/531/Robinson+R44+Raven+II [cited 27/04/2021]

have to be taken into account when determining the pricing [54].

1. Since eVTOLs use electric motors and have multiple rotors for propulsion, their noise level is estimated to be a 75 % less than the noise produced by a helicopter. This is important for a urban vehicle.
2. The electric motors eliminate the complex rotation mechanism and fuel system, which should simplify the structure of the VTOL. This should reduce the maintenance costs significantly.
3. The eVTOL will most likely be safer than a typical helicopter. Firstly, helicopters are difficult to manoeuvre, which can induce potentially catastrophic pilot errors. Furthermore, because the lift and thrust is produced by a single rotor, failure of this rotor will surely result in catastrophic failure. eVTOLs can be equipped with multiple rotors, such that the other rotors can compensate in case one fails.

Table 3.3: Comparison of payload speed and range for helicopters, business jets and the eVTOL project[6]

Vehicle Type	Number of passengers	Typical Range [km]	Typical Cruise Speed [km/h]
Small business jets	6-8	2800-4600	800
Helicopters	4-11	460-650	240
Wigeon	4	300	100-300

However, the competitors within the eVTOL industry must also be analysed. All the investigated eVTOL concepts are still in development, and most of them do not provide the estimated price. However other relevant performance parameters such as the speed, number of passengers, and range were available. These are plotted in Figure 3.7 below. The name of each of the eVTOLs is presented [7] [8]:

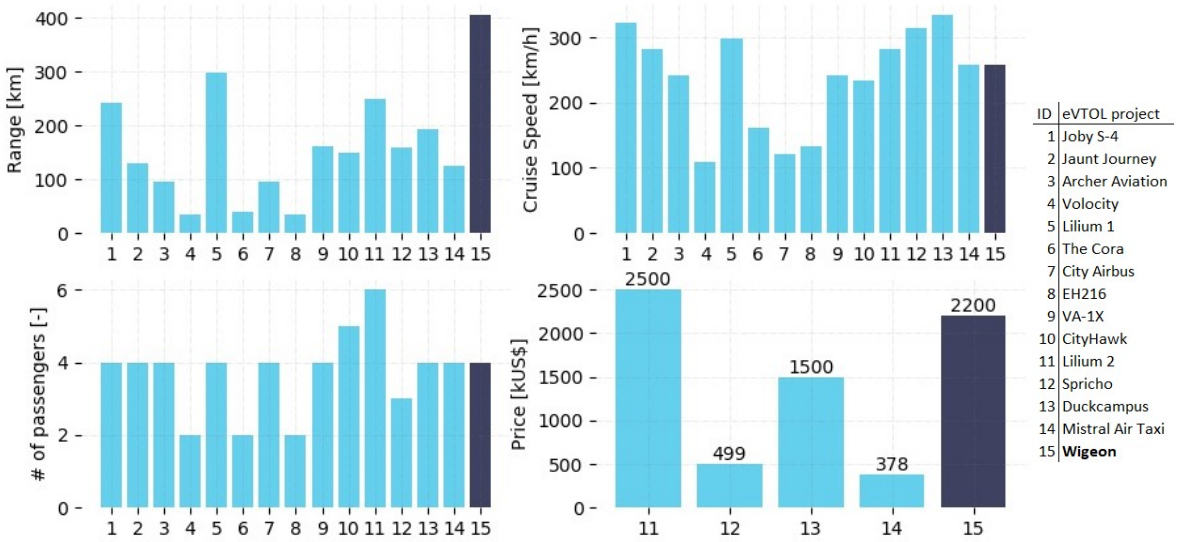

Figure 3.7: Range, cruise speed, number of passengers, and price comparison for selected eVTOL aircraft in the development phase [1, 22, 131].

It can be observed that at 300 km, this eVTOL project would match the highest available range out of all of these options, which is achieved by the Lilium jet. Thus it could also be recommendable to further increase the range in order to have the highest range out of all the eVTOL options. In terms of speed, the Wigeon is able to cruise at 270 km/h making it one of the fastest against all competitors and against trains and cars. A customer will most likely prefer the option that is fastest in order to reduce the travel time. For a number of different possible routes in Switzerland and the west coast of the US, Lilium estimated that their routes would be between 4 and 8 times faster in all cases than trains or cars, which suggests that improving travel times compared to traditional travelling methods should not be an issue [9]. The price estimation for the 3 eVTOL projects applied different methods and differ greatly, but none of the concepts have been put into production. This implies that the accuracy of the values is not verified.

[7] URL http://interactive.aviationtoday.com/avionicsmagazine/february-march-2021/10-evtol-development-programs-to-watch-in-2021/ [cited 28/04/2021]
[8] URL https://lilium.com/jet [cited 29/04/2021]
[9] URL https://lilium.com/newsroom-detail/why-regional-air-mobility [cited 29/04/2021]

4 Financial Plan

This chapter discusses the long-term monetary objectives of the business and the strategies to achieve them as crafted within the the financial plan. Section 4.1 details the procedure used to estimate the production cost of a single Wigeon eVTOL unit and Section 4.2 expands on the operational costs derived from them. Section 4.3 deals with the financial health of the business by computing the Return on Investment (ROI). Section 4.4 closes the chapter detailing the plan of attack post-DSE if the business were to continue being set up.

4.1. Unit Cost Analysis

This section describes the Eastlake Method (a modified version of the DAPCA-IV method) to reflect development and operational costs of a GA aircraft, as seen in Gudmundsson [53]. The team has used this formulation to estimate the unit cost for a single Wigeon aircraft , under the assumptions that the size and characteristics of such an eVTOL is similar to existing small GA (general aviation) aircraft. The method starts with the computation of the man-hours required for the engineering phase, tooling and manufacturing phase. Details on the computations have been explained previously [71], and the computation yielded 367699, 321440 and 266423 man hours for engineering, tooling and manufacturing correspondingly. These calculations depend on the OEM $W_{airframe}$, maximum level airspeed expressed in KTAS and the number of aircraft to be produced in a five-year span, which was determined to be 1 000 from the market analysis Chapter 3.

Gudmundsson also makes use of a number of different factors depicted by the symbol F with a corresponding subscript to indicate the influence of a system or process in the total cost. F_{CERT} is used to scale the cost based on the certification class of the aircraft. F_{CF} is influenced by the type of flap system used. The eVTOL contains no High Lift Devices (HLD), and thus omits this factor throught the whole process. On the other hand, F_{COMP} accounts for the complexity of including composite materials since the structure combines aluminium and composites. Finally, F_{PRES} depends on whether the aircraft to be designed has a pressurised cabin - which is not the case for the Wigeon. The total cost computation from these aspects follow through from the man-hours needed for each of these processes. As a result, the total costs of engineering, tooling and manufacturing can then be computed with Equation 4.1. Gudmundsson published his book in 2013, and states that the Consumer Price Index relative to the year 2012 CPI_{2012} accounts for the yearly inflation rate when estimating aircraft costs compared to those in the year 2012. These equations include salary rates R, where the values 120, 60, 50 dollars per hour are used for engineering, tooling and manufacturing respectively as suggested by Gudmundsson. As a result, the engineering C_{ENG}, tooling C_{TOOL} and manufacturing C_{MFG} costs can be computed through Equation 4.1:

$$C = 2.0969 \cdot H \cdot R \cdot CPI_{2012} \qquad (4.1)$$

$$C_{BAT} = m_{BAT} \cdot C_{kg} \qquad (4.2)$$

The total cost of development support, C_{DEV}, depends on the number of prototypes to build and test. The team has chosen four for the certification phase. Another component is the cost of quality control, which entails the technicians and equipment required to demonstrate that the product is being designed and manufactured appropriately. The total cost of flight test, C_{FT} operations involves a full certification flight-test program and should also be included. Additionally, the total cost of materials, C_{MAT} has also been computed. The formulas used for the computations of these cost components are provided by Gudmundsson [53] and can also be found in our previous report [71]. The total cost to certify, C_{CERT} is the collection of all costs prior to certification that are needed to develop the product: C_{ENG}, C_{DEV}, C_{FT} and C_{TOOL}. It is considered as the total fixed costs used later for the break-even analysis. In addition to the total fixed costs, there are several aircraft systems needed for every aircraft unit whose cost can be broken down. The cost of the engine powerplant is computed from Equation 4.3 and respectively based on the shaft-horsepower [131]. The cost of the propeller, C_{PROP} is also included in the analysis [71].

$$C_{PP} = N_{PP} \cdot \left(0.0022 \cdot P_{SHP}^3 - 0.4209 \cdot P_{SHP}^2 + 48.62 \cdot P_{SHP} + 1612\right) \tag{4.3}$$

The cost of the battery can be estimated through its mass m_{BAT} and specific cost of the battery C_{kg} with Equation 4.2. As a result, Equation 4.4 yields the unit cost per aircraft by combining the total fixed cost, manufacturing cost, quality control cost and material cost per aircraft with the engine, battery, landing gear (C_{LG}) and avionics (C_{AV}) costs. Gudmundsson also suggests an estimation for the last two. Finally, Equation 4.5 computes the number of aircraft required to produce and sell to reach the break-even point, the point where the total revenue is equal to the total costs and from which all posterior sales will result in profit.

$$\text{Unit Variable Cost} = \frac{C_{CERT} + C_{MFG} + C_{QC} + C_{MAT}}{N} + C_{LG} + C_{AV} + C_{PP} + C_{PROP} + C_{BAT} \tag{4.4}$$

$$N_{BE} = \frac{\text{Total Fixed Cost}}{\text{Unit Price} - \text{Unit Variable Cost}} \tag{4.5}$$

Table 4.1 collects the results of evaluating the Eastlake cost estimation method for the Wigeon aircraft from which it can be observed that the price requirement, VTOL-STK-09, of $ 6 000 000 is satisfied. Furthermore, the Wigeon also complies with the production and development cost requirements, VTOL-COS-1 and VTOL-COS-3.

Table 4.1: Cost breakdown and break-even expectation for the Wigeon aircraft.

Parameter	**Value**	**Parameter**	**Value**
Cost of Engineering [$]	110 658 033	Cost of Flight Operations[$]	1 018 110
Cost of Development Support [$]	3 577 069	Cost of Tooling [$]	48 368 155
Certification Cost [$]	163 621 367	**Certification Cost [€]**	137 442 030
Certification Cost [$/unit]	163 621	Avionics Cost [$/unit]	15 000
Manufacturing Cost[$/unit]	400 896	Powerplant Cost [$/unit]	276 742
Quality Control Cost [$/unit]	65 146	Propeller Cost [$/unit]	60 183
Material Cost[$/unit]	47 310	Battery Cost [$/unit]	88 619
Unit Variable Cost [$]	1 117 516	**Unit Variable Cost [€]**	938 714
Unit Retail Price [$]	2 200 000	**Unit Retail Price [€]**	1 848 000
Break-Even Number of Units	152		

4.2. Direct Operational Cost

For calculating the operational cost of the aircraft a number of different aspects have to be taken into account. As in Section 4.1 the method used is Eastlake for General Aviation aircraft, but with some modifications to account for the fact that the plane is electric. Furthermore, to simplify this analysis, it is assumed that the aircraft performs eight 300 km flights every day of the year. The first part to calculate is the maintenance cost, which depends on the flight hours, the hourly rate of the mechanic, which is assumed to be 60 $\$/h$, and the ratio of flight to maintenance hour of the Wigeon, which using the Eastlake method has been estimated to be 0.38 [53]. For storage a cost of 3000 $ per year is assumed, as indicated by Gudmundsson. The insurance cost is also included, and depends directly on the aircraft price. The inspection costs for the aircraft as well as the engine overhaul is also included. Where the inspection cost is estimated to be 500 $ per year [53] and the engine overhaul can be computed by the formulas provided by Gudmundsson [53]. All of these apply to both general aviation aircraft and the eVTOL; however, the following cost apply only to the eVTOL, as they are related to the battery and energy consumption. The battery replacement cost per year was calculated with Equation 4.7:

$$C_{B,ENER} = DoD \frac{B_m \; E_{kg} \; C_{kWh} \; Q_{\text{FLGT}}}{F_{cycle}} \tag{4.6}$$

$$C_{B,REP} = \frac{B_m \; C_{kg} \; Q_{\text{FLGT}}}{F_{cycle} \; N_{cycles}} \tag{4.7}$$

Where B_m is battery mass in kg, C_{kg} is the price of the battery per kilogram, Q_{FLGT} is the number of flight hours per year and N_{cycles} is the number of discharge cycles that the battery can last . The last two are obtained from Chapter 9. Finally, F_{cycle} is the number of flight hours per cycle, which assuming a 300km trip, is 1.3. The cost of the energy also has to be taken into account. For this calculation a price of 0.41 $\$ - \text{kWh}$ is used, which is the electricity price in Germany [120]. The following formula is used to calculate the total cost of electricity. The specific energy of the batteries E_{kg} is obtained from Chapter 9. Apart from this, the cost, of the pilot should be added, as the owner is not expected to be able to pilot the aircraft. A salary of 40 $\$$/hour is assumed. Finally, the following table presents the total direct operational costs for the Wigeon divided into the relevant sub parts.

Table 4.2: Operational costs breakdown.

Cost fraction	**Value**	**Cost fraction**	**Value**
Maintenance Cost [$/year]	86 640	Engine Overhaul Fund [$/year]	304 500
Storage Cost [$/year]	3 000	Energy cost [$/year]	223 217
Battery replacement cost [$/year]	13 128	Pilot's salary [$/year]	152 000
Annual Insurance Cost [$/year]	38 000	**Total yearly cost [$]**	820 485
Cost per flight hour [$]	216	**Cost per flight hour [€]**	182

4.3. Return on Investment

Once the cost breakdown has been determined, the team then started developing a timeline and allocating monetary resources destined to the different business phases planned. The business and the eVTOL idea was launched with the start of the DSE during the spring of 2021. This also marks the start of the engineering and development phase, where the team's main focus is the design and development of the eVTOL product. The development cost includes all those early investments needed to startup the company. In the case for this particular eVTOL product, a preliminary estimate of these costs include engineering, development support and other costs as described in Section 4.1. The team believes that a strong initial investment of around $210 million is needed to reach the end of the development stage. Having the finished, detailed design is a milestone set to 2025. Overlapping the latest stages of the development phase, the team has deemed appropriate to allocate a fraction of the manufacturing cost to start building the first number of prototypes to be used for testing and certification. According to the FAA [47], modern commercial aircraft can take between three to five years to certify, while new designs range between five and nine years. The team expects that certification for a small eVTOL, similar to small general aviation aircraft should take for around five years despite being a new category of aircraft. As a result, the aircraft should be fully certified by 2030. However, in order to start production and sales immediately after, the team plans to spend the remaining manufacturing, quality control, material and certification costs over the remaining certification period - totalling close to $ 700 million or 600 million € investment without profit. Yearly breakdown of these costs is presented in Table 4.3.

The first units are expected to be manufactured and sold by 2031, the first year where the business will create revenue and profit. At this point, production costs are high and thus the team has established a production cost 20% higher than the one estimated from Section 4.1. The production cost is expected to reach its nominal value by 2035, where 200 aircraft shall be produced and sold. In contrast to the market analysis conducted earlier [5] , the new insight gained has made the team move up the objective of producing and selling 200 aircraft per year from 2040 to 2035, after which the team expects to keep growing, selling more units and cutting even more production costs. The team has capped the potential number of sales to 1250 per year after 2035 with a production cost of 90 % the stipulated value from Section 4.1 as a conservative approach. Reasons to believe in a future decrease in costs include the employee's learning curve, optimisation of different processes, end to outsourcing parts and processes for a cheaper, own development and many more. The team has unanimously set a retail price tag of $ 2.2 million or 1.8 million €, with a sensible profit margin and deemed competitive as required from the market analysis.

Table 4.3: Profit & Loss (P&L) Statement. All cash flows expressed in $.

	Development					Certification				
Timeline	2021	2022	2023	2024	2025	2026	2027	2028	2029	2030
Cash-Flow	-1 636 214	-17 983 203	-31 057 764	-47 419 901	-129 361 031	-51 335 120	-71 379 917	-99 412 960	-101 778 442	-125 608 012

Timeline	2031	2032	2033	2034	2035	2036	2037	2038	2039	2040	2041	2042	2043	2044	2045
Units Sold	5	25	50	100	200	500	1 250	1 250	1 250	1 250	1 250	1 250	1 250	1 250	1 250
Retail Price	2 200 000	2 200 000	2 200 000	2 200 000	2 200 000	2 200 000	2 200 000	2 200 000	2 200 000	2 200 000	2 200 000	2 200 000	2 200 000	2 200 000	2 200 000
Unitary Cost	1 341 019	1 341 019	1 229 268	1 173 392	1 117 516	1 106 341	1 061 640	1 005 765	1 005 765	1 005 765	1 005 765	1 005 765	1 005 765	1 005 765	1 005 765
Revenue	11 000 000	55 000 000	110 000 000	220 000 000	440 000 000	1 100 000 000	2 750 000 000	2 750 000 000	2 750 000 000	2 750 000 000	2 750 000 000	2 750 000 000	2 750 000 000	2 750 000 000	2 750 000 000
Cost of Sales	6 705 097	33 525 486	61 463 391	117 339 201	223 503 241	553 170 521	1 327 050 493	1 257 205 730	1 257 205 730	1 257 205 730	1 257 205 730	1 257 205 730	1 257 205 730	1 257 205 730	1 257 205 730
Gross Margin	4 294 903	21 474 514	48 536 609	102 660 799	216 496 759	546 829 479	1 422 949 507	1 492 794 270	1 492 794 270	1 492 794 270	1 492 794 270	1 492 794 270	1 492 794 270	1 492 794 270	1 492 794 270
% Sales	39%	39%	44%	47%	49%	50%	52%	54%	54%	54%	54%	54%	54%	54%	54%
Operating Expense	-1 320 000	-6 600 000	-13 200 000	-26 400 000	-52 800 000	-132 000 000	-330 000 000	-330 000 000	-330 000 000	-330 000 000	-330 000 000	-330 000 000	-330 000 000	-330 000 000	-330 000 000
Profit from Operations	2 974 903	14 874 514	35 336 609	76 260 799	163 696 759	414 829 479	1 092 949 507	1 162 794 270	1 162 794 270	1 162 794 270	1 162 794 270	1 162 794 270	1 162 794 270	1 162 794 270	1 162 794 270
Taxes	-743 726	-3 718 628	-8 834 152	-19 065 200	-40 924 190	-103 707 370	-273 237 377	-290 698 567	-290 698 567	-290 698 567	-290 698 567	-290 698 567	-290 698 567	-290 698 567	-290 698 567
Net Profit	2 231 177	11 155 885	26 502 457	57 195 599	122 772 569	311 122 109	819 712 130	872 095 702	872 095 702	872 095 702	872 095 702	872 095 702	872 095 702	872 095 702	872 095 702
%	20%	20%	24%	26%	28%	28%	30%	32%	32%	32%	32%	32%	32%	32%	32%
Cash-Flow	2 231 177	11 155 885	26 502 457	57 195 599	122 772 569	311 122 109	819 712 130	872 095 702	872 095 702	872 095 702	872 095 702	872 095 702	872 095 702	872 095 702	872 095 702

Table 4.4: Summary of NPV, IRR and ROI obtained for the eVTOL tandem wing concept.

Net Present Value (NPV) [$]	1 190 515 133
Internal Rate of Return (IRR)	18.16 %
Initial Investment [$]	676 972 563
Return on Investment (ROI)	75.86 %

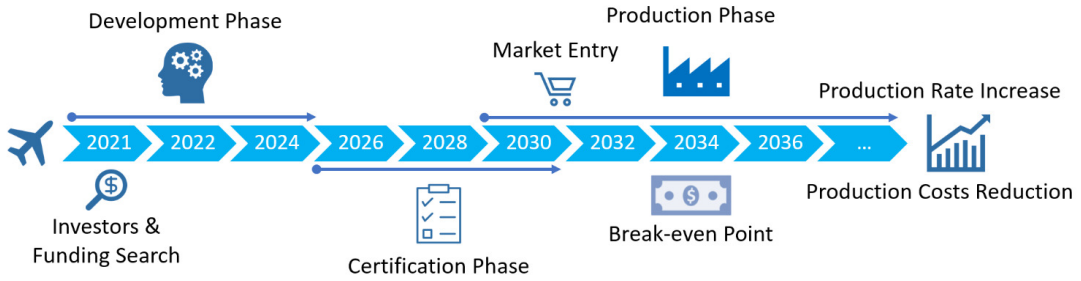

Figure 4.1: Timeline and long-term strategy for the eVTOL model market launch and expectations.

Additionally, the business has to deal with other non-technical costs including CapEx (or Operating Expense) and taxes. Deloitte [40] conducted a statistical study claiming that the average CapEx tends to be 12 % of the total revenues. Furthermore, corporate tax rates for businesses headquartered in The Netherlands is of 25 %. Table 4.3 collects all expected cash flows chronologically, depicting the different stages and evolution of the business. The spreadsheet crafted to do so computes the Net Present Value (NPV), Internal Rate of Return (IRR) and Return on Investment (ROI) for the tandem wing concept (collected in table 4.4), following the trade-off selection detailed in chapter 2. The model assumes a yearly discount rate of 6 %. Figure 4.1 then illustrates the long-term strategy and plan constructed from conducting this financial investigation. Figure 4.1, also shows that the development time is 5 years, which complies with requirement VTOL-COS-2.

4.4. Future Development of the Project

This section covers the prospects and next steps of the project after the DSE ends. The first section is the Project Design and Development Logic, which covers and explains the next steps for the project. The second section is the project Gantt chart, which puts the activities from the first section into a timeline.

4.4.1. Project Design & Development Logic

This section addresses the Project Design and Development logic, which consists on the planning of the activities to be performed after the current phase of the project ends (end of the DSE). Figure 4.2 contains a flow diagram of these actions.

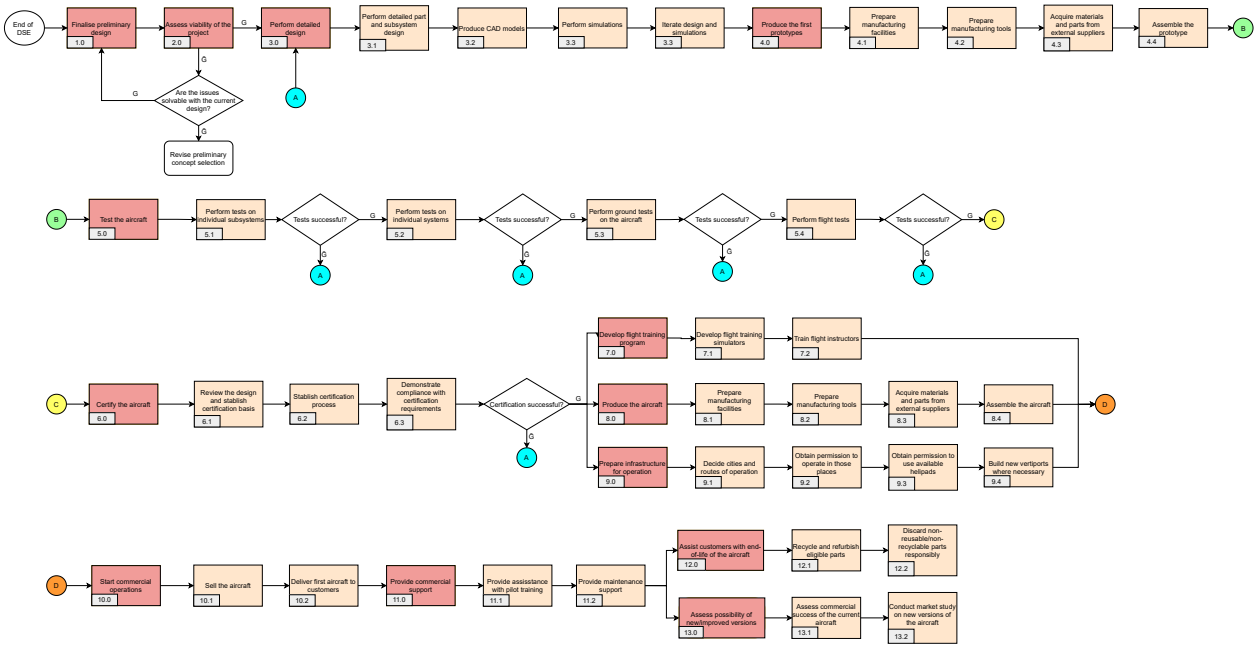

Figure 4.2: Flow diagram of actions to be performed for the project continuation after the Design Synthesis Exercise

The first step after the DSE is to finalise the preliminary design, addressing all areas that could not be finalised within the resources of this project. Once the preliminary design is finalised, the team needs to perform a viability assessment of the design, and make sure it complies with requirements. If the design is feasible, the next step is to perform a detailed design. In case it is not feasible, the team needs to analyse whether the issues found are solvable. If so, the preliminary design needs to be modify such that the issues are solved; otherwise, the project would need to go back to concept selection, to revise the configuration chosen and select one that can meet the requirements that were not met originally.

In the detailed design phase, there are four steps to be performed. First, the detailed part and subsystem design of the vehicle, the creation of CAD models of such parts and subsystems, and based on those two,

perform detailed simulations of the performance of the vehicle. After these simulations the design needs to be iterated accordingly and simulated again, until a final design is reached.

After the detailed design, the first prototypes need to be built. This includes preparing the manufacturing facilities need for this, preparing the manufacturing tools to be used, acquiring the necessary materials and parts from external suppliers, training the staff and assembling the prototype.

Once the prototypes are built, the aircraft can be tested. The testing phase should start with tests on individual subsystems and parts. After these are tested, the whole aircraft can start ground tests to assess the integration of the subsystems. If these tests are passed, the aircraft can start the final phase of testing, the flight tests. In this phase, the whole aircraft is tested in missions of increasing difficulty, from hover tests and short flights to exemplary missions. In case the tests are not successful, the detailed design needs to be amended so that the issues encountered are solved.

Once the tests are completed and passed, the aircraft can go into certification. The certification process described here is the process followed by EASA[1]. First, the team should present the design to EASA, who will decide the certification category that applies to the aircraft. Following this, the team and EASA will decide how the compliance with the certifications requirements will be demonstrated. These tasks can be performed before testing starts to accelerate the process. Lastly, this compliance should be demonstrated, possibly in parallel to the ground and flight tests of the aircraft, after which EASA will certify the vehicle. If the certification were not successful, the team would need to go back to the detailed design phase to amend the issues found.

After certification is successful, three parallel steps will need to be carried out. On the one hand, a flight training program has to be developed, which includes developing flight testing software and simulators, and training flight instructors. On the other hand, the aircraft needs to enter commercial production, for which the manufacturing facilities and tools need to be prepared, materials and parts from external suppliers need to be acquired, and the aircraft need to be assembled. Lastly, the company needs to prepare and organise the operations phase and the infrastructure that is going to be used. This includes identifying the regions of operation of the vehicle, and consequently obtaining the necessary permissions to fly in such regions and to use available helipads where possible. Lastly, in places where helipads are not available or sufficient, or where the commercial prospects justify it, the company needs to commission the construction of helipads or vertiports to operate the vehicle.

After the previous steps, once the first aircraft enter production, the company can start with commercial operations, selling the aircraft and delivering it to customers. Once the first aircraft are in the market, the company has to provide commercial support to customers, through assistance with training the pilots and with maintenance of the vehicles. After some years in the market (circa 15 years, the design operational life of the aircraft), the first aircraft will start to retire. The company should then provide EOL support to its customers, recycling and refurbishing the parts which can be used in newer models, and discarding in a responsible manner the parts and materials that cannot be recycled.

As a last consideration, the company should assess the commercial success of the aircraft, and evaluate the possibility of releasing improved models with e.g. more passenger capacity or different ranges.

4.4.2. Project Gantt chart

This section contains the Gantt chart of the activities of the Project Design and Development Logic described in Section 4.4.1. The Gantt chart can be seen on Figure 4.3.

The project is set to continue for approximately 10 years until the first aircraft are delivered. Immediately after testing and certification there is a period of 9 months without tasks. This is to account for the likely delays in testing and certification. If everything were to go according to plan, the tasks after this gap could be started earlier.

[1] https://www.easa.europa.eu/domains/aircraft-products/aircraft-certification [cited 20 May 2021]

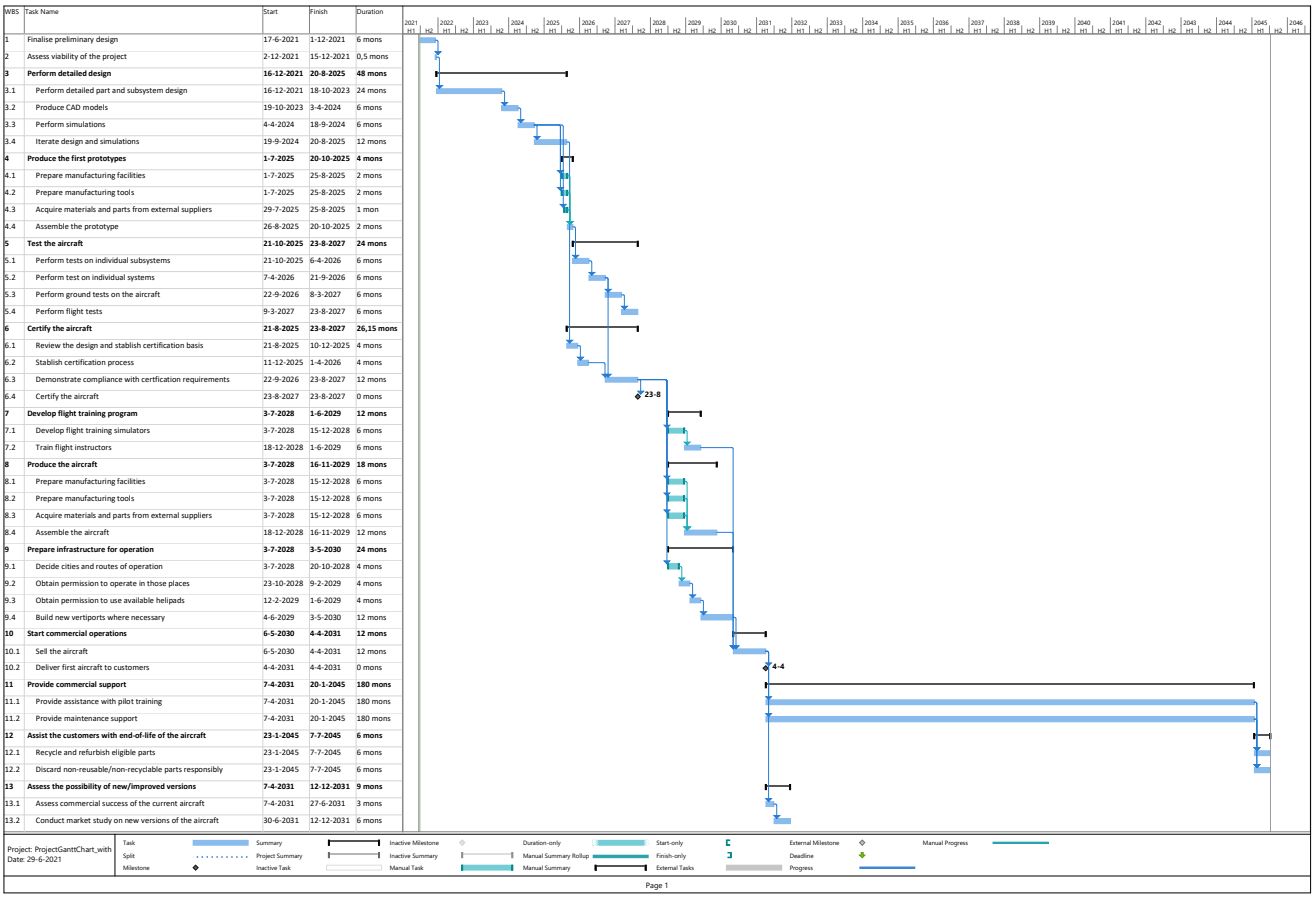

WBS	Task Name	Start	Finish	Duration
1	Finalise preliminary design	17-6-2021	1-12-2021	6 mons
2	Assess viability of the project	2-12-2021	15-12-2021	0,5 mons
3	**Perform detailed design**	**16-12-2021**	**20-8-2025**	**48 mons**
3.1	Perform detailed part and subsystem design	16-12-2021	18-10-2023	24 mons
3.2	Produce CAD models	19-10-2023	3-4-2024	6 mons
3.3	Perform simulations	4-4-2024	18-9-2024	6 mons
3.4	Iterate design and simulations	19-9-2024	20-8-2025	12 mons
4	**Produce the first prototypes**	**1-7-2025**	**20-10-2025**	**4 mons**
4.1	Prepare manufacturing facilities	1-7-2025	25-8-2025	2 mons
4.2	Prepare manufacturing tools	1-7-2025	25-8-2025	2 mons
4.3	Acquire materials and parts from external suppliers	29-7-2025	25-8-2025	1 mon
4.4	Assemble the prototype	26-8-2025	20-10-2025	2 mons
5	**Test the aircraft**	**21-10-2025**	**23-8-2027**	**24 mons**
5.1	Perform tests on individual subsystems	21-10-2025	6-4-2026	6 mons
5.2	Perform test on individual systems	7-4-2026	21-9-2026	6 mons
5.3	Perform ground tests on the aircraft	22-9-2026	8-3-2027	6 mons
5.4	Perform flight tests	9-3-2027	23-8-2027	6 mons
6	**Certify the aircraft**	**21-8-2025**	**23-8-2027**	**26,15 mons**
6.1	Review the design and stablish certification basis	21-8-2025	10-12-2025	4 mons
6.2	Stablish certification process	11-12-2025	1-4-2026	4 mons
6.3	Demonstrate compliance with certfication requirements	22-9-2026	23-8-2027	12 mons
6.4	Certify the aircraft	23-8-2027	23-8-2027	0 mons
7	**Develop flight training program**	**3-7-2028**	**1-6-2029**	**12 mons**
7.1	Develop flight training simulators	3-7-2028	15-12-2028	6 mons
7.2	Train flight instructors	18-12-2028	1-6-2029	6 mons
8	**Produce the aircraft**	**3-7-2028**	**16-11-2029**	**18 mons**
8.1	Prepare manufacturing facilities	3-7-2028	15-12-2028	6 mons
8.2	Prepare manufacturing tools	3-7-2028	15-12-2028	6 mons
8.3	Acquire materials and parts from external suppliers	3-7-2028	15-12-2028	6 mons
8.4	Assemble the aircraft	18-12-2028	16-11-2029	12 mons
9	**Prepare infrastructure for operation**	**3-7-2028**	**3-5-2030**	**24 mons**
9.1	Decide cities and routes of operation	3-7-2028	20-10-2028	4 mons
9.2	Obtain permission to operate in those places	23-10-2028	9-2-2029	4 mons
9.3	Obtain permission to use available helipads	12-2-2029	1-6-2029	4 mons
9.4	Build new vertiports where necessary	4-6-2029	3-5-2030	12 mons
10	**Start commercial operations**	**6-5-2030**	**4-4-2031**	**12 mons**
10.1	Sell the aircraft	6-5-2030	4-4-2031	12 mons
10.2	Deliver first aircraft to customers	4-4-2031	4-4-2031	0 mons
11	**Provide commercial support**	**7-4-2031**	**20-1-2045**	**180 mons**
11.1	Provide assistance with pilot training	7-4-2031	20-1-2045	180 mons
11.2	Provide maintenance support	7-4-2031	20-1-2045	180 mons
12	**Assist the customers with end-of-life of the aircraft**	**23-1-2045**	**7-7-2045**	**6 mons**
12.1	Recycle and refurbish eligible parts	23-1-2045	7-7-2045	6 mons
12.2	Discard non-reusable/non-recyclable parts responsibly	23-1-2045	7-7-2045	6 mons
13	**Assess the possibility of new/improved versions**	**7-4-2031**	**12-12-2031**	**9 mons**
13.1	Assess commercial success of the current aircraft	7-4-2031	27-6-2031	3 mons
13.2	Conduct market study on new versions of the aircraft	30-6-2031	12-12-2031	6 mons

Figure 4.3: Gantt chart of the high level tasks to be carried out after the Design Synthesis Exercise ends.

The commercial support phase is represented in the Gantt chart for 15 years, the design operational life of one aircraft. This is just a representation of the life cycle for one aircraft. It is expected that the project will continue further, with new units being sold throughout the years, but for clarity in the graph, only the operational life of one aircraft is shown.

5 Functional Analysis

This chapter lays out the functions that the Wigeon must perform. This includes all stages from production to disposal. Figure 5.1 contains a detailed breakdown of the functions, while their chronological order is highlighted in Section 5.2.

5.1. Functional Breakdown Structure

In order to provide an overview of the system, and identify the functions it needs to perform, a functional breakdown structure (FBS) was made of the entire aircraft life-cycle, with emphasis on the operation of the aircraft.

As can be seen from Figure 5.1, there are three main phases to the aircraft's life that will be discussed and analysed by the team. All of them, except for phase 2, are broken down into two levels in Figure 5.1. This gives a general overview of what these phases entail. When it comes to phase 2 - *Operate aircraft*, it has been broken down in 4 levels, with level 4 being included only where deemed necessary. The decision to provide more detail in this phase was due to the fact that this is the longest stage of the life of an aircraft and that the functions of the aircraft itself are showcased.

The breakdown of the *Operate aircraft* focuses specifically on a mission cycle, starting from pre-flight actions and ending on post-flight actions. Additional functions have been included, such as continuous functions of aircraft and dealing with emergency situations. Continuous functions are active throughout the mission and are thus not possible to put in the chronological order. For the same reason, they have been omitted from the Functional Flow Block Diagram in the next section.

5.2. Functional Flow Block Diagram

The functional flow block diagram (FFBD), shown in Figure 5.2, is useful when it comes to analysing a nominal flight and understanding the chronological order of the functions involved. For the sake of efficiency and clarity, the FFBD for *Operate aircraft* displayed is expanded to level 3 only. Although concise, this level provides enough detail in order to gain a deeper understanding of the aircraft's functionality. Other phases are given to level 2, just like in the FBS.

The nominal mission is quite standard for all long range passenger aircraft, with a few deviations with regards to the fact that the aircraft in consideration is a VTOL aircraft. Possible deviations from the nominal mission, like loiter and diversion, are also considered. The reasons for the loiter and diversion are not given, but these are closely related to *Deal with emergencies* column in Figure 5.1. The top level functional flow is simply: *perform pre-flight actions, take-off, cruise, (extend mission, deal with emergencies), land, perform post-flight actions*, in that order. Nevertheless, each of these top level functions are quite complex and comprise of multiple lower level functions. This reveals another use of the FFBD, to show the breakdown of functions involved.

At times, it happens that functions run in parallel. In such cases, the use of an *AND* connector is made. These are most common in 'child' functions, the 'parent' of which is continuous function, such as cruise. It is also common to see functions that split into several alternative paths. These functions are implemented using an *OR* connector.

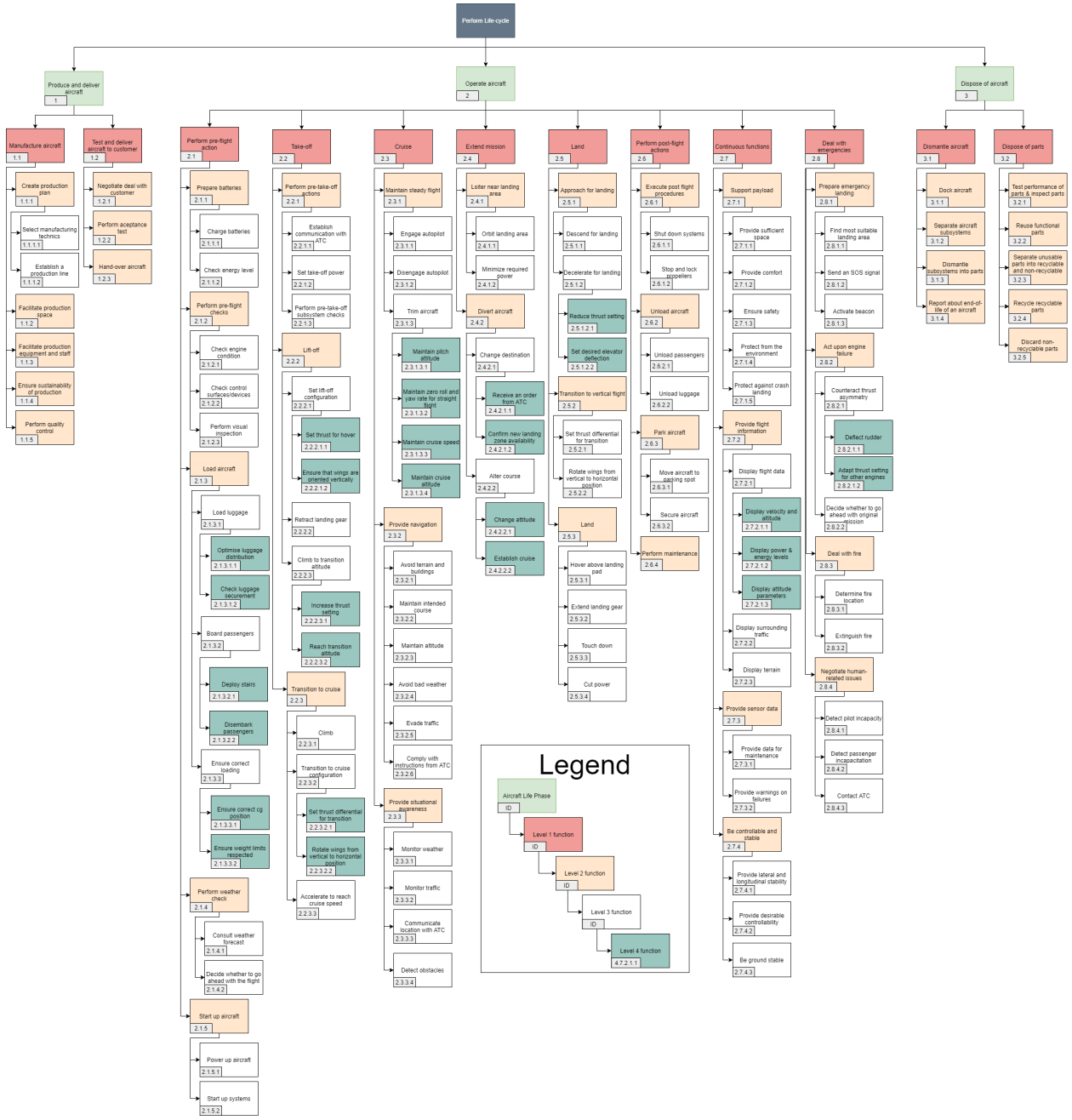

Figure 5.1: Functional Breakdown Structure of the Wigeon's mission.

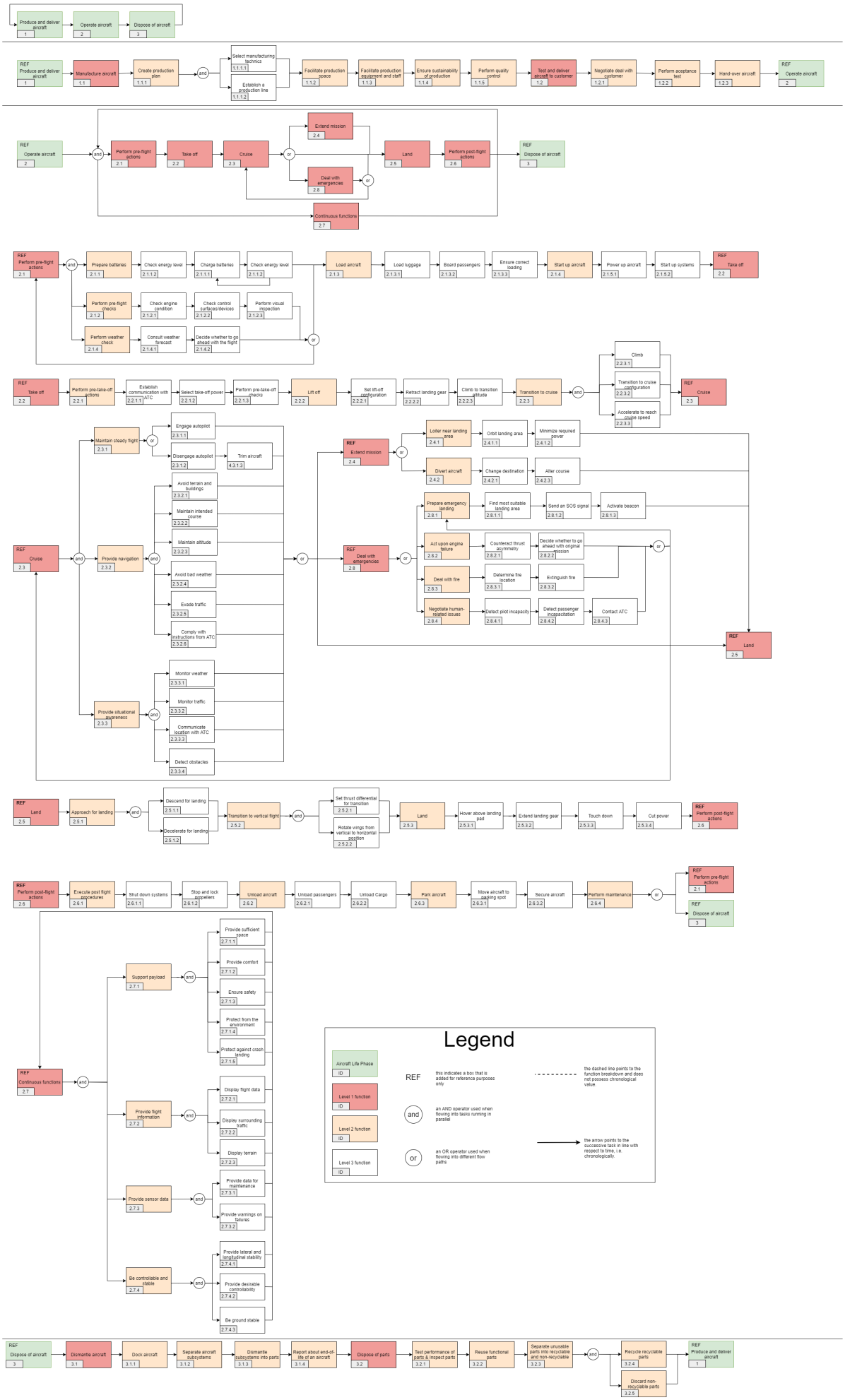

Figure 5.2: Functional Flow Block Diagram of the Wigeon's mission.

6 Technical Risk Analysis

Technical risk is a part of every system and subsystem. In order to deliver a successful design, it is vital to make sure that all the important risks are identified and managed properly. In Section 6.1 relevant risks are listed, and newly found risks are explained. They are also given a score and plotted in a risk map. The most severe risks are managed in Section 6.2.

6.1. Risk Assessment & Identification

In this section, the most relevant technical risks associated with the design of the aircraft are identified. A short explanation is given as to why a risk is relevant, and a score is given based on the likelihood and consequence of each risk. The risk score itself is the product of these two. If this score is higher than 8, the risk has to be managed. The scale used to determine the scoring is given in Table 6.1 and Table 6.2 for the probability of occurrence and the consequence, respectively. The probabilities assigned to each risk are for the entire lifetime of the aircraft. In Table 6.4, the scores for the risks listed below are given.

Table 6.1: Probability scores. Obtained from [49]

Score	Probability (P)	Chance
1	$p < 1\%$	very low
2	$1\% \leq p < 30\%$	low
3	$30\% \leq p < 50\%$	medium
4	$50\% \leq p < 70\%$	high
5	$p \geq 70\%$	very high

Table 6.2: Consequence scores.

Score	Consequence (C)
1	Negligible impact
2	Small performance reduction
3	Moderate performance reduction
4	Partial mission failure
5	Complete mission failure

Table 6.3: Risks with the respective descriptions and scores.

Table 6.3

ID	Risk	Description	Score (P,C)
RT.1	Not meeting range requirement	It is possible that during the testing of the aircraft it does not meet the range requirement of 300 km. This could occur due to approximations during the design phase, as these accumulate over time. Although the probability of this is not high provided a good design, it could still occur. The consequence of this risk occurring depends on the customer, as some may still be satisfied and some may be totally dissatisfied.	1, 3
RT.2	Insufficient thrust during take-off	Mistakes during propeller design could lead to a maximum thrust that is lower than expected. Depending on how much lower it is, the aircraft might not be able to take-off and transition. A small reduction in thrust should not have a large effect. The probability of this happening can vary somewhat, with a small reduction in thrust being more probable than a larger one. Use of design tools and models that are properly validated should ensure a low probability.	2, 4
RT.3	Short circuit	Short circuits lead to partial or full failure of the power system. As explained in Section 9.6, redundancy is build into the power subsystem, and no single points of failure are present. The probability of an entire power failure is thus very low. The consequence of a complete power failure can cause the aircraft to crash, as the fly-by-wire system might also stop working.	2, 5
RT.4	Engine failure during cruise	Engine failure during cruise involves both failure due to internal and external factors. Internal factors could be a propeller breaking or an engine that stops working. External factors would be factors like environmental damage, i.e. hail, birds, dust/sand etc. Having an engine fail entirely is rare, but the consequence should not be severe, as the aircraft is designed such that it can still fly with all engines on one wing inoperative.	3, 3
RT.5	Engine failure during vertical flight	Occurring from reasons similar to engine failure during cruise, engine failure could have serious consequences, depending on how many engines fail. Due to the high number of engines, a failure is more likely. The aircraft is however designed such that it can still take off when an engine fails. Assuming a single engine failure, this should not impact the eVTOL severely.	3, 4

RT.6	Damage during maintenance/ground operation	This risk entails accidental damage occurring during maintenance or ground operation. The severity of this risk varies greatly. The aircraft could sustain a paint scratch, but could also be critically damaged in a collision with any sort of ground machinery. The probability of this is hard to predict, but can be assumed low due to the current maintenance regulations.	1, 4
RT.7	Running out of energy during flight	Although an unlikely scenario, due to the heavy dependence on electrical energy for an eVTOL, this risk has to be considered. This risk could occur due to pilot error or due to the malfunction of the battery. Since not only the engines, but also the control system relies on electrical energy, he consequence of this is of high concern and such situation should definitely be considered as an emergency situation.	1, 5
RT.8	Unacceptable noise level	This risk is important since the primary purpose of this aircraft is to provide comfortable transportation in populated environments. Propeller tip vortices of the front wing interacting with those of the rear wing and propeller-wing interaction are sources of noise that might impact the Wigeon. Although not life-threatening, failing to comply with noise regulations could deem the aircraft illegal to fly.	2, 2
RT.9	Aircraft price is too high	If during detailed design a necessity for expensive materials arises or the cost estimation rises substantially, the end price of the Wigeon could increase. A longer than expected design and development process could increase the price even further. Even if the aircraft performs better than its competition, a high price may limit its attractiveness. Since the aircraft will likely use aluminium, material is unlikely to cause an increase in cost. Also the preliminary design phase is essentially done for free, leading to a cost reduction. The chances of a prohibitively expensive aircraft are thus low.	1, 3
RT.10	Operating cost is too high	A high operating cost may be caused by the need for frequent repairs, or a rise in electrical energy prices. Electric engines generally need less maintenance than combustion engines, leading to a reduction in operating cost. On the other hand, batteries may need replacement after a high number of charging cycles is performed. The probability of this risk is small, but the consequence can be considerable, as customers might opt for more affordable alternatives.	2, 4
RT.11	Landing gear not deploying	The landing gear mechanism could fail because it gets stuck or because of an actuator failure. When this happens during landing, the aircraft is forced to make a belly landing. When landing vertically, this forced the aircraft to land on the front wings, which could cause substantial damage to the wing and the wing rotation mechanism. When the landing gear doesn't retract during take-off, the aircraft can just land again.	1, 4
RT.12	Sensor failure	Failure of the sensors that provide information about the state of the aircraft could cause the pilot or control system to respond to faulty readings. In normal conditions, the pilot should be able to notice this in time based on the outside view. In low visibility conditions, it might however cause the aircraft to crash.	2, 4
RT.13	Emergency landing on water	Having a fully electric vehicle becomes a worrisome hazard if the electronics and wiring are not protected from the environmental factors, such as water or moisture. An extreme case of this would be a crash-landing on water. Due to the damage to the structure, the vulnerable circuitry and batteries could get exposed, putting passengers and the pilot into a dangerous situation. The chance of such a crash landing happening is low, but the outcome would be disastrous.	1, 5
RT.14	No available landing spots	An important area for operation for eVTOL's is in cities, where space is costly. This will likely lead to relatively small 'vertiports'. A consequence of this can be lack of space when multiple aircraft try to land. Using effective air traffic management systems, the probability of this risk is still moderate, as eVTOL flights will not always be scheduled days in advance. To avoid this, the aircraft already has a 15 minute loiter time in cruise. The consequence is moderate, as the aircraft will have to divert or even land in an unprepared area. It should, however, not damage the aircraft or injure the passengers.	2, 3
RT.15	Failure of wing-tilt mechanism	Since the Wigeon is a tilt-wing design, the consequence of a failure of the tilting mechanism is more severe than for a tilt-rotor design. If one wing is stuck, or tilts uncontrollably, a large moment can be created and make the aircraft uncontrollable. The effects of this can be reduced by rotating the functioning wing to the same position as the malfunctioning wing. Since rotation happens during transition, where usually the speed and altitude are low, it could prove difficult to react in time, although a computerised emergency response could be helpful. A stuck wing might also make a vertical landing impossible, requiring a conventional landing. If this happens during take-off, the aircraft usually has enough energy left to reach a normal airport. When the wing gets stuck during landing, this might not be the case, forcing an emergency landing.	1, 4
RT.16	Propeller ground strike	The open propellers of the Wigeon can lead to a propeller striking the ground. Since in VTOL operations the propellers are tilted upward, this is not likely to cause issues. If the aircraft would also be used for conventional landings, propeller strikes on the front wing are more likely to happen.	1, 4
RT.17	Propeller causing injury	Another risk associated with the open propellers is that passengers or ground crew could be injured if the propellers are rotating while on the ground. The consequences of this are severe, possibly leading to a deadly accident. Apart from the risk of physical injury, the propellers being in close proximity to the cabin entrance door might make the aircraft less attractive for customers.	2, 4

RT.18	Failure to react to high load factors	If the control system or the pilot do not react in time to high load factors, there is a risk of exceeding these. This would damage the aircraft or even cause a crucial component such as a wing to fail, leading to a crash. Although the probability of exceeding these load factors is low, the consequence is severe and should be addressed.	2, 4
RT.19	Bird strike	A bird strike is not a common occurrence but could be quite severe depending on what damage has been sustained by the aircraft. Moreover, the chance of a bird strike increases due to the low cruise altitude. The consequence is directly related to amount of damage sustained by the aircraft. It can range from a reduction in visibility if the windshield is hit,an engine failure, or minor structural damage.	2, 3
RT.20	Incorrect model of stall behaviour	Transition occurs at speeds very close to stall speed. The nature of the flow in these situation is non-linear as is rather difficult to predict. The propeller-wing interaction caused by the distributed propulsion further increases complexity. It may be possible that during testing the flow behaves not as it was predicted, for instance flow separates too early, causing a loss of lift during transition. The consequence of this is also hard to predict, just as the behaviour, and could range from minor to detrimental.	3, 3
RT.21	Control system failure	As the aircraft shows slight lateral instability and high sensitivity to control inputs, further explained in Chapter 11, there is a heavy reliance on the control system. Moreover, transition and hover flights are fully reliant on the control system. Failure of this would prove detrimental. The system could fail due to multiple reasons, the obvious ones being power failure and short circuits, and other possibilities incomplete shut down, but rather malfunction. During transition from cruise to hover, flow attachment is usually sudden and might cause the control system to pitch down more than expected. Although with extensive control system design this risk could be avoided but is still not zero and thus should be managed properly.	2, 5
RT.22	Strong hover gusts	During hover, it is likely that at some point the aircraft will encounter a strong lateral gust. During such gusts, the control system or the pilot could choose to bank the aircraft into the gust in order to stabilise the aircraft. If this occurs too close to the ground, there is a risk of striking the front wing on the ground. The likelihood of this happening is not high and could be lowered even further by avoiding flight in rough winds. Although the damage to the aircraft could be severe, the passengers would sustain minimal injuries due to very low altitude.	2, 4
RT.23	Overestimation of fatigue life	Components such as joints and lugs most times fail in fatigue. It is possible that using analytical and numerical methods overestimated the fatigue life. Then the aircraft would fail sooner than expected, shortening its lifetime dramatically. Constant inspection of such joints could prevent unforeseen failures. As lugs are designed to be safe-life, failure of such a component could lead to a crash. On the other hand, if the fatigue life of a rivet joint is overestimated, this would not have a detrimental effect on the structure as rivets are fail-safe.	2, 5

Table 6.4: Risk map before managing the risks. The colour of the cells is based on the risk score, which is the product of the probability and consequence scores.

Consequence						
	5	RT.7, RT.13	RT.3, RT.21, RT.23			
	4	RT.6, RT.11, RT.15, RT.16	RT.2, RT.10, RT.12, RT.17, RT.18, RT.22	RT.5		
	3	RT.1, RT.9	RT.14, RT.19	RT.4, RT.20		
	2		RT.8			
	1					
		1	2	3	4	5
		Probability				

6.2. Risk Prevention and Mitigation

In the following section, mitigation or prevention strategies are given to reduce the most severe risks. The revised risk map can be seen in Table 6.6.

Table 6.5: Risks with the respective descriptions and scores.

Table 6.5

ID	Risk	Prevention	Mitigation	Score (P,C)
RT.2	Insufficient thrust during take-off	To prevent insufficient thrust, special attention should be payed to validating the models used to analyse the propellers. This can be done using detailed CFD analysis.	If the aircraft turns out to have insufficient thrust in a late design stage, new engines and/or propellers will have to be selected. This can be expensive and might require redesign of the power subsystem. Therefore, the focus should be on prevention.	1, 3
RT.3	Short circuit	To prevent shorting, or at least prevent it during the flight, the power system has to be checked before every take-off. A thorough check of the power system should be conducted every 6-12 months at least. Again, redundancy is added in the design of the power system to reduce this risk further.	Once the circuit has been shorted, there must always be a back up power system that will ensure aircraft's safe landing. Then the faulty power system could either be replaced or repaired. The switch from the failed power system to the back up one should ideally be instantaneous.	1, 4
RT.4	Engine failure during cruise	To reduce the likelihood of an engine failing during cruise, redundancy could be build in by having redundant windings. Also an engine check will have to be performed before each flight. A more thorough inspection should be performed every 6-12 months, to be able to discover underlying issues early on.	If an engine does fail during cruise, the aircraft is still controllable, and can still fly, since multiple engines are used. The mission might have to be shortened however, since the range could be impacted.	2, 3
RT.5	Engine failure during vertical flight/hover	Performing an engine check before every flight should reduce the probability of the engine failure occurring during vertical flight or hover flight. As for the power system, a thorough technical check should be conducted every 6-12 months, since a simple check is not always enough. Having multiple windings in one engine adds redundancy, which decreases the chance of engine failure.	If the failure does occur, the propulsion system is designed in such a way that the remaining engines are still able to lift the aircraft, while remaining stable and controllable. This translates into a higher thrust-to-weight ratio required from the propulsion system. Such situation should also be introduced in pilot training.	2, 3
RT.10	Operating cost is too high	Designing for low cost operation during the aircraft's life time is the best way to prevent this risk. This involves ensuring easy repairability, maintenance and minimal infrastructure requirement.	In case operating costs are concluded to be high, they have to reevaluated. The manufacturer should devise and provide efficient operation practises to the operators through short-term training. Needless to say, contingency for this type of situation is very cost dependent and prevention should be the main focus.	1, 4
RT.12	Sensor failure	Redundancy should be introduced in sensors and instruments. Pre-flight checks of the entire avionics system would also help prevent this risk.	In a situation where a sensor or an instrument fails, an automatic switch should be made to the operational one. The pilot must be notified of this failure. To prevent the control system from interpreting the inputs inaccurately, the pilot should be able to override the effected part of the control system without affecting the functioning elements.	1, 3
RT.17	Propeller causing injury	To prevent propeller blades from injuring people, it could be required for the aircraft to be shut down completely while on the ground until everyone has boarded the aircraft and the helipad is cleared. Training ground crews and preventing passengers from entering helipads unattended can also reduce the probability of injury.	There is little that can be done once someone has been injured. It can however be required for every vertiport to be equipped with first aid kits and to be accessible to ambulances.	1, 4
RT.18	Failure to react to high load factors on time	Having a fly-by-wire system can help prevent this risk by overtaking the control when approaching extreme load factors. An inclusion of a flight manual stating maximum manoeuvre speeds would decrease the probability of such an instance occurring even further.	In case such loads are indeed met, there is already a safety factor that will prevent the structure from failing. Needless to say, the structure may still sustain some structural damage. Such damage could be in forms of local yielding, buckling. Repairs will have to be made once the aircraft has landed. In addition, the load factors should be reduced immediately by reducing the speed or angle of attack.	1, 4

RT.20	Incorrect model of stall behaviour	Validating the aerodynamic models of stall behaviour as early on as possible should largely prevent large discrepancies between predicted and actual stalling behaviour.	If validation is not possible, or if there are large variations in stall behaviour for the aircraft, a new take-off and landing trajectory could be devised. This trajectory could circumvent an early stall by remaining in vertical configuration longer. The energy needed for take-off and landing might increase because of this.	2, 2
RT.21	Control system failure	To prevent a control system failure, redundancies should be build into it to reduce the probability of occurrence as much as possible, given a fly-by-wire controlled aircraft.	If the aircraft is too unstable to fly after a control system failure, a ballistic parachute system could be considered, based on the failure rate of the control system. If the aircraft is still flyable, no additional contingency plan is needed, although it might be necessary to land conventionally, to prevent the pilot from doing the transition completely manually.	1, 4
RT.22	Strong hover gusts	Preventing strong gusts can only be done by not flying at strong wind weather conditions. Preventing damage could be done by climbing quickly in the first seconds of flight, to get clearance from the ground.	If a strong gust happens, the effects can be minimised by having a good control system that instantaneously reacts to the disturbance, eliminating the reliance on the pilot's reaction time.	1, 4
RT.23	Overestimation of fatigue life	Preventing such a risk mainly consists of a high-fidelity FEM analysis of the aircraft joints. Continuous inspections could also alert the operators sooner, preventing such a failure during flight, which would be the worst case.	In case the fatigue life is indeed overestimated, the components that are responsible for the short fatigue life could be replaced or repaired. For the future developments, such components should be redesigned to ensure to fulfill the designed lifetime.	1, 5

Applying the risk management plans outlined above to the risks gives them new scores. These are plotted in Table 6.6. Note that all the risks are now in the acceptable zone.

Table 6.6: Risk map after managing the most sever risks. The managed risks have been highlighted.

Consequence						
	5	RT.7, RT.13, **RT.23**				
	4	**RT.3**, RT.6, **RT. 10**, RT.11, RT. 15, RT.16, **RT. 17, RT.18, RT. 21, RT.22**				
	3	RT.1, **RT.2**, RT. 9, **RT.12**	**RT.4**, **RT.5**, RT. 14, RT.19			
	2		RT.8, **RT.20**			
	1					
		1	2	3	4	5
		Probability				

7 Aerodynamic Design

In this chapter, the aerodynamic design and analysis of the Wigeon aircraft is presented. Firstly the wing planform and configuration is introduced in Section 7.1, followed by a revisit to airfoil selection in Section 7.2. Section 7.3 then gives further details about wing performance aspects, and is followed by the determination of the aircraft's drag polar in Section 7.4. Next, a model for the aircraft behaviour during transition is described in Section 7.5. Section 7.6 then describes the procedure used to carry out a thorough CFD analysis. Finally, the sensitivity analysis of the aerodynamic design and the verification and validation procedures are discussed.

7.1. Wing Configuration and Planform

Based on the design point, the wing loading of the aircraft is found. By diving the estimated weight of the aircraft by the wing loading the surface area of the wings can be found. For the Wigeon, a tandem configuration was chosen in the conceptual and prelminary designs [71], meaning that the lifting surface will be divided into two wings, where both create an approximately equal amount of lift. The configuration will have a negative stagger - the horizontal distance between the front and rear wing). These imply that the front wing is laid low and the rear wing is placed high. Another parameter related to tandem configurations is the gap, which is the vertical distance between the two wings. These imply that the front wing is laid low and the rear wing is placed high. The objective to place the wings in such a way is to achieve minimum interference between both wings seeking to lower the value of induced drag to improve the aircraft's efficiency and range.

In order to simplify the initial sizing process, trapezoidal wing planforms without twist are assumed. Since the aircraft will fly at Mach numbers significantly below transonic speeds, the sweep at quarter chord is chosen to be 0 for all lifting surfaces. Furthermore, the taper ratio is chosen to be 0.45 in order to obtain a lift distribution as close to elliptical as possible with a trapezoidal wing without sweep [100, 113]. The front low wing has a dihedral angle of 5 degrees to improve lateral stability, as suggested by Raymer [102]; while the rear high wing presents no dihedral, as high wing configurations provide better lateral stability [102]. The aspect ratio is limited by the fact that the wingspan cannot surpass 14m in order to satisfy the requirement that the aircraft must be capable of landing on heliports [5].

Using the surface area, taper ratio and aspect ratio, a number of relevant wing parameters can be computed. The wingspan can be found using equation 7.9, and the root and tip chords are calculated with formulae 7.1 and 7.3 respectively. The MGC and MAC are assumed to be equal, and thus the $\bar{c}$ can be computed using equation 7.4, and its location along the span is calculated with equation 7.2. The X_{LEMAC} is found with formula 7.5 and the sweep at any position along the chord is found with 7.6 [100].

$$c_r = \frac{2S}{(1+\lambda)b} \tag{7.1}$$

$$Y_{MAC} = \frac{b}{6} \cdot \frac{1+2\lambda}{1+\lambda} \tag{7.2}$$

$$c_t = \lambda c_r \tag{7.3}$$

$$\bar{c} = \frac{2}{3} \cdot c_r \cdot \frac{1+\lambda+\lambda^2}{1+\lambda} \tag{7.4}$$

$$X_{LEMAC} = Y_{MAC} \cdot tan(\Lambda_{LE} \cdot \frac{\pi}{180}) \tag{7.5}$$

$$tan(\Lambda_{x/c}) = tan(\Lambda_{LE}) - \frac{x}{c}\frac{2C_r}{b}(1-\lambda) \tag{7.6}$$

For tandem wing aircraft with similar span wings, it is also possible to present the aspect ratio and span of the aircraft as if the aircraft had a single wing. This was done by slightly modifying the formulae presented by Scholz et al [114]. for tandem wing aircraft, as presented below. It follows that the equivalent span can then be calculated with Equation 7.11.

$$s_i = \frac{S_i}{S_{ref}} \quad (7.7) \qquad AR_i = \frac{b_i^2}{S_i} \quad (7.9)$$

$$AR = 0.5(s_1 AR_1 + s_2 AR_2) \quad (7.8) \qquad S_{ref} = S_1 + S_2 \quad (7.10)$$

$$b = \sqrt{0.5(s_1 AR_1 + s_2 AR_2) S_{ref}} \quad (7.11)$$

Table 7.1 below presents these parameters for the final version of both wings. Since both wings were finally chosen to be the same, only one column of results is presented. The height of the winglets for each wing is also added to the table. As it can be seen on the table, the span of 8.21 metres complies with requirement VTOL-GND-1, which dictates the maximum horizontal dimension of the plane, 14 metres, in order to be able to operate from common helipads. This, in turn, makes the aircraft compliant with VTOL-LFT-6, which requires the aircraft to be able to take off and land in conventional helipads. Also regarding the external dimensions of the aircraft, VTOL-GND-2 concerns the maximum dimensions for storage of the aircraft in standard hangars. The dimensions of the Wigeon are similar to those of the Cessna 172, both in terms of fuselage length and span, which therefore suggests that the aircraft will be storable in current facilities, and thus this requirement is met.

Table 7.1: Wing planform parameters for the three concepts. For the double wing configurations, the values for one of the two wings are given.

Parameter	Values	Parameter	Values
S [m^2]	9.91	C_t [m]	0.749
b [m]	8.21	$\bar{c}$ [m]	1.27
AR [-]	6.80	$\Lambda_{c/4}$ [rad]	0.00
C_r [m]	1.67	λ [-]	0.45
h_{WL1}[m]	0.5	h_{WL2}[m]	0.5

7.2. Airfoil Selection

Despite the NASA LANGLEY LS0417 being chosen as the airfoil during the previous design phase [71], the selection was repeated to account for the changes in surface area, and cruise speed of the design. To perform the airfoil selection, the value for the design lift coefficient must be found. The design lift coefficient can be found by rearranging the lift equation to yield C_L:

$$C_{L_{des}} = \frac{W}{0.5\rho V^2 S} \quad (7.12) \qquad C_{l_{des}} = \frac{C_{L_{des}}}{\cos^2 \Lambda_{LE}} \quad (7.13)$$

In order to obtain the design lift coefficient for the airfoil, the leading edge sweep of the wing must be taken into account, which can be done using Equation 7.13. The selection criteria that are used to select the airfoil are listed below, with its corresponding weight. Each airfoil is granted a score between 0 and 5 for each criteria, only using integers:

- $C_{d_{min}}$[1/9]: The lower the minimum drag of the airfoil, the more efficient cruise will be.
- C_L at $C_{d_{min}}$[1/9]: The closer this value is to the design lift coefficient, the better.
- Drag bucket range[1/9]: The larger the drag bucket is the better, as the airfoil can be used for a different design lift coefficient in case it changes. This criteria was evaluated quantitatively by computing the range of C_l values for which the C_d stayed within 0.001 of the minimum C_d.
- C_m at $C_{L_{des}}$[1/9]: The higher the C_m the better for the controllability of the aircraft, as trimming should be easier during cruise.
- $\frac{C_l}{C_d}$ at $C_{L_{des}}$[1/9]: The higher the lift drag ratio the more efficient cruise will be.
- $C_{L_{max}}$[2/9]: The higher the maximum lift coefficient, the better. A higher lift coefficient will increase the wing loading, which will therefore reduce the surface area of the wing.
- Stall characteristics[1/9]: An airfoil which has an smoother stall curve and does not experience a extremely sudden loss of lift is consider safer and thus better in this criteria. This criteria was evaluated qualitatively
- Thickness over chord ratio[1/9]:A higher thickness over chord is considered better as it reduces the structural weight of the wing.

Firstly, airfoils with the required characteristics for the Wigeon were searched in airfoil databases. Based on the data presented in the databases the following airfoils were selected for the trade off: EPPLER715, NACA23015, NASA LANGLEY LS1 0417, NACA63(3)-618, EPPLER 793 and NACA44017. The characteristics of the 3 best scoring airfoils are summarised in Table 7.2 below.

Table 7.2: Summary of characteristics of the best 3 airfoils. Simulation settings: M = 0, Ncrit = 9, and Re = 4500000. For $C_{L_{max}}$ Re = 2500000, due to the lower speed at stall. $C_{l_{des}} = 0.500$.

Criteria	NASA LANGLEY	Scores	EPPLER 793	Scores	NACA 44017	Scores
$C_{d_{min}}$[-]	0.00411	5	0.00600	3	0.00610	3
C_l for $C_{d_{min}}$[-]	0.318	3	0.577	4	0.528	5
Drag bucket [-]	0.3	3	1.0	5	0.6	4
$C_{m_{c/4}}$ at $C_{l_{des}}$[-]	-0.0617	3	-0.123	2	-0.0137	5
C_l/C_d at $C_{l_{des}}$[-]	89.2	5	84.8	4	86.6	4
$C_{L_{max}}$[-]	1.84	5	1.71	3	1.82	5
Stall characeristics	Safe	5	Safe	5	Safe	5
t/c [-]	0.17	5	0.156	4	0.17	5
Score -		39/45	-	33/45	-	41/45 %

The highest scoring airfoil, NACA44017 was chosen for the Wigeon aircraft. It is also worth noting that for the wingtips and vertical tail, the NACA 0012 has been chosen as the airfoil. Since this surfaces are not meant to produce lift, a camber is not necessary. Furthermore, a thickness to chord ratio of 0.12 helps reduce the profile drag produced by these parts of the aircraft.

7.3. Wing Performance

The performance of airfoil has to be transformed to that of a finite wing with the characteristics of the wing planform. To achieve this the DATCOM method is used. Below, equation 7.14 illustrates how to compute the lift slope [91] [102].

$$\frac{dC_L}{d\alpha} = C_{L_\alpha} = \frac{C_{l_\alpha}\ AR}{2 + \sqrt{4 + \left(\frac{AR\ \beta}{\eta}\right)\left(1 + \frac{\tan(\Lambda_{0.5C})^2}{\beta^2}\right)}} \tag{7.14}$$

Where β is the Prandtl-Glauert correction for compressibility and η is the airfoil efficiency factor which can be assumed to be 0.95. The interference with the fuselage decreases the lift slope and thus must be taken into account. Equation 7.15 shows how to obtain a factor that can be applied to the lift slope of the wing to account for fuselage interference [20].

$$K_{wf} = 1 + 0.025\left(\frac{w_f}{b}\right) - 0.25\left(\frac{w_f}{b}\right)^2 \tag{7.15}$$

$$C_L = s_1 \cdot \frac{dC_{L1}}{d\alpha}\alpha + s_2 \cdot \frac{dC_{L2}}{d\alpha}\alpha\left(1 - \frac{d\epsilon}{d\alpha}\right) \tag{7.16}$$

Where w_f is the maximum width of the fuselage. For the double wing concepts, the downwash on the second wing is critical to investigate the wing performance and aircraft behaviour. This was calculated using the Lifting Line theory code explained in Section 7.3.2. Having a finite wing also changes the $C_{L_{max}}$. From DATCOM Formula 7.17, the reduction in maximum lift coefficient can be found [91] [102]. Also, the stall angle can be estimated using formula 7.18:

$$C_{L\ max} = \left[\frac{C_{L\ max}}{C_{l\ max}}\right] C_{l\ max} + \Delta C_{Lmax} \tag{7.17}$$

$$\alpha_s = \frac{C_{L\ max}}{C_{L_\alpha}} + \alpha_{0L} \tag{7.18}$$

For the Wigeon, since it has a very low leading edge sweep, the $\left[\frac{C_{L\ max}}{C_{l\ max}}\right]$ ratio can be estimated to be 0.9[91]. ΔC_{Lmax} is a constant to account for compressibility effects, however, due to the low speed of the aircraft which is below 0.2 M during both cruise and landing, this term can be ignored. For the Wigeon, this formula had to be modified to account for the effect of the down wash. This is shown in equation 7.19.

$$C_{L\ max} = s_1\left[\frac{C_{L\ max}}{C_{l\ max}}\right] C_{l\ max} + s_2\left[\frac{C_{L\ max}}{C_{l\ max}}\right] C_l\left(\alpha_s - \frac{d\epsilon}{d\alpha}\alpha_s\right) \tag{7.19}$$

7.3.1. Wing tip modelling

Wing tips increase the aerodynamic efficiency of the wing by physically stopping the airflow on the high pressure side of the wing from moving to the low pressure side at the tip; thus reducing the induced angle of attack of the wing, which reduces induced drag. This can be modelled by increasing the effective AR of the wing. Equation 7.20 shows how this can be achieved [115].

$$AR_{eff} = \left(1 + \frac{2}{k_{WL}} \frac{h_{WL}}{b}\right)^2 AR \tag{7.20}$$

Where h_{WL} is the height of the winglet and k_{WL} is an efficiency factor for the winglet. When $k_{WL} = 1$, the effect of the winglet is the same as increasing the span of the wing by that amount. For a modern blended winglet, a value of $k_{WL} = 2$ can be used as an estimation [115].

However, the wing tip configuration is different for each wing. The winglets of the front wing point downward in an attempt to separate the tip vortices of the front wing as far away as possible from the inflow onto the rear wing. Additionally, the component of outwash from the propeller rotation further helps the vortex stream from propagating inwards. This reduces the downwash caused by the vortices themselves and reduces the interference of the vortex on the propellers on the second wing. On the other hand, the rear winglets have a more conventional design to de-energise the vortex generation, just like in a regular airliner. This helps achieve a significant reduction in the induced drag from the rear wing itself to further increase the lift over drag ratio.

7.3.2. Wing modelling using Lifting Line Theory

Lifting Line Theory is the first mathematical model to ever be developed to predict and understand the aerodynamic behaviour of a finite wing. Ludwig Prandtl suggested the use of a continuous vortex sheet (as illustrated in Figure 7.3) to be able to compute the lift distribution along the span of said wing. Such a model is valid for slender, unswept high aspect ratio wings under inviscid flow. Nonetheless, the lift distribution for a tandem wing aircraft like the Wigeon cannot be calculated independently with Prandtl's classical lifting line. In this project, the methods of several studies have been combined to address the double-lifting-surface layout that the Wigeon presents. Firstly, DeYoung and Harper published a method that evaluated the lift distribution over wings with arbitrary sweep, twist, taper and lower aspect ratios heavily reliant on Weissinger's publication about lift distribution over swept wings [42, 127]. Additionally, the effects derived from both horizontal and vertical wing spacing reported by Cheng and Wang were also included into the program generated for this purpose [27].

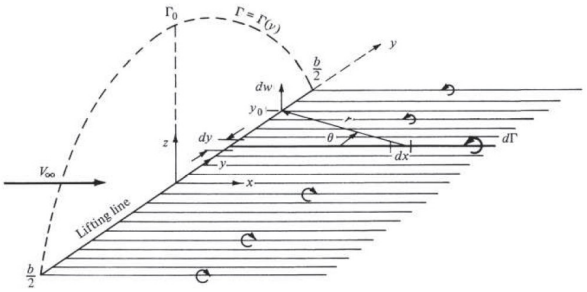

Figure 7.1: Superposition of an infinite number of horseshoe vortices along the lifting line. [7]

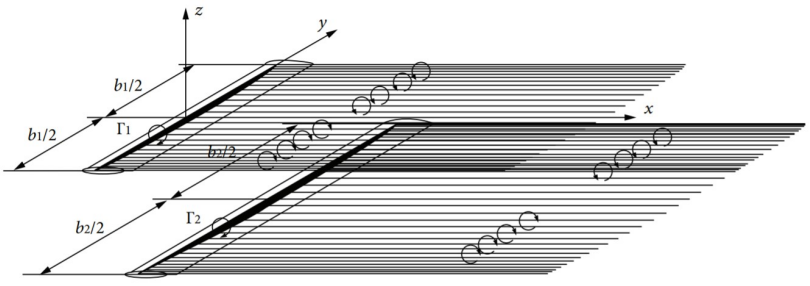

Figure 7.2: Prandtl's model for the bound vorticity and the trailing vortex parallel to the x-axis generated by tandem wings. [27]

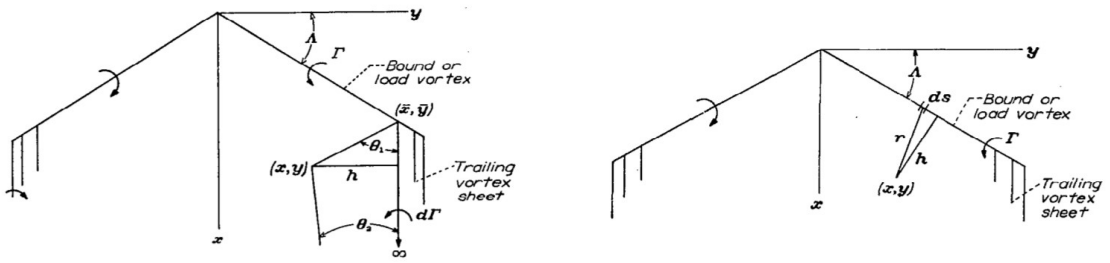

Figure 7.3: Downwash induced by the trailing vortex sheet (left) and the load vortex sheets (right). [42]

Lifting line modelling relies on determining downwash induced by each of the vortex sheets as DeYoung and Harper illustrate in Figure 7.3. The downwash from the trailing vortex at any point in the XY plane of a single wing is given in Equation 7.21. Similarly, the downwash generated from the swept load vortex on which the circulation is varying continuously can be found in Equation 7.22:

$$dw_{xy} = \frac{d\Gamma}{4\pi h}\left(\cos\theta_1 + \cos\theta_2\right) \tag{7.21}$$

$$dw_{xy} = \frac{\Gamma h ds}{4\pi r^3} \tag{7.22}$$

The definition of the geometric variables defined in Equation 7.23 and Equation 7.24 follow from Figure 7.3, and are needed to evaluate the downwash integrals from the different vortices.

$$\begin{aligned} h &= y - \bar{y} \\ \cos\theta_1 &= \tfrac{x-\bar{x}}{\sqrt{(x-\bar{x})^2+(y-\bar{y})^2}} \end{aligned} \tag{7.23}$$

$$\begin{aligned} h &= x\cos\Lambda \pm y\sin\Lambda \\ r &= \sqrt{(x-\bar{x})^2+(y-\bar{y})^2} \end{aligned} \tag{7.24}$$

The total downwash at any point from the XY plane is the sum of the integral forms of Equation 7.21 and Equation 7.22. Through the use of non-dimensional relations shown in Equation 7.25 and Equation 7.26, the non-dimensional total downwash integral then follows in Equation 7.27 and also represents the total induced angle of attack from the vortex effects of a single wing:

$$\begin{aligned} \eta &= \tfrac{y}{b/2} \\ \bar{\eta} &= \tfrac{\bar{y}}{b/2} \end{aligned} \tag{7.25}$$

$$G = \frac{\Gamma}{bV} \tag{7.26}$$

$$(\alpha_i)_\eta = \left(\frac{w}{V}\right)_\eta = \frac{1}{\pi}\int_{-1}^{1}\frac{G'(\eta)d\bar{\eta}}{\eta-\bar{\eta}} + \frac{b/c}{2\pi}\int_{-1}^{1} L(\eta,\bar{\eta})G'(\bar{\eta})d\bar{\eta} \tag{7.27}$$

Equation 7.27 makes use of the so-called Weissinger L-function, shown in Equation 7.28, which takes two different forms depending on the sign of the coordinate η. When η is negative, the Weissinger L-function is equal to its value when η is positive added to an additional term dependent on the wing geometry:

$$L(\eta,\bar{\eta}) = \begin{cases} \frac{1}{(b/c)(\eta-\bar{\eta})}\left(\frac{\sqrt{[1+(b/c)(|\eta|+\bar{\eta})\tan\Lambda]^2+(b/c)^2(\eta-\bar{\eta})^2}}{1+(b/c)(|\eta|+\eta)\tan\Lambda} - 1\right) & \bar{\eta} \geq 0 \\ \qquad\qquad \ldots + \frac{2\tan\Lambda\sqrt{[1+(b/c)|\eta|\tan\Lambda]^2+(b/c)^2\eta^2}}{[1+(b/c)(|\eta|-\eta)\tan\Lambda][1+(b/c)(|\eta|+\eta)\tan\Lambda]} & \bar{\eta} \leq 0 \end{cases} \tag{7.28}$$

Given an arbitrary load distribution, a continuous circulation distribution can be approximate by means of a Fourier series in Equation 7.29. A taper ratio was previously selected to allow for a lift distribution as reassembling to a perfect elliptic distribution as achievable.

$$\Gamma(\theta) = 2bV_\infty \sum A_n \sin n\theta \tag{7.29}$$

The following spanwise trigonometric variable ϕ is introduced accompanied by the intermediates m, n and μ, as means to determine the sectional lift along an arbitrary number of stations along

the wing and allows to express the non-dimensional circulation as a function of this variable.

$$\phi_n = \frac{n\pi}{m+1} \tag{7.30}$$

$$G = G(\phi) = \sum_{\mu=1}^{m} a_\mu \sin n\phi_n \tag{7.31}$$

The aerodynamic characteristics are then computed by evaluating the procedure. For symmetrically loaded wings, expressions for the Wing lift coefficient and induced drag coefficient are found with a quadrature and collected in Equation 7.32 and Equation 7.33 correspondingly. More information about the mathematical series coefficients $b_{\nu\nu}$ and $b_{\nu n}$ can be found in DeYoung and Harper's paper.

$$C_L = \frac{\pi AR}{m+1}\left(G_{\frac{m+1}{2}} + 2\sum_{n=1}^{\frac{m-1}{2}} G_n \sin\phi_n\right) \tag{7.32}$$

$$C_{D_i} = \frac{\pi AR}{m+1}\sum_{\nu=1}^{m} G_\nu \left(b_{\nu\nu}G_v - \sum_{n=1}^{m} b_{\nu n}G_n\right)\sin\phi_\nu \tag{7.33}$$

Finally, Weissinger's method implemented in the code is able to retrieve the non-dimensional circulation over spanwise stations as given by Equation 7.34 . As a result, it is possible to revert back the transformation and express back in terms of sectional lift and sectional lift coefficient.

$$\begin{aligned} G(\phi) = \tfrac{2}{m+1}\,[&(\sin\phi_1 \sin\phi + \sin 2\phi_1 \sin 2\phi + \ldots + \sin m\phi_1 \sin m\phi)\, G_1 + \\ &(\sin\phi_2 \sin\phi + \sin 2\phi_2 \sin 2\phi + \ldots + \sin m\phi_2 \sin m\phi)\, G_2 + \\ &\vdots \\ &(\sin\phi_m \sin\phi + \sin 2\phi_m \sin 2\phi + \ldots + \sin m\phi_m \sin m\phi)\, G_m] \end{aligned} \tag{7.34}$$

$$L = C_L q_\infty S = \int_{-b/2}^{b/2} L'dy = \int_{-b/2}^{b/2} c_l(y)\cdot c(y)\cdot q_\infty \quad dy \tag{7.35}$$

This model is valid for finite wings with variable chord, arbitrary sweep, twist, taper and lower aspect ratios (in contrast to regular lifting line theory) under inviscid flow. To account for wing wing interaction, the downwash induced by the first wing on the second wing was calculated by accounting for the circulation of the trailing and load vortex sheets as shown in Figure 7.3 by using Equations 7.22 and 7.21 and including also the z coordinate, as there exists a vertical gap between the wings. Figures 7.4 and 7.5 provide numerical outputs for $\alpha = 9$ and are shown below:

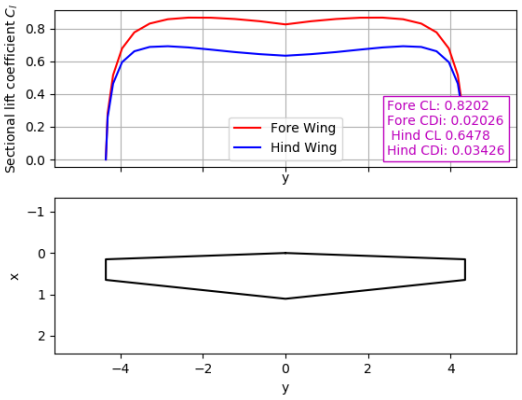

Figure 7.4: Sectional lift coefficient distribution over both wings.

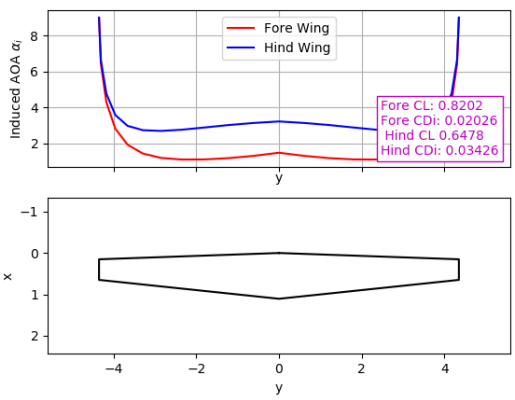

Figure 7.5: Induced angle of attack distribution over both wings.

7.3.3. Propeller wing interaction

Propeller wing interaction is an aspect of the Wigeon's aerodynamics that cannot be neglected, since a large fraction of the Leading Edge of the wings is covered by the propellers due to the use of distributed propulsion. In order to predict the effect of propeller's on lift, the method presented by Bouquet et al [17].

$$C_{L_{tot}} = C_{L_{\mathrm{W+S}}} + C_{L_{\mathrm{P}}} + C_{L_{\mathrm{T}}} \tag{7.36}$$

Where $C_{L_{\mathrm{W+S}}}$ is the lift coefficient from the wing including the slipstream effect of the propellers, $C_{L_{\mathrm{P}}}$ accounts for the lift produced by the normal force, which is neglected, and finally, $C_{L_{\mathrm{T}}}$ is the lift from thrust, which is computed using Equations 7.37 and 7.38 below[17]:

$$C_{L_T} = C_T \sin\alpha \tag{7.37}$$

$$C_T = \frac{T}{\frac{1}{2}\rho V^2 S} \tag{7.38}$$

For the lift coefficient of the wing for slipstream, the following equation is used for each wing [17]:

$$C_{L_{\mathrm{W+S}}} = \frac{2}{S_i}\left(\frac{\pi}{4}b_{\mathrm{W}}^2 - n_e\frac{\pi}{4}D^{*2}\right)\sin\varepsilon + n_e\frac{\pi D^{*2}}{2S_i}\frac{(V+\Delta V)^2}{V^2}\sin\varepsilon_{\mathrm{S}} \tag{7.39}$$

Where S_i is the area of the wing, n_e is the number of propellers on the wing. To compute D^* and ΔV the equations below can be used [17]:

$$\frac{\Delta V}{V} = \sqrt{1 + C_T\frac{S_{\mathrm{W}}}{n_c\frac{\pi}{4}D^2}} - 1 \tag{7.40}$$

$$D^* = D\sqrt{\frac{V+\Delta V/2}{V+\Delta V}} \tag{7.41}$$

Where D^* is the diameter of the contracted slipstream due to the propeller, which is calculated from the propeller diameter D and the effective velocity increase due to the slipstream, which is computed using Equation 7.40. Another parameter needed is the downwash produced by the wing in and out of the slipstream, which are ϵ_S and ϵ respectively. Equations 7.42 and 7.43 can be applied [17].

$$\sin\varepsilon_{\mathrm{S}} = \frac{2C_{L_{\alpha_{s,\,\mathrm{eff}}}}}{\pi A_{s,\mathrm{eff}}}\sin\alpha_{\mathrm{S}} \tag{7.42}$$

$$\sin\varepsilon = \frac{2C_{L_{\mathrm{W}}}}{\pi A_{\mathrm{W}}} \tag{7.43}$$

Where $A_{s,\mathrm{eff}}$ is the effective aspect ratio of the fraction of the wing in the slipstream, and $\alpha_{s,\,\mathrm{eff}}$ is the effective angle of attack of the wing when inside the slipstream [17]. Overall, by using this model, the propeller has a very significant effect on the performance of the aircraft, as the C_{L_α}, $C_{L_{max}}$ and α_{0L} change; however, the magnitude of this change depends on the thrust level of the propellers. There are other effects to propeller wing interaction that this model does not address, such as the reduction in pressure drag due to higher Reynolds numbers, or the effects on the lift distribution along the span caused by the rotation direction of the propeller. The effects of the propeller wing interaction on the wing performance can be observed in Table 7.3. A qualitative aspect that is taken into account in the design if the effect of having the wing tip placed propeller have outboard rotation. By doing this the effective angle of attack close to the tip increases due to the tangential component of the velocity generated by the propeller blades, which points upwards, this would complement the effect of the wingtips and increase the effective aspect ratio; however it is also possible that unexpected interactions could occur.

7.3.4. Aerodynamic centre and pitching moment

The Aerodynamic centre and pitching moment at the aerodynamic centre where computed using the airfoil data from XFLR5. The moment and normal force data where linearised with respect to the angle of attack using a linear regression, which yielded close fits with R squared values above 0.985, then the ac was computed using Equation 7.44. For computing the moment at the ac Equation 7.45 [82] is applied using all the available data points, and then the average is taken.

$$\frac{x_{ac}}{c} = \frac{x}{c} - \frac{\frac{\partial C_{m_x}}{\partial\alpha}}{\frac{\partial C_N}{\partial\alpha}} \tag{7.44}$$

$$C_{m_{ac}} = C_{m_x} + \left(\frac{x_{ac}}{c} - \frac{x}{c}\right)C_N \tag{7.45}$$

Then for obtaining the $C_{m_{ac}}$ of the wing Raymer [102] proposes the following formula:

$$C_{m_{ac,w}} = C_{m_{ac,\mathrm{airfoil}}}\left(\frac{AR\cos^2\Lambda}{AR + 2\cos\Lambda}\right) \tag{7.46}$$

7.3.5. Summary

Finally, the performance of the wing planform is summarised below for three different thrust levels.

Table 7.3: Lift curve characteristics of the wing planform of the Wigeon at 3 different levels of thrust per engine, with $A_{prop} = 0.95\text{m}^2$, $V = 72$ m/s and $n_e = 12$.

Parameter	T = 0	T = 150 N	T = 300 N
$\alpha_{0L}[^\circ]$	-3.30	-3.25	-3.22
C_{L_α}	3.68	3.78	3.89
$K_{wf}C_{L_\alpha}$	3.54	3.63	3.73
α_s	20.58	20.58	20.58
$C_{L_{max}}$	1.48	1.51	1.55
$C_{m_{ac,w}}[-]$	-0.00287	-0.00287	-0.00287
$x_{ac}[-]$	0.284	0.284	0.284

As can be observed a number of assumptions were made when incorporating the effect of the propellers. It was assumed that the stall angle remains unchanged, although due to the higher effective Reynolds number produced by the propeller slipstream, it is possible that stall could be slightly postponed; however, since this is not investigated in the paper in which this model is proposed, this included has not been implemented in the calculations [17]. Furthermore, the aerodynamic centre and its moment coefficient were also assumed to be unaffected by the wing propeller interaction.

7.4. Drag Polar

In order to estimate the drag polar of the aircraft, the component drag method is used, with a modification that was made to include the XFLR5 airfoil data in the polar. This modification is based on the drag polar formula suggested by Traub [65], which is shown below:

$$C_D = C_{\text{dmin}} + k_p \left(C_L - C_{\text{lmd}}\right)^2 + k_i C_L^2 \tag{7.47}$$

Where the lift dependent profile drag and induced drag of the wing are separated, however, instead of estimating the profile drag using a quadratic regression, the airfoil data from XFLR5 is used. The parasitic drag of the non lifting surfaces is computed by applying Equation 7.48

$$C_{D_0} = \frac{1}{S_{ref}} \sum_c C_{f_c} \cdot FF_c \cdot IF_c \cdot S_{wet_c} + C_{D_{misc}} \tag{7.48}$$

Here, FF is the form factor for estimating the pressure drag due to viscosity, the interference factor , IF is the interference factor to take into account the drag resulting from the interactions of different components and S_{wet} which is the wet surface area of the component. $C_{D_{misc}}$ was included in the parasitic drag by applying a 1.05 factor to the CD_0 value of each component [91]. C_f, the skin friction coefficient is computed based on the Reynolds number and the type of flow. For the fuselage it was assumed that 10% of the flow is laminar, while for the wingtips and tail 35% of the flow was assumed to be laminar [91]. Then the skin friction coefficient can be computed using equation 7.49.

$$C_f = \begin{cases} \frac{1.328}{\sqrt{Re}} & \text{Laminar} \\ \frac{0.455}{(\log Re)^{2.58}(1+0.144M^2)^{0.65}} & \text{Turbulent} \end{cases} \tag{7.49}$$

For the wing, the profile drag was computed by multiplying the airfoil drag by the interference factor, which was taken to be 1.1 for both wings based on empirical data [91]:

$$C_{d_{wing}} = IF_w C_{d_{airfoil}} \left(\frac{C_L}{\cos^2 \Lambda_{LE}}\right) \tag{7.50}$$

$$C_{D_u} = \frac{3.83 u^{2.5} A_{\text{max}}}{S_{ref}} \tag{7.51}$$

The wet area of the fuselage was calculated by assuming a simplified shape, where the nosecone is modelled with a parabolic shape, the cabin section as a cylinder and the tail cone as a cone. This results in Equation 7.52 [91]:

$$S_{w,f} = \frac{\pi D}{4}\left(\frac{1}{3L_1^2}\left[\left(4L_1^2 + \frac{D^2}{4}\right)^{1.5} - \frac{D^3}{8}\right] - D + 4L_2 + 2\sqrt{L_3^2 + \frac{D^2}{4}}\right) \tag{7.52}$$

Where L1 is the length of the parabolic section, L2 is the length of the cylindrical section and L3 is the length of the conical section. Another drag components related to the fuselage is the upsweep drag, which can be found by applying Equation 7.51. Where u is the upsweep angle of the tail cone in radians and A_{max} is the biggest cross sectional area of the fuselage. It was chosen to be 8.43 degrees, as adding upsweep was needed to increase the vertical gap h between the two wings. The base drag of the fuselage, C_{d_b}, is not be considered as the base area of the fuselage design is 0 in order to reduce drag. The remaining component of the drag is the lift induced drag. For this, only the inviscid part of the induced drag has to be taken into account, since the viscous part is accounted for using Equation 7.50, hence the inviscid part of the Oswald efficiency factor, which can be approximated as the span efficiency factor to be used [65]. In order to calculate induced drag, the method proposed by Schiktanz et al. for tandem aircraft with similar spans for both wings is used [114]. Where e_{ref} is the span efficiency factor of a wing with the equivalent aspect ratio of the two wings combined, which was found by linearly interpolating data for different AR and taper values from Nita et al [87].b is the equivalent span and h is the vertical gap between the wings at the MAC. Then the lift induced drag can be calculated with Equation 7.53:

$$C_{D_i} = \frac{C_L^2}{\pi A R e_{tan}} \tag{7.53}$$

$$\frac{e_{\text{tan}}}{e_{\text{ref}}} = 0,5 + \frac{1 - 0,66 \cdot h/b}{2,1 + 7,4 \cdot h/b} \tag{7.54}$$

Where AR is the AR for both wings calculated in Equation 7.8. The resulting drag polars are shown below, both for the airfoil and the entire aircraft in Figure 7.6. Furthermore, Table 7.4 shows the relevant parameters for describing the drag polar of the Wigeon aircraft, and Figure 7.7 presents a breakdown of the drag cor

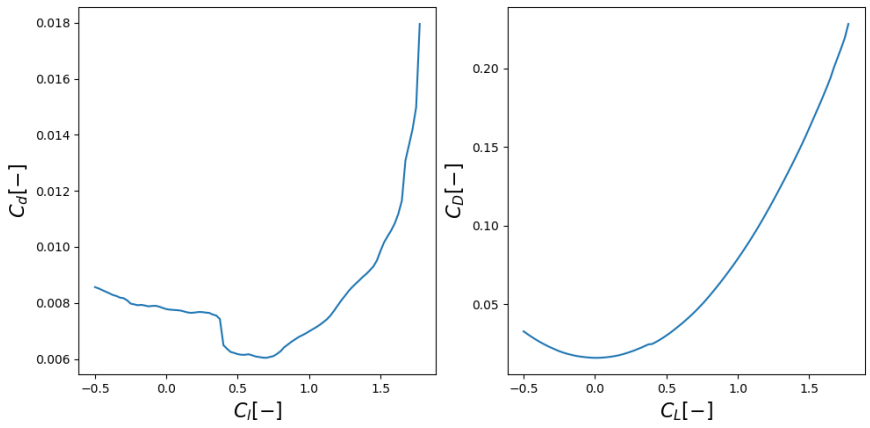

Figure 7.6: The left graph shows the drag polar of the NACA44017 airfoil, the right graph shows the drag polar of the entire aircraft. The airfoil data is for the following settings: Re= 4500000, Ncrit = 9, M = 0.

Table 7.4: The components of minimum drag, the constant of the drag polar and the maximum lift over drag ratio for all three configurations.

Parameter	Value
$C_{D_{0,fus}}$ [-]	0.00437
$C_{D_{0,Tail,Wingtips}}$ [-]	0.000565
$C_{d_{min,wing}}$ [-]	0.00604
C_{d_u} [-]	0.00296
k_i [-]	0.0637
$\frac{C_L}{C_D}_{max}$ [-]	16.3

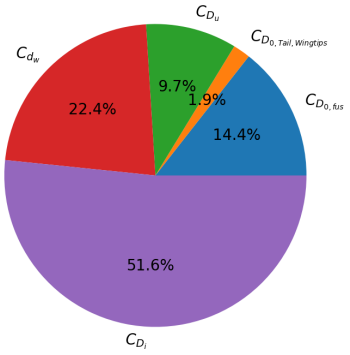

Figure 7.7: Drag component breakdown at cruise conditions, $C_L = 0.496$, $C_D = 0.0304$.

7.5. Aerodynamics Model for Transition

An Aerodynamics model had to be created in order to calculate the energy consumption during the transition phase of the mission. For this, a model created by Martins et al [25] has been modified to fit the Wigeon's characteristics. The post stall lift and drag for the wing was calculated and the drag of the fuselage was added; however, its lift was neglected. For the post stall lift the following formulae are needed [25]:

$$C_L = A_1 \sin 2\alpha + A_2 \frac{\cos^2 \alpha}{\sin \alpha} \tag{7.55}$$

$$A_2 = (C_{L_s} - C_1 \sin \alpha_g \cos \alpha_s) \frac{\sin \alpha_s}{\cos^2 \alpha_s} \tag{7.56}$$

$$A_1 = \frac{C_1}{2} \tag{7.57}$$

$$C_1 = 1.1 + 0.018\,(s_1 AR_1 + s_2 AR_2) \tag{7.58}$$

For post stall drag, a similar set of equations can be used [25]:

$$C_D = B_1 \sin \alpha + B_2 \cos \alpha \tag{7.59}$$

$$B_2 = \frac{C_{D_s} - C_{D_{max}} \sin \alpha_s}{\cos \alpha_s} \tag{7.60}$$

$$B_1 = C_{D_{max}} \tag{7.61}$$

$$C_{D_{max}} = \frac{1.0 + 0.065\,(s_1 AR_1 + s_2 AR_2)}{0.9 + t/c} \tag{7.62}$$

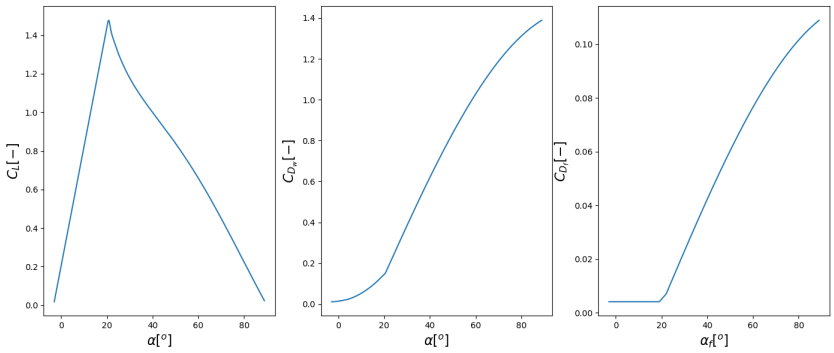

Figure 7.8: C_L alpha curve, and C_D alpha curves for the wing and fuselage separately for the transition models. Values are shown from $\alpha = -3^o$ to $\alpha = 90^o$

For the fuselage, the $C_{D_{max}}$ was estimated based on the C_D of a cylinder, which based on empirical data, is approximately 1.18 with respect to its cross sectional area, thus in order to find the C_D for this situation it has to be multiplied by $\frac{A_{fus}}{S_{ref}}$. The reason why the wings and the fuselage are considered separately is that the aircraft uses a tilt wing mechanism, meaning that the angle of attack of the wing and fuselage are independent. This yielded the following models above. Before stall, the drag polars calculated in Section 7.4

were used. It can be noticed that this results in the initial part of the fuselage polar to be flat, which is due to the model assuming the parasitic drag of the fuselage does not vary with C_L. This is inaccurate; however, its effect should not be too great as the fuselage drag is considerably lower than the drag from the wings in the post stall model, as the $C_{D_{max}}$ of the fuselage is approximately 0.105 while for the wing it is approximately 1.4, which can be seen in Figure 7.8.

7.6. CFD Analysis

CFD is a powerful tool that is regularly used to solve complex fluid mechanics problems numerically and the fluid's interactions with some defined boundary conditions. The setup of the simulation was built around the geometry found of interest to investigate. The novelty and complexity of such a tandem tilt-wing configuration push the team's interest in performing such a simulation to analyse, optimise and verify the performance of the design before testing any costly prototypes. Due to the limited power capability and time, it was decided to remove the fuselage and propulsion systems to ease the investigation of wing-wing interactions. Figure 7.9 illustrates the wing geometry within the outline of the selected domain and its corresponding dimensions.

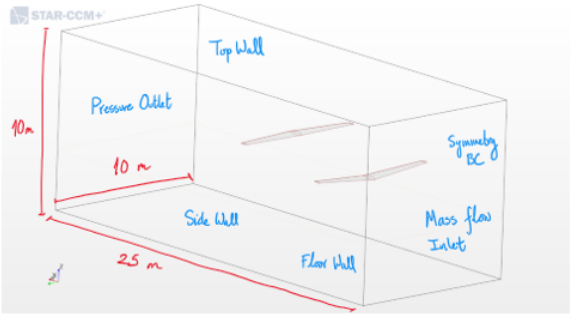

Figure 7.9: Simulation definition for the tandem wing geometry, with annotated domain dimensions and boundary conditions.

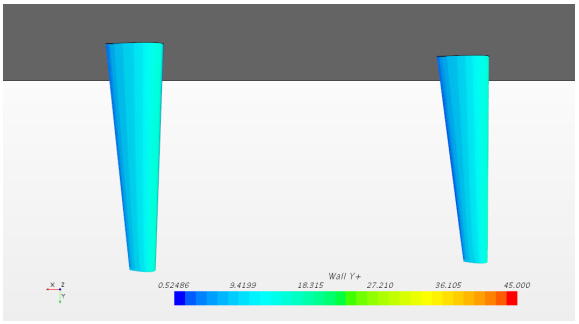

Figure 7.10: y^+ distribution over the two wings.

Once the geometry was imported, Star-CCM+ offers a large number of different physic models to carry out the simulation. Given the nature of the problem, the simulation was carried on a fluid domain where a three-dimensional incompressible air flow reigned. In addition, the computer would utilise a steady RANS solver which incorporated the use of SST k-omega turbulence with all y^+ wall treatment. The k-omega turbulence is a linear eddy viscosity hybrid model which combines the benefits of k-omega, very accurate when dealing with strong pressure gradients and flow separation; while k-epsilon is very accurate when solving far away from the wall.

The program was then configured to create an automated mesh through a surface remesher, a prism layer mesher and a trimmer. One can observe in Figure 7.12 the resolution of the mesh close to the wing surface boundary condition, as well as the 11 prism layers used to predict the boundary layer. The volume mesh generated is comprised of around 12 million cells for this simulation.

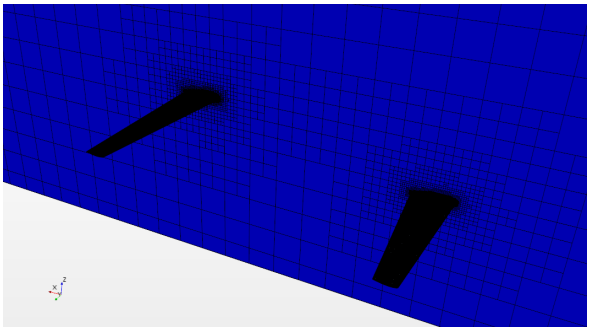

Figure 7.11: Meshing of the fluid region around both wings.

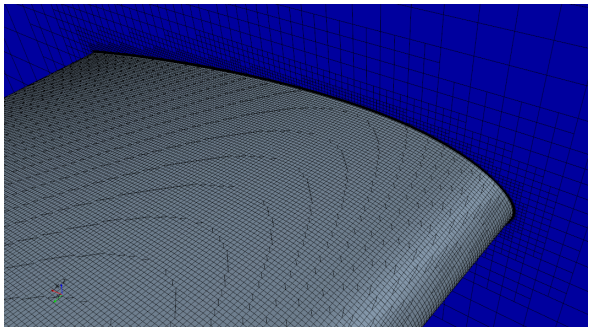

Figure 7.12: Close-up and mesh details of the wing.

However, from Figure 7.10 one can observe that the y^+ value computed at the wing boundaries lies within the buffer region where $5 < y^+ < 30$. This implies that the calculation suggests that the flow on these points lies midway between been fully dominated by viscous effects and turbulence. As a result, shear stresses due to viscous and turbulence stresses are of similar magnitude and it becomes very difficult to accurately predict the velocity profile of the boundary layer. A future recommendation is to adapt the prism layer sizing to mould the y^+ close to 1, where the k-omega turbulence model works the best.

The results of the simulation after 400 iterations (when residuals converged to asymptotes) are collected on Figure 7.13 and a mesh convergence study on Table 7.8. Figure 7.13 illustrates the pressure distribution around the wings and allowed the team to gather a better understanding of how the airflow behaves around and what the Wigeon's external shape attempts to handle it. On the other hand, the quantitative results gathered for the aerodynamic properties can later be used for verification and validation purposes with the models presented previously in this chapter.

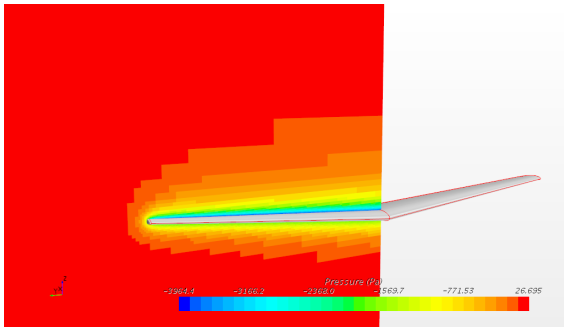

Figure 7.13: Pressure distribution on the front wing's surroundings.

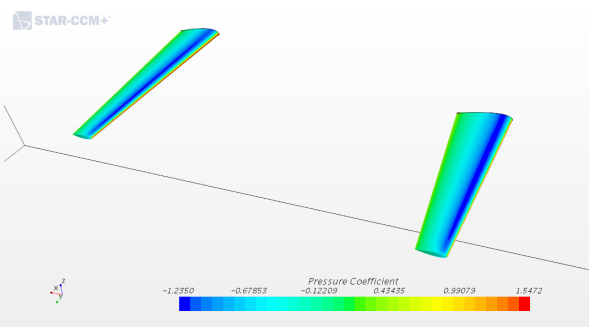

Figure 7.14: Pressure coefficient distribution over the wing surfaces.

Table 7.5: Grid convergence study for the tandem wing CFD simulation

Number of Cells	Time to run	C_L (front/rear)	C_D (front/rear)	Sdr Residual
≈ 5 M	5 h 00 min	0.0509 / 0.0292	0.00639 / 0.00664	3.65 E -2
≈ 6 M	6 h 00 min	0.0538 / 0.0327	0.00629 / 0.00655	8.27 E -3
≈ 8 M	8 h 40 min	0.0547 / 0.0366	0.00612 / 0.00622	6.41 E -3
≈ 12 M	13 h 20 min	0.0555 / 0.0384	0.00605 / 0.00590	5.74 E -1

7.7. Sensitivity Analysis

In this section, the sensitivity of wing placement and wing tip design with regard to aerodynamic performance of the Wigeon are explored. The reasons to include such sensitivity analyses were to check whether the design point of the Wigeon was optimal or if it could be further improved upon. Additionally, they were also used to test the volatility of the performance indicators associated to those design variables.

7.7.1. Stagger and Gap

When a preliminary estimate was first needed, the team decided to place the wings as far apart as the fuselage length and height allowed to. Further development of the project allowed to explore how wing placement affected aerodynamic properties as well as stability and control traits.

As a result, a sensitivity analysis was performed to investigate how volatile some parameters are with respect to wing stagger and gap. Munk was one of the pioneers who investigated phenomenon associated with tandem wings and presents Equations 7.63 and 7.64 to compute the additional induced lift coefficient gain and the penalty in terms of induced drag from placing a second wing depending on their relative locations [83]:

$$\Delta C_L = 2\, C_L \frac{S}{b^2}\left(\frac{1}{k^2} - 0.5\right)\frac{b}{R}\frac{S_t}{b} \tag{7.63}$$

$$C_{D_i} = C_D - \frac{C_L^2}{\pi}\left(\frac{S_1}{b_1^2 k_1^2} - \frac{S_2}{b_2^2 k_2^2}\right) \tag{7.64}$$

These equations contain a number of unfamiliar parameters of which Munk explains in detail. k is a parameter determined empirically which influences the so called Munk factor and depends on the stagger-gap ratio. R represents average distance between the middle of a wing and the origin of the longitudinal vortex from the other wing being modelled. Additionally, K and E are the complete elliptic integrals evaluated for the intermediate p.

$$p = \frac{1}{\sqrt{1 + G_p^2}} \tag{7.65}$$

$$\frac{R}{b} = \frac{\pi}{4}\frac{\sqrt{1 + G_p^2} - G_p}{K(p) - E(p)} \tag{7.66}$$

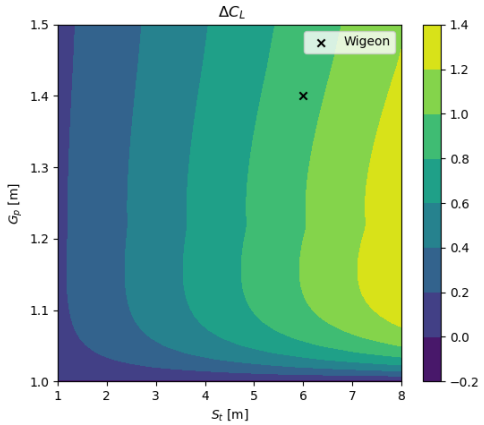

Figure 7.15: Sensitivity analysis for induced lift coefficient in terms of stagger and gap.

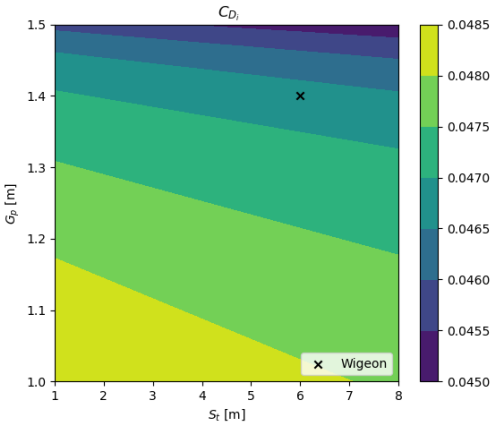

Figure 7.16: Sensitivity analysis for induced drag coefficient in terms of stagger and gap.

From Figure 7.15, one can observe that having a gap between wings of 1 meter or lower is highly detrimental in terms of performance because Munk's formula predicts a negative change of lift coefficient. this could be explained by the fact that the closer wings are together, the more noticeable is the effect of downwash from the first wing on the second wing. This effect is mitigated the further apart the wings are placed, as suggested by the contours from Figure 7.15. However, the plot from Figure 7.16 further reinforces this idea, from which we can observe that the drag penalty increases when gap is reduced. The optimisation code that was created by the team and discussed in Chapter 13 takes into account a large number of variables, including stagger and gap, to find the best design solution which fits within the requirements.

7.7.2. Wingtip efficiency and laminar flow fraction on fuselage

One of the values that was assumed which could affect the performance of the aircraft is the efficiency of the wing tips, k_{WL}. From literature a value of 2 was chosen, however, this value can change significantly with small differences in the geometry, as the design of an efficient winglet is complicated [115]. Another aspect that was estimated is the boundary layer on the fuselage skin. It was taken to be 10% laminar; however this is only a preliminary estimation. Thus, the effect of changing these parameters should be investigated to ensure that, if in reality, they are different than their assumed values, it does not have significant consequences in the aerodynamic performance of the Wigeon. A sensitivity analysis was created to evaluate the effect of these parameters in the L/D ratio of the Wigeon in cruise. The result can be observed in Figure 7.17.

As can observed, from the graph, the sensitivity of the L/D ratio is considerable for the wingtip efficiency, but specially for values closer to 1, which are less realistic. On the other hand, for the laminar fraction the sensitivity is quite low. This is probably due to the fact that the induced drag is a much greater fraction of the drag than the parasitic drag of the fuselage, as shown in Figure 7.7.

7.8. Verification and Validation

For this section, firstly the verification activities for the aerodynamics code are described, then the validation activities for the code and for the Wigeon aircraft in the future are discussed.

7.8.1. Verification

A number of different unit tests were created to ensure no errors exist in the code. Most of these tested that the behaviour of the code was as expected by changing inputs and observing how the output responded to these inputs. Examples of these are for instance Increasing the Aspect ratio and checking that the induced drag is reduced, and that the lift slope of the aircraft increases by the expected amount.

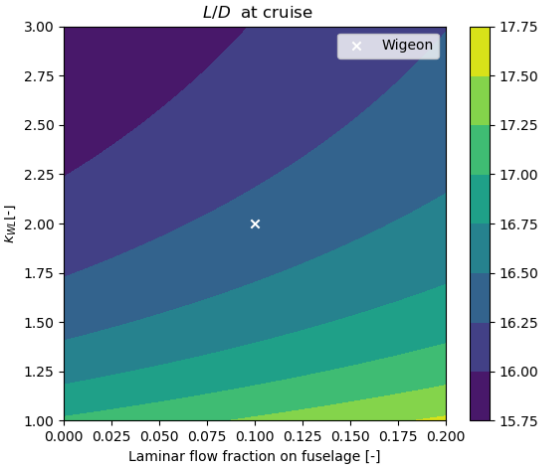

Figure 7.17: Sensitivity Analysis of the wingtip efficiency and fraction of laminar boundary layer of the fuselage.

For verifying the calculations related to induced drag, the XFLR5 Vortex Lattice Method software was used. A number of inviscid analyses were completed for a range of -5 to 5 degrees angle of attack, using different tandem wing configuration geometries. Then the resulting values for the span efficiency factor, which were obtained based on the resulting C_L and C_{Di} of the XFLR5 simulation, are compared to the values obtained from the estimation method used in the optimisation of the eVTOL. The comparison is shown in Table 7.6 below:

Table 7.6: Comparing span efficiency factors from analytical optimisation method and XFLR5 software, $S_{ref} = 17$ m^2, $V = 70$m/s.

S_1/S_2[-]	AR[-]	h[m]	l_h[m]	e_{XFLR5}[-]	e_{LLT}	e[-]	Error$_{XFLR5}$ [%]	Error$_{LLT}$ [%]
1	3.75	1.4	6	1.338	1.172	1.310	2.14	10.53
0.5	3.75	1.4	6	1.401	1.204	1.311	6.86	8.16
0.8	3.75	1.4	6	1.335	1.204	1.311	1.83	8.16
1	4.5	1.4	6	1.32	1.179	1.288	2.48	8.46
1	3.75	1.2	6	1.304	1.142	1.277	2.11	10.57
1	3.75	1.4	4.5	1.337	1.155	1.310	2.06	11.83

As can be seen, the results match for the most part, with the error being below 2.5% for most measurements except for the case in which the surface areas of each wing have a ratio of 0.5. This is probably due to the fact that although in case the wings have different spans, the function can still be used by taking an average span, it was created for situations were the spans of the tandem wings are almost identical; thus, the more difference in span, the less accurate the function becomes. However, it seems that if the difference is smaller, the function still makes a very accurate prediction for wings with more similar spans, as for a area ratio of 0.8, the error is only 1.83%. For the LLT, the situation is different, the error is over 10% for 3 cases; however, certain aspects indicate that this is due to the inaccuracies that occur in lifting line codes for low aspect ratios, as explained in Section 7.3.2. For a single wing with AR = 7.5, the code predicts a span efficiency factor of 0.911, where as XFLR5 predicts 0.997 and the method used in the optimisation code predicts 0.991, which means the error of the LLT code for a single wing is 8.17 %, which is close to the errors for two wing systems.

Another drag estimation that was verified using a different model is the parasitic drag of the fuselage. The model is for verification was created by Nicolosi et al. [86] and is based on CFD calculations. In order to make this comparison, the fuselage had to be modified, as the current model of the fuselage was too short

and the graphs presented in the paper could not be used to obtain certain coefficients. The model is based on the following formula [86]:

$$C_{D,fus} = (K_n S_n + K_c S_c + K_t S_t)\, C_{D,fp} \frac{1}{S} \tag{7.67}$$

Where K_n, K_t and K_c are factors which depend on the geometry of the nosecone, tail cone and cabin respectively. The parameters used for the comparison and the results are shown in the table below:

Table 7.7: Significant parameters for fuselage drag verification and results. $S_{ref} = 70$ m^2, $V = 72$m/s

S_n[m^2]	S_c[m^2]	S_t[m^2]	K_n[-]	K_c[-]	K_t[-]	$C_{D,fus,ver}$[-]	$C_{D,fus}$[-]	Error[%]
6.44	24.9	9.22	1.75	1.22	0.80	0.00673	0.00618	8.31

As seen in Table 7.7 the results of the two methods have a noticeable difference. One of the differences between the two methods is that Nicolasi et al assumes that the boundary layer is turbulent in the entire fuselage, while in this report it is assumed that 10% of the surface has laminar flow. If this is changed to 0, the value of for $C_{D,fus}$ increases to 0.00681, which is very close to the result of the new method. Another aspect to be taken into account is that the component drag method considers upsweep drag separately. If this component was added to C_{D_0}, the parasitic drag yielded by the component drag method would be significantly greater.

7.8.2. Validation

For validating the lift and drag polar predictions for the Wigeon, the CFD simulation presented in Section 7.6. This is limited to the performance of the wings, since the fuselage, tail and wingtips are not included in the CAD model used in the CFD. The drag component method was then used for comparison, by accounting only for the wing. The input lift is the average of the lift values that the CFD simulations gave as results.

Table 7.8: Grid convergence study for the tandem wing CFD simulation

Method	C_L**[-]**	C_D**[-]**
$\approx$ 5 M Cells CFD	0.04005	0.00652
$\approx$ 6 M Cells CFD	0.0433	0.00642
$\approx$ 8 M Cells CFD	0.0457	0.00617
$\approx$ 12 M Cells CFD	0.0470	0.00598
Drag component	0.0441	0.00786

As can be observed, the drag estimation seems to be conservative when compared to the CFD results. Due to the low lift of the CFD simulation, the differences are mostly due to the profile drag estimations, as the induced drag is low at such low lift coefficients. The drag estimation of the component method is 25% higher than the estimation by the CFD, which suggests that the profile drag of the wing is extremely conservative. In the future, more CFD tests at different angles of attack should be completed in order to obtain a full drag polar and lift curve for the wings.

For validation of the Aerodynamics performance of the Wigeon aircraft, a number of future steps have to be taken after the DSE. Firstly, a down scaled 3D model of the aircraft, including functioning propellers is needed. Once a model is completed, it will be possible to validate the aerodynamic coefficients of the Wigeon by preparing wind tunnel experiments and analysing the data measured using scales. Apart from evaluating aerodynamic performance quantitatively, a qualitative experiment including flow visualisation would be useful to determine whether the air is behaving as expected around the aircraft shape. performing wind tunnel testing with a number of iterations of the design, a flight test will be possible once the first prototype is build. In this test the predicted aerodynamic performance and behaviour of the Wigeon will be tested for cruise, stall and transition, which will allow for a direct comparison between the expected lift and drag performance of the aircraft and the reality.

8 Propulsion

The propulsion subsystem design for the Wigeon project consisted mainly in the design of propellers to maximise efficiency and ensure that the wide variety of needed thrust levels can be achieved. This chapter contains an explanation of the process followed to design such propellers.

8.1. Propeller Positioning and Sizing

This section covers the procedure used to determine the number of engines of the aircraft and the size of their propellers.

8.1.1. Number of engines

The first step to design the propellers is to select a number of engines and to size them. The selection of the number of engines is based on assessing the benefits of having fewer, bigger engines or more, smaller engines. This has an effect in a wide range of issues, summarised in the list below.

1. **Disk loading:** Bigger engines allow for more total area and hence a lower disk loading, which improves efficiency in hover.
2. **Ground clearances:** More propellers means smaller radii, which therefore allows for more ground clearance when the wings are in horizontal position.
3. **Propeller-wing interaction:** Bigger engines have a higher slipstream height, which results in a higher increase in lift due to the propeller slipstream for the same slipstream velocity [85].
4. **Propeller-propeller interaction:** For the same front and rear wing separation, smaller front engines with lower slipstream heights allow to more easily place the engines such that the second row of propellers does not ingest their slipstream. This slipstream ingestion can lead to big losses in thrust from the second row of propellers [121] and increase noise emissions.
5. **Blade rotation mechanism:** The propellers need a mechanism to alter the pitch of the blades. With very small propellers, implementing a mechanism for this function becomes more difficult.
6. **Safety in OEI conditions:** More engines mean more redundancy, and with more, smaller engines a failure of one of them has a smaller effect on controllability in hover and on total thrust.

The aircraft features two wings, and it was decided to place the same number of engines with the same size on each wing, for two reasons. First, to distribute the thrust evenly and to minimise differences in propeller loading. Here it is worth noting that due to the fact that the CG of the aircraft is closer to the front wing, the front engines need to provide higher thrust during hover. However, due to reason 4) in the previous list, having more, bigger engines in the front wing was deemed not beneficial overall, and more smaller engines would decrease hover efficiency. This is because hover is a very small part of the mission compared to cruise, and slipstream ingestion would lead to thrust reduction and hence a need for more power during the entire cruise phase of the mission. Secondly, having all engines with the same size is simpler and cheaper for manufacturing, since only one electrical engine and two different blade designs are needed (due to the fact that the propellers are rotating in opposite directions on each side of the fuselage, to be further discussed in Section 8.1.2).

Thus, the possible number of engines considered were 8, 12 and 16, which translates to 2, 3 or 4 per half wing. Having only 4 engines was not possible due to lack of redundancy, and having more engines would mean having too highly loaded and very small propellers, which would also suffer from the fact that the wing would block and disturb a big part of the slipstream. Having 8 engines was ruled out because maximising the radius would lead to propellers with 1 m radii (the sizing procedure is explained in Section 8.1.2), which would not be acceptable for ground clearances with wings in horizontal position (e.g. for emergency landings in a conventional configuration). Having 8 engines with smaller radii would be a solution to this, but it would eliminate the benefits of having less engines. Having 16 engines would lead to propellers with only

30 cm of radius and disk loadings above 600 kg/m^2. The small radius would already pose problems with the wing and nacelle blocking the slipstream, and the disk loading was deemed too high. Thus, the selected number of engines was 12, which means 3 per half wing.

8.1.2. Positioning and sizing

The second step to design the propellers is to select the placement of the engines and to assess the available space for the propellers. It was decided to place one propeller at the tip of the wing for two reasons: first, this allows to maximise the radius of the propellers and thus the area, which results in a lower disk loading; secondly, having outboard rotating propellers at the tips of the wings can help to counteract the wingtip vortices, hence reducing drag [117], and is beneficial for noise. Figure 8.1 shows a schematic diagram of the positioning of the engines and of the geometrical parameters that define the sizing and positioning procedure,

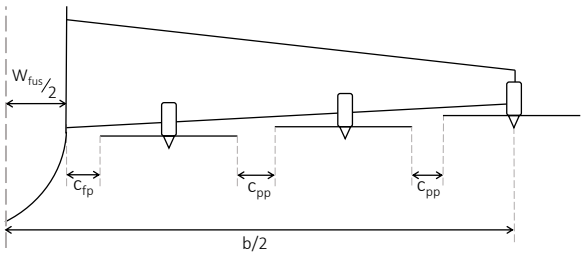

Figure 8.1: Definition of the geometrical dimensions used for the lateral positioning of the propellers.

The leftmost vertical dashed line in Figure 8.1 is the symmetry plane of the aircraft, halfway through the fuselage. The distance to the wingtip from this line is half of the span, b/2. Part of this length is taken by half of the fuselage width, $w_{fus}/2$. To avoid problems with wing positioning and rotation, it was decided to leave a clearance between the propeller tip and the maximum width of the fuselage, and not the local width. This clearance is c_{fp} and has a value of 0.3 m. The distance between propeller tips is defined by c_{pp}, the propeller-propeller clearance, which was also assumed to be 0.3 m (see Section 8.8 for further information). The remaining space is taken by the two inboard propellers and half of the tip propeller. This is generalised in Figure 8.1 for an arbitrary number of propellers, where N_{prop} is the number of propellers per half wing.

$$R = \frac{\frac{b}{2} - \frac{w_{fus}}{2} - c_{fp} - (N_{prop} - 1) \cdot c_{pp}}{2N_{prop} - 1} \tag{8.1}$$

For 3 propellers per half wing - with clearances of 0.3 m, a fuselage width of 1.38 m and a span of 8.2 m - the final radii of the propellers is 0.5029 m. This also defines the spanwise positioning of the propellers.

8.2. Design of the Propeller Blades

The design of the propellers is based on blade element momentum theory (BEM). This theory analyses the performance of propeller blades by dividing each individual blade into a number of stations. These stations are there analysed as 2D airfoils to compute their individual thrust and drag, and later added to obtain the overall performance of the propeller. Other correction factors to account for 3D effects are also included in the process to improve the accuracy of the method.

In order to design effective blades for the propellers, a procedure laid down by Adkins and Liebeck, based on similar work by Larrabee [66], was used. The procedure by Adkins and Liebeck, presented in their paper *Design of Optimum Propellers* [2], modifies Larrabee's equations to eliminate small angle approximations and other assumptions that only apply to lightly loaded propellers.

8.2.1. Blade geometry

The first step is to define the velocities that act on the blade and their corresponding angles. A sketch of this geometry can be seen on Figure 8.2.

In Figure 8.2, w is the local effective velocity of the flow acting on the blade. It has two components; one parallel to the disk plane and one perpendicular to it. The component perpendicular to the disk plane is V(1+a), where V is the freestream speed, and a is the axial interference factor. Before arriving to the propeller, the freestream air is accelerated due to the action of the propeller, and this is represented with interference factor a. Thus, the term V(1+a) represents the speed corrected with this acceleration. The component parallel to the disk plane is Ωr (1-a′), where Ω is the rotational speed of the propeller in rad/s, r is the local radius of the blade and a′ is the rotational interference factor. Similarly to what happens with the freestream speed, the parallel component of the speed is not simply the rotational speed Ωr; a correction factor of (1-a′) has to be applied to represent the fact that the flow is also rotating in the same direction as the blades due to the action of the propeller.

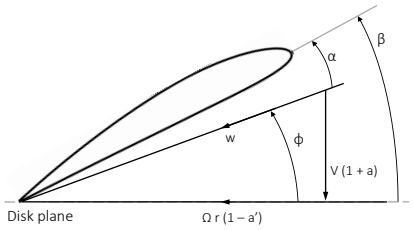

Figure 8.2: Velocities acting on the blade station with their corresponding angles. Based on [2].

This effective velocity acts in the blade at an angle Φ with respect to the disk plane, which is not necessarily aligned with the blade chord. This difference in angle is the local angle of attack of the blade, α. Lastly, β is the local pitch angle of the blade, defined as the angle between the disk plane and the chord of the blade airfoil. As it can be seen in Figure 8.2, β can be also defined as $\beta = \alpha + \Phi$.

In order to minimise the loss of the propellers, the vortex sheet shed by the propeller blades has to be a regular screw surface, as described by Betz [12] (as cited in [2]). Betz derived this condition for lightly loaded propellers, in which the contraction of the propeller wake is neglected, but Theodorsen demonstrated that this condition also applies to highly loaded propellers [123] (as cited in [2]). This translates to the fact that the local radius at each station times the tangent of the local flow angle has to be constant throughout the blade (r · tan(Φ) = const.).

8.2.2. Momentum theory

The thrust of a propeller, according to momentum theory, is defined as $T = \dot{m}(V_e - V_\infty)$. In this equation $\dot{m}$ is the mass flow, V_e is the slipstream speed of the propeller and V_∞ is the freestream velocity.

To calculate these parameters, the disk plane of the propeller can be divided into annuli with an area equal to 2πrdr, where r is the local radius at the annulus and dr is its width (See Figure 8.3).

The speed of the flow at this annulus is V(1+a), as explained in Section 8.2.1, so the mass flow per unit radius is equal to 2πrρV(1+a). Further into the wake, the slipstream speed increases to approximately V(1+2a), according to momentum theory [50], as cited in [2]. Thus, using the mass flow per unit radius, the slipstream speed and simplifying, the thrust per unit radius of the propeller can be rewritten as shown in Equation 8.2.

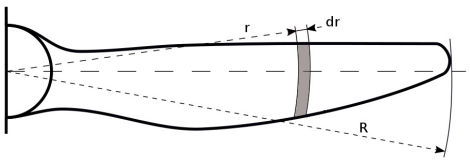

Figure 8.3: Blade station with local radius r and width dr. Over one revolution this blade station describes an annulus with an area equal to 2πrdr. Modified from original [128].

$$T' = 2\pi r \rho V(1+a) \cdot (V 2aF) \tag{8.2}$$

F, the loss of momentum factor, is included in the equation to account for radial movement in the flow [2].

8.2.3. Circulation around the blade

The lift per unit radius produced by an airfoil, according to the Kutta-Joukowski theorem, is equal to $\rho V\Gamma$, where ρ is the density and Γ is the circulation around the airfoil. This theorem can also be applied to the blade sections, as shown in Equation 8.3. Instead of the freestream speed, the local flow speed w is used. This equation computes the lift per unit radius of the whole propeller, and not of a single blade, and thus the lift of the station is multiplied by the number of blades B. Downstream into the wake, the circulation in an annulus is represented by Equation 8.4 [2].

Instead of the freestream speed, the local flow speed w is used. This equation computes the lift per unit

radius of the whole propeller, and not of a single blade, and thus the lift of the station is multiplied by the number of blades B. The circulation in an annulus downstream into the wake is shown in Equation 8.4 [2].

$$L' = B\rho w\Gamma \quad (8.3) \qquad \Gamma = \frac{2\pi r F w_t}{B} \quad (8.4)$$

F is the momentum loss factor, as previously described, and w_t is the swirl velocity of the slipstream. This velocity can be rewritten in terms of the displacement velocity of the vortex sheet as $w_t = v'\sin(\Phi)\cos(\Phi)$ (see [2] for a derivation). By introducing the term ζ, the displacement velocity ratio v'/V, this equation can be further rewritten into $w_t = \zeta V \sin(\Phi)\cos(\Phi)$. Equation 8.4 can then be written as Equation 8.5. To simplify this equation, the parameter $G = F \sin(\Phi)\cos(\Phi)$ is introduced, and using $r = V/\Omega$ the previous equation becomes:

$$\Gamma = \frac{2\pi r F \zeta V sin(\Phi) cos(\Phi)}{B} \quad (8.5) \qquad \Gamma = \frac{2\pi r \zeta V G}{B} \quad (8.6)$$

These previous equations relate to the lift of the blades, but the parameters of interest for a propeller are not the lift and drag, but the thrust produced by the propeller and the torque needed to produce such thrust. The thrust per unit radius and the torque as a function of lift and drag are defined as shown in Figure 8.4.

The lift of the blade is defined as perpendicular to w, and the drag as parallel to w. From this definition, it can be seen in the image that $T' = L' \cos(\Phi) - D' \sin(\Phi)$, and $Q'/r = L' \sin(\Phi) + D' \cos(\Phi)$. The thrust per unit radius had also been described in Equation 8.2. By setting this equation equal to the new definition of T′ it can be seen that:

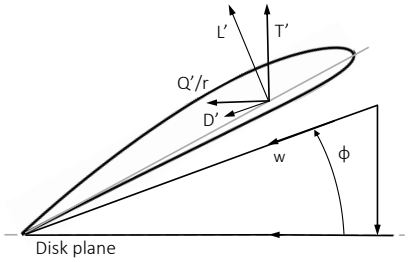

Figure 8.4: Definition of thrust and torque of the propeller blade. L′ and D′ are perpendicular and parallel to w, respectively. Based on [2].

$$2\pi r\rho V(1+a)\cdot(V2aF) = L'cos(\Phi) - D'sin(\Phi)$$

$L' \cos(\Phi) - D' \sin(\Phi)$ can be rewritten as $L' \cos(\Phi) \cdot (1 - \varepsilon \tan(\Phi))$ by factoring out the term $L' \cos(\Phi)$ and introducing the parameter ε, the D/L ratio. L′ can be substituted by Equation 8.3, and Γ in that equation can be substituted by Equation 8.6. Lastly, from Figure 8.2 it can be seen that $V(1+a) = w \sin(\Phi)$. Using these relations and reordering results in the definition for the interference factor a shown in Figure 8.2.3 [2].

$$a = \frac{\zeta cos^2(\Phi)(1 - \varepsilon\, tan(\Phi))}{2}$$

From [2], the term $\tan(\Phi)$ can be rewritten as Equation 8.7, where λ is the tip speed ratio, $V/\Omega R$, and ξ is the non-dimensional radius of the propeller, r/R. With this, Equation 8.7 can be rewritten as Equation 8.8

$$tan(\Phi) = (1 + \frac{\zeta}{2})\frac{\lambda}{\xi} \quad (8.7) \qquad r\ tan(\Phi) = (1 + \frac{\zeta}{2})R\lambda \quad (8.8)$$

Since ζ, λ and R are constants, this relates to the aforementioned Betz condition: $r \tan(\Phi)$ is constant.

8.2.4. Blade design for a specified thrust

The purpose of this approach is to design a propeller blade that can produce a specific thrust with minimum losses. Thus, T is an input to the method. To introduce it into the equations, the non-dimensional thrust T_c is used, defined by $T_c = \frac{T}{q_\infty A_{prop}}$.

In this equations A_{prop} is the area of the propeller and q_∞ is the freestream dynamic pressure. Adkins and Liebeck, in their design procedure, rewrite this parameter as $T'_c = I'_1\, \zeta - I'_2\, \zeta^2$ [2], by using the previously mentioned definition of T′. The primes in these parameters represent $d/d\xi$. I'_1 and I'_2 are defined by Adkins and Liebeck as show in Equation 8.9 and Equation 8.10 [2].

$$I'_1 = 4\xi G\ (1 - \varepsilon\ tan(\Phi)) \quad (8.9) \qquad I'_2 = \lambda 2G\ (1 - \varepsilon\ tan(\Phi))\ (1 + \frac{\varepsilon}{tan(\Phi)})\ sin(\Phi)\ cos(\Phi) \quad (8.10)$$

The constraint equation for the design defined in [2] is shown in Equation 8.11. As mentioned before, ζ has

to be constant for a design with minimum losses.

$$\zeta = \frac{I_1}{2I_2} - \sqrt{\left(\frac{I_1}{2I_2}\right)^2 - \frac{T_c}{I_2}} \tag{8.11}$$

I_1 and I_2 are I'_1 and I'_2 integrated from the hub of the propeller to the tip, as shown in Equation 8.12 and Equation 8.13. The hub has a a non-dimensional radius of ε_0, and the tip has a non-dimensional radius of 1.

$$I_1 = \int_{\varepsilon_0}^{1} I'_1 d\varepsilon \tag{8.12}$$

$$I_2 = \int_{\varepsilon_0}^{1} I'_2 d\varepsilon \tag{8.13}$$

8.2.5. Blade geometry

The next step is to define a blade geometry that meets the conditions described above. In Equation 8.3 the lift per unit radius of one blade had been defined as $\rho w \Gamma$. From the basic lift equation, L′ can also be defined as $L' = C_l \frac{1}{2} \rho w^2 c$, where c is the local chord length. By putting those equations together and simplifying, Equation 8.14 can be obtained, where wc is the product of local flow speed times local chord. Using Equation 8.6 and $r = V/\Omega = \lambda R$, the equation for wc can be rewritten as seen in Equation 8.15.

$$wc = \frac{2\Gamma}{C_l} \tag{8.14}$$

$$wc = \frac{4\pi\lambda R\zeta VG}{BC_l} \tag{8.15}$$

From Figure 8.2 it can be seen that $w = V(1+a)/\sin(\Phi)$. Thus, if the product wc is know, the chord can be calculated by $c = wc/w$. The last parameter that still needs to be defined is the momentum loss factor F, which can be defined using Equation 8.16 [2].

$$F = \frac{2}{\pi} arccos(e^{-\frac{B}{2}\frac{1-\xi}{sin(\Phi_t)}}) \tag{8.16}$$

8.2.6. Design of the blade for a given condition

This procedure allows to design a blade optimised for a specific flight condition and propeller characteristics. Thus, the flight speed V and atmospheric parameters are known. The propeller radius R, the number of blades B and the propeller rpm are also known inputs to the method. This procedure is iterative and requires an initial estimate for the displacement velocity ratio ζ. The authors of the paper suggest using $\zeta = 0$ [2].

The first step is to calculate the flow angle at the tip, Φ_t. Using Equation 8.8 and the fact that ξ is 1 at the tip, the flow angle at the tip, Φ_t, is defined as $\Phi_t = arctan\left(\left(1 + \frac{\zeta}{2}\right)\lambda\right)$.

As mentioned above, the Betz condition for minimum loss is $r \tan(\Phi) = \text{constant}$. This means that, since the flow angle at the tip is know, the flow angle distribution throughout the blade can be calculated with $r \tan(\Phi) = R \tan(\Phi_t)$, which can be rewritten as:

$$\Phi = arctan\left(\frac{tan(\Phi_t)}{\xi}\right)$$

Now that Φ is known, F can be calculated with Equation 8.16. This implies that G is now known. V, R and B are inputs to the method, ζ is known from the initial estimate, and λ is only dependent on inputs parameters, and hence also known. Thus, only C_l is needed to calculate the product wc from Equation 8.15.

The first thing to obtain C_l is to select an airfoil. For this project a NACA 4412 airfoil has been chosen. It is a popular airfoil which is commonly used in wide range of applications and provides good performance for this application. In order to obtain the lift and drag polars of the airfoil, XFOIL was used. The airfoil was simulated at Mach = 0 for Reynold's numbers ranging from 100,000 to 5,000,000 in steps of 100,000. This data was then saved into a database which was used inside the program to obtain the relevant airfoil data. Lastly, since the airfoil data was analysed at M=0, it was corrected using the Prandtl-Glauert correction factor $\sqrt{1 - M^2}$, where M was approximated using the speed Ωr, since w is not yet known.

In order to minimise drag losses in the blades, the L/D ratio at each blade section should be maximised. For this, the following approach was used in the design procedure:

For each blade station, different C_l values, varying in steps of 0.05, were used to calculate wc with Equation 8.15. With wc known, the Reynold's number at the blade station was calculated using Equation 8.17, in which μ is the dynamic viscosity of the air.

$$Re = \frac{wc \cdot \rho}{\mu} \tag{8.17}$$

With the Reynold's number known for that particular C_l, the airfoil data corresponding to that Reynold's number was retrieved. For each C_l value the corresponding C_d and α were retrieved. The D/L ratio (ε) was calculated and stored. This was done for the entire range of C_l values, and the one with a lowest D/L ratio was selected. This procedure was then repeated for each blade station.

This resulted in the optimal C_l distribution in the blade for minimum D/L. However, due to inaccuracies in the airfoil data, the resulting distribution was not smooth, but contained peaks in certain stations that would lead to peaks in the chord distribution, and hence to a very irregular blade. To avoid this, the C_l distribution was regressed approximated with a 1D polynomial and, a smooth lift distribution was recalculated. With this final lift distribution, the product wc was calculated again. Once again, the Reynold's number was calculated, and the C_d and α corresponding to the new C_l were obtained thereafter.

This procedure was then done for each station in the blade. After this, the distribution of ε throughout the blade was known, and the axial interference factor a was calculated using Figure 8.2.3. After this, the local flow speed w was obtained using $w = V(1+a)/\sin(\Phi)$.

Now that both wc and w are known, the chord distribution of the blade can be obtained. The last geometrical parameter to be calculated is the pitch distribution, β. Since the pitch angles Φ were calculated before, and the angles of attack were obtained from airfoil data, the pitch can be calculated as $\beta = \alpha + \Phi$.

This defines the full geometry of the blade. The last step is to analyse the performance and compute the updated displacement velocity ratio, ζ. For this, Equation 8.9 and Equation 8.10 where calculated and integrated to obtained I_1 and I_2. Lastly, the updated value for ζ was obtained using Equation 8.11. This procedure was iterated until the difference from the old and new ζ was smaller than 0.1%.

The last step is to compute the propeller efficiency. The propeller efficiency is defined T_c/P_c, where P_c is the non-dimensional power coefficient. In order to calculate it, two new variables are introduced, Equation 8.18 and Equation 8.19, obtained by [2] in the same manner as Equation 8.9 and Equation 8.10.

$$J_1' = 4\xi G(1 + \frac{\varepsilon}{tan(\Phi)}) \tag{8.18}$$

$$J_2' = 2\xi G\ (1 + \frac{\varepsilon}{tan(\Phi)})\ (1 - \varepsilon\ tan(\Phi))\ cos^2(\Phi) \tag{8.19}$$

These variables are then integrated from hub to tip in the same way as I_1 and I_2.

$$J_1 = \int_{\varepsilon_0}^{1} J_1' d\varepsilon \tag{8.20}$$

$$J_2 = \int_{\varepsilon_0}^{1} J_2' d\varepsilon \tag{8.21}$$

With J_1 and J_2 known, P_c can be obtained with $P_c = J_1\ \zeta + J_2\ \zeta^2$ [2]. With this, the propeller efficiency can be calculated and the propeller design is finalised.

8.3. Analysis of the Blades in Off-Design Conditions

The blades designed for one specific condition in Section 8.2 need to also meet the different thrust requirements from different flight conditions, such as hover. For this analysis, a different procedure based on the same principles was used. This method was obtained from the same paper by Adkins and Liebeck [2]. This analysis takes a fully defined propeller from which the radius, number of blades and blade geometry are known, together with the flight conditions and rpm.

The first step is to define the coefficients C_y and C_x. Figure 8.5 shows the definition of these coefficients. Based on this image, C_y and C_x can be defined in terms of C_l and C_d, as shown in Equation 8.22 and Equation 8.23.

$$C_y = C_l\ cos(\Phi) - C_d\ sin(\Phi) \tag{8.22}$$

$$C_x = C_l\ sin(\Phi) + C_d\ cos(\Phi) \tag{8.23}$$

With these definitions, and using $T' = L'\cos(\Phi) - D'\sin(\Phi)$, and $Q'/r = L'\sin(\Phi) + D'\cos(\Phi)$, as previously

described, the thrust and torque per unit radius can be redefined as Equation 8.24 and Equation 8.25.

$$T' = C_y \frac{1}{2}\rho w^2 Bc \quad (8.24) \qquad Q'/r = C_x \frac{1}{2}\rho w^2 Bc \quad (8.25)$$

The procedure to analyse the thrust is iterative, and it is started with an initial estimate for Φ. This initial estimate for the Φ distribution throughout the blade is obtained from Equation 8.8, by assuming that ζ is 0.

Since β is known from the blade geometry, the angle of attack at each section can be obtained from subtracting the flow angle from the blade pitch angle. From this angle of attack, the C_l and C_d of the blade sections can be obtained. For this, the same airfoil data as in Section 8.2 was used. For this, an initial estimate for the Reynolds number is needed. This initial estimate is obtained by using the formula $Re = Vc\rho/\mu$ with the speed as Ωr, which are both known, and c as the chord of each blade station, also known from blade geometry. The atmospheric parameters ρ and μ are also known from the flight conditions. With an estimate for Re, and α known, the lift and drag coefficients of the blade sections can be obtained. Since Φ is also known, C_y and C_x can also be calculated.

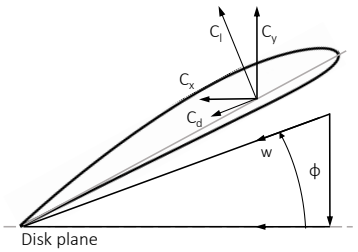

Figure 8.5: Definition of the coefficients C_y and C_x of the blade section. Based on [2]

The next step is to calculate the axial and rotational interference factors, a and a′, using Equation 8.26 and Equation 8.27 [2].

$$a = \frac{\sigma K}{F - \sigma K} \quad (8.26) \qquad a' = \frac{\sigma K'}{F + \sigma K'} \quad (8.27)$$

In these formulas, F is the momentum loss factor, described in Equation 8.16; σ is the solidity of the propeller, defined by $\sigma = \frac{Bc}{2\pi r}$; and K and K′ defined by Equation 8.28 and Equation 8.29, obtained from [2].

$$K = \frac{C_y}{4sin^2(\Phi)} \quad (8.28) \qquad K' = \frac{C_x}{4sin(\Phi)cos(\Phi)} \quad (8.29)$$

Since all parameters needed in these equations are known, a and a′ can be calculated. From Figure 8.2 it can be seen that the local flow speed w is:

$$w = \sqrt{(V(1+a))^2 + (\Omega r(1-a'))^2}$$

Since V and Ω are known from the flight conditions and propeller settings, and the interference factors have been calculated, the speed w can be obtained. This speed is used to calculate more accurately the Reynold's number to obtained more precise airfoil data for the next iteration.

The estimate for Φ is updated using Equation 8.30, which can be derived from Figure 8.2.

$$\Phi = arctan\left(\frac{V(1+a)}{\Omega r(1-a')}\right) \quad (8.30)$$

This procedure is then iterated until a convergent value for Φ is found. After this, the thrust can be calculated with Equation 8.24. Lastly, the efficiency of the propeller can be calculated using $\eta = J\frac{C_T}{C_P}$. In this equation J is the advance ratio of the propeller, defined as V/(nD), where n is the rotational speed in rps and D is the diameter. C_T and C_P are new definitions of the thrust and power coefficients, given by Equation 8.31 and Equation 8.32 [2].

$$C_T = \frac{T}{\rho n^2 D^4} \quad (8.31) \qquad C_P = \frac{T}{\rho n^3 D^5} \quad (8.32)$$

C_T can be easily obtained, as the thrust is known, but C_P needs to be obtained in another manner. For this, Adkins and Liebeck give Equation 8.33 [2].

$$C'_P = \frac{\pi^4 \sigma C_x \xi^2 F^{32}}{4\left((F + \sigma K')cos(\Phi)\right)^2} \quad (8.33)$$

Integrating C'_P from the propeller hub to the tip results in the power coefficient, which can then be used to

compute the efficiency. One downside from this efficiency formula is that it does not work for if V is 0, e.g. in hover, since in that case J would be 0 and the efficiency would also be 0.

8.4. Final Propeller Design and Performance Parameters

The design goal is to design an optimum propeller for cruise, since cruise represents the majority of the mission time. However, sizing the propellers for just cruise thrust results in small propellers that do not allow to reach the necessary thrust levels in hover. Thus, an extra factor was applied to the design thrust to obtain a propeller that met the requirements. The procedure to select this factor was to first try with 1 (cruise thrust), then check the maximum available thrust with the resulting propeller geometry, and accept the design if it met the thrust requirements. If not, the factor was increased and the procedure repeated. With this, a factor of 2.6 was obtained as the minimum factor to achieve the necessary geometry. This factor was then applied to the cruise thrust of 153.63 N, resulting in a design thrust of 400 N. The flight conditions at the design point are a cruise speed of 72.19 m/s and a height of 1 km. The atmospheric values were obtained from this height in the International Standard Atmosphere.

The propeller radius is 0.5029 m (see Section 8.1), and the chosen number of blades of the propeller was 6. This is because more blades are less noisy (see Section 8.5), due to smaller pressure increments per blade for the same thrust, and result in more efficiency (as seen in the sensitivity analysis presented in Section 8.6.1), but too many small blades are more difficult to manufacture with enough structural integrity, and make it more difficult to introduce a blade pitching mechanism, due to the already small size of the shaft. The non-dimensional hub radius, ξ_0, was assumed to be 0.1, which allows for enough space for the shaft and blade connection.

The last parameter needed is the rpm at the design condition. The maximum allowable rpm level is 4790.5, based on a limit tip Mach number of 0.75. Going beyond this Mach number would result in shock waves at the tips, which would lead to big losses and high noise levels. With this maximum value in mind, it was chosen to design the propellers for 1350 rpm at the design condition. All of the aforementioned parameters combined lead to a design which allows to meet the maximum thrust requirement at maximum rpm. The resulting propeller has an efficiency of 81% at the design condition and a solidity of 0.36. The propeller solidity represents how much area of the propeller disk is occupied by the blades and how much is air. The value of 0.36 is relatively high, and this is due to the high disk loading of the propellers.

The next step to analyse the propellers is to see whether they can meet the maximum thrust requirement. For controllability in OEI conditions, the TW ratio needed is 1.5 (see Section 11.2.5). With a MTOM of 3024.8 kg (including contingencies as defined in Chapter 14) and 12 engines this results in a required maximum thrust per engine of 3707.9 N. In order to achieve this, the propellers are accelerated up to maximum rpm (4790.54), and the blades are pitched down by 45 degrees with respect to the design condition (this means reducing β in Figure 8.2). This results in a thrust per engine of 3745.14 N. These values were obtained at a height of 500 metres. The reason why this height, and not sea level, was chosen is to allow for a safety margin and for controllability in higher operations. It is worth noting that the inflow speed for this condition was chosen to be 10 m/s. This is because the analysis method does not work well for inflow speeds of 0 m/s (as mentioned in the previous section, it would lead to an efficiency of 0). However, with lower inflow speed the thrust of the propeller increases[1], which means this is a conservative estimate. Having this conservative estimate for maximum thrust is also good for the design, since some of the effects which are not modelled (such as the effect of the nacelle behind the propeller) might lead to lower thrust levels.

Next is to analyse the propellers in stable hover. With a MTOM of 3024.8 kg (using contingencies) and 12 propellers, the thrust per engine required to hover is 2471.93 N. By accelerating the propeller to 4000 rpm and reducing the pitch angle of the blades by 45 deg, the necessary thrust is achieved. This is also calculated at a height of 500 metres above sea level.

Table 8.1: Thrust settings at cruise, hover and full thrust conditions (values per engine).

Parameter	Cruise	Hover	Full thrust
Thrust [N]	157.82	2502.42	3745.14
RPM	1090	4000	4790.5
$\Delta\beta$ [deg]	0	-44	-45

[1] https://www.mh-aerotools.de/airfoils/prpstati.htm [cited 21 June 2021]

The last step is the nominal cruise condition
analysis, since the design point was for a higher thrust level. To achieve the cruise thrust of 153.6 N, the pitch was kept at the design condition and the rpm of the propeller were reduced to 1090 rpm, resulting in a cruise thrust per engine of 157.82 N.

The results from these analyses can be found in Table 8.1, and the resulting propeller geometry can be seen in Figure 8.6 to Figure 8.8.

Figure 8.6: Side view of the blade angle in cruise condition

Figure 8.7: Side view of the blade angle in hover condition

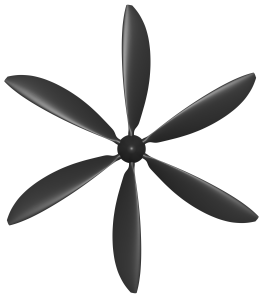

Figure 8.8: Top view of the optimised propeller geometry in hover condition

8.5. Noise Analysis

One important aspect of aircraft that operate in urban environments is their noise emission. Noise can have a negative effect on social sustainability, and it is regulated. If the noise emitted by the aircraft does not comply with these regulations, the aircraft cannot fly. In the particular case of the Wigeon, the noise comes mostly from the propellers. This section presents a preliminary method to estimate the propeller noise in cruise condition, obtained from [75]. This method is for isolated propellers, and hence only serves as a preliminary estimation for the Wigeon, in which the noise will be affected by the interactions between the propellers (see Section 8.8 for further recommendations).

The formula used to calculate the farfield noise (at a distance further than 1 diameter of the propeller) for a single propeller is shown in Equation 8.34 [75].

$$SPL = L_1 + 20\ log_{10}\left(\frac{4}{B}\right) + 40\ log_{10}\left(\frac{15.5}{D}\right) + C_{Mach} + C_\theta - 20\ log_{10}(r-1) \tag{8.34}$$

In this equation, the first term L_1 is the reference noise level, obtained from Figure B.2 in [75]. It is based on the engine power, and for the Wigeon in cruise condition, it was determined to be 107 dB. The next two terms are corrections for the number of blades, B, and propeller diameter, D (in ft). The next term, C_{Mach}, is a correction for the tip Mach. In cruise condition, the tip Mach number for the Wigeon is slightly below 0.3, for which the correction factor, obtained from Figure B-3 in [75], is -19 dB. C_ϑ is a correction which accounts for the direction in which the noise is being calculated, and it is obtained from Figure B-8 in [75]. For this calculation, it was decided to use a correction of +4 dB, which the maximum value of the average curve, to obtained the noise at the position in which is is maximum. Lastly, the last term, where r is the distance in ft at which the noise is to be calculated, accounts for the noise attenuation due to propagation.

As shown in the equation, a higher number of blades results in less noise. This is due to the fact that, with more blades, the pressure increments to the flow is introduced in a more distributed manner. This reason contributed to the chosen number of blades for the propeller.

With this formula, the noise from one propeller during cruise at 100 metres from the aircraft is determined to be 65.06 dB. The 100 metre distance was chosen as a sample distance to evaluate the noise. Similarly, for 1000 metres (cruise height), the noise is 45.03 dB. To calculate the combined noise from all propellers, Equation 8.35 was used, in which L represents the noise in dB. For the 12 propellers combined, the noise levels at 100 m and 1000 m are 75.85 dB and 55.83 dB, respectively.

$$L_{tot} = 10 \log_{10} \left(\sum_{i=1}^{n} 10^{(L_{prop,\ i}/10)} \right) \tag{8.35}$$

8.5.1. Compliance with requirements

With the achieved maximum thrust values, the vehicle can achieve a maximum T/W ratio of 1.37 with one engine inoperative, thus making the aircraft compliant with VTOL-LFT-1 and -4, which require a T/W ratio with OEI of 1.16 and a lift of 3128 N, respectively. Moreover, this maximum thrust per engine allows for OEI controllability and for enough thrust to perform the mission safely, including landing, and hence the vehicle is compliant with VTOL-LFT-8. Lastly, this TW ratio allows the vehicle to take off and land vertically, and thus compliant with VTOL-STK-4 and VTOL-STK-5.

The achieved cruise thrust of 158 N complies with requirement VTOL-THR-1, which requires 153 N for cruise. Since the propellers allow for a wide range of thrust levels, this requirement is met with enough margin so that the required cruise thrust can be met in the event the cruise drag increases significantly. Moreover, this cruise thrust is used to achieve a speed of 260 km/h, thus making the aircraft compliant with VTOL-PRF-5-PRP-1. In addition to this, the propellers are able to achieve enough thrust to comply with the rate of climb of VTOL-PRF-7-PRP-1.

8.6. Sensitivity Analysis

In order to see the effects of the input parameters on the results of the propeller design and analysis, a sensitivity analysis has been performed.

8.6.1. Sensitivity of the design procedure

The first part of the sensitivity analysis concerns the blade design procedure explained in Section 8.2. For this procedure, the sensitivity analysis was divided into two parts, one concerning the inputs that are not a design choice (freestream speed, which comes from the flight conditions, and propeller radius, which is determined by the procedure laid down in Section 8.1) and one concerning the design variables that can be chosen (propeller rpm and number of blades). Since the goal of the procedure is to maximise efficiency, the parameter of interest is the efficiency of the propeller. The results of this sensitivity analysis can be seen in Figure 8.9 and Figure 8.10. From Figure 8.9 it can be seen that a higher radius increases efficiency, which is expected as it decreases disk loading. This lead to the design goal of maximising the radius of the propellers. The cruise speed V, since it selected based on requirements from other departments, did not influence the design process of the propellers. The graph also includes the final design point for cruise condition. From Figure 8.10, it can be seen that more blades mean more efficiency, which partly explains the reasoning behind the selected number of blades, explained in Section 8.4. For the rotational speed, the design value chosen is below the optimal one. The reason for this is that the thrust needed for cruise is very low compared to the maximum thrust required, and this last value needs to be achieved at a rotational speed of at most 4790 rpm, and thus this margin was needed.

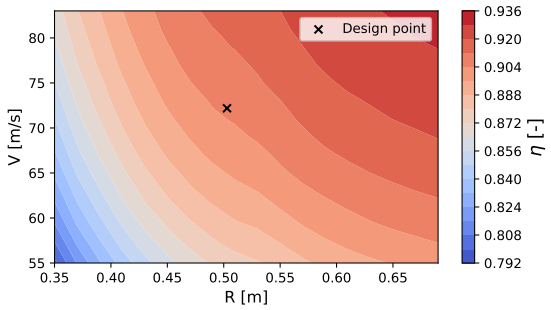

Figure 8.9: Sensitivity analysis of propeller efficiency in the design procedure to variations in freestream speed and propeller radius

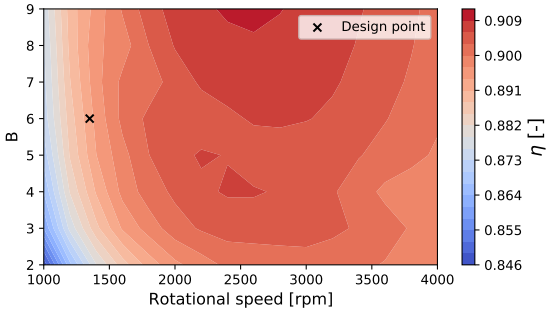

Figure 8.10: Sensitivity analysis of propeller efficiency in the design procedure to variations in rpm and number of blades

8.6.2. Sensitivity of the propeller analysis

The second part of the analysis concerns the procedure to analyse the propeller in off-design conditions. For this part, the sensitivity analysis was conducted for both the effect on propeller efficiency and on thrust. These sensitivity analyses show the change in thrust and efficiency with change in rpm and blade pitch. There is no design point included because this analysis is used to evaluate the performance at arbitrary conditions, not at the design one. It can be seen that with an increase in rpm the thrust increases, and thus the efficiency also decreases due to the higher disk loading, as expected. For changes in pitch, the results are not so linear. This is because a change in pitch results in a change in the angle of attack of the blade, and thus the airfoil coefficients, which in turn have an effect on the interference factors a and a′. These factors affect the speed seen by the blade, which thus affects the flow angle Φ, and as a result the aforementioned parameters are affected again. Due to this, it is difficult to predict the precise effects that changing the blade pitch will have. As a result, in order to obtain the best performance when selecting a change in pitch and rpm to meet the thrust requirements in the hover and maximum thrust conditions (Section 8.4), the performance of the propeller was computed over a wide range of pitch angles, after which the best was selected.

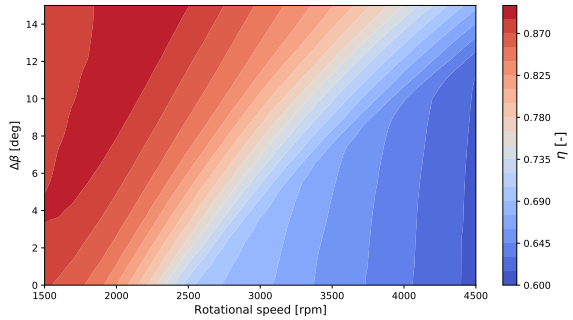

Figure 8.11: Sensitivity of the efficiency to changes in rpm and pitch angle of the blade in the off-design analysis procedure

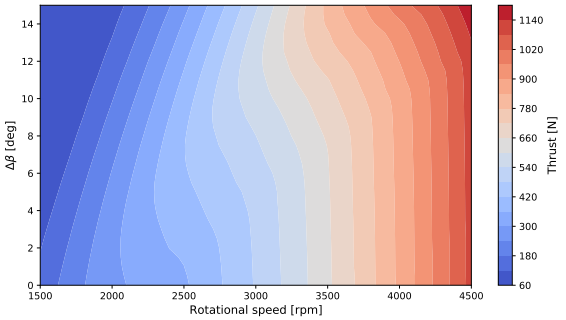

Figure 8.12: Sensitivity of the thrust to changes in rpm and pitch angle of the blade in the off-design analysis procedure

8.7. Verification and Validation

The first step to verify the design procedure for the blades has been performed by comparing the propeller exit speed calculated by the design method with the exit speed calculated with Actuator Disk Theory (ADT). The exit speed of the design procedure is calculated by using the displacement velocity ratio as shown in Equation 8.36, and for ADT Equation 8.37 is used.

$$V_{e,BEM} = V(1+\zeta) \tag{8.36}$$

$$V_{e,ADT} = \sqrt{\frac{2T_{cr}}{\rho A_{prop}} + V^2} \tag{8.37}$$

Doing this comparison for a range of blades results in Figure 8.13.

From the figure, a few conclusions can be derived. First of all, the exit speed of the BEM method is higher (which means lower efficiency). This makes sense because BEM uses more accurate calculations and accounts for more losses, which result in lower efficiencies. Secondly, it can be seen that, with an increasing number of blades, the exit speed of BEM approaches that of ADT. This makes sense because actuator disk theory can be compared to analysing a propeller with infinitely many blades. Even for a high number of blades, the values for BEM remain around 5 m/s higher than those of ADT, which is a result of the assumptions of each method.

A second verification test performed was to plot the efficiency of the propeller against the advance ratio, J = V/(nD). The test consists on comparing the shape of the graph with the expected one. The resulting plot is shown in Figure 8.14. When compared to a reference plot[2], the shape of the plot is as expected, with an increase in efficiency up to a certain advance ratio, after which a decline in efficiency is seen. Thus, the test is considered passed.

[2]http://www.epi-eng.com/propeller_technology/selecting_a_propeller.htm [cited 27 June 2021]

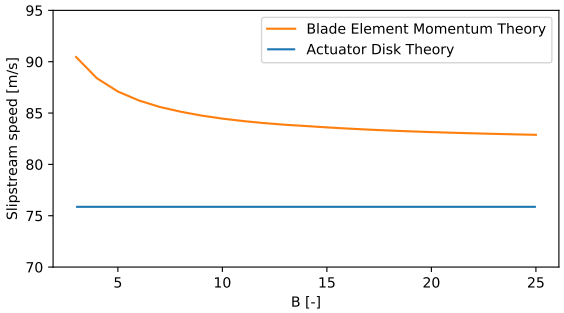

Figure 8.13: Estimated exit speed of the propeller calculated with ADT and BEM, respectively.

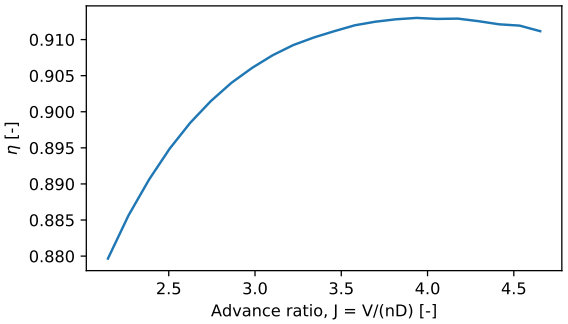

Figure 8.14: Efficiency of the propeller against advance ratio J

8.7.1. Validation plan

In order to validate the propeller design, there are two main options. A first step, best suited in the preliminary phase of the design, would be to perform an accurate CFD simulation with a validated program. This would provide good data to check the calculations, although it would be limited to the accuracy of the program itself, of the geometry and of the boundary conditions. A second, more accurate, step would be to manufacture a prototype of the propeller and test it. This is more time-consuming and expensive, and thus cannot be used early on nor repeated continuously, so it is best suited to validate the final design.

8.8. Future Recommendations

This section covers the aspects of the propulsion design that need further improvement on the future.

Stall of blade sections: The aerodynamic data for the airfoil has been computed in XFOIL, which loses accuracy in the post stall region of the lift polar. Since parts it the blades might be stalled during operation, it is important to ensure that the post-stall aerodynamic data of the airfoil is available and accurate. This is one of the points where the procedure needs improvement, for example by performing CFD simulations of the airfoil to obtain more accurate post-stall data.

Effects of interactions: Due to the complexity of their analysis, the effects of propeller-wing and propeller-propeller interaction have not been modelled. Since these interactions can have big effects on performance, quantifying them is important for a successful design. For propeller lateral separation, a clearance c_{pp} of 0.3 m was chosen. However, a sensitivity analysis on the effect of this clearance could not be performed. Despite this, it is known that this lateral separation can have an impact in noise and aerodynamic performance of the propellers. Another effect of propeller-propeller interaction is slipstream ingestion in the second row of propellers. This has not been modelled during the DSE, but it also can lead to big losses in thrust [121] and to an increase in noise, so quantifying its effect is also important. Lastly, the effect of the propeller blockage due to the wing has not been modelled either, which can also affect propeller performance, and thus it will also have an effect on the positioning of the propeller with respect to the wing, in terms of height and depth.

Airfoil selection: Another point is the airfoil selection. For this project a NACA4412 airfoil was assumed, but a dedicated airfoil selection to select an optimal one can improve the quality of the design.

Aeroacoustic simulation: The noise analysis presented here is a semi-empirical method which might not be accurate for the Wigeon configuration, specially considering the interactions between rotors. Hence, to overcome this, a more accurate aeroacoustic simulation of the aircraft is needed.

9 Power

The chapter is about the design of the power subsystem. In Section 9.1, a summary of the previously done trade-off is given, and is explained how the final battery type was selected. In Section 9.2, some theoretical background information is explained, and the characteristic values for the battery are given. In Section 9.3, the power budget is outlined. The battery size is calculated in Section 9.4, and the remaining powertrain components are discussed and sized in Section 9.5. The battery configuration is detailed in Section 9.6. Section 9.7 shows the means of compliance of the power system. Section 9.8 gives a sensitivity analysis for the battery configuration. Verification and validation is discussed in Section 9.9 and future recommendations are given in Section 9.10. The final section, Section 9.11 is about aircraft system characteristics and gives an overview of the electric layout of the aircraft.

9.1. Energy Storage Method Selection

This section is about the high level type of energy storage. It summarises the trade-off between hydrogen combustion and batteries, and gives the reasons for the final battery type selected.

One of the first things to do for the power system is selecting the energy storage method. Two types of energy source were considered, namely batteries and hydrogen. If hydrogen was used as the energy source, hydrogen fuel cells would be used for converting the energy into power. Batteries were found to be the better choice, due to their higher volumetric energy density, better safety and higher practicality. Electricity is also more readily available than hydrogen. Hydrogen has the potential to become a viable option in the future, but this requires further research and development.

The next choice was the specific battery type. Four types were considered: lithium-ion, lithium-sulfur, lithium-metal and solid state lithium batteries. A trade-off was conducted to select the best type of Wigeon, based on: specific energy, volumetric energy density, power density, cost and safety. After the trade-off, it was found that solid state lithium batteries are the best battery type for the aircraft. For more details on both the hydrogen-battery decision and the battery trade-off, see the midterm report [71].

9.2. Battery Information and Characteristic Values

This section provides technical background information on batteries. Some terminology is explained, and the characteristic values for the battery of the Wigeon are given and elaborated upon.

A number of parameters influence the battery sizing: The specific energy, the volumetric energy density, the power density, the depth of discharge (DoD) and the capacity in the battery at the end of life (EOLC). The specific energy is the energy stored per mass [Wh/kg]. The volumetric energy density is the energy divided by volume [Wh/l]. The power density is the maximum power the battery can deliver per kilogram [W/kg]. The DoD is a measure for how far a battery is discharged. A higher DoD means that more of the energy of the battery is used, but a higher DoD also causes a lower number of lifecycles before the EOLC is reached. Each charge-discharge cycle causes a small decrease in the maximum capacity of a battery. The EOLC is the ratio of the capacity that the battery should still have left at the end of life to the initial capacity.

The battery has a specific energy volumetric energy density and power density of respectively 500 Wh/kg, 1000 Wh/l and 6500 W/kg. These values are based on this paper by Luhan Ye [132], and then adapted to be more realistic for a commercial product. The battery has an anode of lithium and a cathode of $LiNi_{0.8}Mn_{0.1}Co_{0.1}O_2$. This combination gives a good performance, but the cathode contains cobalt. More information on the sustainability can be found in Section 15.3.3.

The DoD is chosen to be 0.8 or 80%. This is in line with other electric vehicles [1]. A DoD of 80% means that

[1] URL https://chargedevs.com/newswire/ev-tech-explained-why-do-evs-restrict-the-amount-of-battery-capacity-that-can-be-used-for-driving/ [cited 29/06/2021]

the battery has a deep discharge, since deep discharge is defined as having a DoD higher than 50%. From Ye, [132], it can be seen that the battery has a long lifecycle, and can withstand these discharges over the design life. The required EOLC was set to be 85%. Initially, a value of 80% was chosen. However, based on 3 flights per day, 85% remaining capacity would be reached after 7.5 years. This is half of the design lifetime, which would mean that the batteries are replaced one time during the service life of the aircraft. As well as maintaining total capacity over its lifetime, solid state batteries charge very quickly. A charge of 80 % is reached within 15 minutes[2], and it is estimated that a full charge takes 25 minutes.

9.3. Power Budget

In this section, the power budget for non-propulsion related systems is discussed. A power budget gives an overview of the power required for elements of the power subsystem other than the motors. The power budget can be found in Table 9.1. The values are based on Farrington [46], Pranoto [97] and Pipistrel[3].

Table 9.1: Overview of elements using power

Element	Required power [W]
Avionics	252
Air conditioning	3000
Battery temperature management	369.5
Autopilot	151
Trim	54
Passenger power	400
External lights	117
De-icing mechanism	3000
Landing gear rotation mechanism	50
Wing rotation mechanism	31.4

The power required for rotating the wing is computed by first calculating the torques around the rotation centre. These include the pitching moment from the airfoil, the moment due to the weight of the wing and the weight of the power and propulsion systems. Additionally, the torque required for accelerating the airfoil was calculated using $T = I \cdot \ddot{\theta}$. This gave a total required torque of 350.8 Nm. When using a rotation time of 35 seconds (Section 10.4.2), and computing the power using $P = T \cdot \omega$ gives a final required power for rotation of 15.7 W. This calculation is preliminary and contains some uncertainties. For example, the required moment can change due to wind, especially at high angles of attack. Moreover, the efficiency of the motor is unknown as well as gear efficiency. To account for this, a safety factor of 2 was chosen. This gave a final required power for the wing rotation mechanism as 31.4 W.

All elements except the landing gear and wing rotation mechanism are assumed to be used throughout the entire flight. When adding up these individual contributions, a total continuous power of 7343.3 W is found. Both the rotation mechanisms are only active for short times. The landing gear mechanism is active right after take-off and before landing, and the wing rotation mechanism is active during transition.

All these contribution are small compared to the propulsive system, at about 1% of the power or less. This is a small contribution, but not very far off from normal aircraft [24]. Since the non-propulsion elements only use a small portion of the total energy, and a contingency is used in the sizing of each component, see Chapter 14, the estimates of Table 9.1 were deemed sufficient for this stage of the design.

[2]URL https://www.quantumscape.com/wp-content/uploads/2021/02/Data-Launch-Updated-Post-Presentation-20210107-2.pdf [cited 29/06/2021]

[3]URL https://www.pipistrel-aircraft.com/aircraft/electric-flight/batteries-systems-and-bms/ [cited 29/06/2021]

9.4. Battery Sizing

The battery sizing procedure starts with the following formula, where the battery is sized both for total energy required and peak power, and then the largest is taken:

$$m_{bat} = \frac{E_{\text{req}}}{E_{\text{sp}}} \cdot \frac{1}{\text{DoD} \cdot \text{EOLC}} \qquad m_{bat} = \frac{P_{\text{max}}}{P_{\text{den}}} \cdot \frac{1}{\text{DoD} \cdot \text{EOLC}} \tag{9.1}$$

Where E_{req} is the required energy [Wh], E_{sp} is the specific energy [Wh/kg], P_{max} is the peak required power [W] and P_{den} is the power density [W/kg]. It was found that the sizing for energy gave a higher required mass than sizing for the power. The required mass for power is 409.4 kg whereas the required mass for energy is 886.2 kg.

The volume and price of the battery can be computed with the following equation:

$$v_{bat} = m_{bat} \cdot \frac{E_{\text{sp}}}{E_{\text{vol}}} \cdot \frac{1}{1000} \tag{9.2}$$

Where E_{vol} is the volumetric energy density [Wh/l]. The division by 1000 is there to convert from litres to cubic meters. This gives the following final battery volume: 335 l or 0.335 m^3.

9.5. Remaining Powertrain Characteristics

This section is about the sizing of the powertrain used in the Wigeon, excluding the battery. There are several types of electric engine, like the direct current motor, the the induction motor and the permanent magnet motor. The permanent magnet motor has a very high energy density and a high efficiency [56, 70], which is why this is the type of engine chosen for Wigeon.

The powertrain does not only contain the batteries and the motors. To control the electric motor, a motor controller is needed. Additionally, the weight of the shaft and of the propeller blades is incorporated, and this gives a final specific power for the power train. A final specific power of 3.6 kW/kg was estimated, based on Calnetix[4] and magniX[5]. This estimate is conservative in order to avoid an optimistic weight estimation which might cause an unrealistic design. The final mass can be found by dividing the maximum power by the specific power of the powertrain. This gives a final value for the mass of the powertrain of 502.6 kg.

Based on the products from magniX[5], the required voltage for the engine was determined. It is estimated that a voltage of 500 V is required for the electric motors.

9.6. Battery Configuration

This section is about configuring the batteries with the idea of safety in mind. First, the philosophy behind the design strategy is explained. Then, the method to calculate the configuration is calculated and then the final values are presented. The method for configuring batteries presented in this section works for both the batteries for the propulsion system and for the non-propulsion system, however, in this section only the configuration for the propulsion batteries is computed. The required voltage is not known for the non-propulsion elements, which makes it impossible to give an accurate configuration for these batteries.

Safety is a major factor in the design of the Wigeon. In the power department, safety is mainly achieved by reducing the impact of failure of the batteries. This can be achieved with a negligible weight penalty. Other options which were considered are adding an additional motor controller to the engine. This is not easily doable and required a split shaft for the engine. It would make the shaft heavier, and the mass of the motor controllers in the aircraft would also double. Besides this, having a single engine fail is not a situation that is desired, but a situation which has been designed for (see Section 11.2.4). Thus, it was decided that the weight penalty was worse than the additional redundancy. However, what is achievable is to not allocate a single battery to each wing, but to split this battery into two parts. This way, when one of the batteries fails, there still is half the energy available for the motor. This is shown in Figure 9.3b.

[4]URL https://www.calnetix.com/high-speed-electric-motor-generators [cited 29/06/2021]
[5]URL https://www.magnix.aero/products [cited 29/06/2021]

Batteries can be connected in two ways: in series or in parallel. When connected in series, the total current is the same as the current provided by each battery, and the total voltage is the sum of each individual voltage. When connected in parallel, the total current is the sum of the individual currents, and the total voltage is the same as the voltage of a single battery. Examples for both ways of connecting are found in Figure 9.1.

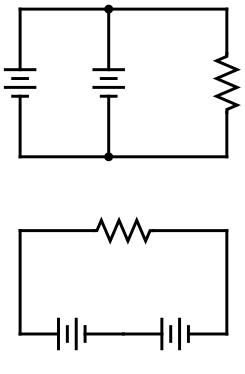

Figure 9.1: Example circuits for parallel (top) and series (bottom)

A battery consists of individual battery cells. Each cell has a nominal voltage and a capacity. The total energy of the battery can be found by multiplying the voltage and capacity, see Equation 9.4. For the Wigeon, it is assumed that the cells have an internal capacitance of 5 Ah, and the nominal voltage is 3.7 V. This is comparable to current battery cells[6].

In Equation 9.4, E is energy, C is capacity and V is voltage. Using Equation 9.4, the total energy stored in a single cell can be calculated and equates to 18.5 Wh.

$$V_{tot} = \sum_{i=1}^{n} V_i \tag{9.3}$$

$$E = C \cdot V \tag{9.4}$$

The following formulas can be used to calculate the total number of cells. Note that the ceil operator is used, because battery cells are always an integer and have to be rounded up as otherwise the required minima are not met.

$$n_{c_{mot}} = \text{ceil}\left(\frac{E_{tot} \cdot \%_{\text{mot}}}{100 \cdot E_c}\right) \tag{9.5}$$

$$n_{c_{misc}} = \text{ceil}\left(\frac{E_{tot}\,(1 - \%_{\text{mot}})}{100 \cdot E_c}\right) \tag{9.6}$$

Where n_c is the number of cells, $\%_{\text{mot}}$ is the percentage of energy that goes to the motors and E_c is the energy stored in a single cell. $\%_{\text{mot}}$ is 99 %, and E_c is 18.5 Wh. Combining this with the total energy required, this gives us that $n_{c_{mot}}$ is 16114, $n_{c_{misc}}$ is 163 and thus the total number of cells is 16277.

$$n_{c_{ser}} = \text{ceil}\left(\frac{V_{mot}}{V_c}\right) \tag{9.7}$$

$$n_{c_{par}} = \text{ceil}\left(\frac{n_{c_{mot}}}{n_{c_{ser}}}\right) \tag{9.8}$$

Using Equation 9.3, rewritten as Equation 9.7, the required number of battery cells that have to be placed in series to achieve the minimum voltage is calculated and comes out to be 136. The number of cells that have to be placed in parallel such that all cells are used is computed using Equation 9.8, and is 119.

Every step so far can be done, regardless of the number of batteries that actually has to be created, since total energy has been used. However, the Wigeon features 12 propellers, and each propeller has 2 batteries. This means that 24 different batteries are required. To ensure modularity, which is convenient for maintenance, it is required that all batteries have the same number of cells in parallel. This means that the number of cells in parallel has to be scaled up to the nearest number that is a multiple of 24, the total number of individual batteries. In such a case, the number of cells in parallel increases from 119 to 120.

$$n_{c_{new}} = n_{c_{par_{new}}} \cdot n_{c_{ser}} \tag{9.9}$$

$$\text{increase} = \frac{n_{c_{new}} - n_{c_{old}}}{n_{c_{old}}} \cdot 100\% \tag{9.10}$$

From Equation 9.9, the the number of cells has increased by 206, which is a 1.27% increase over the initial value of 16114 for the motors. The new number of cells for the motors is 16320 and the new total is 16483.

9.7. Compliance with Requirements

This section is contains the requirements that the power system strives to achieve. VTOL-PLD-3 requires the aircraft to have a cabin climate control system, and VTOL-PLD-3-POW-1 states that the climate control system should have a power of at least 2000 W. As can be seen in Table 9.1, the air conditioning has a power of 3000 W, so these requirements are met. The next requirement to check is VTOL-MFA-7, which states that the control system shall consume less than 1000 W. From Table 9.1, it can be seen that this requirement is met, as the sum of avionics, trim and auto pilot is only 457 W. VTOL-PRF-3-POW-1 states

[6] URL https://melasta.com/cells/lithium-polymer-li-po-batteries-cells-.html [cited 29/06/2021]

that the power system shall store 280 kWh. It stores 301.1 kWh, so this requirement is also met.

VTOL-SAF-6-POW-1 States that the power system shall have redundancy. There are parts of the power system where there are redundancies, like for example in the computers, which all have an internal backup system (see Section 9.11). However, there are no redundant batteries, since there is a big weight penalty for adding those. The batteries are split in two per motor, so that one of the batteries can fail but sufficient power can still be achieved.

The power subsystem shall allow for replenishing in 30 minutes, as by VTOL-EFG-1-POW-1. As stated in Section 9.2, the battery can reach 80% capacity in 15 minutes and a full charge in 25 minutes, which means this requirement is met. This also means that the total ground turnaround time of the aircraft can be kept below 45 minutes, which therefore translates to compliance with requirement VTOL-EFG-1. VTOL-ENV-1 and ENV-2 state that the aircraft shall not emit greenhouse gases nor particulate matter during operation. VTOL-STK-12 states that no polluting substances should be emitted during operation. Since the power system is fully electric, these requirements are met.

9.8. Sensitivity Analysis

This section gives a sensitivity analysis for the effect of the cell parameters on the battery configuration. As shown in Section 9.4 and Section 9.5, the sizing procedure for the components of the power subsystem is linear and does not require a sensitivity analysis. The procedure in Section 9.6 contains assumptions on C_{cell} and V_{cell}. The graphs below show the increase in percentage of the total number of battery cells with respect to the cell capacity (Figure 9.2).

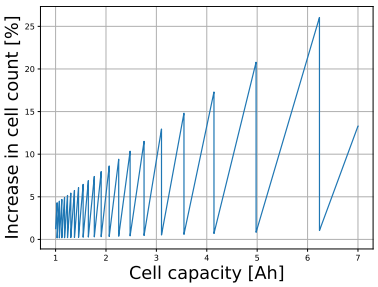

Figure 9.2: Percentage increase of number of cells required for battery configuration with respect to cell capacity

When increasing C_{cell}, the total number of cells decreases. The number of total cells still has to be divisible by 24, since there are 24 different batteries. The increase in cells is caused by this, until the excess is 24, at which point it goes back to 0 and the percentage of excess cells is reset. This process causes the sawtooth-like shape in the figure.

The total voltage of the battery is determined by the number of cells in series. From the sensitivity analysis, it was found that a minor change in V_{cell} has a major effect on the increase in number of cells. For example, for $V_{cell} = 3.7$, the increase in number of cells is 1.27%. When doing the same calculations with $V_{cell} = 3.71$, this increase is 20.75%. This is caused by the sizing procedure. Currently, the battery sizing is done for a specific voltage (500 V), whereas a more realistic method would size the batteries for a range of voltages. This would lessen the sensitivity for increase in number of cells due to the nominal cell voltage.

9.9. Verification and Validation

This section is about the verification and validation procedures used and to be used, to assure that the tools and the final design perform as intended.

To verify the calculations, the computations have been done by hand and cross-checked. Then a CICD test was used to check that the outputs of the code were equal to the analytical outputs, to verify that the calculations were conducted as intended. To further verify the created batteries, a next step could be to use a program like Circuitlab [29] to verify that the performance that is expected is actually achieved.

To validate the batteries, a real life version should be constructed and tested. This can first be done on a smaller scale, eventually scaling up to test the entire system.

9.10. Future Recommendations

This section is about points in which the power subsystem design can be improved in the future. Instead of configuring the batteries for a specific voltage, a range of workable voltages should be used. This would

reduce the sensitivity of the configuration to the cell voltage. Besides this, the variance in cell voltage can be taken into account for a more thorough analysis. The internal resistance of the batteries influence, and placing cells in series adds these resistances and reduces the efficiency.

A more detailed analysis of the temperature management system could be done. A constant power required for cooling is now assumed, but this is not normally the case, as there is more power pulled from the batteries during take-off, transition and landing than during cruise.

9.11. Aircraft System Characteristics

This section is about the general characteristics of the electronics and power system of the aircraft. In Figure 9.3a, a global overview of the electronic connections inside the aircraft is shown. Since most likely the non-propulsion element of the power subsystem operate at a lower voltage than the 500 V for the motors (see Section 9.5) it was decided that these non-propulsive elements is powered by a separate battery.

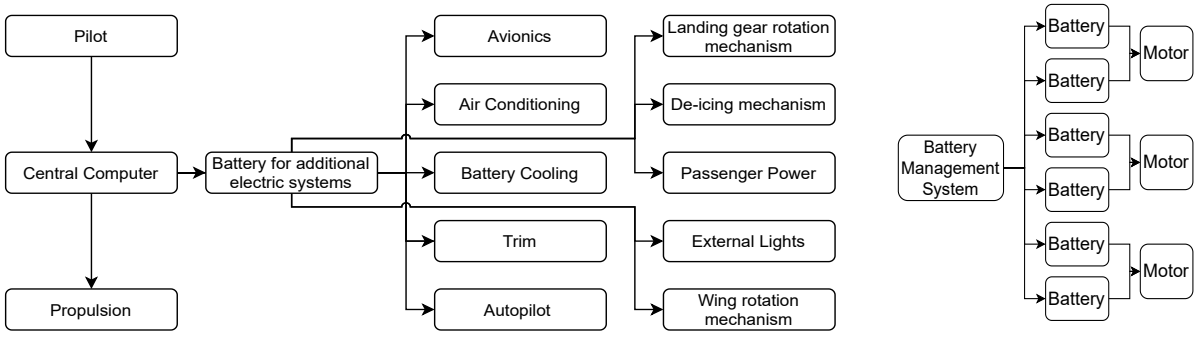

(a) Overview of the structure of the electronic subsystems

(b) Overview of the structure of the power system for half of a wing

Figure 9.3: Global overviews for electric systems

In Figure 9.3b, an overview of the way the connections are done for half a wing is shown. All of the batteries are controlled by a computer, which controls the amount of power towards the propellers and checks if the batteries are still in a good operating condition i.e. they do not have a voltage drop, a temperature spike or another anomaly. Each motor is powered by two batteries. Each motor is controlled by a dedicated controller (not shown in the image, located right next to the motor).

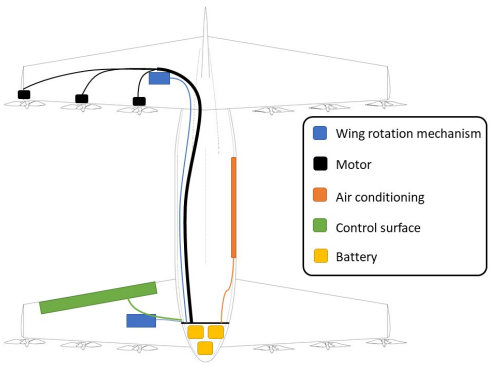

Figure 9.4: An overview of a subset of the electrical wiring going through the plane

Figure 9.4 gives an overview of a part of the wiring of the aircraft. It is important that the wires are connected such that they are failure proof, and do not suffer a single point of failure. A challenge with the Wigeon is that the wings rotate around a single point, which means that the electrical wires that need to go to the wing (i.e. for propulsion, control surfaces and lights on the wingtips) all need to go close to the rotation mechanism, since otherwise there is a lot of change in required cable length. This is indicated in Figure 9.4 with the wire going to the control surface on the front wing, and the wires going to the propulsion system on the rear wing.

Any wiring that is not going to the front wing is wired via the top side of the fuselage. This reduces the chance of damage to the wires on impact, and in case a landing on water occurs, it positions the electric wiring further away from the water. The propulsion wiring consist of separate wires, bundled together to save space inside the fuselage. After passing through the rotation mechanism, the wire splits in three, going to the respective electric motor.

10 Flight Performance

An important selling point for any aircraft is its performance. In this chapter, several methods to assess the performance of an eVTOL aircraft are explained. In Section 10.1 the models used to estimate the energy and power consumption of the aircraft during operation are presented, together with their simulation results. Other performance estimates are shown in Section 10.2, where the rate of climb is evaluated, and a payload-range diagram is constructed. In Section 10.3, a sensitivity study is conducted with respect to some important operational characteristics. Finally, verification and validation is performed in Section 10.4.

10.1. Energy Estimation

This section outlines the procedure used to estimate the energy and power consumption during a mission. First the workings of the model used for take-off and landing is explained in Section 10.1.1. In Section 10.1.2 the implementation of the model to simulate take-off and landing is given. Section 10.1.3 presents the method used to estimate the power and energy consumption during cruise. The results of these models are given in Section 10.1.4.

10.1.1. Model

To model the aircraft during take-off and landing, a method similar to that found in [44] was used. In this method, the required wing angle and thrust are found by prescribing the values for the acceleration in x- and y-direction.

The equations of motion expressed in a normal-to-earth vehicle carried reference frame are shown in Equation 10.1 and Equation 10.2. In these equations θ_T represents the angle with which the wings are rotated with respect to the x-axis. To simplify the analysis, the variation in pitch of the fuselage is ignored. To get the drag of the fuselage, it is assumed that it is parallel to the flow at all times, except when flying in vertical flight configuration, where it is assumed the fuselage is at 90 degrees.

$$\sum F_X : -D\cos\gamma - L\sin\gamma + T\cos\theta_T = ma_x \tag{10.1}$$

$$\sum F_Y : -D\sin\gamma + L\cos\gamma + T\sin\theta_T - W = ma_y \tag{10.2}$$

To calculate the lift and drag in the equations of motion, the angle of attack is needed. Since the aircraft has tilting wings, the angle of attack of the wings depend on the direction of the incoming flow and the angle of rotation of the wings. Assuming there is no wind the angle of the incoming flow equals the flight path angle γ. The angle of attack can then be found by subtracting the flight path angle from the wing angle.

By combining the equations of motion, an expression for the required wing angle for a certain target acceleration can be obtained. Plugging the resulting angle back into Equation 10.1 or Equation 10.2 and rearranging leads to a required thrust.

During the simulation, Equation 10.1 and Equation 10.2 were solved again for a_X and a_Y, with the calculated thrust and wing angle. The calculated accelerations were then used in a time stepping forward Euler simulation to obtain velocity and position of the aircraft.

Since the required thrust and wing angle are not necessarily a continuous function throughout the flight, some additional constraints were added. Because the wing rotates with a finite speed, the wing angle was

only allowed to vary within $\pm\omega_w dt$ of its previous value, where ω_w is the rotational speed of the wing and dt the time step used for the simulation.

To estimate the energy used, the thrust at each time step was converted to available power, using the method found in [25], as shown in Equation 10.3. In this equation the velocity $V_{\infty\perp}$ is the speed perpendicular to the propeller disk. The factor κ corrects for power losses not considered in the derivation of this equation, and was assumed equal to 1.2, as per [25].

$$P = TV_{\infty\perp} + \kappa T\left(-\frac{V_{\infty\perp}}{2} + \sqrt{\frac{V_{\infty\perp}^2}{4} + \frac{T}{2\rho A_{\text{disk}}}}\right) \tag{10.3}$$

The available power was converted to brake power by dividing it with the propulsive efficiency at that flight stage. For simplicity, only two efficiencies were considered, one in cruise and one in vertical flight. The efficiency at a certain speed was found by interpolation. Multiplying the brake power with the time step size yields the energy required during that step. Summing the energy at each time step gives the total energy needed by the engines.

10.1.2. Take-off and landing

To obtain a smooth trajectory from the ground to cruise, or vice versa, a proportional controller was implemented. This controller was applied on the speeds in x- and y-direction and on the altitude. Equation 10.4 shows the proportional controller used for the vertical speed. A maximum value for the magnitude of the vertical speed was applied, to constrain the rate of climb.

Since the model described in Section 10.1.1 takes target accelerations as input, the vertical speed from the controller is used as an input for another controller, see Equation 10.5. A similar controller (Equation 10.6) was applied for the speed in x-direction, where the target speed is just the required speed at the end of the manoeuvre. To ensure passenger comfort, the accelerations were limited to 0.5g in x-direction, and 0.2g in y-direction.

$$v_{y,target} = -0.5(h - h_{cruise}) \tag{10.4}$$

$$a_{y,target} = -0.5(v_y - v_{y,target}) \tag{10.5}$$

$$a_{x,target} = -0.5(v_x - v_{x,target}) \tag{10.6}$$

A final constraint was added to ensure safety close to the ground. When approaching 15 m of altitude during descend with a horizontal speed higher than 0.25 m/s, the vertical speed is set to zero. This makes the aircraft hold its altitude while slowing down. As soon as the speed is low enough, the aircraft is allowed to descend below 10 m and land. When taking of, the horizontal speed is also set to zero when below 10 m. The altitude of 10 m has been chosen such that nearby obstacles can be cleared safely, and to allow the pilot enough time to react during transition at low altitudes.

10.1.3. Cruise

Cruise was done slightly different. Cruise was assumed to be at a constant speed and altitude. For this speed the lift-to-drag ratio can be found. Putting these values into Equation 10.7 [106] gives the brake power required. In this equation η represents the propulsive efficiency at a speed V.

The energy consumption during cruise is calculated by first finding the time spent in cruise. It is assumed that the distance needed for the take-off and landing manoeuvre can be ignored. This can be done not only since they are relatively short when flying at a low cruising altitude, but also since the aircraft will likely have to comply with air traffic regulations during climb and descend. The cruise speed is that where L/D is maximal, which is 72 m/s for the Wigeon. Using this speed, the time spent in cruise can be calculated.

Multiplying this with the required brake power yields the energy needed for cruise. This procedure can also be used to estimate the energy needed for loiter. The speed and lift-to-drag used for this should be those for which the required power is minimal.

Since manoeuvres performed by transport aircraft usually involve very small g-loads, they should thus not increase the required power significantly. Furthermore, only a very small portion of the total flying time will consist of manoeuvring. Therefore these were not considered in the analysis.

$$P_{br} = \frac{C_D}{C_L} \frac{WV}{\eta} \tag{10.7}$$

10.1.4. Simulation results

Take-off and landing

Figure 10.1 presents the results of the simulation of the aircraft during take-off. It can be noted that the engines are rotated early in the manoeuvre (Figure 10.1e), and that the aircraft reaches cruise speed before reaching the cruising altitude. This is shown in Figure 10.1b. This might not be optimal, since the aircraft then needs to perform a large part of the climb at a non-optimal speed. In a later design stage, this could be optimised. In Figure 10.1a it can be noted that it takes 12 km for the Wigeon to reach cruising altitude. The accelerations during take-off stay within $\pm$ 0.2 g, as shown in Figure 10.1d, indicating relatively good passenger comfort. The initial spike of in acceleration is an artefact from the initialisation of the simulation. The power needed during take-off can be found in Figure 10.1f. Most of the power is needed for the initial part, where the aircraft flies in vertical configuration. The maximum power of 1.7MW is also the maximum power needed in any phase of the flight, and was used to size the power and propulsion subsystems. The maximum power needed when applying a contingency of 10 % to the MTOM can be found in Table 10.1.

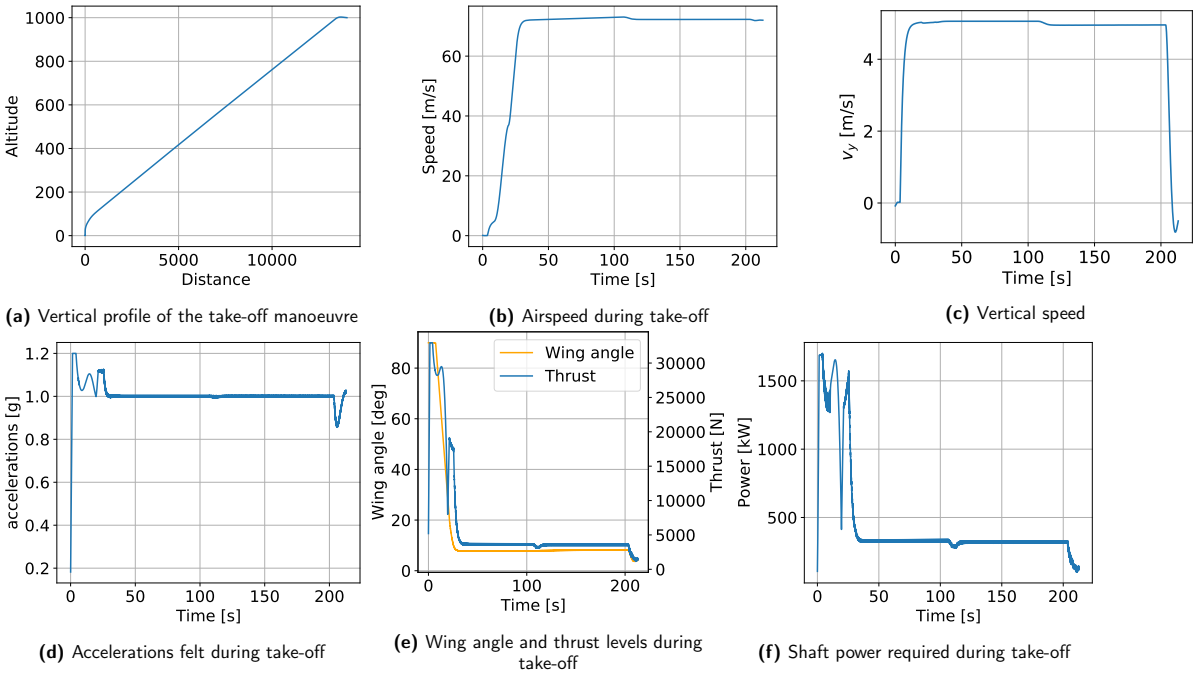

(a) Vertical profile of the take-off manoeuvre

(b) Airspeed during take-off

(c) Vertical speed

(d) Accelerations felt during take-off

(e) Wing angle and thrust levels during take-off

(f) Shaft power required during take-off

Figure 10.1: Variation of different states during the take-off manoeuvre

Figure 10.2 shows the simulation results of the aircraft during landing. The landing manoeuvre takes longer than the take-off manoeuvre. This is mainly caused by the need to slow down after the initial descend, which mainly happens after descending to 15 meters. The reason the aircraft keeps it speed during descent can

be attributed to the high aerodynamic performance, and the lack of drag from the propellers in the model. Before optimising the landing trajectory, this should first be quantified. Note that the eVTOL remains in cruise configuration until right before landing (Figure 10.2e). Also for landing the accelerations remain largely within $\pm$ 0.2 g, see Figure 10.2d. In Figure 10.2f the power peaks when the aircraft has transitioned to vertical flight, although the peak is lower than during take-off.

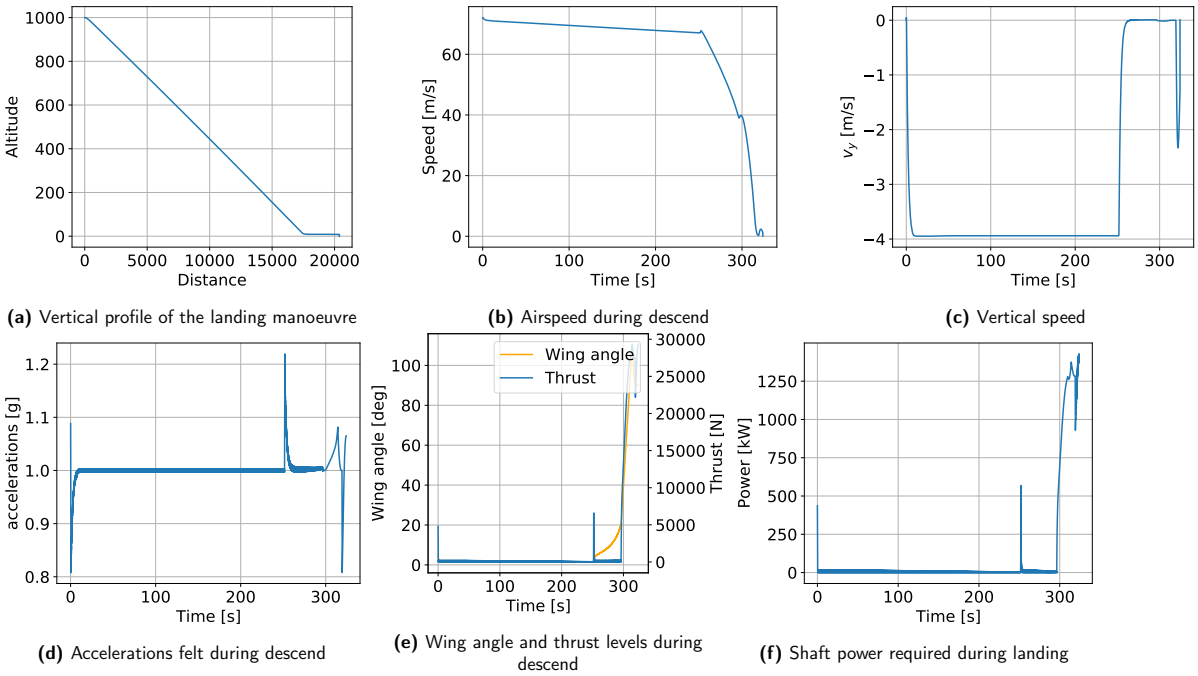

(a) Vertical profile of the landing manoeuvre

(b) Airspeed during descend

(c) Vertical speed

(d) Accelerations felt during descend

(e) Wing angle and thrust levels during descend

(f) Shaft power required during landing

Figure 10.2: Variation of different states during the landing manoeuvre

In Figure 10.1a and Figure 10.2a it can be noted that in total more than 30 km is needed to take-off and land. As this distance is not considered for the range, it introduces an additional margin to the range of roughly 10 %, if the direction for climb and descend is unrestricted.

Energy and power

Using the method described in Section 10.1.1 and Section 10.1.3, the required energy for a standard 300 km mission including 15 minutes of loiter time was calculated, with and without mass contingency applied. The results can be seen in Table 10.1. Note that the battery is sized including the mass contingency. If the aircraft mass would not increase later on, this means the range increases to 400 km. The breakdown of this energy for the different phases of flight can be found in Figure 10.3. It can be seen in this figure that a substantial part of the energy is used for take-off, this can partly be eliminated by cruising lower.

Figure 10.3: Energy consumption for the different phases of a standard mission.

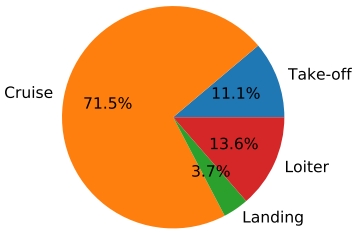

Table 10.1: Maximum power and total energy needed for a 300 km mission including 15 minutes of loiter.

	w contingency	**w/o contingency**
P_{max}	1.8 MW	1.7 MW
E_{tot}	884 MJ	1084 MJ

10.2. Performance Evaluation

In this section, different performance parameters of the aircraft are calculated. First the rate of climb in horizontal and vertical flight configuration is considered in Section 10.2.1. After that, a payload range diagram is constructed in Section 10.2.2

10.2.1. Climb performance

An important metric to evaluate the performance of an aircraft is the climb performance. This not only tells how fast an aircraft can climb when flying at a certain speed, but also gives the maximum speed, and the speed at which climb is most efficient. For a VTOL aircraft, two different climbs can be considered, the climb performance in cruise configuration, and in vertical configuration.

For the rate of climb in cruise configuration, Equation 10.8 was used, setting a maximum value on the rate of climb equal to the speed at which the maximum ROC is considered. This is necessary since Equation 10.8 allows climb angles greater than 90 degrees. The maximum thrust was found by reversing Equation 10.3. The reason thrust was used instead of power was that for low speeds, the assumption that power is constant for a propeller aircraft does not hold. The drag was found based on the lift coefficient required for steady flight, which has to be reduced by a factor $\cos\gamma$ for steep climb angles.

$$ROC = \frac{T_{max} - D}{W} V \tag{10.8}$$

The climb performance chart for the eVTOL in cruise configuration is shown in Figure 10.4a. In this figure it can be seen that the aircraft is able to reach very high climb speeds, around 43 m/s. This can be attributed to the fact that the engines are sized for vertical take-off, where they need to lift the entire aircraft, and where the engines are less efficient. The effects of altitude are also shown in this chart. It can be seen that the maximum rate of climb does not diminish much with altitude. The maximum speed, where the rate of climb equals zero does however vary with altitude. When flying at 1000 m, the speed at which the climb rate is maximised is 84 m/s. Note that this is higher than the speed at which C_L^3/C_D^2 is maximal. This can be attributed to the fact that the assumption that the climb angle is small can no longer be applied here, as the climb angle at the maximum rate of climb is 30 °.

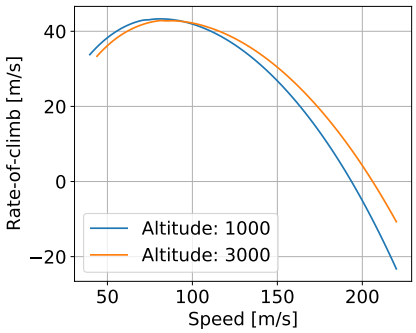

(a) Rate of climb in cruise configuration

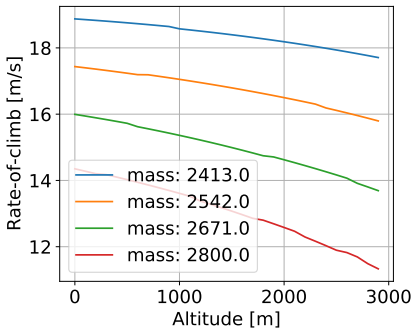

(b) Rate of climb in vertical configuration

Figure 10.4b presents the climb performance of the aircraft in vertical flight configuration. The climb rates have been plotted against altitude. It can be seen that the rate of climb reduces with altitude.

The effects of a varying mass have also been added. This has a large influence, since the weight of the aircraft directly counteracts the thrust in vertical flight. These rates of climb were found by assuming the thrust of the aircraft acts directly up. The equation of motion is represented by Equation 10.9, when the aircraft is in a steady climb. The speed in this equation equals the rate of climb, since the aircraft climbs vertically. The thrust for a certain velocity is found by reversing Equation 10.3. Since this equation cannot be solved analytically, a solution is found by iterating from an initial guess for the rate of climb.

$$T(V) - D(V) - W = 0 \tag{10.9}$$

10.2.2. Payload-range

An important performance parameter for the operation of an aircraft is the relationship between payload mass and range of the aircraft. Payload range diagrams were constructed for the eVTOL, and can be seen in Figure 10.5. To construct these, the energy consumption for take-off and landing was subtracted from the total energy capacity of the aircraft. The remaining energy was then used to calculate the range in cruise. The distance covered while climbing or descending was ignored. In the payload range diagram shown below, it can be seen that the range does not change significantly with payload. Removing one passenger would increase the range by less than 20 km.

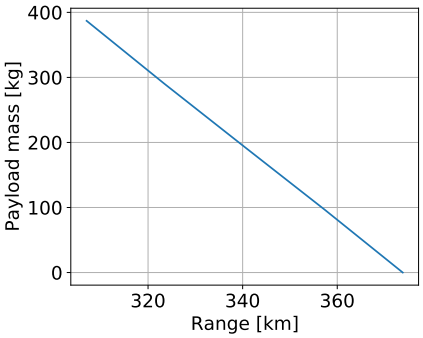

Figure 10.5: Payload-range diagram

10.3. Sensitivity Study

In this section, the sensitivity of the range and block speed to different operational parameters is investigated. The block speed is defined here as the mission range divided by the total time needed to fulfil that mission. This allows to identify the parameters to which special attention should be payed during design, or during operation. The high aircraft ranges shown in this section are caused because the 15 minutes of loiter were not considered.

10.3.1. Cruising altitude

Figure 10.6a and Figure 10.6b show the sensitivity of the range and block speed for the eVTOL aircraft to the cruising altitude, respectively. It can be seen that lower altitudes should be favored. While the range shortens with altitude, so does the block speed. This is caused by the increased time needed to climb and descend, the distance of which is not counted towards the range. Using the results from the range-cruising altitude sensitivity analysis, it was decided to size the aircraft for a 1000m cruising altitude. As this altitude will most likely be lower during operations, it provides a conservative estimate for the required energy.

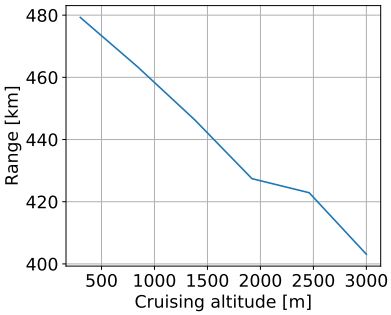

(a) Sensitivity of the aircraft range to cruising altitude.

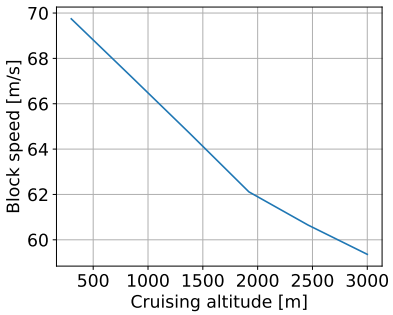

(b) Sensitivity of the mission block time to cruising altitude

Figure 10.6: Sensitivity of different mission parameters to a changing cruising altitude

10.3.2. Cruise speed

A sensitivity study was also performed with respect to cruise speed. This is useful since it allows to quantify the effect of the aircraft flying at a non-optimal speed. Figure 10.7 shows the achievable range when flying at

a certain cruise speed. It can be observed that the speed for maximum range of 72 m/s is that for maximum L/D, which is confirmed by theory [106]. From the figure it can be concluded that flying at the optimal cruise speed is important, although small deviations do not change the range significantly. It is assumed that the pilot and the control system are able to maintain the cruise speed to within $\pm$ 5 m/s. As can be seen in the graph, this does not influence the range by more than 10 km. Hence no additional energy reserves should be allocated to allow for a deviation in cruise speed.

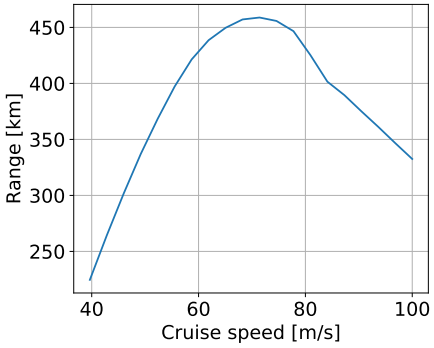

Figure 10.7: Sensitivity of the aircraft range to cruise speed

10.3.3. Wind

Since the aircraft will encounter wind during operation, it is important to quantify its effects on range. To simplify the analysis, only head- and tailwinds have been considered. Figure 10.8a shows how the range of the aircraft is affected, where negative wind speeds are tailwinds.

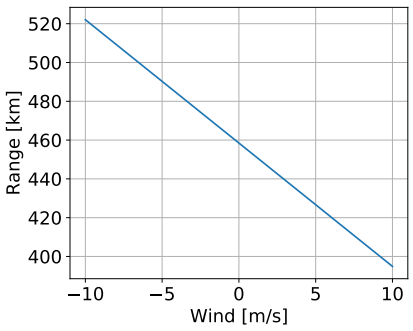

(a) Sensitivity of the aircraft range to wind

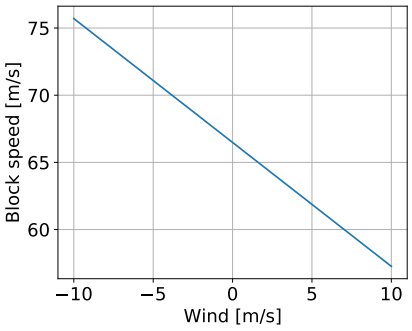

(b) Sensitivity of the mission block time to wind

Figure 10.8: Sensitivity of different mission parameters to a range of wind speeds.

Clearly, wind has a large effect on range, even a common headwind of 5 m/s reduces the range by more than 20 km. Note that when constructing these graphs, it was assumed that the aircraft flies at the optimum speed for still air, which might not be optimal in wind. As can be expected, also the block speed is influenced by wind, as can be seen from Figure 10.8b.

10.4. Verification and Validation

The following section outlines the verification procedure used. Also the model validation and requirement validation strategies are explained.

10.4.1. Verification

Verification was done by performing unit tests on different parts of the model code. This was mostly done by using simple inputs, where the output is easy to either calculate manually or using another method to compare.

These tests included verifying whether the aircraft did not cover any distance if the target velocity equalled zero when climbing. It was also tested that the aircraft did not move if the target altitude and speed were both zero when taking off. Another test was to compare the outputted energy and distance of a slightly descending profile and a slightly climbing profile, to see whether the descend and climb parts of the transition model agreed. Furthermore, the aircraft was put in a steady flight in the descending part of the transition model. The outputted energy should then equal that predicted by the cruise energy estimation part of the model.

Also the performance assessment part of the model was verified. Here the maximum speed predicted by the climb charts was compared to the maximum speed found by setting thrust equal to drag. Furthermore, the climb chart for vertical flight was verified by first setting the thrust equal to zero, and comparing the rate of climb with the analytical solution for its terminal velocity. To test the thrust part of the vertical climb code, it was set equal to the weight, and checked if the rate of climb equalled zero. The numerical inverse of the thrust vs power relationship (Equation 10.3) was verified by first calculating the power associated with a certain thrust and speed, and then numerically inverting the power back to thrust. Finally, the energy needed for an standard mission was calculated in the energy calculation part of the script. This energy was inputted in the range calculation. The resulting range should equal that initially used for the energy estimate.

Some parts of the sensitivity analysis were also verified. Here the optimal cruise speed indicated by the maximum in Figure 10.7 was compared to the theoretical value calculated at the minimal C_L/C_D. The influence of the wind was verified by varying the wind speed to $\pm$ the cruise speed. When the headwind equals the cruise speed, the range should equal zero. When the tailwind equals the cruise speed, the range should be twice that when there is no wind.

10.4.2. Validation

Validation is split into two parts. First it has to be established whether the models used to simulate Wigeon's performance represent reality well enough. Secondly, assuming the models are accurate, the aircraft performance has to be validated, to see if the requirements are satisfied.

Model validation

In this design stage, validation was focused on the parts that have the most influence on the final energy. Due to their limited influence (<15%) on the required energy, validation of the landing and take-off simulation will be done at a later stage.

It is further assumed that the power estimation for cruise (Equation 10.7) is valid, since it was found in an engineering handbook [106]. This limits validation of the energy estimation mainly to the data it uses as an input; the drag polar, weight, and propulsive efficiency. This is done in the respective chapters of Chapter 7, Chapter 12 and Chapter 8.

The models used for rate of climb in cruise configuration are derived from the forces acting on an aircraft in equilibrium, found in [106]. It is assumed that these are valid. As for the energy estimation, validation should focus on the data used. For the rate of climb in vertical configuration, validation will be done using a representative test setup, possibly a scaled demonstrator. This is needed since the model used was not taken from other research or books.

As an additional validation method, a test flight campaign with a prototype will be performed later on. This is the most accurate way to validate performance models. In this campaign, power and energy consumption can be measured directly. Also the rate of climb in different configurations can be quantified experimentally here.

The prototype might differ from the production aircraft, being scaled or altered to ensure quick manufacture. To account for this, the parameters used in the model should be changed accordingly.

Product validation

Cruising altitude Following VTOL-STK-14, the Wigeon should cruise above 305 m. As the aircraft was sized assuming a cruising altitude of 1000 m, it can indeed cruise higher than 305 m. Another requirement related to altitude is VTOL-STK-17, which dictates that the cabin pressure should be higher than the equivalent pressure at 2500 m. This requirement is fulfilled by cruising lower than that altitude. Furthermore, the operational ceiling of 3000 m set by VTOL-PRF-7, is satisfied, as the aircraft still maintains a positive rate of climb at this altitude. This is reflected by Figure 10.4a.

Transition related requirements VTOL-LFT-3 requires the aircraft to transition from hover to cruise over 20 km. Looking at Figure 10.1a, it can be seen that the aircraft reaches cruise in about 13 km, although this depends on the cruise altitude. Following VTOL-PRF-1 and VTOL-PRF-2, the Wigeon should transition from vertical to horizontal flight in 60 seconds, and transition from horizontal to vertical flight in 60 seconds as well. Given that the former takes 35 s, and the latter 50 s, this requirement is fulfilled. Furthermore, during descent the aircraft should not encounter accelerations higher than 3 m/s^2. This is indeed the case, accelerations caused by controlling the aircraft stay below 2.45 m/s^2, as can be seen in Figure 10.2d. Following VTOL-PRF-7-PRP-1, the Wigeon should be able to produce enough thrust to reach a rate of climb of 10 m/s. This is satisfied, since according to Figure 10.4a the aircraft can climb at more than 40 m/s. According to VTOL-STK-4 and VTOL-STK-5, the aircraft has to be able to take of and land vertically. As could be observed in the simulation results of the take-off and landing, this is indeed possible.

Loiter According to VTOL-PRF-3, the eVTOL should be able to loiter for 15 minutes after cruising for 300 km. Given the fact that the battery was sized for this explicitly, this requirement is fulfilled. Furthermore, contingencies used to size the battery should give the aircraft additional loiter time.

Cruise With a stall speed of 40 m/s, VTOL-LFT-7, which dictates a stall speed of 45 is satisfied. Requirement VTOL-PRF-5 sets a minimum cruise speed of 150 km/h. This is the case, as the cruise speed of the aircraft is 260 km/h.

Mission time According to VTOL-STK-3, the Wigeon should be able to perform a 300 km mission in between 1 and 3 hours. If the aircraft cruises at 72 m/s, the time spent in cruise is 69 minutes. Adding to that the 9 minutes needed for take-off and landing, it can be concluded that this requirement is fulfilled

Range The most relevant requirement for flight performance is the range (VTOL-STK-2). To validate the range, a Monte Carlo simulation is performed on the energy calculation. By randomly varying the mass, the maximum lift coefficient, the wing surface, the disk area and the maximum power around $\pm$ 10% of their nominal values, the energy required to fulfil a 300 km mission and 15 minute loiter is calculated. The results are plotted in the histogram in Figure 10.9. The average energy needed was 804 MJ, significantly less than the 1084 MJ found earlier, since no contingencies were included to the mass. The standard deviation of the energies was 67 MJ. Even if two standard deviations are added to the average energy, the new energy (940 MJ) is still below the energy of 1084 MJ for which the battery was sized. It can thus be concluded that the range requirement VTOL-STK-2 is fulfilled. This analysis also proves that VTOL-ENV-3 is satisfied. This requirement dictates a maximum energy consumption of 400·10^{-4} kWh/km/kg. Dividing the the energy capacity of 1084 MJ by the range and the mass, and converting to kWh gives a value of 358·10^{-4} kWh/km/kg.

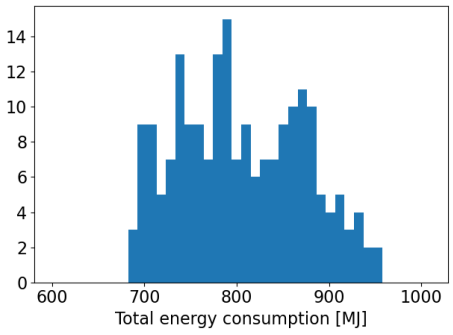

Figure 10.9: Histogram containing the resulting energies needed for a standard mission, when randomly varying aircraft design parameters up to 10 %

11 Stability and Control

One of the major challenges of eVTOL design are the diverse operating conditions of the aircraft, which lead to different dynamic behaviour throughout mission phases. This chapter addresses how the eVTOL was designed to meet stability and controllability requirements. First, the criteria for stability and control are derived in Section 11.1. The design choices to meet these criteria are elaborated and motivated in Section 11.2, where it is decided to use both differential thrust and control surfaces instead of rotating the entire wings as it was deemed to be more inefficient (in terms of speed and power consumption). Given the resulting aircraft parameters, an analysis of the open-loop vehicle dynamics is presented in Section 11.3, while Section 11.4 lays out the design for a closed-loop feedback controller. Section 11.5 evaluates compliance of the design with the relevant requirements and Section 11.6 explains procedures for verification and validation of the methods used.

11.1. Criteria for Stability and Controllability

To be able to design for stability and controllability, their respective criteria need to be defined and related to design variables. In this section, the stability and controllability criteria are derived for hover, cruise and during ground operations. These can be found in Section 11.1.1, Section 11.1.2, and Section 11.1.3, respectively.

11.1.1. Hover

In hover mode, the oncoming airspeed experienced by the vehicle is very low. Therefore, aerodynamic control surfaces are not an effective means of control so thrust vectoring or differential thrust must be used. In order to quantify the controllability of the eVTOL in hover, the Available Control Authority Index (ACAI) developed by Du et al. [34] is used. It was designed to evaluate available control authority of multirotor vehicles with fixed rotors (with the possibility to account for rotor wear and failures) and is derived from a state-space system describing hover dynamics. It assumes that differential thrust is the only means of control to affect the 8 states in hover which are altitude h, the roll angle ϕ, the pitch angle θ, the yaw angle ψ, the vertical speed v_h, the roll rate p, the pitch rate q, and the yaw rate r.

The full derivation and calculation procedure for the ACAI is omitted in this report for sake of brevity. The detailed explanations can be found in [34] and [71]. The calculation was implemented in Python using the Matlab Toolbox [35] developed by the authors of [34] as an example and means of verification. For the design, it is only relevant to know that the ACAI must be positive to allow for hover controllability.

The relevant design parameters for the ACAI are the maximum thrust and position of the rotors, the CG position, the eVTOL mass, the reactive torque coefficient k_μ, the direction of rotation of the rotors, and efficiency parameters η_i that can be used to simulate rotor failure or wear.

11.1.2. Cruise

In horizontal flight, there are nine state variables to be controlled [62]. As in conventional aircraft, the Wigeon controls these states using the control surfaces that create rolling, pitching, and yawing moments.

The choice of aerodynamic control surfaces (as opposed to differential thrust and thrust vectoring) was based on the findings of Chen [26], who found that conventional aerodynamic surfaces are much more effective for steady level flight than thrust vectoring.

All control moments depend on the location of the centre of gravity, since that determines the moment

arm that the control force has. However, M is especially affected because the weight acts in the X-Z-plane. Therefore, only the criterion for pitch controllability is be addressed here while roll and yaw criteria are discussed in Section 11.2.4, where the control surfaces are sized.

The free body diagram of the tandem wing configuration representing straight, symmetric horizontal flight including aerodynamic forces and the weight can be seen in Figure 11.1.

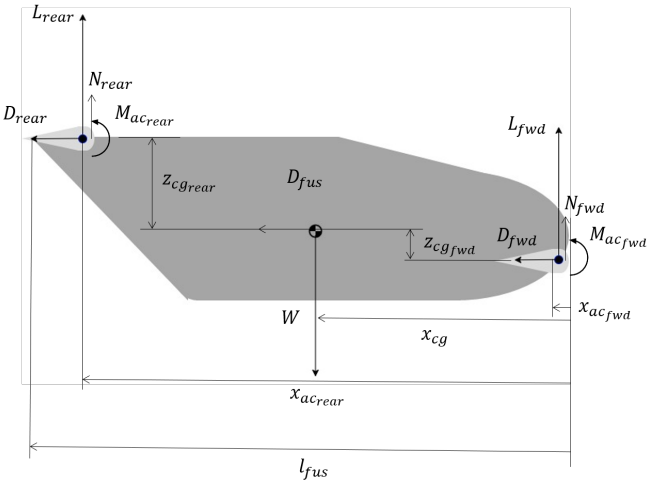

Figure 11.1: FBD showing all aerodynamic loads at horizontal flight with associated distances for the tandem wing configuration.

The non-dimensional moment at the CG is as follows:

$$C_m = C_{m_{ac_{fwd}}} \cdot \frac{S_{fwd}\bar{c}_{fwd}}{S\bar{c}} - C_{D_{fwd}} \cdot \frac{z_{cg_{fwd}} S_{fwd}}{S\bar{c}} + C_{T_{fwd}} \frac{z_{cg_{fwd}} S_{fwd}}{S\bar{c}} + C_{L_{fwd}} \cdot \frac{(x_{cg} - x_{ac_{fwd}}) S_{fwd}}{S\bar{c}}$$
$$+ \left(\frac{V_r}{V}\right)^2 \cdot (C_{D_{rear}} \cdot \frac{z_{cg_{rear}} S_{rear}}{S\bar{c}} - C_{L_{rear}} \cdot \frac{(x_{ac_{rear}} - x_{cg}) S_{rear}}{S\bar{c}} + C_{m_{ac_{rear}}} \frac{S_{rear}\bar{c}_{rear}}{S\bar{c}} - C_{T_{rear}} \frac{z_{cg_{rear}} S_{rear}}{S\bar{c}}) \tag{11.1}$$

The subscript fwd is for the forward wing and $rear$ is related to the most aft wing. C_{T_i} is the thrust coefficient defined as the thrust normalised by the dynamic pressure force. V_r is the velocity felt by the rear wing. S and $\bar{c}$ are the mean aerodynamic chord and area of the entire aircraft. In this section the following are assumed to be as:

$$S = S_{fwd} + S_{rear} \tag{11.2}$$

$$\bar{c} = s_{fwd} \cdot \bar{c}_{fwd} + s_{rear} \cdot \bar{c}_{rear} \tag{11.3}$$

with s_i being the ratio of the wing area S_i by the total area S. $C_{m_{ac}}$ is the aerodynamic moment coefficient at the aerodynamic centre, x_{ac} is the horizontal location of the aerodynamic centre and $z_{cg_{rear}}$ and $z_{cg_{fwd}}$ are the vertical distances between the aerodynamic centre of the rear wing and forward wing respectively and the centre of gravity. It can be seen that the normal force components are neglected as they are known to be small and can be neglected when the free stream is normal to the propeller area [25].

In order to evaluate the aircraft's natural controllability without differential thrust or thrust vectoring, thrust is neglected for further estimations. The further the centre of gravity moves forward, the more difficult it becomes to pitch the aircraft up. In order for it to be controllable, the aircraft must be able to attain $C_m > 0$ even at its most forward centre of gravity position.

$$x_{cg} > \frac{1}{C_{L_{fwd}} + C_{L_{rear}} \frac{S_{rear}}{S_{fwd}} \left(\frac{V_r}{V}\right)^2} \Bigg\{ C_{L_{fwd}} x_{ac_{fwd}} + C_{D_{fwd}} z_{cg_{fwd}} - C_{m_{ac_{fwd}}} \bar{c}_{fwd}$$
$$- \left(\frac{V_r}{V}\right)^2 \frac{S_{rear}}{S_{fwd}} \left(-C_{L_{rear}} x_{ac_{rear}} - C_{m_{ac_{rear}}} \bar{c}_{rear} + C_{D_{rear}} z_{cg_{rear}}\right) \Bigg\} \tag{11.4}$$

The limit of controllability is the trim condition where $C_m = 0$.

$C_{L_{fwd}}$ can be influenced by installing mobile surfaces on the trailing edge of the front wing. The distributed rotors would increase their effectiveness and help to achieve higher magnitudes of C_L. These mobiles surfaces are elevators (with elevator deflection δ_e) which increase the control authority over the aircraft.

The limiting factor for static open-loop stability is at high velocities. Hence, the aircraft must be statically stable at cruise where the highest velocity is achieved.

In order to estimate the stability properties of the design, for a step disturbance in the angle of attack α, the moment equation seen in Equation 11.1 is differentiated w.r.t. to α leading to:

$$C_{m_\alpha} = \partial C_m/\partial\alpha = -C_{D_{\alpha_{fwd}}} \cdot \frac{z_{cg_{fwd}} S_{fwd}}{S\bar{c}} + C_{L_{\alpha_{fwd}}} \cdot \frac{(x_{cg} - x_{ac_{fwd}})S_{fwd}}{S\bar{c}}$$
$$+ C_{D_{\alpha_{rear}}} \cdot (1 - \frac{\partial\epsilon}{\partial\alpha}) \cdot \frac{z_{cg_{rear}} S_{rear}}{S\bar{c}} \left(\frac{V_r}{V}\right)^2 - C_{L_{\alpha_{rear}}} \cdot (1 - \frac{\partial\epsilon}{\partial\alpha}) \cdot \frac{(x_{ac_{rear}} - x_{cg})S_{rear}}{S\bar{c}} \left(\frac{V_r}{V}\right)^2 \quad (11.5)$$

where $\frac{\partial\epsilon}{\partial\alpha}$ is the downwash effect felt by the rear wing. The latter can be estimated using Equation 11.6 from [95] (with the addition of η_ϵ).

$$\frac{d\epsilon}{d\alpha} = \eta_\epsilon \frac{K_{\epsilon_\Lambda}}{K_{\epsilon_{\Lambda=0}}} \frac{C_{L_{\alpha_{fwd}}}}{\pi A R_{fwd}} \left\{ \frac{r}{r^2 + m_{tv}^2} \frac{0.4876}{\sqrt{r^2 + 0.6319 + m_{tv}^2}} + \left[1 + \left(\frac{r^2}{r^2 + 0.7915 + 5.0734 m_{tv}^2}\right)^{0.3113}\right] \cdot \left[1 - \sqrt{\frac{m_{tv}^2}{1 + m_{tv}^2}}\right] \right\} \quad (11.6)$$

where $m_{tv} = 2 \cdot v_t/b$ (where v_t is the vertical distance between the rear wing aerodynamic centre and the forward wing aerodynamic centre). An assumption was made based on the geometry of the aircraft that both wings are assumed to be perfectly straight, this results in v_t being equal to the maximum height of the fuselage. The parameter $r = 2 \cdot (x_{ac_{rear}} - x_{ac_{fwd}})/b_{fwd}$ (with b_{fwd} being the span of the forward wing) and K_{ϵ_Λ} is a function of the quarter chord sweep angle $\Lambda_{c/4}$ of the forward wing [95].

The factor η_ϵ is a correction factor applied to the downwash gradient to better match the results obtained using the lifting line theory (see Section 7.3.2). Figure 11.2 shows an exemplary sensitivity analysis of the downwash gradient, which reveals that Equation 11.6 overestimated the downwash gradient by roughly a factor of 2. Therefore, it is set that $\eta_\epsilon = 0.5$.

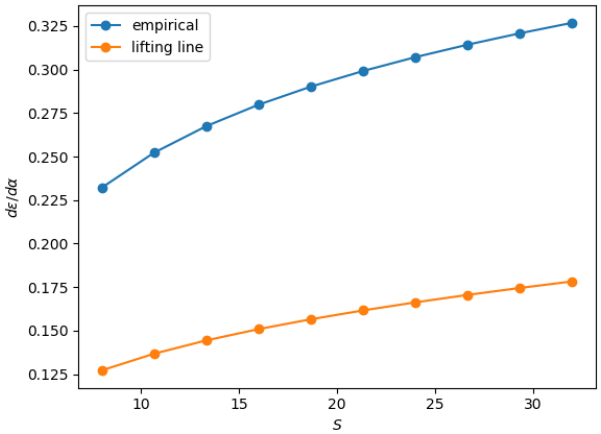

Figure 11.2: Variation of the downwash gradient of the front wing on the rear wing with changing total wing surface are (where the ratio of wing areas is kept constant). Both results obtained using Equation 11.6 and lifting-line theory are displayed.

Furthermore, for propeller aircraft, an additional downwash is created due to the propellers which has to be taken into account. This is written as follows [95]:

$$\left(\frac{d\epsilon}{d\alpha}\right)_p = 6.5(sin(6\phi))^{2.5} \cdot \left(\frac{\rho \cdot P_{br}^2 \cdot S_{fwd}^3 \cdot C_{L_{fwd}}^3}{l_h^4 \cdot W^3}\right)^{1/4} \quad (11.7)$$

where ϕ is the angle between the wings defined as $\phi = arcsin(m_{tv}/r)$, P_{br} is the shaft power per engine and $C_{L_{fwd}}$ is the lift coefficient for the cruise condition.

It is now essential to estimate the drag derivatives
C_{D_α} using the polar drag equation leading to:

$$C_{D_{\alpha_i}} = 2 \cdot C_{L_{\alpha_i}} \frac{C_{L_i}}{\pi A R_i e_i} \tag{11.8}$$

with C_{L_i} being the lift coefficient of one of the wings in cruise condition.

For static longitudinal stability $C_{m_\alpha} < 0$ (such that the aircraft restores its initial state after a disturbance in angle of attack). This hence results in the neutral stability CG position curve as follows:

$$x_{cg} = \left(\frac{C_{L_{\alpha_{fwd}}} x_{ac_{fwd}} + C_{D_{\alpha_{fwd}}} z_{cg_{fwd}} + (C_{L_{\alpha_{rear}}} \frac{x_{ac_{rear}} S_{rear}}{S_{fwd}} - C_{D_{\alpha_{rear}}} z_{cg_{rear}})(1 - \frac{\partial \epsilon}{\partial \alpha}) \left(\frac{V_r}{V}\right)^2}{C_{L_{\alpha_{fwd}}} + C_{L_{\alpha_{rear}}} \frac{S_{rear}}{S_{fwd}} (1 - \frac{\partial \epsilon}{\partial \alpha}) \left(\frac{V_r}{V}\right)^2} \right) \tag{11.9}$$

11.1.3. Ground

For stability and controllablity on the ground, two criteria were used: the maximum turn-over angle and the minimum load on the steering wheels. The former requires that the centre of gravity of the aircraft must be located at an angle of 55 degrees above the line connecting the nose wheels and the rear wheels. This criterion was originally proposed for tricycle landing gears in [94], but was extended to quadricycle landing gears as shown in Figure 11.3.

The purpose of this requirement is to avoid the the eVTOL tipping over to the side while taxiing. The load criterion on the steering wheels (which are the nose wheels in the case of the Wigeon) is related to controllability [94]. It requires that at least 8% of the total aircraft weight must rest on the steering wheels for them to achieve their function.

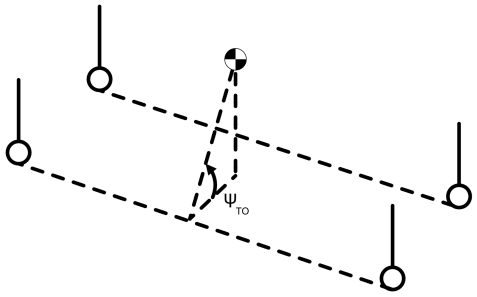

Figure 11.3: Definition of the turn-over angle for a quadricycle landing gear.

11.2. Design for Stability and Controllability

With the criteria for stability and controllability established, it was investigated how to incorporate them in the design.

11.2.1. Centre of Gravity Excursion

The stability and controllability properties of the eVTOL are very sensitive to the location of the centre of gravity. This location depends on the positioning of the aircraft components (which make up the operational empty weight), as well as the loading state. Figure 11.4 shows the so-called loading diagram, which illustrates the movement of the centre of gravity location during the loading and boarding of the aircraft. The eVTOL must be stable and controllable on the ground and in the air for any centre of gravity within this range, such that it can be flown with different loading configurations. With only 7 cm, the range of centre of gravity is very small. This is due to the passengers, which make up the largest portion of the payload, being located close to the centre of gravity. Furthermore, the use of batteries means that neither the mass nor the centre of gravity location change during refuelling.

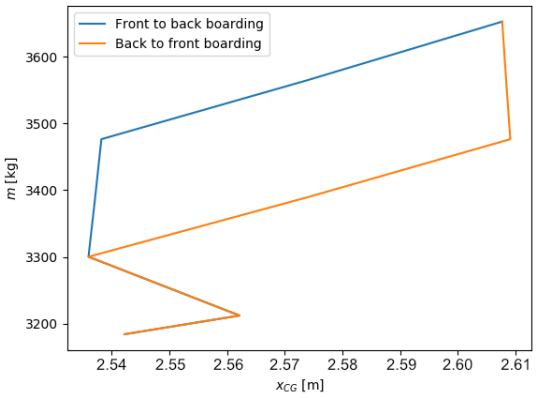

Figure 11.4: The loading diagram of the eVTOL, showing the change of the centre of gravity x-position as a function of the loading state (origin at the nose, x-axis pointing aft). The assumed order of loading in this case is first luggage, then the pilot, and finally the passengers. Two alternative boarding patterns are shown: back to front and front to back.

11.2.2. Relative wing sizing and placement

As Equation 11.9 shows, the location of the neutral point and thus static longitudinal stability in cruise depends strongly on the geometry and positioning of the wings. More specifically, it depends on the ratio of wing surfaces S_{rear}/S_{fwd}, $x_{ac_{fwd}}$, $x_{ac_{rear}}$, $z_{cg_{fwd}}$, and $z_{cg_{rear}}$. Moreover, there are indirect geometric dependencies through other terms in Equation 11.9.

$C_{L_{\alpha_{fwd}}}$ and $C_{L_{\alpha_{rear}}}$ do not only depend on the C_{l_α} of their respective aerofoils (which were selected for aerodynamic efficiency in Section 7.2). Instead, they are given by Equation 7.14. From which it can be seen that C_{L_α} depends on wing aspect ratio, sweep and aerofoil lift slope. The last two were taken as fixed based on aerodynamic considerations elaborated in Section 7.1. Therefore, the aspect ratio AR remains as a free variable.

Another implicit geometric dependency of the neutral point location stems from the downwash gradient $\frac{\partial \epsilon}{\partial \alpha}$. As shown in Equation 11.6 and Equation 11.7, this parameter depends on the aspect ratio AR_{fwd}, span b_{fwd} and surface area S_{fwd} of the forward wing, and the horizontal and vertical distance between the wings (Δx and Δz, respectively). Note that Equation 11.9 neglects the impact of the upwash of the rear wing on the front wing. This was deemed an acceptable simplification as analysis using lifting line theory showed the upwash gradient to be an order of magnitude lower than the downwash gradient.

In addition to this, there are dependencies on the vertical wing positions, aspect ratios and cruise lift coefficients through the drag contributions. Finally, the term $(V_r/V)^2$ was taken as 1, which is the value suggested by Oliviero [93] for a high-mounted stabiliser. This was found to represent the tandem wing configuration best.

As for the forward CG limit for pitch controllability, similar geometric dependencies could be identified. Again, S_{rear}/S_{fwd}, $x_{ac_{fwd}}$, $x_{ac_{rear}}$, $z_{cg_{fwd}}$, and $z_{cg_{rear}}$ are directly included in the equation (Equation 11.4). However, this time, the only influence of the aspect ratio is on the drag coefficients of the wing, which is a small effect that makes controllability less dependent on aspect ratio. In addition to these, the length of the mean aerodynamic chords $\bar{c}_{fwd}$ and $\bar{c}_{rear}$, as well as the maximum increase in $C_{L_{fwd}}$ that the elevators can offer. This is discussed in more depth in Section 11.2.4.

A sensitivity study of the neutral point and controllability limit found that S_{rear}/S_{fwd} and AR_{fwd} were the most powerful parameters to affect the stability and controllability limits of the aircraft. The relative wing size strongly affects both stability and controllability, while the front wing aspect ratio mainly impacts stability. A_f is especially important since it not only impacts the lift slope of the front wing, but also the downwash which in turn impacts the rear wing.

Having identified these two key design variables allowed to plot the constraints affecting wing placement and sizing as contour lines in a 2D plot with S_{rear}/S_{fwd} on one axis and AR_{fwd} on the other. Such a plot

can be seen in Figure 11.5. Note that the total wing area was kept constant as to not affect the lift of the aircraft in cruise.

The plot shows that a small aspect ratio on the front wing is required for longitudinal stability. This implies an increase in induced drag. Also, since the root chord is limited in order to not interfere with other elements of the aircraft, the small aspect ratio would require a short wingspan. The consequent reduction in the space available for rotors on the front wing could mean that rotors would have to be relocated from the front wing to the back wing, meaning that the front rotors would have to perform at a higher throttle setting in hover than the rear engines. Reducing the number of engines on the front wing could also have a negative impact on control redundancy in hover. The outcome of this analysis agrees with the results from [16], who found that reducing the aspect ratio of the front wing in a tandem-wing eVTOL aircraft to 25% of the rear wing could allow it to be longitudinally stable.

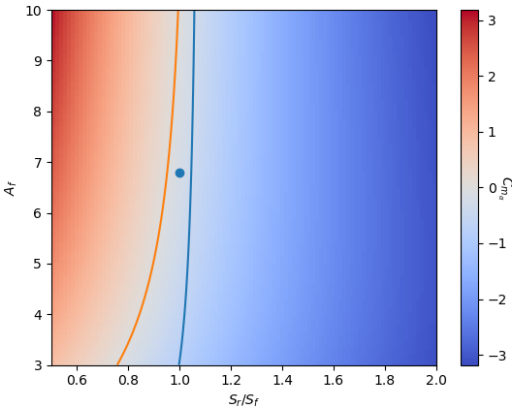

Figure 11.5: Heat map showing C_{m_α} as a function of the front wing aspect ratio and the ratio between wing surface areas. The orange line indicates the limit for static longitudinal stability, while the blue line indicates the limit for pitch controllability at stall. The blue line denotes the design point of the Wigeon.

11.2.3. Landing gear placement

The placement of the landing gear was very restricted in the design of the Wigeon aircraft due to crashworthiness considerations that dictate that no stiff structure shall be located directly below human occupants. Therefore, the rear landing gear was placed far aft behind the passenger cabin (at 4.76 m from the nose) and the traditional single nose gear was replaced by two gears (at 1.36 m from the nose) to be able to place them next to the pilot rather than below.

With this configuration in mind, the ground stability and controllability of the Wigeon were evaluated based on the criteria outlined in Section 11.1.3, as well as three additional criteria: clearance of the wings when they are vertical, clearance of the rotors when the wings are horizontal, and the maximum tip-back angle. The last two requirements are common in conventional aircraft, but would only be relevant for emergency situations for the Wigeon. This is because in a conventional mission, it would land vertically with the rotors oriented upwards. However, it was chosen to design the landing gear to tolerate a landing with wings in horizontal configuration on a regular airfield. This could allow for a safe landing if the rotation mechanism of one or both wings should fail during cruise.

The critical requirement for clearance was found to be the root chord of the wing when in vertical position. This dictates the required height of the landing gear. The track width of the landing gear is determined by the turn-over requirement. The corresponding equations are Equation 11.10 and Equation 11.11. Note that it was chosen to use the same track width for the front and rear wheels. This is because reducing the track width in one of them would have required an increase in the other in order to satisfy the turn-over requirement. Therefore, this design minimises the maximum track width.

$$\tan(\psi_{to}) = \frac{z_{cg} + h_{lg}}{tw/2} \qquad (11.10) \qquad \tan(\phi_{cl}) = \frac{\tan(\Gamma) y_{rot} + h_{lg} + z_f - r_{rot}/2}{y_{rot} - tw/2} \qquad (11.11)$$

Here, ψ_{to} is the turn-over angle, z_{cg} is the z-location of the aircraft's centre of gravity, h_{lg} is the height of the landing gear, tw is the track width of the landing gear, ϕ_{cl} is the clearance angle, Γ is the front wing's dihedral, y_{rot} is the spanwise location where the wing rotates, z_f is the z-location of the front wing root chord, and r_{rot} is the maximum length of the chord behind the rotation point (i.e., radius of the circle traced by the trailing edge of the front wing when rotating). In order to increase the clearance for the rotated wing, z_f was decreased 10 cm compared to its real value (leading to a 10 cm higher landing gear).

Solving these two equations for h_{lg} and tw with the recommended values $\psi_{to} = 55$ degrees and $\phi_{cl} = 5$ degrees from [94] and applying the additional 10 cm clearance yields a landing gear height of 0.9278 m and

a track width of 2.220 m. The track width is therefore 0.8400 m wider than the fuselage, meaning that the landing gear must be deployed 0.4200 m outboard of the fuselage.

11.2.4. Vertical tail and control surface design

In the previous steps of the project, it was found that the tandem wing was unstable in the lateral direction and hence required a vertical tail. In this section the various steps to size the vertical tail and the various control surfaces are performed. First, all the required estimations are performed for the vertical tail. Secondly, control surfaces are sized accordingly to ensure optimal control authority over all the different degrees of freedom of the aircraft.

Vertical tail and rudder sizing

This section presents the different required steps to size of the vertical tail, in terms of its required surface area, starting from an initial estimate obtained using a Class I method. This is followed by a stability requirement and finally a controllability requirement derived from a OEI condition. The highest value obtained from either the stability or controllability requirement is chosen as the final design.

In order to initialise the analysis and sizing, a so-called class I method [110] is used. This method assumes a vertical tail volume coefficient $\bar{V}_v$ which yields an equation for the tail area S_v being as follows:

$$S_v = \bar{V}_v \cdot \frac{Sb}{l_v} \tag{11.12}$$

where l_v is the vertical tail moment arm as $l_v = (x_v - x_{cg})$. A value of 0.04 for the volume coefficient is chosen using values found in [110]. Furthermore, it is assumed that the vertical tail is placed at the end of the fuselage. Due to the assumed small size of the vertical tail w.r.t. to the fuselage length, l_{fus}, this results in initial estimate for the aerodynamic centre of the vertical tail to be $x_v \approx l_{fus}$. Additionally, an estimate of the root chord, c_{v_r}, must be performed from the surface area and taper ratio λ_v. Furthermore, b_v is the vertical tail span which can be obtained from $b_v = \sqrt{AR_v \cdot S_v}$. An assumed aspect ratio value is hence necessary and is a design variable. This value is initially assumed to be 1.25, chosen using [110] and later its sensitivity to S_v and b_v is verified in order to find a more optimal value. Furthermore, another design variable is the TE (trailing edge) sweep angle, $\Lambda_{v_{TE}}$ which is also wished to be maximised or optimised (in order to increase the effective moment arm l_v and in order to have rudder outside the wake of the rear wing as much as possible). The final design variable is the taper ratio, λ_v, chosen to be 0.4 in order to obtain an approximated elliptical side force distribution. With these design variables, it is possible to compute the required aerodynamic and geometric properties starting from the MAC and the root chord using Equation 7.4 and Equation 7.1 respectively.

Having the obtained the initial values, a more accurate estimate of the moment arm, l_v, can be done by using the x-and y-positions of the LEMAC of the vertical tail (which are a function of the TE sweep), assuming that the root chord is entirely on the fuselage and finally that the aerodynamic centre is at quarter-chord of the MAC. The moment arm becomes:

$$l_v = l_{fus} - c_{v_r} + X_{LEMAC_v} + 0.25 \cdot \bar{c}_v \tag{11.13}$$

It is now possible to present the two different requirements that the vertical tail must satisfy.
Having initialised the vertical tail design, the stability requirement must be specified. In fact, in order to have lateral static stability it must hold that: $C_{n_\beta} > 0$. This stability derivative has multiple components: the wing terms, the fuselage term and finally the vertical tail component.

First the wing contribution, for unswept wings (at quarter-chord) is derived using [102] and is as follows:

$$(C_{n_\beta})_w = C_L^2 \cdot \frac{1}{4\pi AR_w} \cdot \frac{S_w b_w}{Sb} \tag{11.14}$$

where the subscript w refers to one wing and C_L is the lift coefficient at cruise. The second required terms for the computation of C_{n_β} is the fuselage term estimated using [21] with Equation 11.15 and Equation 11.16:

$$(C_{n_\beta})_{fus} = -\frac{2\nu}{Sb} \quad (11.15) \qquad \nu = \int_0^{l_{fus}} \frac{\pi}{4} \cdot w(x)^2 dx \quad (11.16)$$

where ν is the effective volume of the fuselage and $w(x)$ is the width as a function of the longitudinal position x starting from the nose. This are approximated with an elliptical shape resulting in $w(x) = (w_{max}/2) \cdot \sqrt{1 - \left(\frac{x}{l_{fus}/2}\right)^2}$.

The third term is related to the vertical tail as follows:

$$(C_{n_\beta})_v = -C_{Y_{v_\alpha}} \cdot \left(1 - \frac{d\sigma}{d\beta}\right) \cdot \left(\frac{V_v}{V}\right)^2 \cdot \frac{S_v l_v}{Sb} \quad (11.17)$$

where $(C_{Y_{v_\alpha}})_v$ is the derivative of the side force coefficient C_Y (of the vertical tail) w.r.t α. This derivative is basically negative C_{L_α} of the vertical tail. σ is the side wash (assumed to be 0 for simplicity) and V_v is the velocity of the airflow at the vertical tail (assumed to be equal to the aircraft airspeed as the flow would be undisturbed due to the height difference between the wings). The final equation relating to the stability requirement for S_v can be derived and results in Equation 11.18.

$$S_v = \frac{(C_{n_\beta} - (C_{n_\beta})_{fus} - (C_{n_\beta})_{w,rear+fwd})}{C_{L_{v_\alpha}}} \cdot \frac{Sb}{l_v} \quad (11.18)$$

where C_{n_β} is taken to be 0.0571 in order to provide a sufficient stability margin as found in [36] and to account for the previously defined assumptions.

For the controllability condition, the vertical tail should provide a sufficient counter-acting yaw moment for an asymmetric thrust condition.

In order to obtain a reasonable estimate, several design variables must be identified being the maximum rudder deflection $\delta_{r_{max}}$, the span and chord ratio of the rudder and the vertical tail $\frac{b_r}{b_v}$ and $\frac{\bar{c}_r}{\bar{c}_v}$ respectively and the minimum controllable speed V_{MC}. These were estimated using [89] and can be summarised in Table 11.1.

Table 11.1: Lateral design variables.

Design variable	Value/Range
$\delta_{r_{max}}$ [°]	25
b_r/b_v [-]	0.7-1.0
$\bar{c}_r/\bar{c}_v$ [-]	0.15-0.4
V_{MC}/V_{stall} [-]	1.2

For the geometric parameters such as $\frac{b_r}{b_v}$ and $\frac{\bar{c}_r}{\bar{c}_v}$, a sensitivity analysis towards S_v is performed in order to verify the most optimal pair of values for the lowest area.

Additionally, the same is performed for a combination of $\Lambda_{v_{TE}}$ and AR_v.

For the controllability requirement, the vertical tail and rudder must be sized in such a manner that an OEI condition can be controlled, where the OEI is defined in this section as losing all engines from one side of the aircraft. The created yaw moment due to an asymmetric thrust condition can be computed using Equation 11.19 to Equation 11.21 [36]:

$$N_a = N_E + N_D \quad (11.19) \qquad N_E = 2\sum_i^n \frac{T}{n_E} y_i \quad (11.20) \qquad N_D \approx 0.25 \cdot N_E \quad (11.21)$$

where N_E is the sum of the individual asymmetric yaw moments due to an asymmetric thrust per engine T/n_E, with a moment arm y_i and finally n being the number of engines on one half-wing. N_D is the yaw moment due to the drag of the engine (which for variable pitch propellers is a quarter of N_E [36]) and n_E is the number of propellers.

It is now possible to show the yaw moment equilibrium equation which relates to the lateral trim condition obtained with Equation 11.22 and Equation 11.23 [89]:

$$N = N_0 + N_a + N_{\delta_r} \cdot \delta_r + N_\beta \cdot \beta + N_{\delta_a} \cdot \delta_a = 0 \quad (11.22) \qquad C_{n_{\delta_r}} = -C_{L_{v_\alpha}} \cdot \frac{S_v l_v}{Sb} \cdot \tau_r \cdot \frac{b_r}{b_v} \quad (11.23)$$

with $N_0 = 0$ as the vertical tail has a symmetric airfoil, $C_{n_{\delta_r}}$ is the yaw control derivative w.r.t rudder deflection and τ_r being the rudder effectiveness which is as follows [89]:

$$\tau_r = 1.129 \cdot \left(\frac{\bar{c}_r}{\bar{c}_v}\right)^{0.4044} - 0.1772 \quad (11.24)$$

Assuming that the aircraft is not slipping ($\beta = 0$) and no aileron deflection is applied ($\delta_a = 0$), an equation for S_v can be obtained. The aforementioned is as follows:

$$S_v = \frac{N_a}{0.5\rho V_{MC}^2 \cdot C_{L_{v_\alpha}} \cdot l_v \cdot \tau_r \cdot (b_r/b_v) \cdot \delta_r} \quad (11.25)$$

Having derived the stability and controllability limits for S_v with Equation 11.18 and Equation 11.25, the limiting case must be identified and as a result the highest value obtained from both equations is used for the final design.

It is now possible to find the sensitivity of the surface area S_v and the span b_v for the set of design variables and in the same time find an optimal value. First, the $\Lambda_{v_{TE}}$ with AR_v pair is selected as can be seen in Figure 11.6.

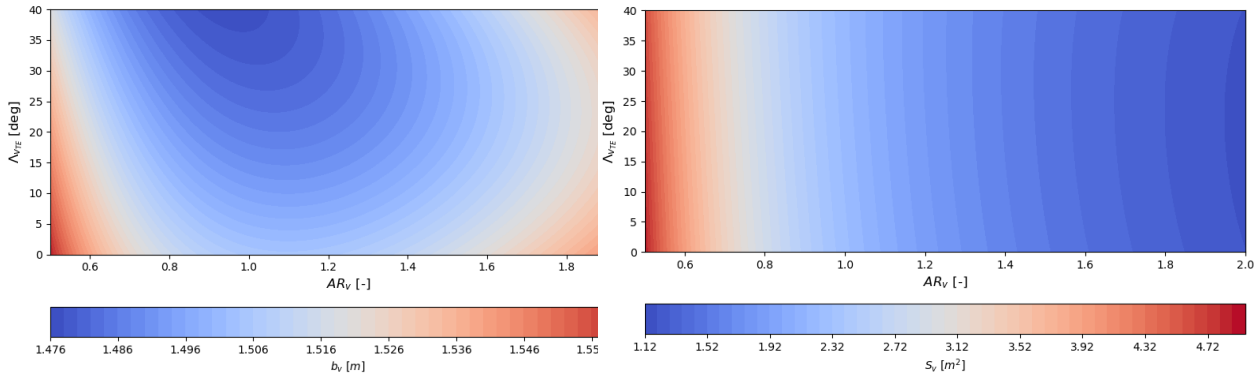

(a) Sensitivity of the vertical tail span, b_v as a function of $\Lambda_{v_{TE}}$ with AR_v.

(b) Sensitivity of the vertical tail span, S_v as a function of $\Lambda_{v_{TE}}$ with AR_v.

Figure 11.6: Sensitivity analysis of both b_v and S_v parameters.

It can be easily seen, that S_v has a very low sensitivity to the sweep angle, whereas it decreases with increases AR_v. The span, b_v, on the other hand has a localised minimum around $(AR_v = 1.05, \Lambda_{v_{TE}} = 39°)$. It is therefore necessary to find a compromise between both the surface area and the span, and it must be noted that the larger the span and sweep, the larger the required structure to support it, which increases the mass. It is hence decided that an AR_v of 1.4 and a TE sweep of 25 ° is the most optimal when taking into account all the aforementioned. Finally, it is now possible to select the required $\frac{b_r}{b_v}$ and $\frac{\bar{c}_r}{\bar{c}_v}$ in order to match the both the controllability and stability (represented as a black contour line) requirements and can be seen in Figure 11.7.

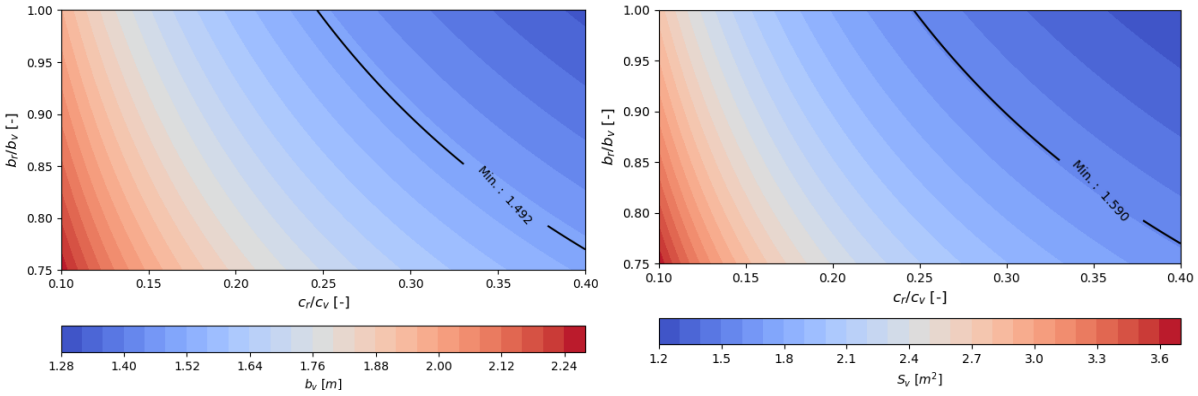

(a) Sensitivity of the vertical tail span, b_v as a function of $c\frac{b_r}{b_v}$ and $\frac{\bar{c}_r}{\bar{c}_v}$, for the selected aspect ratio and sweep.

(b) Sensitivity of the vertical tail span, S_v as a function of $\frac{b_r}{b_v}$ and $\frac{\bar{c}_r}{\bar{c}_v}$, for the selected aspect ratio and sweep.

Figure 11.7: Sensitivity analysis of both S_v and b_v for the controllability design variables and the stability requirement.

From Figure 11.7, it can clearly be seen that both variables are sensitive and affected in the same manner by the design variables. Therefore, to provide the most optimum values in terms of stability and to provide less stress to the vertical tail, the values are taken to be: $\frac{b_r}{b_v} = 1.0$ and $\frac{\bar{c}_r}{\bar{c}_v} = 0.24$.

Finally, following the S_v estimation it is possible to estimate all geometric properties of the vertical tail and rudder. These can be visualised in Figure 11.8.

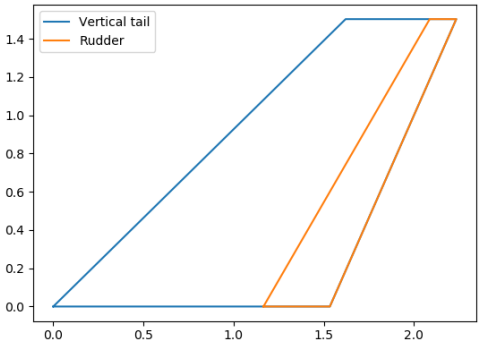

Figure 11.8: Visualisation of the vertical tail and rudder with geometrical properties $b_v = 1.503$ m, root chord $c_{v_r} = 1.534$ m and tip chord $c_{v_t} = 0.613$ m.

Elevator Sizing

The elevator is an essential control surface for pitch control authority, especially it is vital at low speeds as it is the limit of controllability. As it was done for previous control surfaces, it is required to assume a range for a set of design variables in order to obtain the best elevator sizing possible (that can be found in [90]). Additionally, upon further scrutiny of both the aileron and elevator sizing, the pitching control surface will be an elevon placed on both the forward and rear wings, working in a similar manner to an aileron but for pitch control. The choice of designing a simple elevator or an elevon was verified by checking what are the required geometric properties for pitch control at the lowest speed and it was found that high span ratio values were needed. It was noted that a certain increase in $C_{L_{fwd}}$ and a decrease in $C_{L_{rear}}$ are needed in order to obtain a feasible CG range. This ensures not only that the aircraft can be trimmed at stall, but also that the elevators can be utilised to control the aircraft in all other horizontal flight conditions. The general lift coefficient equation can be seen in Equation 11.26. The previously described required increase in lift coefficient, caused by the elevator deflection, can be identified and re-written in Equation 11.27.

$$C_{L_i} = C_{L_{\alpha_i}} \cdot \alpha + C_{L_{\delta_{e\,i}}} \cdot \delta_e \tag{11.26}$$

$$\Delta C_{L_i} = \pm C_{L_{\delta_{e\,i}}} \cdot \delta_e \tag{11.27}$$

Where $C_{L_{\delta_{e\,i}}}$ is the control derivative of one of the lift coefficients w.r.t a deflection input. It can be observed that for the rear wing, the required change in lift coefficient is negative whereas for the forward a positive change is required to obtain better pitching up capability. The control derivative can estimated using Equation 11.28 [90] with an additional derived correction factor to account for the fuselage width clearance:

$$C_{L_{\delta_{e\,i}}} \approx \tau_e \cdot \frac{b_e}{b_i} \cdot C_{L_{\alpha_i}} \tag{11.28}$$

where τ_e is the elevator effectiveness which can also be computed using Equation 11.34, where the ratio to be used is S_e/S_i. It must be also noted that the aircraft's control derivative $C_{L_{\delta_e}}$ is different from the above. However, this aircraft derivative is not required as the elevator is designed for a specific increase and decrease in the forward and rear lift coefficient, respectively, and not for the entire aircraft. It can therefore be possible to optimise for the best set of S_e/S_i and b_e/b_i, where a special attention must be placed on the chord ratio as well in order to minimise the impact on the wing box. As a last note, a clearance w_{clear} of 0.5 m is taken in order to account for a local fuselage width of 1 m.

Finally, the elevators must be able to trim and allow for a pitching up moment at stall which can be translated to $C_m > 0$. Using Equation 11.1, it can be seen that the moment coefficient is a function of both lift coefficient and hence by extension the elevator deflection δ_e and the respective wing control derivatives. In order to affect as less as possible the flow of the rear wing, a maximum elevator deflection of 10° is chosen (which is smaller than what can be found in [90]). The sensitivity analysis of the pitching moment coefficient w.r.t S_e/S_i, $\bar{c}_e/\bar{c}_i$ and the elevator span ratio b_e/b_i can now be performed and visualised in Figure 11.9.

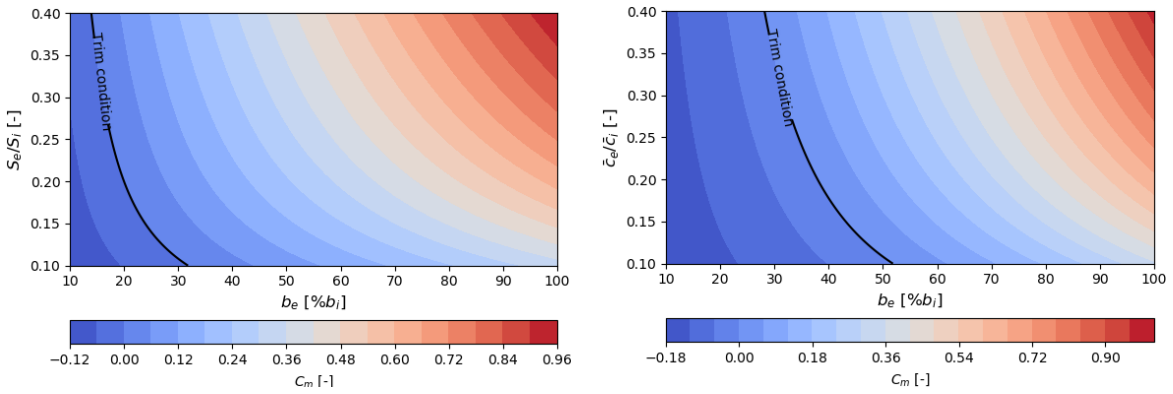

(a) Sensitivity of C_m as a function of area ratio $\frac{S_e}{S_i}$ and b_e in percentages of wing span b_i.

(b) Sensitivity of C_m as a function of $\frac{\bar{c}_e}{\bar{c}_i}$ and b_e in percentages of wing span b_i.

Figure 11.9: Sensitivity of the pitching moment coefficient w.r.t. S_e/S_i, $\bar{c}_e/\bar{c}_i$ and b_e for a maximum elevator deflection of $\delta_e = 10°$.

A similar pattern is observed for both the area and chord ratio design variables due to their geometric relationship. However, it can be noticed that the moment coefficient is slightly more sensitive to the chord ratio showing a smaller design space. For the elevon wingspan ratio, a value of $\frac{b_e}{b_i} = 0.868$ is selected due to the fuselage clearance constraint. The outer limit of the elevator is placed at 99% of the wing's span in order to ensure good roll control when designing the ailerons. As it was previously mentioned, the limiting design variable is the chord ratio which is selected to be $\frac{\bar{c}_e}{\bar{c}_i} = 0.25$. In the same manner as for the rudder, the selected design ratios can be multiplied by the wing geometric properties in order to obtain the elevator size.

Aileron sizing

In order to design and size the ailerons, the roll rate requirement for small aircraft is needed. The aircraft must be able to roll faster or at the same rate as demanded by regulations. This involves a combination of the airfoil aerodynamics, wing geometry and finally a control derivative estimation.

As a first step, some design variables must be identified and defined. These are: the aileron-wing surface and span ratio, S_a/S_i and b_a/b respectively and the maximum aileron deflection $\delta_{a_{max}}$. The aileron span is found by assuming the inner and outer positions, b_1 and b_2 respectively, leading to $b_a = b_2 - b_1$ as can be seen in Figure 11.10. The chosen values and ranges of the geometric parameters are summarised in Table 11.2 as seen in literature [116].

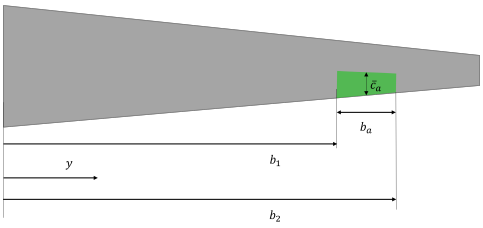

Figure 11.10: Aileron geometry, position w.r.t the wing and coordinate y used.

Table 11.2: Aileron design variables.

Design variable	Value/Range
$\delta_{a_{max}}$ [°]	± 30
$b_2/(b_i/2)$ [-]	0.70-0.95
S_a/S_i [-]	0.05-0.2

Due to the elevon wingspan and relative position on both wings, $b_2 = 0.99 \cdot b_i/2$.The outer position of the aileron is hence slightly higher than as it can be found in Table 11.2. A maximum deflection of $\delta_{a_{max}} = \pm 30°$ is assumed. Furthermore, a particular attention must be noted on the range of S_a/S_i (which can be seen in Table 11.2), as for conventional aircraft the typical range is 0.05-0.1 [116]. This difference is taking into account the tandem wing nature of Wigeon, hence S_i can reach values that are less than half the value of the total area S. This hence explains the higher maximum limit set for the surface ratio and the lower limit for the inner limit.

Having defined the necessary geometric properties, the physical problem can be explained. Due to its relatively small mass, the aircraft must be able to roll 60 ° in 1.3 s [92]. This is further confirmed for V/STOL aircraft in [62], where the requirement is slightly lower. For this the following equilibrium equation for steady roll is used:

$$\mathcal{L} = \mathcal{L}_\beta \cdot \beta + \mathcal{L}_p \cdot \frac{pb}{2V} + \mathcal{L}_{\delta_r} \cdot \delta_r + \mathcal{L}_{\delta_a} \cdot \delta_a = 0 \tag{11.29}$$

where p is the roll rate and for a pure roll $\beta = 0$ and no deflection in rudder is used $\delta_r = 0$. The latter with the regulation requirement yield the following:

$$p = -\frac{2V}{b} \cdot \frac{C_{l_{\delta_a}}}{C_{l_p}} \cdot \delta_{a_{max}} \geq \pm \frac{60 \cdot \pi/180}{1.3} \tag{11.30}$$

with V being the slowest speed at which a controlled roll manoeuvre can be performed which is assumed to be V_{MC}. It is further assumed that the wing is straight. This assumption is supported by the fact that the sweep at quarter-chord is 0 and due to that the wing is approximately straight. It is now possible to estimate two required derivatives, $C_{l_{\delta_a}} = \frac{dC_l}{d\delta_a}$ and $C_{l_p} = \frac{dC_l}{d\frac{pb}{2V}}$, obtained using simple strip theory[21, 108, 62]. These can be found using Equation 11.31 [116] and Equation 11.32 [108].

$$(C_{l_{\delta_a}})_i = -\frac{C_{L_{\alpha_i}} \tau_a c_{r_i}}{S_i b_i} \left[\frac{y^2}{2} + \frac{2}{3} \frac{\lambda_i - 1}{b_i} y^3 \right]_{b_2}^{b_1} \tag{11.31}$$

$$(C_{l_p})_i = -\frac{(C_{l_{\alpha_i}} + C_{d_{0_i}}) c_{r_i} b_i}{24 \cdot S_i} (1 + 3\lambda_i) \tag{11.32}$$

where C_{l_α} and C_{d_0} are lift curve slope and zero lift drag coefficient of the wing airfoil and i refers to either the forward or rear wing. It must be noted that in order to obtain the aircraft's $C_{l_{\delta_a}}$ and C_{l_p}, a correction factor which accounts for the different wing sizes has to be implemented. This is due to the definition of

the aircraft's roll moment coefficient C_l as:

$$C_l = \frac{\mathcal{L}_{fwd} + \mathcal{L}_{rear}}{0.5\rho V^2 \cdot Sb} = C_{l_{fwd}} \cdot \frac{S_{fwd} b_{fwd}}{Sb} + C_{l_{rear}} \cdot \frac{S_{rear} b_{rear}}{Sb} \left(\frac{V_r}{V}\right)^2 \tag{11.33}$$

where b is the span of the entire aircraft defined previously in Equation 7.11. Finally, τ_a is the aileron effectiveness that can be estimated using Equation 11.34 [116].

$$\tau_a = -6.624 \cdot \left(\frac{S_a}{S_i}\right)^4 + 12.07 \cdot \left(\frac{S_a}{S_i}\right)^3 - 8.292 \cdot \left(\frac{S_a}{S_i}\right)^2 + 3.295 \cdot \left(\frac{S_a}{S_i}\right) + 0.004942 \tag{11.34}$$

With all the aforementioned, it is now possible to proceed with the sizing procedure. This must ensure that Equation 11.30 is satisfied and with an assumed b_2 value, optimal values for S_a/S_i and b_1 can be obtained through a sensitivity analysis. Additionally, the aileron is constrained within the geometry of the elevon and this is evaluated as follows:

$$\frac{S_a}{S_i}(b_1) = \frac{1}{S_i} \frac{c_{a_t} + c_{a_r}(b_1)}{2} \cdot 2 \cdot b_a(b_1) \tag{11.35}$$

with c_{a_t} and c_{a_r} being the tip and root chords respectively. All the aforementioned can be visualised with Figure 11.11.

From Figure 11.11, it can be seen that both variables affect the roll rate of the aircraft in a similar manner. The intersection of the geometric constraint from Equation 11.35 and the roll requirement is the most optimum design for the aileron. This is found to be: $\frac{S_a}{S_i} = 0.115$ and $b_1 = 0.4703 \cdot b_{fwd}/2$.

The final elevon design can be be visualised (for the forward wing) in Figure 11.12.

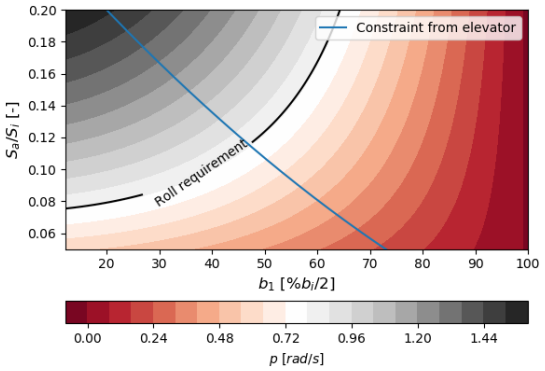

Figure 11.11: Sensitivity analysis of the roll rate, p, as a function of the surface ratio S_a/S_i and the inner dimension b_1.

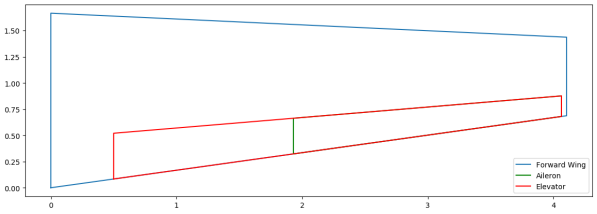

Figure 11.12: Elevon geometry visualisation for the forward wing.

11.2.5. Controllability in hover

As outlined in Section 11.1.1, the ACAI is a useful indicator to evaluate controllability of a multicopter vehicle in hover. With a CG location of 2.604 m behind the nose and a thrust-to-weight ratio of 1.5, the value of the ACAI is 667.7. Since this is positive, the Wigeon is controllable in hover. The value remains above zero if any of the engines fail, allowing the Wigeon to satisfy the OEI condition.

11.3. Dynamic Analysis

In this section, the dynamic behaviour of the aircraft is analysed, first by deriving a novel analytical model for the implementation of stability derivatives and secondly by implementing a state-space model.

11.3.1. Stability and control derivatives

An analytical model is derived for the tandem wing aircraft in order to show a novel preliminary method to estimate stability derivatives of the aerodynamic forces and moments X (forward force), Z (down force) and M (pitch moment) for longitudinal motions and Y (side force), $\mathcal{L}$ (roll moment) and N (yaw moment) for lateral motion. The state variables for longitudinal motion are: the dimensionless velocity perturbation $\hat{u}$, the angle of attack α, the pitch angle θ, and the dimensionless pitch rate $\frac{q\bar{c}}{V_0}$. In the case of lateral motion the state variables are: the side-slip angle β, the bank angle ϕ, the dimensionless roll and yaw rates $\frac{pb}{2V_0}$ and $\frac{rb}{2V_0}$ respectively. This method combines both known semi-empirical methods (that are adapted to account for a two-winged aircraft) and new physical derivations. The preliminary model is verified using stability derivatives obtained for other aircraft from [62].

Longitudinal aerodynamic forces

The corresponding longitudinal aerodynamic force coefficients C_X and C_Z are as follows:

$$C_X = C_L sin(\alpha) - C_D cos(\alpha) + C_T \quad (11.36) \qquad C_Z = -C_L cos(\alpha) - C_D sin(\alpha) + C_T i_T \quad (11.37)$$

with α being the angle of attack, C_T being the thrust coefficient defined previously and i_T being the effective incidence angle of the propeller total thrust force w.r.t to the stability axis system.

When estimating the dynamic stability behaviour of the aircraft, the main focus is on small disturbances that deviate the aircraft from its trim (equilibrium) condition. Due to the aforementioned the small angle approximation can be used for the angle of attack. This results in:

$$C_X \approx C_L\alpha - C_D + C_T \quad (11.38) \qquad C_Z \approx -C_L - C_D\alpha \quad (11.39)$$

The aerodynamic pitching moment coefficient, C_m, has already been derived and can be found in Equation 11.1.

Velocity stability derivatives

The first stability derivatives to be discussed in this section are the derivatives w.r.t $\hat{u} = \frac{\Delta V}{V_0}$, the change in initial velocity normalised by the initial velocity V_0 (in trim condition). The derivatives are hence C_{X_u}, C_{Z_u} and C_{m_u}. Using Equation 11.38, Equation 11.39 and Equation 11.1 and the transformation $\frac{d}{d\hat{u}} = M\frac{d}{dM}$, the equations are as follows:

$$C_{X_u} = \frac{M_0^2}{1-M_0^2} C_{L,0}\alpha_0 - 3C_{D,0} - 3C_{L,0} tan(\gamma_0) - M_0 C_{D_M} \quad (11.40)$$

$$C_{Z_u} = -\frac{M_0^2}{1-M_0^2} C_{L,0} - M_0 C_{D_M}\alpha_0 \quad (11.41)$$

$$C_{m_u} = M_0 \cdot \left[C_{L_{M_{fwd}}} \cdot (x_{cg} - x_{ac_{fwd}}) \cdot \frac{S_{fwd}}{S\bar{c}} - C_{L_{M_{rear}}} \cdot (x_{ac_{rear}} - x_{cg}) \cdot \frac{S_{rear}}{S\bar{c}} \left(\frac{V_r}{V}\right)^2 \right] + C_{T_{u_{fwd}}} \frac{z_{cg_{fwd}} S_{fwd}}{S\bar{c}} - C_{T_{u_{rear}}} \frac{z_{cg_{rear}} S_{rear}}{S\bar{c}} \left(\frac{V_r}{V}\right)^2 \quad (11.42)$$

where the subscript 0 relates to the initial equilibrium condition being the cruise condition, M_0 is the initial mach number, γ_0 is the initial flight path angle and finally $C_{L_{i_M}}$ and C_{D_M} are the lift and drag derivatives w.r.t mach number which account for compressibility effects. The latter drag term terms can be approximated to 0 compared to the lift term as the aircraft will fly in the subsonic incompressible regime. This also was already done for Equation 11.42 (which was derived by differentiating Equation 11.1 w.r.t $\hat{u}$), where the drag terms are neglected. The aforementioned C_{L_M} derivative and C_{T_u} were found in [21], where for the latter the constant power case was taken.

Angle of attack stability derivatives

The derivatives can be found in Equation 11.43 and Equation 11.44.

$$C_{X_\alpha} = C_{L_\alpha}\alpha_0 + C_{L,0} - C_{D_\alpha} + C_{T_\alpha} \qquad (11.43) \qquad C_{Z_\alpha} = -C_{L_\alpha} - C_{D_\alpha}\alpha_0 - C_{D,0} \qquad (11.44)$$

where it is assumed that thrust is not a function of the angle of attack leading to $C_{T_\alpha} = 0$. For C_{m_α}, the equation was already derived and can be found in Equation 11.5.

Pitch rate stability derivatives

A general estimate for the change in geometric angle of attack must be first done in order to estimate the required stability derivatives C_{Z_q} and C_{m_q} which effects are dominant during a pull-up manoeuvre. It is also essential to mention that the forward force term C_{X_q} is usually neglected as seen in both [62, 21], leading to $C_{X_q} \approx 0$.

For an idealised pull-up manoeuvre several aspects are assumed. First, the velocity V and the load factor n is assumed to be constant. Secondly, it is assumed that the aircraft motion follows a perfect circle with a radius R, assumed to be significantly larger than the size of the aircraft. The general situation can be portrayed in Figure 11.13.

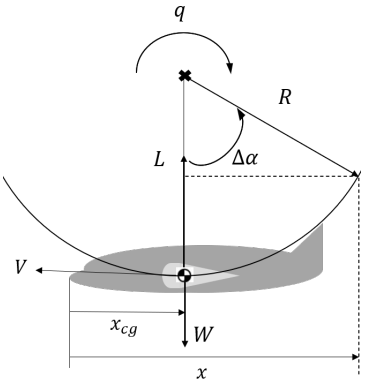

Figure 11.13: Simplified representation of an idealised pull-up manoeuvre with velocity V, radius R and pitch rate q for a generic aircraft.

The change in geometric angle of attack can be estimated by the following equation, where it has been assumed that as the radius R is significantly larger than the overall length of the aircraft, the small angle approximation can be used. Additionally, the radius R can be expressed as a function of the pitch rate q and velocity V with $R = V/q$. From the latter, Equation 11.45 can be rewritten into Equation 11.46.

$$\Delta\alpha \approx sin(\Delta\alpha) = \frac{x - x_{cg}}{R} \qquad (11.45)$$

$$\Delta\alpha = \frac{(x - x_{cg})}{\bar{c}} \cdot \frac{q\bar{c}}{V_0} \qquad (11.46)$$

Having derived the general equation for the change in angle of attack, it is now possible to estimate the stability derivatives of the down normal force and pitching moment defined as C_{Z_q} and C_{m_q} respectively.

For the latter, the approximation $C_Z \approx -C_L$ and the change in lift due to the pitch rate q can be used as seen in Equation 11.47.

$$\Delta C_L = -C_{L_{\alpha_{fwd}}} \cdot \frac{(x_{cg} - x_{ac_{fwd}})}{\bar{c}} \cdot \frac{S_{fwd}}{S} \cdot \frac{q\bar{c}}{V_0} + C_{L_{\alpha_{rear}}} \cdot \frac{S_{rear}(x_{ac_{rear}} - x_{cg})}{S\bar{c}} \left(\frac{V_r}{V}\right)^2 \cdot \frac{q\bar{c}}{V_0} \qquad (11.47)$$

The derivative can hence be identified which leads to:

$$C_{Z_q} \approx C_{L_{\alpha_{fwd}}} \cdot \frac{(x_{cg} - x_{ac_{fwd}})}{\bar{c}} \cdot \frac{S_{fwd}}{S} - C_{L_{\alpha_{rear}}} \cdot \frac{(x_{ac_{rear}} - x_{cg})}{\bar{c}} \cdot \frac{S_{rear}}{S} \left(\frac{V_r}{V}\right)^2 \qquad (11.48)$$

From the latter, the moment coefficient derivative is as follows:

$$C_{m_q} \approx -\left(C_{L_{\alpha_{fwd}}} \cdot \frac{S_{fwd}(x_{cg} - x_{ac_{fwd}})^2}{S\bar{c}^2} + C_{L_{\alpha_{rear}}} \cdot \frac{S_{rear}(x_{ac_{rear}} - x_{cg})^2}{S\bar{c}^2} \left(\frac{V_r}{V}\right)^2\right) \qquad (11.49)$$

Angle of attack rate stability derivatives

These stability derivatives are due to the time difference associated to the front wing downwash which affects the rear wing. The latter alters the lift force on the rear wing and hence also the pitching moment. These derivatives are defined with the dimensionless change of angle of attack $\frac{\dot{\alpha}\bar{c}}{V_0}$. The effect on the vehicle drag can be neglected [21], which leads to $C_{X_{\dot{\alpha}}} \approx 0$.

In order to find an analytical estimate of the rest of the derivatives, first the time difference that the flow takes between both wings can be approximated in Equation 11.50 and the downwash can hence be linearised and computed with Equation 11.51 [21].

$$\Delta t \approx \frac{(x_{ac_{rear}} - x_{ac_{fwd}})}{V_0} = \frac{l_w}{V_0} \qquad (11.50) \qquad\qquad \epsilon(t) \approx \left[\epsilon_0 + \frac{d\epsilon}{d\alpha} \cdot (\alpha - \dot{\alpha}\Delta t)\right] \qquad (11.51)$$

The additional lag term can be identified and accounted for with the aid of the product rule $\frac{d\alpha}{d\dot{\alpha}\bar{c}/V_0} = \frac{d\epsilon}{d\alpha}\frac{l_w}{\bar{c}}$ which leads to the following:

$$C_{Z_{\dot{\alpha}}} = -C_{L_{\alpha_{rear}}} \cdot \frac{S_{rear}}{S} \cdot \left(\frac{V_r}{V}\right)^2 \cdot \frac{d\epsilon}{d\alpha}\frac{l_w}{\bar{c}} \qquad (11.52)$$

$$C_{m_{\dot{\alpha}}} = -C_{L_{\alpha_{rear}}} \cdot \frac{S_{rear}}{S} \cdot \left(\frac{V_r}{V}\right)^2 \cdot \frac{d\epsilon}{d\alpha}\frac{l_w(x_{ac_{rear}} - x_{cg})}{\bar{c}^2} \qquad (11.53)$$

Side-slip stability derivatives

Now it is time to start with the lateral motions. For the latter, the derivatives of the side force Y, yaw moment N and roll moment $\mathcal{L}$ must be estimated for a small disturbance in side-slip angle β.

First, the dominant term to C_{Y_β} is from the vertical tail and can be estimated as follows:

$$C_{Y_\beta} \approx -C_{Y_{v_\alpha}} \cdot \left(1 - \frac{d\sigma}{d\beta}\right) \cdot \left(\frac{V_v}{V}\right)^2 \cdot \frac{S_v}{S} \qquad (11.54)$$

with the different lateral parameters being already defined in Section 11.2.4. The yaw moment derivative, C_{n_β}, was also already presented in the same section. The last stability derivative, C_{l_β} has multiple terms that depend on lift distribution, vertical tail position and wing characteristics (dihedral, quarter-chord sweep and lift curve slope) and position. These were obtained by combining a semi-empirical method from [102] for the wing contribution (corrected by a required factor which was already derived in the previous section) and an approximate analytical estimate due to the vertical tail. This is as follows:

$$C_{l_\beta} = \sum_{w=1}^{2}\left[-\frac{C_{L_{\alpha_w}}\Gamma_w}{4} \cdot 2/3\frac{1+2\lambda_w}{1+\lambda_w} - 1.2\frac{\sqrt{AR_w}Z_{wf}(l_{fus}+w_{fus})}{b_w^2}\right]\frac{S_w b_w}{Sb}\left(\frac{V_w}{V}\right)^2 + C_{Y_{\beta_v}} \cdot \frac{z_v}{b} \qquad (11.55)$$

The first term is the component for both wings and accounts for the wing and wing-fuselage interference. It was obtained from [102] and due to the dual-wing nature of the aircraft, it is averaged per wing with the term $\frac{S_w b_w}{Sb}$. Γ_w is the dihedral angle of the wing and Z_{wf} is the distance above the centre line of the wing. Indeed, a high wing has a negative contribution to the derivative, which hence is stabilising. The final component is due to the vertical moment arm, z_v, from the aerodynamic centre of the vertical tail to the CG of the aircraft. The latter assumes a small initial angle of attack, α_0.

Roll rate stability derivatives

The dimensionless roll rate $\frac{pb}{2V_0}$ stability derivatives are C_{Y_p}, C_{l_p} and C_{n_p}. In order to understand why all the lateral aerodynamic forces and moments change due to a roll rate, it can be understood by a change in the geometric angle of attack (as it was seen for the pitch rate). This change in angle of attack for the vertical tail can be estimated as $\Delta\alpha_v \approx \frac{pz}{V_0} = \frac{z}{b} \cdot \frac{pb}{2V_0}$ and for the wing it is $\Delta\alpha = \frac{2y}{b} \cdot \frac{pb}{2V_0}$.

First, for the side force derivative the dominant term is due to the vertical tail. Due to the 0.4 vertical tail taper ratio, the side force distribution can be approximated to be elliptical on the vertical tail. Hence, using [21], the equation is as follows:

$$C_{Y_p} \approx (C_{Y_p})_v = -\frac{8}{3\pi}\left(\frac{V_v}{V}\right)^2 \cdot \frac{b_v S_v}{bS} \cdot C_{L_{\alpha_v}} \qquad (11.56)$$

The second derivative is C_{l_p} and it is due to a span-wise change in the sectional lift distribution. It has already been estimated previously when sizing the aileron (see Section 11.2.4).

Finally, the yaw moment also changes with the roll rate and can be estimated with:

$$C_{n_p} \approx -\frac{l_v}{b} \cdot (C_{Y_p})_v - \frac{1}{8}\left(C_{L_{fwd,0}} \frac{S_{fwd} b_{fwd}}{Sb} + C_{L_{rear,0}} \frac{S_{rear} b_{rear}}{Sb} \left(\frac{V_r}{V}\right)^2\right) \tag{11.57}$$

where the first contribution is due to the vertical tail and the second one is due to the wings. Due to the angle of attack change, the sectional drag varies along the wing as $\Delta C_d = -(C_{l,0} + C_{d_\alpha}) \cdot \Delta\alpha \approx -C_{l,0} \frac{py}{b} \frac{pb}{2V_0}$. Hence this difference in the $X-$ force along the wing, when integrated over the whole span results in an induced yaw moment (using simple strip theory). An approximation of the integral associated to the tandem wing correction can be seen as the second term of Equation 11.57.

Yaw rate stability derivatives

The last set of stability derivatives are due to a yaw rate $\frac{rb}{2V_0}$, and are the following: C_{Y_r}, C_{l_r} and C_{n_r}. In the same manner as for a pitch rate, a yaw rate induces a change in the geometric angle of attack for all the aircraft's lifting surfaces. This change in angle of attack, is $\Delta\alpha_r = \frac{(x - x_{cg})r}{V_0}$.

With the aforementioned explained, it is now possible to find analytical equations for the three stability derivatives. In a similar manner than for the roll rate derivative, C_{Y_r} represents the change in side force due to an induced change in angle of attack, and its main contribution is due to the vertical tail. This can be written as:

$$C_{Y_r} = 2 \cdot C_{Y_{v_\alpha}} \cdot \frac{S_v l_v}{Sb} \cdot \left(\frac{V_v}{V}\right)^2 \tag{11.58}$$

The roll moment derivative follows from the previous equations and can be written as follows:

$$C_{l_r} = \frac{z_v}{b} \cdot C_{Y_r} + \frac{1}{4} \cdot \left(C_{L_{fwd,0}} \frac{S_{fwd} b_{fwd}}{Sb} + C_{L_{rear,0}} \frac{S_{rear} b_{rear}}{Sb} \left(\frac{V_r}{V}\right)^2\right) \tag{11.59}$$

where the first term is due to the vertical tail (assuming a small initial angle of attack) and the second term is related to the induced change in lift due to a yaw rate (equivalent to a change in angle of attack) which consequently creates a roll moment. The latter equation is an approximation of the integral from simple strip theory by assuming an elliptical distribution of lift over the wing.

The final stability derivative can be estimated using:

$$C_{n_r} = -\frac{l_v}{b} \cdot C_{Y_r} - \frac{1}{4} \cdot \left(C_{D_{fwd,0}} \frac{S_{fwd} b_{fwd}}{Sb} + C_{D_{rear,0}} \frac{S_{rear} b_{rear}}{Sb} \left(\frac{V_r}{V}\right)^2\right) \tag{11.60}$$

where a similar pattern emerges with the first term being due to the vertical tail and the second being an approximation using simple strip theory of the wing contributions.

Control derivatives

Having designed the aerodynamic control surfaces for cruise, the aircraft's control properties are described by the aid of control derivatives. These are the changes in the aerodynamic loadings due to deflections in elevator δ_e (for longitudinal control), aileron δ_a and rudder δ_r (for lateral and directional control). These are summarised in Table 11.3.

A number of observations can be noted in the expressions of the control derivatives. First, the $X-$ and $Y-$ control derivatives to elevator and aileron deflection, respectively, are zero. This is approximation found in literature and can be safely assumed as a preliminary estimate. The second concept which is recurrent in the expression of the control derivatives is τ which refers to the control surface effectiveness and was already

Table 11.3: Definitions and derived equations of the Control derivatives.

Control Derivative	Equation
$C_{X_{\delta_e}} = \frac{dC_X}{d\delta_e}$	$C_{X_{\delta_e}} = 0$ [62]
$C_{Z_{\delta_e}} = \frac{dC_Z}{d\delta_e}$	$C_{Z_{\delta_e}} = \sum_{i=1}^{2}(-1)^i \tau_e \cdot \frac{S_i}{S}\frac{b_e}{b_i} \cdot C_{L_{\alpha_i}} \cdot \left(\frac{V_i}{V}\right)^2$
$C_{m_{\delta_e}} = \frac{dC_m}{d\delta_e}$	$C_{m_{\delta_e}} = -\sum_{i=1}^{2} \tau_e \cdot \frac{S_i}{S}\frac{b_e}{b_i} \cdot C_{L_{\alpha_i}} \cdot \frac{\lvert x_{cg} - x_{ac_i}\rvert}{\bar{c}}$
$C_{Y_{\delta_a}} = \frac{dC_Y}{d\delta_a}$	$C_{Y_{\delta_a}} = 0$ [62]
$C_{l_{\delta_a}} = \frac{dC_l}{d\delta_a}$	$C_{l_{\delta_a}} = \sum_{i=1}^{2} -\frac{C_{L_{\alpha_i}} \tau_a c_{r_i}}{S_i b_i} \cdot \left[\frac{y^2}{2} + \frac{2}{3}\frac{\lambda_i - 1}{b_i} y^3\right]_{b_2}^{b_1} \frac{S_i b_i}{Sb}\left(\frac{V_i}{V}\right)^2$
$C_{n_{\delta_a}} = \frac{dC_n}{d\delta_a}$	$C_{n_{\delta_a}} = -0.2 \cdot C_{L,0} \cdot C_{l_{\delta_a}}$ [102]
$C_{Y_{\delta_r}} = \frac{dC_Y}{d\delta_r}$	$C_{Y_{\delta_r}} = C_{L_{v_\alpha}} \cdot \frac{S_v}{S} \cdot \tau_r \cdot \frac{b_r}{b_v}$
$C_{l_{\delta_r}} = \frac{dC_l}{d\delta_r}$	$C_{l_{\delta_r}} = \frac{z_v}{b} \cdot C_{L_{v_\alpha}} \cdot \frac{S_v}{S} \cdot \tau_r \cdot \frac{b_r}{b_v}$
$C_{n_{\delta_r}} = \frac{dC_n}{d\delta_r}$	$C_{n_{\delta_r}} = -C_{L_{v_\alpha}} \cdot \frac{S_v l_v}{Sb} \cdot \tau_r \cdot \frac{b_r}{b_v}$ [89]

defined previously. This term allows to see how effective the aerodynamic control surface (for a change in deflection) are when translated to a local increase in lift (or side-force). Thirdly, it must be understood that the elevator and aileron are placed on both wings of the aircraft (analogous to an aircraft with both a canard and a tail for the elevator), which leads to the summing nature of the elevator control derivative derived from Equation 11.28 and roll control derivative equations. Finally, for $C_{l_{\delta_a}}$, the equation has been derived and corrected with a combined method using strip theory [108] and [116], as it was explained in Section 11.2.4.

Results

The stability and control derivatives obtained in this section are summarised in Table 11.4.

Table 11.4: Summarised stability and control derivatives for both longitudinal and lateral motion for clean cruise configuration.

Longitudinal Force Derivatives	Normal Force Derivatives	Pitch Moment Derivatives
C_{X_u} = -0.16374	$C_{Z_u} = -0.024899$	$C_{m_u} = 0.0061871$
$C_{X_\alpha} = 0.2487$	$C_{Z_\alpha} = -3.6501$	$C_{m_\alpha} = -0.1320$
$C_{X_{\dot{\alpha}}} = 0$	$C_{Z_{\dot{\alpha}}} = -3.6320$	$C_{m_{\dot{\alpha}}} = -10.0364$
$C_{X_q} = 0$	$C_{Z_q} = -2.4294$	$C_{m_q} = -22.9669$
$C_{X_{\delta_e}} = 0$	$C_{Z_{\delta_e}} = 0$	$C_{m_{\delta_e}} = -3.8147$
Lateral Force Derivatives	**Roll Moment Derivatives**	**Yaw Moment Derivatives**
$C_{Y_\beta} = -0.1443$	$C_{l_\beta} = -0.05192$	$C_{n_\beta} = 0.05404$
$C_{Y_{\dot{\beta}}} = 0$		$C_{n_{\dot{\beta}}} = 0$
$C_{Y_p} = -0.02243$	$C_{l_p} = -0.7462$	$C_{n_p} = -0.02082$
$C_{Y_r} = 0.1469$	$C_{l_r} = 0.1585$	$C_{n_r} = -0.08167$
$C_{Y_{\delta_a}} = 0$	$C_{l_{\delta_a}} = -0.09817$	$C_{n_{\delta_a}} = 0.01013$
$C_{Y_{\delta_r}} = 0.8693$	$C_{l_{\delta_r}} = 0.1746$	$C_{n_{\delta_r}} = -0.4423$

To evaluate the quality of the design with respect to stability, the most interesting stability derivatives are C_{m_α}, C_{n_β}, and C_{l_β}.

C_{m_α} is the dominant term which defines natural longitudinal stability for longitudinal motion. As it can be seen in Table 11.4, it is negative leading to a statically stable aircraft. However, the magnitude is very small and hence it can be expected that the response is poorly damped. The latter means that the aircraft requires a fly-by-wire system in order to dampen the aircraft's motion.

For lateral motions, the stability derivatives C_{n_β} and C_{l_β} define the lateral stability behaviour in terms of

Dutch Roll convergence and spiral stability. The spiral stability limit is determined by the equation:

$$E = C_{L,0} \cdot (C_{l_\beta} \cdot C_{n_r} - C_{n_\beta} \cdot C_{l_r}) = 0 \tag{11.61}$$

For Dutch Roll stability is determined by the Routh's Discriminant which should be positive:

$$R(C_{l_\beta}, C_{n_\beta}) = B \cdot C(C_{l_\beta}, C_{n_\beta}) \cdot D(C_{l_\beta}, C_{n_\beta}) - A \cdot (D(C_{l_\beta}, C_{n_\beta}))^2 - B^2 \cdot E(C_{l_\beta}, C_{n_\beta}) > 0 \tag{11.62}$$

where the relations for A, B, $D(C_{l_\beta}, C_{n_\beta})$ and $E(C_{l_\beta}, C_{n_\beta})$ can be found in [62].
Both can now be plotted in the $(-C_{l_\beta}, C_{n_\beta})$ plane and can be seen in Figure 11.14.

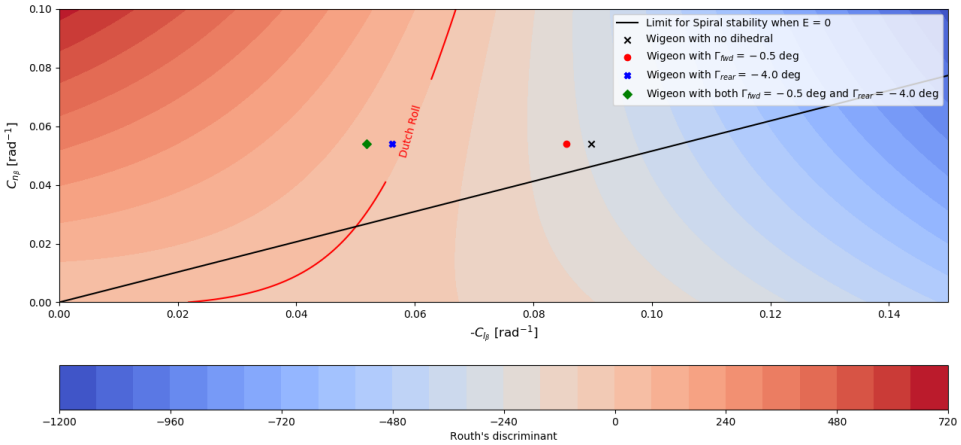

Figure 11.14: Dutch roll and spiral stability limits plotted in the $(-C_{l_\beta}, C_{n_\beta})$ plane. The aircraft is represented by a dot in the plane with its initial properties, and different changes to the dihedral lead to different positions in the space.

From Figure 11.14, it can be seen that Wigeon has both a divergent Dutch Roll and an unstable spiral. Usually, an unstable spiral can easily be dealt with by the pilot as it is a very slow motion. Dutch Roll, however, should be stable as it can be detrimental to passenger comfort. For the latter, a change in the dihedral of the aircraft could be done, as it was previously explained that C_{l_β} is a function of the dihedral angle for both wings (see Equation 11.55). It was observed that if the dihedrals are set to $\Gamma_{fwd} = -0.5°$ and $\Gamma_{rear} = -4.0°$, the aircraft has a convergent Dutch Roll (with a sufficient margin to account for assumptions). The smaller forward dihedral is chosen in order to minimise the risk of the forward wing touching ground during hover or vertical flight, whereas the rear wing dihedral was limited to -4.0 ° so that it does not affect the propellers efficacy and aforementioned computations for yaw control.

11.3.2. Cruise dynamics

The non-dimensional and linearised equations of motion of an aircraft for both symmetric and asymmetric motions have been derived in [62]. A brief overview of the derivation process applied to obtain those equations is provided in this section. The equations of motion expressed in matrix form are transformed in a state-space form in order to simulate the aircraft responses to specific disturbances and control inputs. Those equations of motion were linearised for a steady, straight, symmetric flight in the stability reference frame. This is valid for small disturbances from an initial equilibrium condition of steady, straight, symmetric flight (i.e. being the reference condition). Since the aircraft motion studied in this report was described by a set of linear equations of motion, the stability of a specified equilibrium condition is independent of the input or disturbance.

For the Equations of motion, the stability reference frame has been used. In this system, the x-axis lies in the symmetry plane and its direction is situated along the longitudinal component of the velocity of the centre of gravity. The z-axis also lies in the symmetry plane and points downwards perpendicular to the x-axis. The y-axis points out of the x-z plane as to complete the right-handed coordinate system.

The equations of motion can be rewritten into the following form:

$$\mathbf{C_1}\dot{\vec{x}} + \mathbf{C_2}\vec{x} + \mathbf{C_3}\vec{u} = \vec{0} \tag{11.63}$$

where $\mathbf{C}_1$, $\mathbf{C}_2$ and $\mathbf{C}_3$ are stability matrices, $\vec{x}$ is the state vector containing the required responses and $\vec{u}$ is the input vector. First, the required matrices are derived for the symmetric case, resulting in:

$$\mathbf{C_1} = \begin{bmatrix} -2\mu_c \cdot \bar{c}/V_0 & 0 & 0 & 0 \\ 0 & (C_{Z_{\dot{\alpha}}} - 2\mu_c) \cdot \bar{c}/V_0 & 0 & 0 \\ 0 & 0 & -\bar{c}/V_0 & 0 \\ 0 & C_{m_{\dot{\alpha}}} \cdot \bar{c}/V_0 & 0 & -2\mu_c \cdot {K_{yy}}^2 \cdot \bar{c}/V_0 \end{bmatrix} \tag{11.64}$$

$$\mathbf{C_2} = \begin{bmatrix} C_{X_u} & C_{X_\alpha} & C_{Z_0} & C_{X_q} \\ C_{Z_u} & C_{Z_\alpha} & -C_{X_0} & (C_{Z_q} + 2\mu_c) \\ 0 & 0 & 0 & 1 \\ C_{m_u} & C_{m_\alpha} & 0 & C_{m_q} \end{bmatrix} \tag{11.65}$$

$$\mathbf{C_3} = \begin{bmatrix} C_{X_{\delta_e}} \\ C_{Z_{\delta_e}} \\ 0 \\ C_{m_{\delta_e}} \end{bmatrix} \tag{11.66}$$

where in the symmetric case, the sate vector, $\vec{x} = [\hat{u}\ \alpha\ \theta\ q\bar{c}/V_0]^T$ and $\vec{u}$ is equal to the elevator deflection δ_e.

Second, the same procedure is performed for the asymmetric case resulting in the following:

$$\mathbf{C_1} = \begin{bmatrix} (C_{Y_{\dot{\beta}}} - 2\mu_b) \cdot b/V_0 & 0 & 0 & 0 \\ 0 & -\frac{1}{2} \cdot b/V_0 & 0 & 0 \\ 0 & 0 & -4\mu_b K_{xx}^2 \cdot b/V_0 & 4\mu_b \cdot K_{xz} \cdot b/V_0 \\ C_{n_{\dot{\beta}}} \cdot b/V_0 & 0 & 4\mu_b \cdot K_{xz} \cdot b/V_0 & -4\mu_b K_{zz}^2 \cdot b/V_0 \end{bmatrix} \tag{11.67}$$

$$\mathbf{C_2} = \begin{bmatrix} C_{Y_\beta} & C_{L,0} & C_{Y_p} & (C_{Y_r} - 4\mu_b) \\ 0 & 0 & 1 & 0 \\ C_{l_\beta} & 0 & C_{l_p} & C_{l_r} \\ C_{n_\beta} & 0 & C_{n_p} & C_{n_r} \end{bmatrix} \tag{11.68}$$

$$\mathbf{C_3} = \begin{bmatrix} C_{Y_{\delta_a}} & C_{Y_{\delta_r}} \\ 0 & 0 \\ C_{l_{\delta_a}} & C_{l_{\delta_r}} \\ C_{n_{\delta_a}} & C_{n_{\delta_r}} \end{bmatrix} \tag{11.69}$$

where for the asymmetric case $\vec{x} = [\beta\ \phi\ pb/(2V_0)\ rb/(2V_0)]^T$ and $\vec{u} = [\delta_a\ \delta_r]^T$, where δ_a and δ_r are functions of time or are input to the model as arrays.

The final step requires transforming the matrices $\mathbf{C}_1$, $\mathbf{C}_2$ and $\mathbf{C}_3$ into the state-space matrices **A**, **B**, **C** and **D** in the following:

$$\dot{\vec{x}} = \mathbf{A}\vec{x} + \mathbf{B}\vec{u} \ \ \& \ \ \vec{y} = \mathbf{C}\vec{x} + \mathbf{D}\vec{u} \tag{11.70}$$

where $\vec{y}$ is the output vector which is chosen to be equal to $\vec{x}$, resulting in **C** being the identity matrix and **D** being a matrix containing only zeroes. The computation of **A** and **B** is implemented using Equation 11.71.

$$\mathbf{A} = -{\mathbf{C_1}}^{-1}\mathbf{C_2} \ \ \& \ \ \mathbf{B} = -{\mathbf{C_1}}^{-1}\mathbf{C_3} \tag{11.71}$$

The latter results in $\mathbf{A}_s$ for the symmetric case and $\mathbf{A}_a$ for the asymmetric case.

It can be seen that a set of additional inputs are required. These inputs are the aircraft's non-dimensional inertia are as follows: $K_{xx}^2 = \frac{I_{xx}}{mb^2}$, $K_{yy}^2 = \frac{I_{yy}}{m\bar{c}^2}$, $K_{zz}^2 = \frac{I_{zz}}{mb^2}$ and $K_{xz} = \frac{I_{xz}}{mb^2}$. The final aerodynamic inputs to the state-space system are $C_{L,0}$, C_{X_0} and C_{Z_0} computed as follows:

$$C_{X_0} = \frac{Wsin(\theta_0)}{1/2\rho V_0^2 S} \tag{11.72}$$

$$C_{Z_0} = \frac{-Wcos(\theta_0)}{1/2\rho V_0^2 S} \tag{11.73}$$

which require the weight W, the airspeed V_0, the air density ρ and finally θ_0 which is the initial pitch angle. Finally, the non-dimensional mass μ_c and μ_b must be computed using:

$$\mu_c = \frac{W}{g\rho S\bar{c}} \tag{11.74}$$

$$\mu_b = \frac{W}{g\rho Sb} \tag{11.75}$$

Using the stability and control derivatives given in Table 11.4, the values for the state-space matrices can be computed. Based on this, the poles and zeroes of both the symmetric and asymmetric state-space system were found. They are displayed in Figure 11.15.

In the symmetric system, all poles have negative real parts, meaning that they are open-loop stable. There is one periodic eigenmode (pair of complex poles) and two aperiodic eigenmodes (real poles). This is in contrast to conventional aircraft, which have two periodic symmetric eigenmodes. In the asymmetric system, there is again one periodic eigenmode and two aperiodic modes. This is the same as for conventional aircraft, where the Dutch roll, the aperiodic roll and spiral modes are observed. The spiral mode is unstable for the Wigeon (as for many conventional aircraft), but the other eigenmodes are stable.

This behaviour is favourable in the sense that the aircraft is stable in all modes except the spiral, which can be deemed acceptable due to it being very slow. However, while stability is an essential criterion for controlling an aircraft, it is not the only one. As Figure 11.16 shows, a small step input to the elevator (a typical input given by a pilot to change the pitch angle) results in a very large change in V and θ. Furthermore, the response is very slow to settle on its final value, with a large overshoot in all state variables. This needs to be addressed with a closed-loop fly-by-wire system.

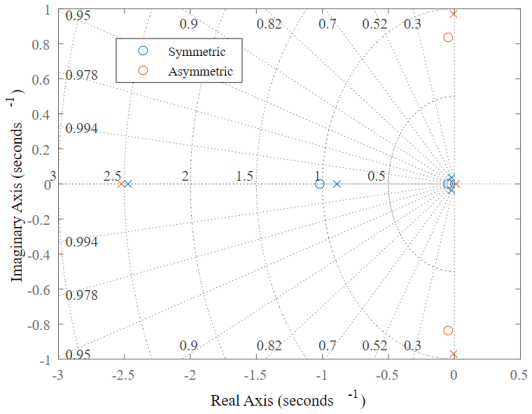

Figure 11.15: Map of the open-loop poles and zeroes of the aircraft in cruise. Crosses indicate poles, circles indicate zeroes.

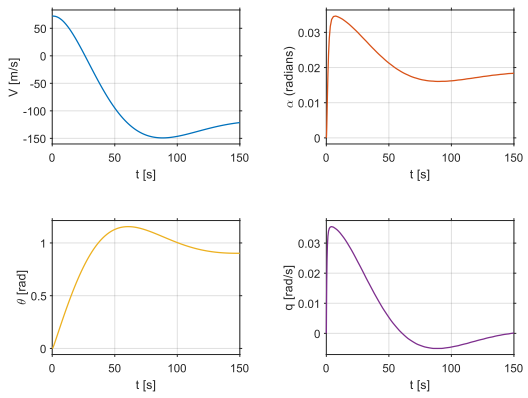

Figure 11.16: Open-loop response of the airspeed V, the angle of attack α, the pitch angle θ, and the pitch rate q to a step elevator input of -0.005 rad.

Figure 11.17 shows the response of the asymmetric states to a pulse-shaped rudder input. The Dutch Roll mode causes high-frequency oscillations in all states, while the unstable spiral mode causes a slow divergence that is especially visible in the roll angle and yaw rate. Since the Dutch roll is very unpleasant for the occupants of an aircraft and can cause nausea, it is essential that the oscillations are reduced.

Finally, Figure 11.18 shows the response of the aircraft states to a pulse-shaped aileron input. The responses are qualitatively similar as for the rudder, except for an initial peak in p, which is the primary function of the aileron. Furthermore, the magnitude of the response is smaller.

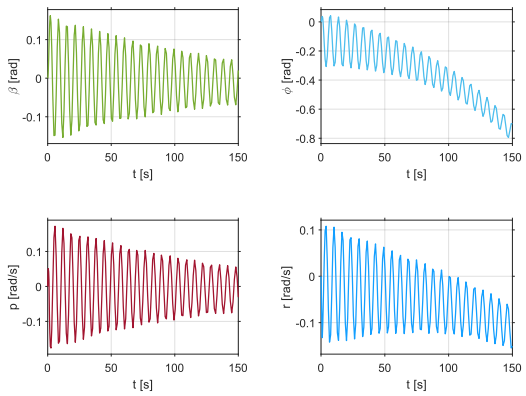

Figure 11.17: Open-loop response of the sideslip angle β, the roll angle ϕ, the roll rate p, and the yaw rate r to a pulse rudder input of 0.025 rad (for 1 second).

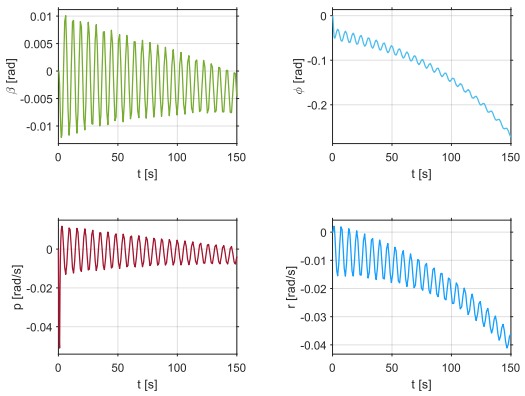

Figure 11.18: Open-loop response of the sideslip angle β, the roll angle ϕ, the roll rate p, and the yaw rate r to a pulse rudder input of 0.025 rad (for 1 second).

It has therefore been established that a controller is required to achieve good handling qualities of the aircraft in cruise. It needs to decrease the response time and overshoot for the elevator response, reduce the oscillations of the Dutch roll and potentially eliminate the instability due to the spiral mode.

11.4. Controller Design

In this section, the design of a closed-loop controller for the Wigeon is described. The purpose of this controller is to improve on the open-loop dynamics of the eVTOL in terms of stability and handling quality. Since the Wigeon spends most of its mission time in cruise, this report focuses on a controller to make the aircraft easy to fly in cruise. The design of controllers for VTOL operation and the transition phase are beyond the scope of this report.

11.4.1. Control allocation

In order to introduce the controller design, it is essential to qualitatively mention the required control allocation.

It is important to know what the pilot commands are and how these commands can be translated to deflections of the aerodynamic surfaces or varying angular speed of the propellers. For cruise, a control stick for pitch, a side stick for roll and pedals for yaw are connected to a flight control system that directly controls the deflections of the control surfaces (through the use of actuators) and corrects accordingly for any instabilities. The pilot can therefore set a certain attitude angle for pitch and a target heading angle for yaw control which automatically sets a roll rate for roll control when a certain turn manoeuvre must be performed, where for the roll rate a certain maximum bank angle is allowed within the flight envelope. Finally, to control the aircraft during hover, a collective lever will be used by the pilot which modulates the speed of the propellers [1]. Additionally, pedals can be used by the pilot to control the rudder, as in for cruise, and during ground operations it can be used as differential braking.

11.4.2. Controller architecture and closed-loop dynamics

By the stakeholder requirements, the Wigeon must have an autopilot system

The high-level overview of the controller architecture (created in Simulink) can be seen in Figure 11.19. While the pitch controller only consists of one feedback loop with a PI (proportional integral) controller, the

[1] URL https://evtol.com/features/behind-the-controls-of-an-evtol-aircraft-a-test-pilots-perspective/ [cited 15 June 2021]

lateral controller is more sophisticated. It is inspired by a lecture by How [61] on a controller for coordinated turns.

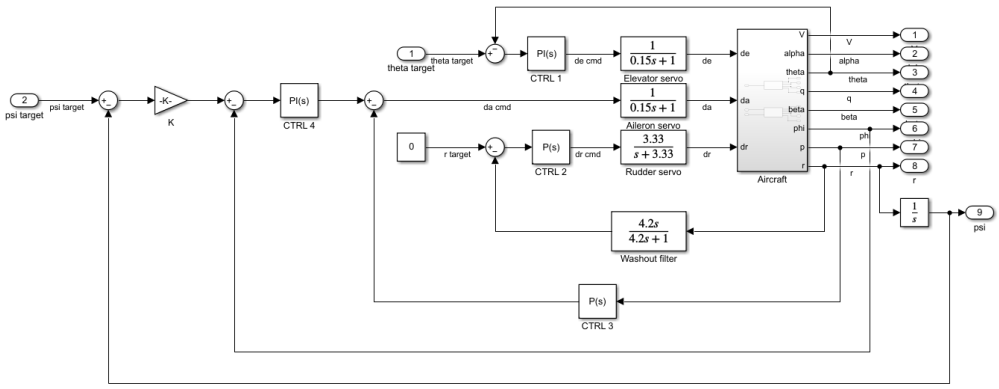

Figure 11.19: Architecture of the controller for cruise.

In order to improve the Wigeon's longitudinal dynamics a feedback loop from the pitch angle θ is used. The pilot sets a target pitch angle θ_{target}, which is compared to the current pitch angle (measured by an inertial measurement unit) and then fed through a PI controller. The dynamics of the elevators are modelled using the transfer function $\frac{1}{0.15s+1}$, which is the transfer function proposed by [61] for the aileron. Modelling the elevator as a transfer function takes into account that its response speed is limited and occurs with a delay.

After tuning the controller gains with Simulink's PID tuner app, the resulting gain and phase margins are 22.3 dB and 147 degrees, as seen in Figure 11.20. The step responses of the longitudinal states to a step input to θ_{target} is shown in Figure 11.21. It can be seen that the aircraft is not only stable, but also responds quickly with minimal overshoot.

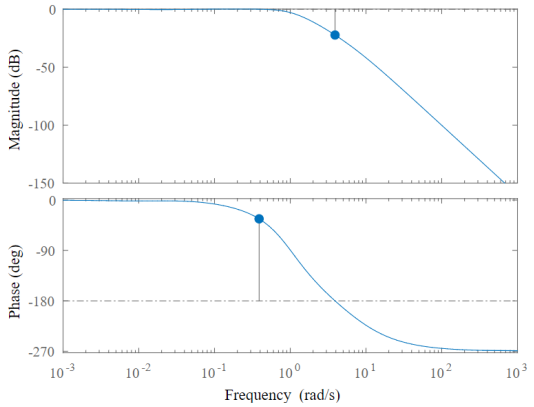

Figure 11.20: Bode plot of the closed-loop response of θ to θ_{target} set by the pilot.

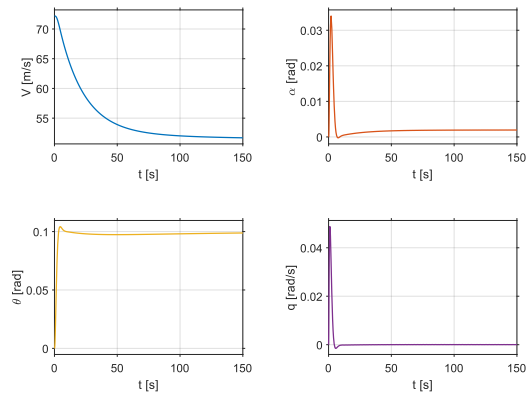

Figure 11.21: Closed-loop response of the airspeed V, the angle of attack α, the pitch angle θ, and the pitch rate q to a step input of 0.1 rad to θ_{target}.

The lateral controller is structured as described by How [61] for a lateral controller that takes a heading input and performs coordinated turns. A gain K calculates the appropriate roll angle ϕ based on the error in the yaw angle ψ. The error in the yaw angle is then fed through a controller block, whose output is compared to the roll rate which has a gain (proportional controller) applied. The output of this comparison is fed as a command to the aileron actuator. At the same time, another feedback loop with a washout filter on the yaw rate attempts to bring the yaw rate to zero. This is the yaw damper designed to reduce low-frequency oscillations (Dutch roll).

The aileron and rudder actuators are modelled as $\frac{1}{0.15s+1}$ and $\frac{3.33}{s+3.33}$, respectively. In order to reduce

oscillations in the response, a PI controller was used for CTRL 4 in Figure 11.19 instead of the proportional controller in the original work.

In Figure 11.22, the Bode plot showing the response of the heading angle ψ to the pilot input ψ_{target} is shown. The system is closed-loop stable with a gain margin of 12.4 dB and a phase margin of -180 degrees. These margins are not as good as for the longitudinal case, so there is further room for optimisation. This is confirmed by the step responses shown in Figure 11.23 are also slower and more oscillatory than for the longitudinal controller.

In Figure 11.24, the poles and zeroes of the open-loop system can be seen. All poles are now stable (with a negative real part), which is an improvement over the open-loop system in Figure 11.15. However, the asymmetric system now has two zeroes in the right half-plane. This can lead to the system's initial response being in the opposite direction of its final value. This can, in fact, be observed in the evolution of r in Figure 11.23. This confirms that in future iterations of the design, the lateral controller may have to be reviewed to improve handling qualities.

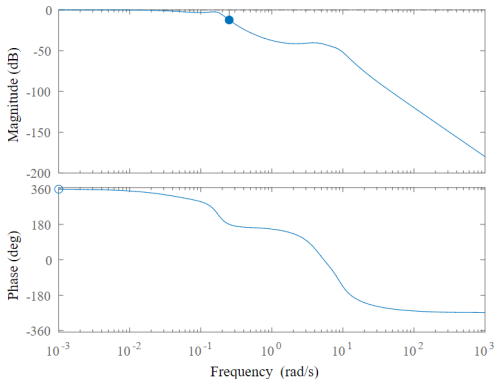

Figure 11.22: Bode plot of the closed-loop response of ψ to ψ_{target} set by the pilot.

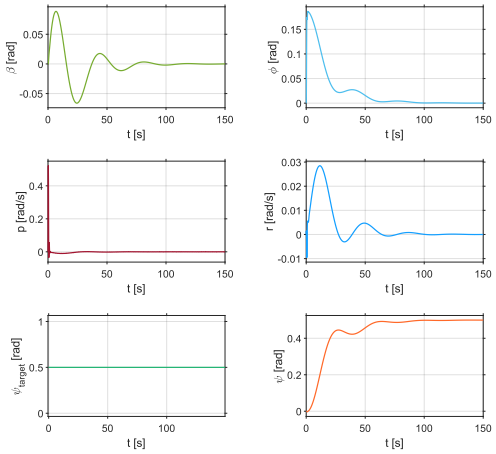

Figure 11.23: Closed-loop response of the sideslip angle β, the roll angle ϕ, the roll rate p, the yaw rate r, and the yaw angle ψ to a step input of 0.5 rad to ψ_{target}.

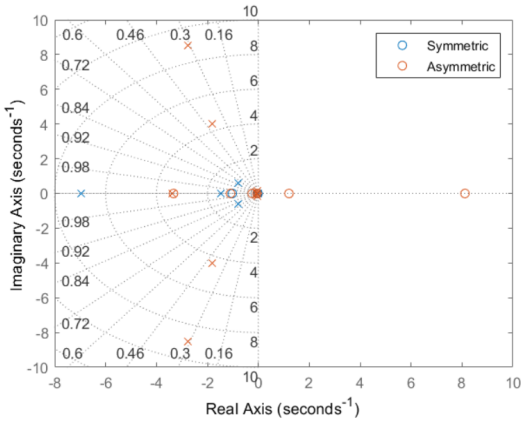

Figure 11.24: Map of the closed-loop poles and zeroes of the aircraft in cruise. Crosses indicate poles, circles indicate zeroes.

11.4.3. Further considerations for controller design

In order to design a controller for the transition phase, certain aerodynamic aspects must be taken into account. These mostly relate to the nature of the flow during transition which becomes very difficult

to predict due to hysterisis. In fact, during transition, there is a sudden change from fully separated to attached flow which in turn translates to a sudden change in lift over the wings. Additionally, the modelling unpredictability is enhanced due to the phenomenon of hysterisis where the stalling characteristics of the aircraft depend on the flow's history. Furthermore, an unpredictable atmosphere can increase the complexity of the model, which e.g. the case of a sudden change in wind gust (whether it is a change in magnitude or direction), the flow over wings may re-attach or separate sooner/later than predicted.

For the pure transition phase itself, the controller must also be able to react accordingly for a range of different situations such as if the flow separates/(re-)attaches first at the forward wing, or if the flow first (re-)attaches/separates at the rear wing or for the rarest case that the nature of the flow changes at the same time for both wings. It can be understood that all these different situations create different and unpredictable pitching moments, that can be aggravated by an unpredictable atmosphere as explained previously. The latter introduces a dangerous transient response, which shows the need for a robust controller.

11.5. Compliance with Requirements

VTOL-SAF-3 states that the Wigeon shall be able to land with gusts of 20 kts. Lateral gusts like these require the aircraft to bank or pitch to create a lateral component in the thrust. Approximating the aircraft as flat plate of dimensions 7.35 m x 1.7 m (representing a rectangular approximation of the eVTOL as seen from the side) allows to estimate the force created by such a gust. According to [2], the drag of a flat plate with an aspect ratio of 5 is given by $D = C_D \frac{1}{2} \rho V^2 A$ with $C_D = 1.2$. Filling in the area $A = 12.50\ m^2$ and wind speed $V = 10.29\ m/s$, this yields $D = 972.8\ N$. To counteract this force with its hover thrust of 29660 N, the aircraft would have to bank a mere 1.880 degrees to the side. This was considered acceptable to comply with the requirement.

For VTOL-MFA-3, VTOL-SAF-4, and VTOL-LFT-8 it is set that the Wigeon should be controllable even during a OEI condition. The vertical tail and rudder were specifically designed to be able to control the aircraft during a OEI condition at cruise (creating more than 700 Nm yaw moment, as required by VTOL-MFA-3-CTR-1), as can be found in Section 11.2.4. With respect to hover, the possibility of variable thrust allows the pilot and the control system to have control authority during an OEI at hover and landing (see Section 11.2.5). By redistributing the thrust to different engines, the pilot is able to create at least a 12 kNm roll moment as required by VTOL-MFA-3-CTR-2.

By VTOL-MFA-5, the Wigeon needs to alert its pilot if an obstacle is within 70 m of it. While this system needs to be designed at a later stage in the project, Lies et al. [68] found that using a combination of low-power radar and light camera could provide a solution for obstacle detection in urban air mobility with detection ranges up to 1 km.

As established in Section 11.3.2 and Section 11.4.2, the aircraft is open- and closed-loop stable in cruise. This means that VTOL-STK-22, VTOL-MFA-2-CTR-1, and VTOL-MFA-2 are satisfied in cruise. Due to the design of the cruise controller in Section 11.4.2, cruise requires no or minimal pilot compensation, which corresponds to satisfactory handling qualities according to EASA [79]. This allows for one human pilot to control the aircraft easily with manual controls, satisfying VTOL-STK-7, VTOL-STK-13, VTOL-CTL-2, VTOL-CTL-3, and VTOL-CRE-1. The controller is a form of autopilot which allows to satisfy VTOL-STK-23 (even though more work could make the Wigeon more autonomous). Furthermore, since control uses a fly-by-wire system, the control stick force can be adapted to meet any requirement (satisying VTOL-CTL-4, VTOL-CTL-4-CTR-1, and VTOL-CTL-4-CTR-2). Therefore, the overall handling requirement VTOL-STK-21, i.e. compliance with handling quality requirements by EASA, is satisfied in cruise. More work is required to meet these requirements in hover and transition as well (and requirements such as VTOL-MFA-6), although the foundations have been laid in Section 11.4.1 by explaining how controls are allocated. Also, a hover control system could be designed based on a drone control system, which are readily available and open source with advanced capabilities such as high-precision autonomous landing [3]. These could also help the Wigeon land autonomously as required by VTOL-MFA-5.

[2] URL https://www.engineersedge.com/fluid_flow/rectangular_flat_plate_drag_14036.htm [cited 17 June 2021]
[3] URL https://docs.px4.io/master/en/advanced_features/precland.html [cited 17 June 2021]

VTOL-SAF-5 refers to the failure rate of the autopilot to be below 10^{-9}. This cannot be investigated in depth at this point due to this being an early stage of the design process. They should be taken into account in subsequent design stages by including redundancy in flight computers and actuators.

11.6. Verification and Validation

This section describes the efforts to verify the methods used to design the Wigeon eVTOL for stability and control. The section closes with the planned Validation process to be done after the DSE project.

11.6.1. Verification of Stability Derivatives Model

The verification of the analytical model is performed in a series of steps. First, a number of small unit tests will be done in order to verify that the expected change in the stability derivatives is correct. And finally, the model's outputs are compared to already existing aircraft, in terms of magnitude and sign, where the latter is of utmost importance and should be similar for a specific number of stability and control derivatives.

Unit Test - CG shift

The unit test performed in this subsection is a shift in the CG of the aircraft. In order to perform a complete and concise unit test verification, only a small number of stability derivatives for both longitudinal (C_{X_α}, C_{m_α} and C_{m_q}) and lateral (C_{n_β} and $C_{n_{\delta_r}}$) motions are shown due to their high number.

Specific simplified equations of the change of longitudinal stability derivatives can be found in [62] and are compared to the ones obtained by the code. For the lateral stability derivatives, the qualitative shift is verified. The results of the latter can be summarised in Table 11.5.

Table 11.5: Summarised Results of the CG Unit Test, the expected outcome of those tests and the actual result.

Verification Test	Expected Outcome	Obtained output
Shift in x_{cg} by factor of 2	$\Delta C_{X_\alpha} = 0$ (no dependency) $\Delta C_{m_\alpha} = 11.973$ (destabilising) $\Delta C_{m_q} = -41.1467$ Decrease in C_{n_β} Decrease in magnitude of $C_{n_{\delta_r}}$	$\Delta C_{X_{\alpha_{model}}} = 0$ $\Delta C_{m_{\alpha_{model}}} = 11.756$ $\Delta C_{m_{q_{model}}} = -33.21419$ $\Delta C_{n_{\beta_{model}}} = -0.062499$ $\Delta C_{n_{\delta_{r_{model}}}} = -0.35528$
Shift in x_{cg} by factor of 0.5	$\Delta C_{X_\alpha} = 0$ (no dependency) $\Delta C_{m_\alpha} = -5.986615$ (stabilising) $\Delta C_{m_q} = -5.54833$ Increase in C_{n_β} Increase in magnitude of $C_{n_{\delta_r}}$	$\Delta C_{X_{\alpha_{model}}} = 0$ $\Delta C_{m_{\alpha_{model}}} = -5.878075$ $\Delta C_{m_{q_{model}}} = -12.9931$ $\Delta C_{n_{\beta_{model}}} = 0.028641$ $\Delta C_{n_{\delta_{r_{model}}}} = 0.162813$

From Table 11.5, it can be seen that the unit test was successful. Even though minor differences in C_{m_α} and large differences in C_{m_q} can be seen, these can be simply explained by the fact that the equations used from [62] are simplified and assume a conventional aircraft configuration, which does not have the same analytical equations. Even with these differences, the trend is still the same and hence with the aforementioned the analytical modules have been independently verified.

Comparison with existing aircraft

This subsection briefly presents the strategy to verify the order of magnitude and sign of the stability derivatives using the reference values for different aircraft in clean cruise configuration found in the appendices of [62]. These values were generated using the vortex lattice method.

First, it is essential to mention the differences. The main difference that was observed is the magnitude

of the derivatives: C_{m_q}, $C_{Z_{\dot{\alpha}}}$, $C_{m_{\dot{\alpha}}}$, $C_{m_{\delta_e}}$, $C_{Z_{\delta_e}}$ and for certain aircraft the down-force $\hat{u}$-derivative C_{Z_u}. For C_{m_q} and $C_{Z_{\delta_e}}$, it can be explained by the fact that both wings are far from the centre of gravity and hence acting as a canard and a tail simultaneously. C_{m_q} is hence approximately doubled, whereas $C_{Z_{\delta_e}}$ is zero due to the way the elevator is used. In fact, the elevator is used in the same manner as an aileron and hence explains that both down-forces for both wings cancel out. This further explains the fact that $C_{m_{\delta_e}}$ is approximately twice as large, as both elevators (instead of one for conventional aircraft) allow for a higher pitching down moment. The $\dot{\alpha}$-derivatives of the Wigeon are mostly 1.5 to twice as large as reference values, which can be explained by their high sensitivity to the specific configuration and atmospheric conditions. Lastly, C_{Z_u} is significantly smaller than for certain aircraft. This is mainly due to the fact that the Wigeon is flying at subsonic speeds which relates to very low compressibility effects. Additionally, aero-elastic effects which also affect the derivative were neglected.

In terms of similarities, it can be observed that the rest of derivatives have identical sign, especially for the dominant stability derivatives w.r.t to their respective angle rates (q, p and r) and the control derivatives which shows that the model uses the same conventions. Last but not least, the assumption of the derivatives $C_{X_{\dot{\alpha}}}$, C_{X_q}, $C_{X_{\delta_e}}$ and $C_{Y_{\delta_a}}$ being zero is also the case of a wide range of different and hence verifying the validity of the assumption.

With the latter, it can be concluded that the model shows results that are very similar to other aircraft and its discrepancies can be easily explained by the dual-wing nature of Wigeon. Hence this confirms that the model can be used as an early preliminary tool to obtain stability and control derivatives of tandem wing (or large canard) aircraft. Computational methods however must still be applied in order to obtain more accurate estimates of the stability behaviour of the aircraft.

11.6.2. Verification of Cruise Dynamics Using Numerical Model

In this section the system test to verify the dynamic model is presented. The verification procedure consists of verifying the value of the eigenvalues of the stability matrix **A**. These define the stability behaviour of the different eigenmotions of the aircraft. Before starting the procedure it is essential to mention that the verification model outputs the eigenvalues in normalised form, defined as $\lambda_c = \frac{\bar{c}}{V_0} \cdot \lambda$ for longitudinal motions and $\lambda_b = \frac{b}{V_0} \cdot \lambda$ for lateral and hence must be transformed to their non-normalised form. The results are summarised in Table 11.6. From Table 11.6, it can be seen that there is no difference between both

Table 11.6: Eigenvalues computed by the model λ, the numerical model for verification normalised λ_c or λ_b eigenvalues and the error

Eigenmotion	**Model eigenvalue** λ	**Numerical model eigenvalue** $\lambda_\mathbf{c}$ or $\lambda_\mathbf{b}$	**Error:Re**(λ), **Im**(λ) **(%)**
Short period	$-2.47; -0.89$	$-0.04332; -0.01557$	0, 0
Phugoid	$-0.0226 \pm 0.0361j$	$-0.0003960 \pm 0.0006318j$	0, 0
Aperiodic roll	$-2.52 \pm 0j$	$-0.28690 \pm 0j$	0, 0
Dutch roll	$-0.00699 \pm 0.97j$	$-0.0007948 \pm 0.1103j$	0, 0
Spiral	$0.0125 \pm 0j$	$0.0014239 \pm 0j$	0, 0

models in terms of stability behaviour of the aircraft. The system test is hence successful and the model implementation of the state-space matrices is confirmed to be correct.

11.6.3. Validation Plan

After the DSE project, multicopter flight data will be researched and used to validate the Hover Control simulation model. Finally, with a 3D model of the aircraft and with further wind tunnel data, a more exact computation of the stability derivatives could be performed which would aid in the validation and model matching procedure. With the final steps in the design, flight data could be acquired in order to estimate the aircraft's stability behaviour. As a consequence the stability model could be refined and further optimised.

12 Structures & Materials

The transfer of structural loads permits the functionality of all systems during all stages of flight. As a result, depending on the magnitude of the loads, the structure also serves as a constraint for the design space. This chapter serves to provide a design for the structure of the long range eVTOL - the Wigeon. Section 12.1 talks about the flight envelope and the loads that are deemed most critical. Section 12.2 demonstrates the wingbox design and Section 12.3 briefly does the same for the fuselage. Then follows the material selection in Section 12.4 and fatigue analysis in Section 12.5. Corrosion is discussed in Section 12.6. General crashworthiness and landing gear design are done in Section 12.7, aeroelasticity analysis is performed in Section 12.8 and weight estimates are shown in Section 12.9. Lastly, validation and verification results and methods are described in Section 12.10.

12.1. Load Identification

It is not enough to simply design a structure, a structure has to be designed for a specific purpose to avoid a waste of resources. In order to establish specific design goals it is important to know the loads acting upon the aircraft in flight. A gust and manoeuvre loading diagrams are necessary in order to understand the critical cases. Once these cases are known, specific failure modes are pinpointed and addressed in the design.

12.1.1. Flight envelope

When computing the gust loading diagram, equation 12.1 (left) is used, wherein u is the gust velocity, V is the flight velocity, and W/S is the wing loading. Three possible gust speeds are given by Certification Specifications (CS) to fulfil requirement VTOL-STS-2-STR-4. The maximum gust velocities are $u_b, u_c, u_d = 20.12, 15.24, 7.62$ m/s and three design velocities, which correspond to the design velocity for maximum gust intensity, cruise velocity, and dive velocity, respectively. The interpolation of the points and using the Equation 12.1 (left) provides the basis for the gust diagram. For the manoeuvre loading diagram, the loads at stall speed are computed using the Equation 12.1 (right):

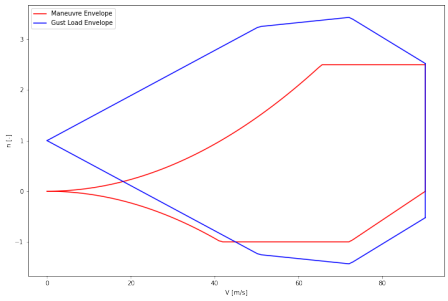

Figure 12.1: The flight envelope

$$n = 1 \pm \frac{\rho \cdot V \cdot C_{L_\alpha} \cdot u}{2 \cdot W/S} \qquad n = \pm \frac{0.5 \cdot \rho \cdot V^2 \cdot C_{L_{max}}}{2W/S} \tag{12.1}$$

Then, the maximum and minimum allowable load factors for the manoeuvre diagram are set by the CS once again. The n_{upper} in this case is 2.5 and n_{lower} is -1. The maximum allowable aircraft speed is defined as the dive speed, V_D, which cuts off the diagram.

Both diagrams are defined for a specific altitude, in this case the design cruise altitude. The diagrams are then combined and the maximum load factor is determined. From cruise speed of 72 m/s it follows that the maximum load factor is 3.4. Moreover, the maximum load factor is multiplied by a safety factor of 1.5, which brings the loads to the so-called ultimate load factor that the structure has to endure. It is a highly unlikely scenario that the aircraft ever meets such high loads, nonetheless it still must be able to sustain them.

12.1.2. Critical load cases & failure modes

The flight envelope results in a multitude of possible flight conditions, but designing the structure to withstand a few critical conditions allows for covering the entire flight envelope using limited analysis. There are 3 critical load cases in conventional flight: take-off, manoeuvres in cruise and landing. However, having an unconventional aircraft requires a different set of critical cases. Concluding from Figure 12.1, a gust in cruise is a crucial situation to consider, as well as take-off and landing with engines at maximum thrust.

Having considered the loads, it is also important to select principal failure modes. According to an article in *Materials Today* [48], fatigue, overload and corrosion are the most common failure modes in aircraft, in that respective order. Overload further breaks down into buckling and yielding. All of these are discussed and designed against further.

12.2. Wingbox Design

The wingbox is the critical load bearing structure of an aircraft wing. Given that the wings are subjected to the most consequential loads of the aircraft, makes the wingbox one of the, if not the most important structure of the Wigeon. Variation between VTOL and cruise configuration loads further adds significance to the wing as a structural component. This section elucidates the process used to design the wingbox, including the skin, spars and stringers.

12.2.1. General shape

Choosing the right shape of the wingbox is crucial as the shape provides the basis for structural rigidity. Nevertheless, the shape is a subject to a lot of constraints, like the shape of the airfoil and engine placement, for example.

Due to the small size of an individual wing, large portion of the weight and cross-sectional area is taken up by the skin, and therefore the skin of the wing can be considered load bearing. As such, the top and the bottom panels of the wingbox are the thickened skin itself. Two spars are present. The design of the wingbox is depicted in Figure 12.3. The wingbox is not of a multicell cross-section, as the loads, specifically shear loads, are not expected to be too large due to the relatively low cruise speed, thrust and weight. No stringers are shown and neither is the variable thickness between spar and the skin, only the general shape of the wingbox is depicted.

On the other hand, having the top and bottom skins of the airfoil as the top and bottom panel of the wingbox introduces complication when it comes to calculations. Therefore, to model this a rectangular wingbox is used. Although this causes some loss of precision, the simplified wingbox has roughly the same second moment of inertia as the real wingbox, making it resist the stresses in a similar fashion. The model is depicted in Figure 12.2.

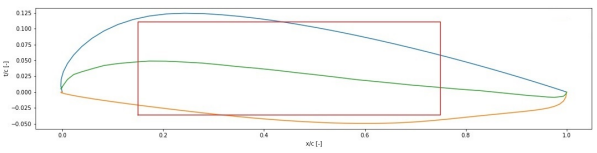

Figure 12.2: Model wingbox, in red.

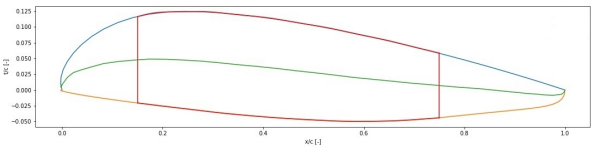

Figure 12.3: Shape of the wingbox, in red.

The spars are placed at 0.15 and 0.75 of chord to allow for engine placement on the leading edge for control surfaces on the trailing edge.

12.2.2. Structural analysis

While modelling loads, all derivatives and integrals are computed quasianalytically (as cosines and sines are approximated by their Taylor expansions) the discretisation error is close to zero. This is with the exception of the aerodynamic loads (lift and drag), which are first regressed with polynomials and then integrated symbolically. This entailed first making free body diagrams, Figure 12.4 and Figure 12.5, depicting the lift and drag distributed on the wing as a function of the spanwise position. The weight of the wing is assumed to be uniformly distributed along the wingspan due to high taper ratio. The thrust and weight of each engine is modelled by a point load on multiple points along the span.

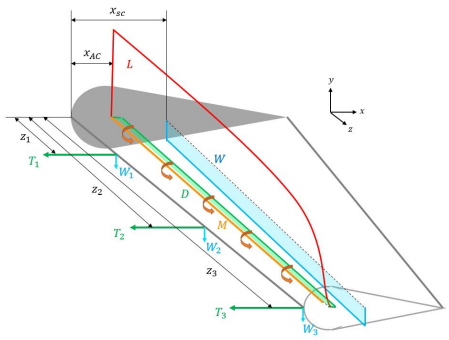

Figure 12.4: Loads on the wing during cruise, not to scale.

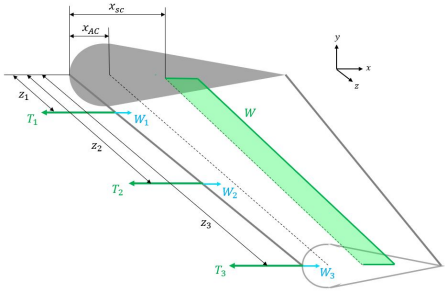

Figure 12.5: Loads on the wing during vertical take-off, not to scale.

Once the reaction forces at the root of the wing are computed using simple equilibrium equations (ie. ensuring the net resultant force and moment is zero) and assuming the root of the wing to be a fixed support, the internal load diagrams are generated using programmatic Macaulay step functions, Figure 12.6 and Figure 12.7. It is evident that the maximum stress is to occur at the root of the wing in cruise configuration.The stresses are computed using the following formulas for shear flow and bending stress [80]:

$$\sigma_z = \frac{M_x y}{I_{xx}} + \frac{M_y x}{I_{yy}} \qquad q_2 - q_1 = \int_{s1}^{s2} \frac{\delta q}{\delta s} ds = -\frac{V_y}{I_{xx}} \int_{s1}^{s2} tyds - \frac{V_x}{I_{yy}} \int_{s1}^{s2} txds \tag{12.2}$$

Where x and y can be parameterised in terms of s given the rectangular geometry. In addition to this, forces acting away from the shear centre produce torque, which further adds to the shear flow, with the shear centre of the model wingbox being coincident with its centre of gravity. This is simply $q = T/(2A)$, where A is the enclosed area of the wingbox. The main contributor to torque around shear centre is lift, due to both large magnitudes and moment arms.

The points of maximum stresses are computed using the recursive interval minimisation (golden search) algorithm. Finally, the Von Mises stress is calculated in order to combine the normal and shear stress with the following formula: $Y = \sqrt{3 \cdot \tau^2 + \sigma_z^2}$ [80]. The failure criterion for Von Mises stresses is usually defined by the tensile yield strength of the material.

Buckling, specifically Euler buckling, is an important failure mode of the structure. Without any stiffening structures, the skin, with the top panel of the wingbox, would buckle at a stress of under 20 MPa, which is not at all desirable. The critical buckling stress of a sheet is defined in Equation 12.3 [81].

$$\sigma_{cr} = C \frac{\pi^2 E}{12(1-\nu^2)} \left(\frac{t}{b}\right)^2 \tag{12.3}$$

$$\sigma_{cc}^{(i)} = \alpha \left[\frac{C}{\sigma_y} \frac{\pi^2 E}{12(1-\nu^2)} \left(\frac{t}{b}\right)^2 \right]^{1-n} \sigma_y \tag{12.4}$$

where E is the Young's modulus, ν is the Poisson ratio, t is the thickness. C is a function of the aspect ratio of the plate and the boundary conditions of the plate, how it is obtained is shown in Figure 12.8, and finally b is either the stringer pitch or the length of the flange, depending on what structure is analysed. α and n are correctional factors, in most cases equal to 0.8 and 0.6, respectively [81].

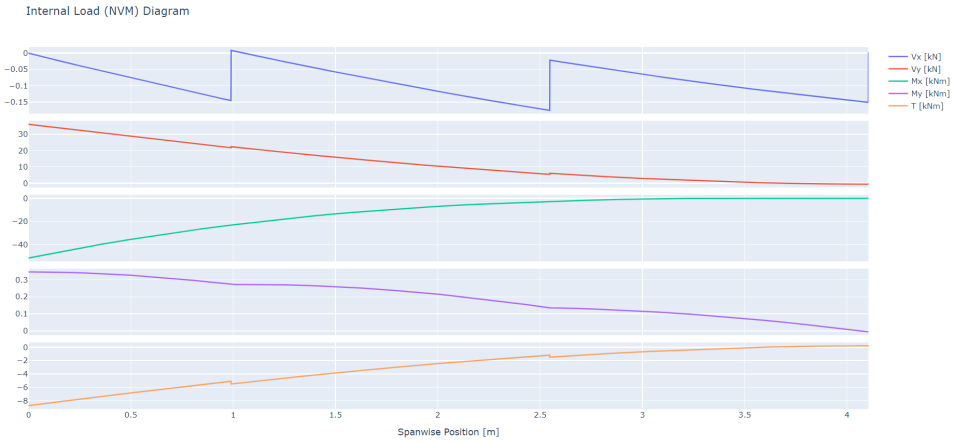

Figure 12.6: Internal load diagrams in cruise.

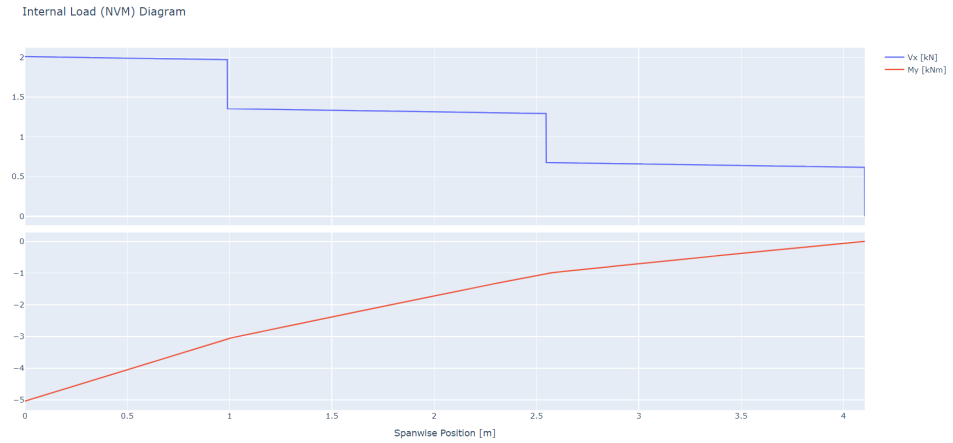

Figure 12.7: Internal load diagrams in take-off with maximum thrust.

To take into account the stringers, their respective critical crippling stress should be computed. In this case crippling and not buckling is considered since each part of the stringer, i.e flanges and webs, are taken into account. This can be done using Equation 12.4. The stringers under consideration are shown in Figure 12.9. During the computation of the buckling stress, a careful approach is taken when determining the boundary conditions of an individual flange. In essence, the flanges that have one free edge have a C of 0.425, causing them to cripple sooner. The flanges that have no free edges, i.e. the vertical flanges, have C equal to 4.

To analyse the Euler buckling of the stiffened panel, a weighted average of the skin and and the stringer critical stresses is taken, instead of analysing the buckling stress of each element individually. However, there is one more effect to consider. The segment of the skin that is directly affected by the stringer will buckle at the same stress as the stringer itself, giving a definition to the 'effective' skin width. This dimension is obtained by the equation of the critical buckling stress of the skin and the crippling stress of the stringer, resulting in Equation 12.5 obtained from [81]. In essence, the structure is considered to fail in buckling when the entire structure, both skin and stiffeners, has buckled.

$$2w_e = t\sqrt{\frac{CE\pi^2}{12(1-\nu^2)\sigma_{ccstr}}} \tag{12.5}$$

For a large panel with a thin skin the torsional stiffness of the stringer is large with respect to the force twisting it, thus producing a clamped edge condition - SSCC [81]. This corresponds to C of 6.98. Otherwise, the boundary condition would again be simply supported on all edges (SSSS), making $C = 4$. This effect additionally stiffens the panel even further.

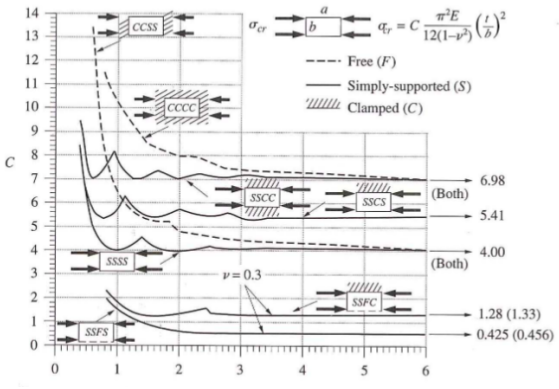

Figure 12.8: Coefficient C versus aspect ratio for several boundary conditions [33].

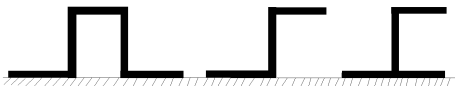

Figure 12.9: (from left to right) Hat, Z, and J stringer cross-section geometries.

12.2.3. Stringer configuration

Stringer pitch and the size of the stringers heavily depends on the stresses induced in the wing at the respective location along the span. The respective stringer geometry under consideration are shown in Figure 12.9.

For instance, taking Aluminium 2024-T4 as a material for both the sheet and the stringer, a wingbox with the top panel being 1m long and having 8 stringers, making stiffener pitch 11.1cm gives the results show in the Table 12.1. All the stringers analysed have the same cross-sectional area - 130 mm^2.

Table 12.1: Performance of different stringers with the same cross-sectional area.

Type	σ_{crskin} [MPa]	σ_{ccstr} [MPa]	$\sigma_{crpanel}$ [MPa]	$\sigma_{crpanel}/A_{panel}$ [MPa/mm^2]
'Hat' stringer	42.74	189.35	176.48	0.087
'Z' stringer	42.74	104.10	134.29	0.066
'J' stringer	42.74	120.83	140.72	0.069

It is clear from Table 12.1 that the 'Hat' stringer is the most efficient when it comes to preventing buckling. The biggest contributor to such performance is the high crippling stress. Having a simple and continuous geometry points to ease of manufacturing. Nonetheless, the 'Hat' stringer would require more rivets for its installation, adding to the labour cost and weight. On the other hand, labour cost is easily reducible with time through the learning curve. Thus the 'Hat' stringer is chosen.

Moreover, the stiffened panel buckling possesses high sensitivity when it comes to the addition of the stringers, for a sample panel of 0.6 m, with each stringer adding about 20 MPa to the critical Euler buckling. This can be seen in Figure 12.10.

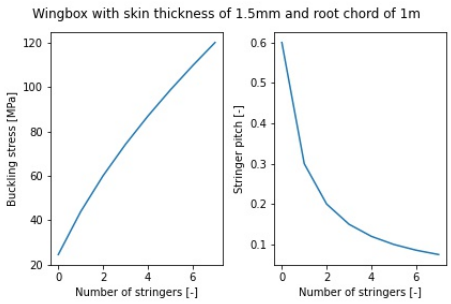

Figure 12.10: Sensitivity of buckling stress with respect to the stringer addition.

12.2.4. Results

Having analysed the internal loads caused in the structure in the cruise configuration it was possible to produce a wingbox design that bears the ultimate loads. These were calculated for an ultimate load factor of $n_{ult} = 5.1$, as described in Section 12.1.1. The resulting parameters of the wingbox are showcased in Table 12.2.

Table 12.2: Final wingbox parameters

σ_{max}[MPa]	τ_{max}[MPa]	σ_{cr}[MPa]	VM_{max}[MPa]	$No.str_t$[-]	$No.str_b$[-]	t_{skin}[mm]	t_{spar}[mm]
-58.26	268.57	63.76	468.82	2	1	1.3	18.7

The stringers have a cross-sectional of 166.5 mm^2. A thick spar can be explained by large shear stresses occurring in the horizontal plane of the wingbox. It was also found that bending loads were not as critical, hence giving low number of stringers and a thin skin. Bending stresses were observed to go down significantly after the thickening of the spar. Given that the structure withstands the ultimate loads, 5.1, without failing, requirements VTOL-STS-1, VTOL-STS-1-STR-1, VTOL-STS-2 and VTOL-STS-2-STR-1 that state that the structure should be able to withstand nominal and ultimate loads without permanent deformation are complied with. As mentioned earlier, a safety factor of 1.5 has been applied to all calculations, satisfying requirement VTOL-STS-2-STR-4.

As the deflection of the wing is not a critical failure mode as the loads towards the tip are dramatically lower and less critical than those in the root, VTOL-STS-2-STR-2 is considered to be compliant for all plausible ranges of deflections.

12.3. Fuselage Design

Fuselage design is inherently different depending on what type of aircraft is being designed. In the case of Wigeon, the cabin is not pressurised due to a low cruise altitude and fuselage mainly has to withstand only aerodynamic loads, support payload weight, and serve as an attachment point for the wings, landing gear and vertical tail. The skin can be considered non-load bearing, again due to lack of pressurisation.

12.3.1. Frame Design

When it comes to the shape of the fuselage, due to a lack of pressurisation, a circular fuselage is not a necessity. Moreover, this makes requirements VTOL-PLD-4 and VTOL-PLD-4-STR-1, relating to withstanding circumferential loads, irrelevant. Following the same justification, the bulkheads can then also be omitted. It is however important to minimise the drag contribution, as the fuselage has a relatively large frontal area. The aerodynamic design of the fuselage is done in Chapter 7 and this section deals only with the structure of the predetermined fuselage shape.

The frame of the fuselage is composed of a simple and lightweight structure with frames and longerons, allowing to shape the skin in a streamlined manner. An example of this is show in Figure 12.11. Relative positions of the central wingboxes going through the fuselage structure, as well as the floor, are shown too. A unique feature of the fuselage is the large window spanning most of its surface, can be seen in Figure 19.1. However, the inside structure of the fuselage remains unchanged by that, as the windows are still separated by the frames behind the transparent surface. This is done because the fuselage has to carry torsional and shear loads, and having such a large cutout would not be optimal for such load transfers.

Although a detailed design of the fuselage has not been done, the payload is relatively light compared to the battery. Hence, it can be assumed, even though not officially proved, that the fuselage can support at least 380 kg of payload, as per requirement VTOL-PLD-2-STR-1.

12.3.2. Wing rotation mechanism

One important requirement for the wing rotation mechanism is that the right and left wings must be rotated at the same angle at all times, to reduce the number of possible failures in hover mode. The rotation mechanism also needs to be precise and be able to lock in the hover and cruise positions. It is also desirable for the mechanism to a sufficient rotation speed. Above all, the failure probability must be as small as possible, because a failure during the transition phase is likely to lead to a crash.

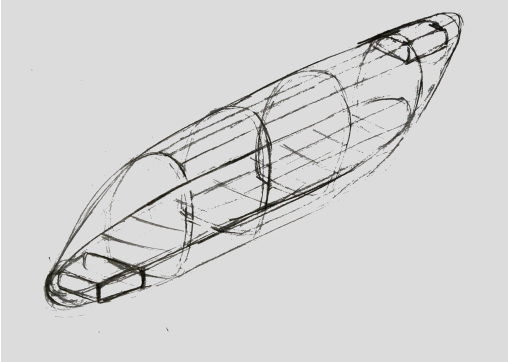

Figure 12.11: Fuselage frame sketch (not to scale).

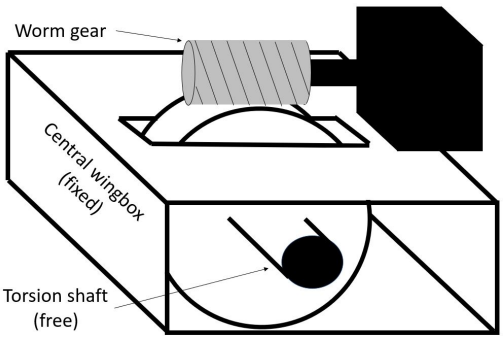

Figure 12.12: Worm gear cutout in the wingbox

All these requirements are perfectly met by a simple worm gear powered by an electric servo. It is precise, self-locking (preventing backdrive), reliable, and it can power a shaft that rotates both sides of a wing simultaneously.

As can be seen in figure 12.12, the worm gear spins the output gear, which is connected to a hollow circular torsion shaft passing through the inside of the central wingbox section. The central wingbox from figure 12.12 is not attached to the main gear. The wingbox stays in place while the gear and shaft rotate inside of it. The electric servo spinning the worm gear can be attached to the wingbox surface or to a separate fuselage frame if needed. As seen in figure 12.13, the translation of the aforementioned shaft is constrained to the central wingbox by bearings, but it's still free to rotate with respect to the wingbox. The use of those bearings has two goals: to prevent the shaft from bending and disconnecting the gears, and to transfer some bending loads from the shaft to the central wingbox. Going into the rotating part of the wing, the shaft connects rigidly to multiple ribs in the wingbox to gradually introduce the loads into the structure. This is also demonstrated in figure 12.13

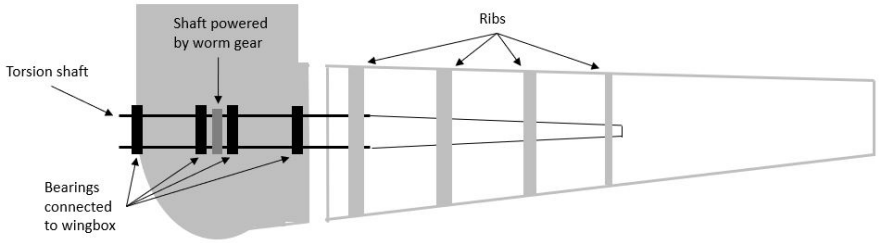

Figure 12.13: Wing rotation mechanism sketch

The most critical part of the shaft is where the central wingbox is connected to the outside wingbox, because that is where all the bending loads are carried by the shaft alone. In further design, the cross section of the shaft should be optimised, considering both the yield strength and the critical buckling stresses. To decrease the shaft's weight, its thickness and diameter can gradually decrease towards the outside of the wing. In a more detailed weight optimisation, the variation of thickness and diameter can also be explored to the inside of this critical point.

The chordwise position of the torsion shaft can also be chosen to minimise the forces required to rotate the wing, thus reducing energy usage. However, due to the difficulty of aerodynamic analysis in transition flight, the shaft positioning cannot be accurately optimised at this stage of the design. For simplicity, the shaft is positioned at the quarter chord location, since the sweep angle is zero and the thickness of the airfoil is the largest, so the inscribed circular shaft is structurally the most efficient. Since the front spar is at 15 % of the chord and the maximum shaft radius that fits in the airfoil is less than 10 % of the chord length, there is no physical interference for placing the shaft at quarter chord.

Since the torsional shaft going into the rotating wing also has its own bending strength, the wingbox at the root of the rotating part of the wing is now severely overdesigned, as both the shaft and the wingbox can

carry the maximum cruise loads with a safety factor by themselves. One solution to fix the overdesign is to decrease the thickness of the wingbox's spars and instead use the torsion shaft as a single large spar. Another way to decrease the mass, since the cruise gust condition introduces much higher bending moments than the hover condition, is to decrease the shaft's thickness and use a locking mechanism to transfer bending loads from the outside wing to the central wingbox in cruise configuration.

Lastly, a proposed alternative wing rotation mechanism which does not fall victim to this issue is one that keeps the central and outside wingboxes connected and rotates the whole wing assembly. In the future, both options shall be explored in more depth. It is worthwhile to note the pitfalls of both mechanisms; the former is highly aerodynamic, but has more structural concerns due to stresses being concentrated in a small beam and the beam / rotation mechanism being a singular point of a critical failure. The latter of the two is highly effective structurally, as the structure compares to a conventional aircraft but is poorer aerodynamically due to the dynamic repositioning of the skin. This additional mechanism of covering up the part of the skin that was previously occupied by the wingbox will occupy additional mass.

12.3.3. Fuselage-wing attachment

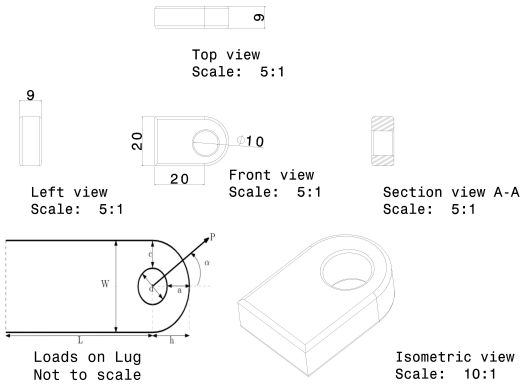

Figure 12.14: Lug geometry & Loads

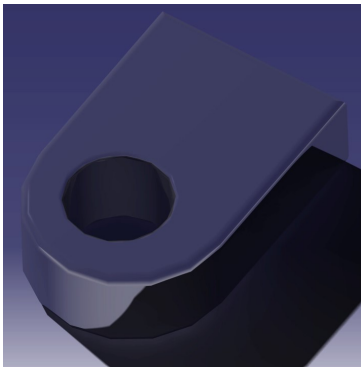

Figure 12.15: Render of Wing-Fuselage Lug

As mentioned earlier, the fuselage acts as an attachment point for wings and the vertical tail. The wings carry the largest loads of the aircraft and thus the attachment must be sufficiently strong in order to withstand the loads transferred from the wing to the fuselage. Therefore, four lugs are used on each wing and the vertical reaction force and moment about vertical axis are combined to determine the load on the lug. The lugs are attached between the two spars to the fuselage frame on both ends of the fuselage. Firstly, the parameters c and a are constraint to be greater than 5 mm to prevent net section and shear tear out failure, respectively. The lug is to be made of aluminium 7075-T6, which permits the calculation of mass with an length of 2 cm.

Looking at the geometry in Figure 12.14 it is evident that the lug geometry can be altered in order to best carry the required loads from the wing. In order to do this, the reaction shear force from the wing was combined to produce the loading P on the lug at an angle α. The main geometric parameters of the lug include the a, d and c parameters seen in Figure 12.14 as well as the (in-plane) thickness of the lug. The method used in sizing this lug was similar to that used by Larsson [67] which relates the shift in SN curve of a reference lug (with $a = c = d = 10[mm]$), with the size and shape of the design lug with the following equation:

$$\frac{\sigma_{a_{\text{nom}}}}{\sigma_{A_{\text{nom}}}} = 1 + \theta \cdot (k_1 k_2 - 1) \qquad k_1 = \sqrt{\frac{ad}{c^2}} \qquad k_2 = \left(\frac{10}{d}\right)^{0.2} \tag{12.6}$$

In the equation, $\theta = 0.25 \log N - 0.5$ if N is in the range of 1000 to 1000000 and $\theta = 1$ for larger N, is the cycle correction factor to account for it being a high or low cycle [67]. The value of N is computed with the SN curve of the reference lug. The stress (of the nominal or net-section stress) of the analysed lug is denoted by σ_a and that of the reference lug, σ_A. Through this, the load was computed by dividing the force applied, P, by the nominal area, $2ct$ for the reference lug with the same thickness as that of the one being analysed. Thereafter, this is substituted into Equation 12.6 in order to compute the equivalent nominal stress in the lug.

Finally, in order to find the real stress around the hole, a stress concentration factor (K_t) was used which is the ratio between the net-section and maximum stress, which is the one that is used to compute the fatigue cycles given a stress amplitude, as shown below [67]. Furthermore, a correction factor was applied in terms of the eccentricity (a/c) of the lug to account for the angle of application of the load, K_α. This method is used in the thesis [64] in conjunction with Larsson's method [67]. With these two factors, the peak stress of the lug can be computed by multiplying these factors and ratios by the stress applied, as displayed below.

$$\sigma_{a_{\text{peak}}} = K_\alpha K_t \left(\frac{\sigma_{a_{\text{nom}}}}{\sigma_{A_{\text{nom}}}} \frac{P}{2 \cdot 10 \cdot t} \right) \qquad K_t = 3.8 \left(\frac{c}{a} \right)^{0.2} \left(\frac{c}{d} \right)^{0.5} \qquad K_\alpha = \alpha(0.007\frac{c}{a} - 0.008) + 1 \quad (12.7)$$

Through this, it is possible to see how the loads and geometry directly impact the stress in the designed lug. In Section 12.5 the modelling of fatigue cycles based on the applied stresses is discussed. The final lug parameters are determined to be a = c = 5mm due to the prevention of net section failure (and shear out when loaded in tension) with a load of P = 3124 N, α = 2.12 degrees. The diameter of the hole is 10 mm which is determined by the bolt. Research shows 10 mm bolts can withstand 9 kN of shear force [45]. This leaves the thickness to be 8 mm in order to not fail in fatigue. The mass of the optimised lug (made of aluminium 7075-T6) is calculated to be 16 grams with a length of 20 mm. Upon performing a Computer Aided Design, the mass is recomputed to be 12 g. The design life of the lug under the current loads is 46000 flights. A model of the lug is presented in Figure 12.15 and a technical drawing to be used for manufacturing is also provided in Figure 12.14.

12.4. Material Selection

Materials are to be selected based on performance but also taking into account the price and sustainability of the material. Furthermore, the manufacturability of the material in question must also be taken into account. First, the material of the wingbox and stringers is determined.

In order to select the material, a material index is derived using a cost function, which is essentially structural mass. However, it is paramount to indicate the primary type of load applied on the structure. This is derived from the stiffness of a cantilever beam in bending. As the wing is composed of a set of panels that shall be light and stiff, the material index is similar in nature to that of a single light stiff panel, shown below along with the definition of stiffness (Keep in mind that considering the stiffness is a requirement obtained from loads, it is not substituted into the left equation), k^*:

$$m = \left(\frac{12k^*}{C_1 b} \right) \cdot (bL^2) \cdot \left(\frac{\rho}{E^{1/3}} \right) \qquad k^* = \frac{C_1 \cdot E \cdot I}{L^3} \quad (12.8)$$

The material is chosen to minimise the cost, $\rho \cdot E^{-1/3}$, and secondarily material cost (as cost in general is optimised with an optimal mass). However, there are additional constraints imposed prior to the selection. Firstly, only metals are considered for the design of the wingbox for their desirable properties, namely their fatigue resistance, which is described in Section 12.5. As composites are governed by even more stochastic processes compared to metals, which are augmented by their brittleness, the fatigue life is a more complex and unpredictable design parameter. Furthermore, their production and material cost far exceeds those of metals, making them less than ideal. They also present health and safety risks due to their abrasiveness and their susceptibility to carcinogenesis, making them less socially sustainable compared to their metallic counterparts. Many times they also require hot curing, which requires additional equipment, further increasing cost. It is also more difficult to inspect composites, which can exacerbate the detrimental effects of corrosion and fatigue, two of the most common reasons why aircraft fail. [28]

However, metals also do not come without their shortcomings either. They are more reactive and less stiff [8]. That being said, they are still be used for their isotropic and predictable design characteristics. With that said, a set of metals was compiled, and ranked based on the material index mentioned above. Upon

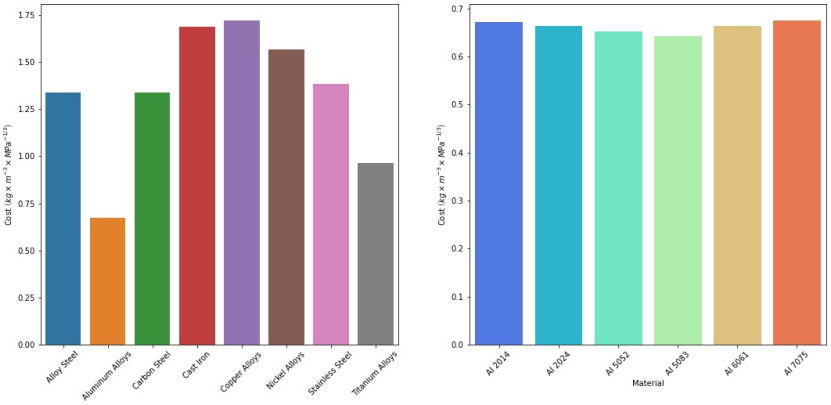

Figure 12.16: Material Cost Function and Selection (higher cost means less desirable)

running the analysis, it was found that the aluminium alloys had the best performance with titanium being a close second. The analysis can be summarised by Figure 12.16.

It can be seen that the best performing alloy is Al 5083, with the lowest cost value in terms of the material index. With this in mind, upon further research it could be claimed that this alloy is a good choice due to its corrosion resistance and low cost, despite its high performance. Furthermore, it has a particularly broad range of production techniques including being one of the cheapest aluminium alloys that can be superplastically formed [32]. That being said, Aluminium 2024-T3 is selected for the aircraft skin. However, its yield strength lacks compared to Aluminium 7075-T6 which is acceptable as the skin of the fuselage does not carry pressure loads and therefore simply has to withstand the weight of the cabin.

Therefore, the one that is selected (given that all aluminium alloys perform similarly well in terms of the cost above), Aluminium 7075-T6 is the one that is selected for the wing structure, including the box and stringers. This is because this alloy is heat treatable, has particularly good corrosion resistance, and thereby boasts an extremely high yield strength of 468 MPa. One downside of this one is its proneness to embrittlement, making it more susceptible to fracture, as well as fatigue crack growth [9]. However, considering its performance and its history of use in aerospace and other automotive applications, Aluminium 7075-T6 seems to be the ideal material for the critical load bearing structures. That being said, considering its susceptibility to microsegregation, a fatigue analysis is conducted in Section 12.5.

In Figure 12.17, the materials used in this aircraft are displayed. For those used in non-structural components such as the cabin, commercial aircraft are deemed to be representative. However, a detailed selection of textiles is not performed due to them having little impact on the structure of Wigeon.

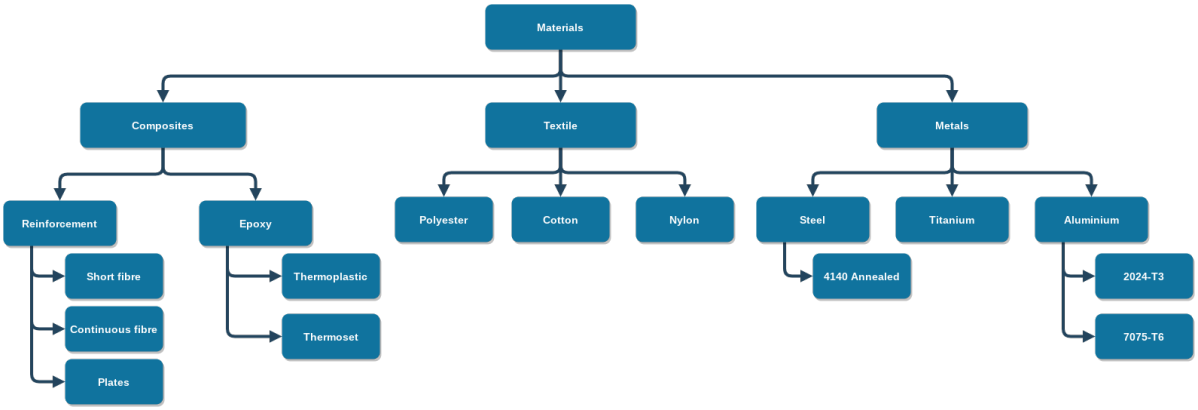

Figure 12.17: Materials most commonly used in the aircraft

12.5. Design Against Fatigue

In order to design against fatigue, the complex and highly stochastic phenomena governing fatigue must be analysed for the structures chosen and the life of the structure is thereafter computed by means of a semi-empirical method.

Firstly, a load cycle for a flight was determined, with the stresses computed for each loading scenario (on the ground, in cruise and in hover mode) and the turnover time incorporated to determine the ground-air-ground cycle. Then, noise in a range of frequencies were added in order to simulate the stochastic gusts, taxiing loads and acoustic loads, as specified in Figure 12.3 and using stress estimations for amplitude [112], shown in the following equation. This assumed the loads could be modelled by a Gaussian model with a standard deviation of roughly $1/3$ of the difference between the mean (zero) and maximum. This then used a normalised Fourier series to simulate the loads at varying frequencies.

$$A(t) = \sum_i A_i \sin(2\pi f_i t) \tag{12.9}$$

Type of load	Character	Number of cycle in the design life time	Period of 1 cycle
ground-air-ground transition cycle	deterministic	10^3 to 10^5	10 min to 10 hrs
pressure cycle of the cabin		10^3 to 10^5	10 min to 10 hrs
maneuvers		4×10^3 to 4×10^5	10 sec to 3 min
turbulence (gusts)	random	10^5 to 10^6	0.1 sec to 10 sec
taxiing loads		10^5 to 10^7	0.05 sec to 1 sec
acoustic loads		10^7 to 10^8	0.001 sec to 0.01 sec

Table 12.3: Periods of different loads on an aircraft structure

The result is the full ground air ground cycle, neglecting manoeuvres. As manoeuvres usually have a relatively similar load factor compared to cruise (although generally little higher), this assumption is valid for the case of this aircraft. The result of which is displayed in Figure 12.18.

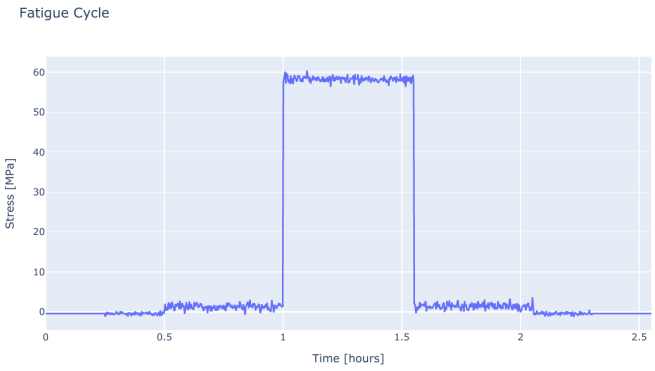

Figure 12.18: Graph showing the fatigue cycle of one flight

As this is a complex variable amplitude load cycle, it could not be analysed directly with the current modelling techniques present. So in order to simplify it so that it could be analysed, the rainflow counting algorithm was used to count the set of load ranges. It can also be seen as segregating the complex variable amplitude load cycles into a set of constant amplitude loads. However, this method does not come without limitations. Firstly, if a small variation is present in the midst of a large load range, the counting algorithm might disregard that in favour of the large load. Secondly, while the algorithm is capable of counting the number of cycles, the information pertaining to the sequence thereof is unavailable [112].

As a result, the time series definition of the fatigue cycle given above is extraneous in the present analysis as only the cycles are extracted therefrom. However, due to the number of cycles being known, the total flight and turnover time can be used as an approximation for the period of the ground air ground cycle. Through this, the design life of the structure can be readily determined.

Once the set of constant amplitude loads are known, their fatigue lives can be determined through the use of the material's Basquin's equation: $S_a^k \cdot N_f = C$ in which S_a is the constant stress amplitude applied, N_f is the number of cycles until failure, and k and C are empirically determined constants. With the material selected and SN curve data the number of cycles can be calculated for each constant amplitude cycle given by the rainflow counting algorithm. The assumptions used in this is that the structure is a continuum with no cracks [112]. In the case of the lug analysis, a regression analysis was performed for the alloys 2024-T3 and 7075-T6 for the reference lug from [67].

This plays a role in the safe-life design philosophy, in which the part shall be replaced after a certain amount of time (ie. design life). It is evident from the fact that this is an empirical relationship that experiments using the same stress amplitude do not necessarily result in the same fatigue life [112]. The model does not account for the size effect [112] which states that the fatigue strength of larger structures is generally less than that of smaller ones due to the increased probability of weak spots for crack nucleation. In order to compute the loads on the wing-fuselage connection lug, it is assumed that each pin carries one half of the shear as well as normal stresses encountered by the wing (see Figure 12.14). With this, and combining the horizontal and vertical reaction forces into one force (P) and direction (α) it was possible to determine the loads on the lug in the air and on the ground.

Another principal in designing against fatigue is the damage tolerance and risk management philosophies. For the former, it is to assume that the structures have cracks to be sure that the aircraft will not fail, and by doing so, using non-destructive testing methods (such as mechanoluminescence film) to detect cracks and repair parts prior to their failure. The latter is to minimise the occurrence of failure and risk as much as possible by predicting fatigue crack growth and other relevant phenomena. In order to model crack growth the Paris Law was used, which models the linear range of the rate of crack growth with respect to the range of stress concentration [112]:

$$\frac{da}{dN} = C \cdot (\Delta K_{eff})^m \quad (12.10) \qquad D = \sum_i \frac{n_i}{N_i} \quad (12.11) \qquad a_f = a_0 + \sum_i \Delta a_i \quad (12.12)$$

Where ΔK_{eff} is the effective stress intensity factor, which is defined below. The number of cycles is then determined using numerical integration. The critical point that is chosen for the fatigue crack is the top right corner of the wingbox at the root of the wing, as that is the structure under the largest stresses and is also the most critical point of failure for the wing: the most critical load bearing structure of the aircraft.

The Paris law has two major limitations. Firstly, it does not account for the stress ratio ($R = K_{max}/K_{min}$), which does affect the crack growth rate. Secondly, though it is an empirical relationship, it does not account for the asymptotic regions prior to and after the linear region of crack growth [112]. While this can be overcome with other methods, due to the lack of data this was not used and as a preliminary prediction the Paris Law was deemed as an acceptable estimate. For crack growth due to varying amplitude, Equation 12.12 is utilised, with Δa being computed by the Paris law for each load cycle. This model does not account for plasticity induced crack closure, which is modelled using the Elber mechanism [112] for Aluminium 2024-T3, given by the equation [112]: $\Delta K_{eff} = (0.5 + 0.4R)\Delta K = (0.5 + 0.4R)\beta\Delta S\sqrt{\pi a}$.

However, there is a major limitation to the above as the alloy employed is Aluminium 7075-T6 whereas the above relationship was found for Aluminium 2024-T3. Once each stress range's cycles to failure is computed (using the SN curve), the Miner's Law (Equation 12.11) can be used to consolidate the total number of cycles until failure, taking into consideration each individual cycle and summing their respective damage to form a cumulative damage.

In the equation for Miner's Rule, D is the cumulative damage done in one flight, n_i is the number of cycles per flight for each stress amplitude and N_i is the number of cycles until failure of that constant stress amplitude,

determined by the SN curve. Once that is done, the design life can be converted using the period of the aircraft's ground air ground cycle, including the turnover time. Miner's rule also has several shortcomings which may impact the validity of the results. Firstly, the change in residual stresses due to past cycles are neglected, as it linearly adds the damage done. Secondly, it does not account for any of the stochastic or probabilistic phenomena associated to the occurrence of fatigue [112].

Overall, it is apparent that fatigue is a complex process that is difficult to fully model. However, given the fatigue life calculated, it is evident that for the most part it is not a critical failure mode in the design by itself. This is due to the fatigue life consisting of 135848000 cycles, which is more than 24000 flights a day for 15 years and the crack propagation life (for a crack positioned at the bottom right corner due to it being in tension for the largest part of the flight and in compression only on the ground), of 1116000 cycles. This is for a crack that is barely detectable by mechanoluminescence film to grow to half the thickness of the wingbox. However, it must be considered that cracks are most often found in connections such as lugs or joints due to high local stress concentrations in the edges. That being said, cracks often arise due to unforeseen circumstances, which make it imperative for periodic inspections to catch the cracks in time, considering most of the fatigue life is spent in crack nucleation rather than crack propagation. Therefore, inspections every 90 days are recommended for this reason, standard for such precautionary measures [43].

On the whole, VTOL-STK-15 requires and operational life of 15 years, and requirement VTOL-STS-1-STR-2 states that the number of flights it should endure before initiating cracks is to be determined. This value is now determined to be 4 flights a day for 15 years, which is 21915 flights. As the fatigue initiation phase is significantly longer than that it is considered compliant with both requirements. As a side note, the reason why 4 flights per day were assumed (and not 3, like it was assumed for battery cycles) is because the batteries are easier to replace, and expected to need replacement, and are hence less critical. With this, the number of cycles of the final lug as described in the section above, is over 40000 which is significantly larger than the necessary amount. With that said, it is evident by the lug analysis that fatigue is a much larger concern in joints in comparison to other structural components.

Also, considering the assumptions in the model used, as well as in the determination of the load cycle, the estimate of the fatigue life is quite conservative. This means that the design is likely to last for the full 15 years as required considering the number of cycles well exceeds that of 4 flights a day. That being said, the reliability analysis and validation of these results is yet to be conducted in the following design phase.

12.6. Corrosion

Corrosion is one of the most critical modes of failure in any aircraft [48]. There are several kinds of corrosion that occur, namely uniform, galvanic, crevice and pitting corrosion. The effects of which are elucidated below.

12.6.1. Localised corrosion

Localised corrosion is an attack on a specific region, in contrast to uniform corrosion which affects the entire surface. Like most alloys of aluminium, Aluminium 7075-T6 is quite resistant to uniform corrosion. That being said, it is particularly susceptible to localised forms of corrosion including pitting and crevice corrosion and is also soft and prone to wear [31]. This makes the operations and repairs more critical than for other alloys that have a failure mode that is easier to predict. This means that regular inspections must be performed in addition to those regarding fatigue cracks in order to assess possible locations of wear. This is due to the uncertainty involved in detecting pits when pitting corrosion occurs, as they are difficult to detect. They can also cause failure with very little weight loss [48]. This makes regular inspections and quality control a necessity.

Crevice corrosion is most likely to happen at joints or other stagnant regions with an electrolyte present [48]. Therefore, the points of assessment shall be those involving connections and other crevices in which a contaminant can appear. For the design, the joints and connections themselves should be overdesigned for the initial load in order to account for this decrease in performance. The critical area in which this can

occur include the wingbox at the root of the wing at the connection between the fuselage and the wing. Therefore, the design of components composed of Aluminium 7075-T6 must be designed to withstand a slight performance degradation, in addition to periodic inspections and quality control.

12.6.2. Galvanic Corrosion

Galvanic Corrosion is the corrosion of dissimilar metals in the presence of an electrolyte [48]. The definition of "dissimilar" is in varying positions on the galvanic series, which is an ordered sequence of metals by their steady state potential. When two metals with a large difference in potential are placed in contact the more reactive (ie. less noble) metal corrodes [134]. The presence of galvanic corrosion thereby incentivises the use of as few materials as possible, which is why most load bearing structural components are to be composed of Aluminium 7075-T6, and the skin of Aluminium 2024-T3.

12.6.3. Corrosion Fatigue

Recent studies have shown that pitting corrosion results in the nucleation of cracks which in turn has a detrimental effect on the fatigue life of the structure. Scamans et al [111] demonstrated the occurrence of fractures associated with pits in a structure made of Aluminium 7075-T6. As cracks usually initiate from a surface flaw, pits give crack propagation an opportunity to cause significant failures. This once again emphasises the importance of quality control and the conduction of regular inspections to detect surface abnormalities including (but not limited to) fatigue cracks as well as pits. As pits are formed relatively slowly, it is generally regarded that "corrosion pits [are] precursors to fatigue cracking" [111].

In addition, Branko N. Popov [96] states in Corrosion Engineering that "corrosion fatigue can be reduced by increasing the tensile strength of a metal or alloy." This is one of the main reasons why Aluminium 7075-T6 was chosen over another stiffer alloy that had a higher material index in Figure 12.16. Lastly, to avoid pits, periodic inspections are recommended (depending on the geographical location) every 15 days in severe zones, 45 days in moderate zones and 90 days in mild zones [43].

Due to the mechanisms outlined in this section, it is evident that the design, given it follows these principals is adherent to requirement VTOL-OPL-1. This is since the materials used in the structure are extremely corrosion resistant and precautionary measures are undertaken to actively prevent and mitigate the detrimental effects of corrosion.

12.7. Crashworthiness

Another important aspect of the final design is the crashworthiness analysis. This section analyses the behaviour of the aircraft during a well-defined crash situation. One scenario, from requirement VTOL-SAF-2, is a crash in hover configuration, in which the airplane must fall a maximum of 5 m, which results in a velocity of 9.9 m/s, after which the landing gear absorbs the initial part of the impact. After the full suspension displacement is used, it is assumed that the landing gear fails and does not carry loads anymore. The rest of the kinetic energy is absorbed by energy-absorbing structures placed below the fuselage floor. Another considered scenario is an emergency landing in cruise configuration, where it is assumed the pilot has enough control over the airplane to perform a hard landing on the "belly" of the fuselage. In this scenario the landing gear must be retracted to satisfy the requirement from CS-27.561(b)(2) [23]. Since the first scenario seems more critical, it is the one used for design of the structure, which is then tested for compliance with the second scenario.

To prevent injury to regular passengers, not necessarily sitting in perfectly upward positions, the maximum deceleration is limited to less than the 20g in a timeframe of 0.1 s shown in figure 12.19. After multiple iterations of the method described below, taking into consideration some multidisciplinary aspects, the acceleration of the cabin has been constrained to 8g for landing gear and to 11g for the energy absorbing structures. The difference in the landing gear's and the structure's acceleration is decided to prevent overdesigning the landing gear for normal operation, also knowing that landing gear assemblies are usually much

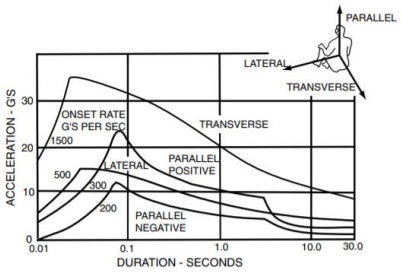

Figure 12.19: Limits of human tolerance to linear acceleration [18]

heavier than crushing structures. As a last note, a short initial peak to overcome the energy absorbing structure's stabilised compression strength lasts around 0.001 seconds [57]. Because of this short duration, the human body feels only an instantaneous velocity change. For the seated position and a time of 0.001 seconds, a maximum acceleration of 500g is survivable [37].

12.7.1. Landing gear design

The objective of landing gear, besides supporting ground movement, is safely decelerating the aircraft's vertical velocity during a landing, without damage to any components. In CS-23.473 (d), a hard landing's maximum vertical velocity is defined as 2.1 m/s, which is used in the following analysis as the maximum impact speed the landing gear should withstand without damage. At higher speeds the landing gear is allowed to fail, but it must do so in a safe way.

The critical requirement for a crashworthy design of this project states that the aircraft must perform a fall from 5 meters above the ground onto a hard surface without significant harm to passengers. This means the maximum impact speed on the landing gear is 9.9 m/s. Therefore, the landing gear must be designed to have a deceleration smaller than 8g on a 9.9 m/s impact and at the same time have sufficient stiffness and strut length to decelerate a 2.1 m/s landing without structural damage.

The landing gear is modelled as a 2D state-space system, with 2 spring-damper assemblies placed on a line, each spring damper assembly symbolising a set of 2 symmetrically placed landing gears. The geometry of the system is taken from section 11, and is demonstrated in figure 12.20, where the front landing gears have the numbers 1 and 2 assigned, and the rear landing gears have the numbers 3 and 4. The dimensions on the diagram can be seen in table 12.4

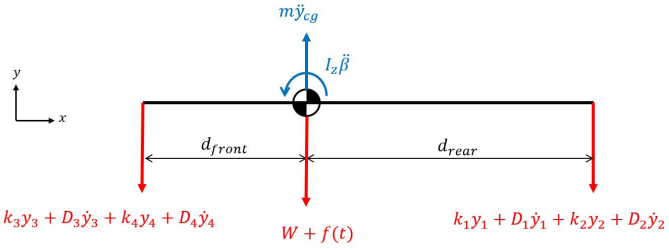

Figure 12.20: The free body and kinetic diagram for the landing gear model

Table 12.4: Wing planform parameters for the three concepts. For the double wing configurations, the values for one of the two wings are given.

Parameter	Values
d_{rear} [m]	2.35
d_{front} [m]	0.85
l_{strut} [m]	0.4
k_1, k_2 [N/m]	40100
k_3, k_4 [N/m]	80200
D_1, D_2 [Ns/m]	4050
D_3, D_4 [Ns/m]	8100

The model itself is governed by equations 12.13 and 12.14, with $f(t)$ modelling the impact momentum with a dirac delta function. These equations are converted to a state space system and solved for a time response of y, β and $\ddot{y}$ with Python's control module.

$$m\ddot{y}_{cg} = -k_1 y_1 - D_1 \dot{y}_1 - k_2 y_2 - D_2 \dot{y}_2 - k_3 y_3 - D_3 \dot{y}_3 - k_4 y_4 - D_4 \dot{y}_4 - W - f(t) \tag{12.13}$$

$$I_z \ddot{\beta} = d_{rear}(-k_1 y_1 - D_1 \dot{y}_1 - k_2 y_2 - D_2 \dot{y}_2) + d_{front}(k_3 y_3 + D_3 \dot{y}_3 + k_4 y_4 + D_4 \dot{y}_4) \tag{12.14}$$

Firstly, the landing gear system is tested at the crash velocity with an assumed initial ratio between the damping and spring constants of the rear and front landing gears, and an initial magnitude of those constants. This ratio is fine-tuned to get a reasonably small pitch angle response during the impact, because the aeroplane should not lean forwards or backwards significantly during landing. A small angle of forward pitch is allowed to increase the strength of the rear gears, to decrease the chance of failure in a conventional landing. Later, the magnitude of the spring and damper constants is fine-tuned to obtain a relatively constant vertical deceleration with a magnitude just below the maximum allowed acceleration, across the entire strut compression length, which is 0.4 m, again from section 11.2.3. The results of this process, including the vertical displacement and acceleration of the centre of gravity, and the pitch angle of the plane, can be seen in figure 12.21. Here black lines on the left graph symbolise displacement limits of the landing gears, l_{strut} from table 12.4 (which are the same as the displacement of the centre of gravity because of the very small pitch angle). The black line on the right graph shows the acceleration limit for the cabin. The spring and damper constants can be found in table 12.4.

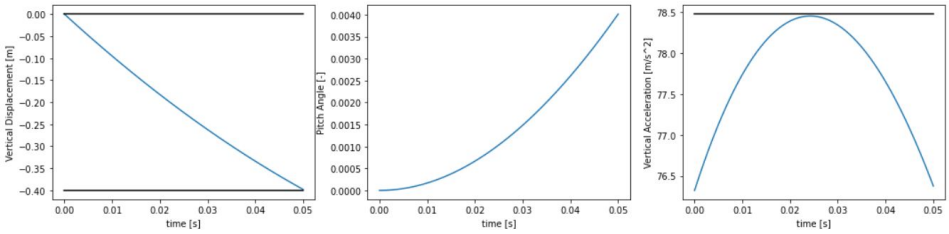

Figure 12.21: Landing gear behaviour in a 9.9 m/s crash

Another important result of the simulation to keep in mind for later is that just after the landing gear fails due to a 9.9 m/s impact, the main body is still moving towards the ground with a velocity of 6.0 m/s.

Finally, one more simulation is done with the optimised spring and damper constants to check if the landing gear survives a hard vertical landing with a velocity of 2.1 m/s. As can be seen in figure 12.22, the landing gear compresses to around half of its stroke length. The pitch angle response is once again comfortably small, and the passengers would accelerate upwards at a rate of about 1.2g, so they would feel an overload of just 2.2g, which could be considered comfortable for the given situation of a hard landing.

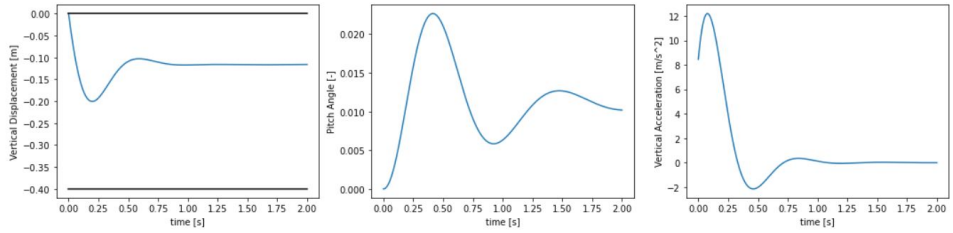

Figure 12.22: Landing gear behaviour in a 2.1 m/s vertical landing

12.7.2. Energy absorbing structure sizing

In the first scenario, after the landing gear reaches its limits and fails, the rest of the energy has to be absorbed by energy absorbing structures below the cabin. There are multiple options for such a structure, for example metal rings, tubes, or a hexagonal matrix [129]. The energy absorbing structures aim at limiting the deceleration on impact to 11g, excluding a short initial peak of much larger acceleration.

The central fuselage's vertical velocity of 6 m/s must be dissipated in a safe way. With a constant acceleration of 11g, 0.17 m is the necessary deceleration distance. The aerodynamically optimised fuselage has a total of 0.65 m of width with this minimum height below the cabin floor.

After researching aluminium, aramid and glass fibre honeycomb structures, the aramid composite material was chosen for its low density. The product with the lowest stabilised compression strength (0.6 MPa) from the aramid structures from HEXCEL [57] was chosen, so that the deceleration loads can be distributed along a greater area, and if the available area is exceeded, a stronger layout can be chosen. The stabilised compression stress, however, is only a short peak stress, which after being overcome, is reduced to the relatively constant crushing stress, which is the stress used for sizing. From composite honeycomb structure crushing experiments [38], it can be found that the crushing stress for a honeycomb structure is around 23 % of the stabilised compression strength. The area of the crashing structure is determined as 1.39 m^2, which is distributed in a strip along the middle of the cabin length, to allow space for the front landing gears next to the pilot. The strip dimensions are summarised in table 12.5.

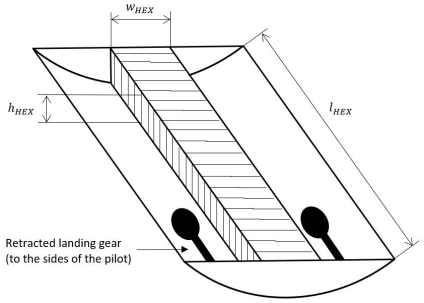

Figure 12.23: Sketch of energy absorbing structure placement

Table 12.5: Wing planform parameters for the three concepts. For the double wing configurations, the values for one of the two wings are given.

Parameter	Values
w_{HEX} [m]	0.375
l_{HEX} [m]	3.70
h_{HEX} [m]	0.167
m_{HEX} [kg]	5.3

With a density of 23 kg/m^3, the entire energy absorbing structure has negligible mass, seen in table 12.5. The landing is urgent, but the pilot still maintains control of the aircraft, at least in gliding flight. It is also assumed the pilot can perform a hard landing on a nearby runway, street or field. Additionally, the landing gear fails and remains retracted to satisfy the requirement from CS-27.561 (b) (2) [23].

12.7.3. Additional considerations

Firstly, batteries should not be placed below the passenger cabin as stiff elements do not provide gradual cabin deceleration during a crash and batteries become a fire hazard during a crash. Instead, considering flight stability, all the batteries are placed inside the nosecone. The battery volume is visualised in figure 2.2b. Because of the batteries' proximity to the pilot, special care should be taken to minimise the risk of fire.

Hard landing injuries can be minimised by including properly designed seat belts and by designing the fuselage frame structure to not deform significantly during a standard crash, to prevent the cabin surfaces deforming into the passengers and keeping the exits operational. This should be achievable, since the frame only experiences the maximum deceleration of 11g. The frame should also be reinforced at its front and back ends to provide extra strength close to where the nose and tail cones shear off.

12.8. Aeroelasticity

Flutter is an important and sometimes overlooked phenomenon in aircraft design. It is the vibration of the structure usually encountered at high speeds. Two kinds of flutter are explored, the wing divergence and propeller whirl flutter. The wing geometry was assumed to be a thin walled rectangle, with a mass moment of inertia about the axis which it rotates. For whirl flutter, the propeller and connection geometry is modelled as a rotating disk on a cylinder. These are consolidated using their individual steiner terms, which is the product of their mass and the square of their distance to the axis about which they rotate: $M \cdot d^2$.

12.8.1. Wing Divergence

Divergence is an aerodynamic phenomenon through which the lift on the wing increases the angle attack due to the deformation, that further perpetuates the magnitude of the lift.

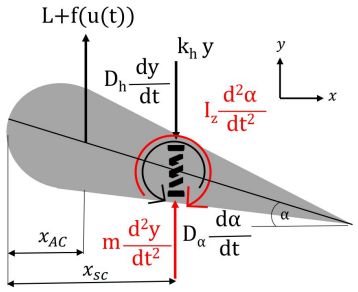

Figure 12.24: Free body and Kinetic diagram wing divergence

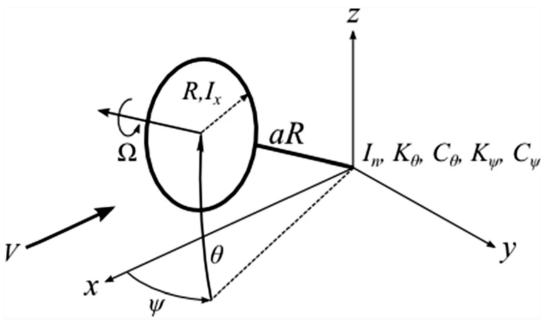

Figure 12.25: Motion of the propeller in two angular degrees of freedom [72]

In order to model this the wing is approximated by a vertical spring and a torsional spring. The resulting spring damper system has two degrees of freedom, one rotational and one vertical translational movement as shown in Figure 12.24. In order to make this problem two dimensional and linear several assumptions were used. This includes the assumption that torsion, weight and lift are uniformly distributed along the wingspan, and that there is negligible horizontal translation. Furthermore, the initial position is set to be at $y = 0$ and angle of attack, $\alpha = 0$, which includes the deformation due to the weight of the wing and engines, as well as aerodynamic loads without disturbances. Through this, the following equations could be derived:

$$M\ddot{y} = C_{L_\alpha}\alpha qS - k_h y - C_h\dot{y} + (q/V)C_{L_\alpha}Su \tag{12.15}$$

$$I_z\ddot{\alpha} = C_{L_\alpha}\alpha qS(x_{cg} - x_{ac}) - k_\alpha\alpha - C_\alpha\dot{\alpha} + (q/V)C_{L_\alpha}Su(x_{cg} - x_{ac}) \tag{12.16}$$

In these equations I_z is the mass moment of inertia of the wing, M is the mass of the end of the wing (analogous to a bending rod with a solid mass at the end), and q the dynamic pressure. Constants k and C are spring and damping constants with their subscripts denoting height (h) or angle (α). The forcing (notice this force also produces a moment) function acting in the y direction was derived in terms of gust velocity u. This was then converted to state space form and solved numerically. The bending and torsional stiffness of the wing is given in the following equations:

$$k_h = \frac{C_1 \cdot EI}{L^3} \tag{12.17}$$

$$k_\alpha = \frac{GJ}{L} \tag{12.18}$$

After performing sensitivity analysis over a large range of gusts, spanwise positions, damping constants and velocities, it became apparent that wing divergence is not a critical failure mode as the system is well damped for a damping ratio, $\zeta = C/(2\sqrt{km})$ around 2%. In Figure 12.26, the vibrations of the wing are presented for an input gust velocity of 17 m/s.

It can be seen in Figure 12.26 that the system is in general well damped. This makes sense as the aircraft itself does not go to very high speeds at which wing divergence is a concern. That being said, this model has yet to be validated with real world data so any conclusions drawn are subject to change. The model is furthermore limited by its assumptions such as the linear decrease in torsional stiffness and constant torsional rigidity as well as second moment of area along the span. These assumptions are extremely limiting but are employed nevertheless because they allow for the use of a linear system. However, requirement VTOL-VIB-1 can be considered fulfilled for the dive speed that is less than 300 m/s as see in Figure 12.27. As the design dive speed is significantly lower (less than 100 m/s) wing divergence is unlikely to be a strong constraint.

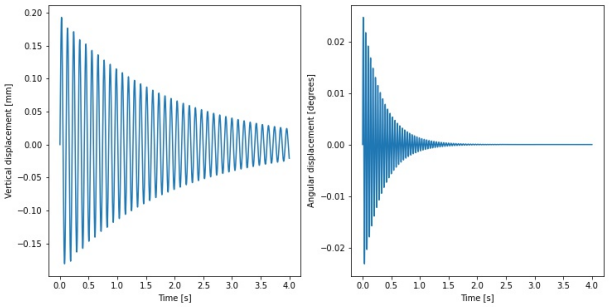

Figure 12.26: Response of system with a gust of 17 m/s

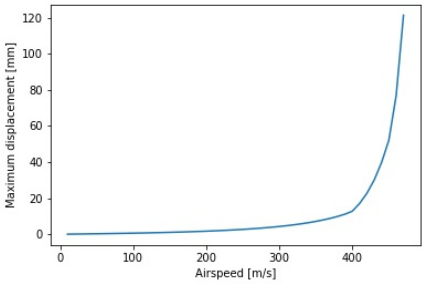

Figure 12.27: Maximum vertical displacement 10 seconds after a 17 m/s gust

12.8.2. Propeller Whirl Flutter

Another key aspect of flutter is propeller whirl flutter. The procedure for analysis was similar to that done by Mair et al [72]. The diagram depicting the propeller in this case is given in Figure 12.25 while the equations to compute the aerodynamic moments are provided below [72]:

$$M_\theta = \frac{N_B}{2} K_a R \left[-(A_3 + a^2 A_1)\frac{\dot{\theta}}{\Omega} - A_2'\psi + aA_1'\theta \right] \tag{12.19}$$

$$M_\psi = \frac{N_B}{2} K_a R \left[-(A_3 + a^2 A_1)\frac{\dot{\psi}}{\Omega} + A_2'\theta + aA_1'\psi \right] \qquad K_a = \frac{1}{2}\rho c_{l,\alpha} R^4 \Omega^2 \tag{12.20}$$

Here, Ω is the angular velocity of the propeller, θ is the pitching angle of the propeller and ψ is the yaw angle of the propellers. The constants A_1, A_2, A_3, A_1' and A_2' are aerodynamic integrals that come from integrating lift along the blade [72]. These integrals are in terms of V, the stream velocity, Ω and R which is the radius of the propeller. Their formulas are given below. In the figure, two moments of inertia are shown, I_x is the moment of inertia about the axis of rotation whereas I_n is the moment of inertia about the y or z axis (which are equivalent due to the assumed rotational symmetry of the propeller). These moments of inertia are computed by the sum of the individual constituents as given in the equations above, including their Steiner terms.

$$A_1 = \frac{c}{R}\int_0^1 \frac{\mu^2}{\sqrt{\mu^2+\eta^2}} d\eta \qquad A_1' = \mu A_1 \qquad \mu = \frac{V}{\Omega R} \tag{12.21}$$

$$A_2' = \frac{c}{R}\int_0^1 \frac{\mu^2\eta^2}{\sqrt{\mu^2+\eta^2}} d\eta \qquad A_3 = \frac{c}{R}\int_0^1 \frac{\eta^4}{\sqrt{\mu^2+\eta^2}} d\eta \tag{12.22}$$

They are integrated numerically. N_B is the number of propeller blades, $c_{l,\alpha}$ is the lift coefficient of the blade airfoil and ρ is the air density at the altitude tested. These were then placed in an equation modelling a spring damper system with the following equations [72]:

$$\begin{bmatrix} I_n & 0 \\ 0 & I_n \end{bmatrix} \begin{bmatrix} \ddot{\theta} \\ \ddot{\psi} \end{bmatrix} + \begin{bmatrix} C_\theta & -I_x\Omega \\ I_x\Omega & C_\psi \end{bmatrix} \begin{bmatrix} \dot{\theta} \\ \dot{\psi} \end{bmatrix} + \begin{bmatrix} K_\theta & 0 \\ 0 & K_\psi \end{bmatrix} \begin{bmatrix} \theta \\ \psi \end{bmatrix} = \begin{bmatrix} M_\theta \\ M_\psi \end{bmatrix} \tag{12.23}$$

In this, I_x represents moment of inertia about the axis of rotation of the propeller and I_n the axis about the pitch and yaw directions. These are equivalent due to the circular symmetry of the assumed geometry.

Finally, K denotes the stiffness of the equivalent spring in the direction specified by the subscript and C the damping coefficient. These equations were then placed in a state space form and solved numerically. It must be considered that this is done for the vertical takeoff condition as the weight of the propeller is not taken into consideration and the free stream velocity is set to 5 m/s. This is due to the fact that this is the critical condition for whirl flutter in which the vibrations of the propeller can adversely affect the aircraft structure.

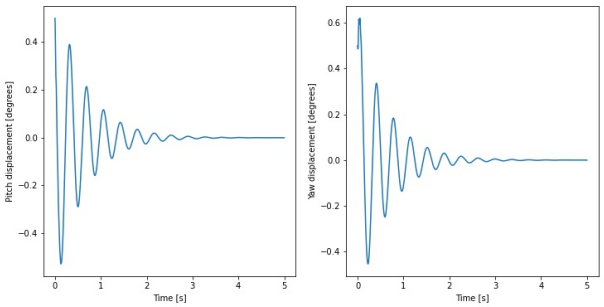

Figure 12.28: Response of system with a 2% damping ratio and initial angle of 0.5 degree at $\Omega = 4000$ RPM

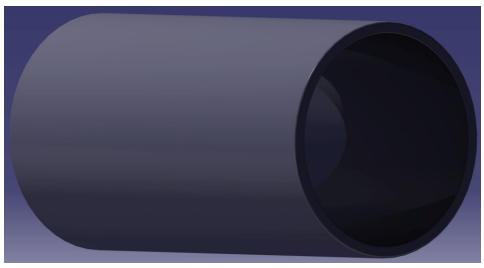

Figure 12.29: Render of Propeller Rod Connection

It can be seen from Figure 12.28 that this system is damped for the angular velocity of 4000 RPM. The propeller support rod is then designed to be made of the annealed steel alloy AISI 4140 for its high strength. It is also made to be a thin walled cylinder with a thickness of 1 cm, outer radius of 10 cm and length of 38.2 cm. This ensures that the vibrations of the propeller are properly damped as seen in Figure 12.28 for all operating ranges of RPM. The short length is also beneficial for the propeller-wing interaction as described in Section 7.3.3 as (among other reasons) the propellers at the wingtips effectively increase the aspect ratio. This steel support has a (bending) stiffness coefficient of 3875.279 [kN/m] (see Equation 12.8) and a 1222 [Ns/m] damping coefficient in both directions. With a computer aided design, the mass of the support structure was computed to be 17.9 kg. This makes it one of the most heavy structures on the aircraft, which is to be expected due to its material. A render of the design is displayed in Figure 12.29.

However, as this model is not validated with real world data the conclusions regarding the true vibrations is limited but it can be used to make general claims regarding the impact of various design choices as outlined above on the vibrations caused by the propeller. On the whole, not all flight conditions have been evaluated, but for the given hover condition which is the most critical point, the aircraft adheres to requirement VTOL-VIB-2. Therefore, its compliance to this requirement is promising but not verified with the given propeller support structure.

12.9. Component Weight Estimation

Firstly, some preliminary mass values are necessary in order to begin estimation of the component weight. This is essentially Class I weight estimation and is done using data from several sources, such as "A review of current technology and research in urban on-demand air mobility applications"[84] and database of an eVTOL directory [118]. It was possible to plot a regression line of Operational Empty Mass versus Maximum Take-off Mass and Maximum Take-off Mass versus Payload. The resulted plots are depicted in Figure 12.30. The data retrieved includes short, medium and long range eVTOLs, which is not ideal for the estimation of the long-range eVTOL, but due to the scarcity of the available data, this method was used. It is obvious that Figure 12.30a provides a much better fit, with RMSE of 166. Figure 12.30b has an RMSE of 814. It was decided not to remove the outliers as most of these are high range eVTOLs and relate most to the mission of the project. Including only high-range eVTOLs provided an even worse fit due to having only 5 data points.

Using the lines plotted in Figure 12.30, it is possible to find the required Maximum Take-off Mass based on the payload requirement. The payload requirement is 475 kg, 88 kg per each passenger and the pilot and 7 kg of luggage. From this, $MTOM = 1930.62$ kg and $OEM = 1565.15$ kg was retrieved, and was used as preliminary weight estimation.

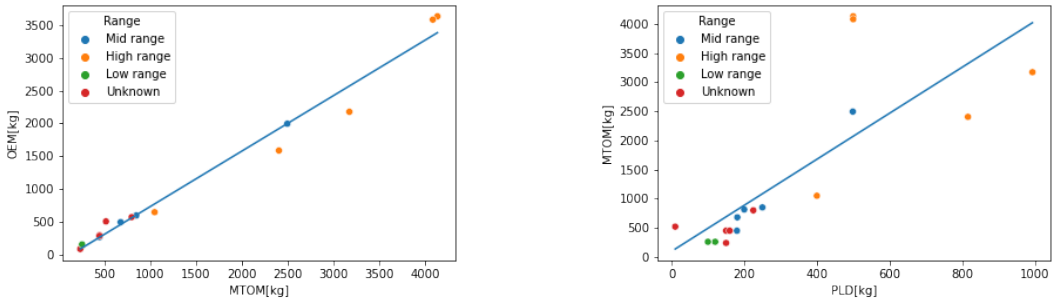

(a) Take off Mass versus Operational Empty Mass

(b) Payload versus Take off Mass

Figure 12.30: Mass Estimation Relationships

Next, Class II weight estimation was possible. The methods used are taken from a book by Dr. Jan Roskam [104]. The specific method used is for general aviation airplanes and is called the "Cessna method". The method is defined for the imperial units, but conversion is made when outputting the result in code. The wing weight is estimated using the following equation [104]:

$$W_w = 0.04674(W_{TO}/2)^{0.397}(S)^{0.360}(n_{ult})^{0.397}(AR)^{1.712} \tag{12.24}$$

where W_{TO}, S, n_{ult}, AR are take-off weight from Class I estimation, wing area, ultimate load factor and aspect ratio, respectively. The actual equation is not exact, the second term, $(W_{TO}/2)^{0.397}$, does not originally include the division by two, but this is necessary as the aircraft is composed of two wings, each carrying roughly half of the weight of the aircraft. The fuselage weight is estimated using the following two equations [104]:

$$Wf_{lowwing} = 0.004682(W_{TO})^{0.692}(P_{max})^{0.379}(l_{fus})^{0.590} \tag{12.25}$$

$$Wf_{highwing} = 14.86(W_{TO})^{0.144}\left(\frac{l_{fus}}{P_{max}}\right)^{0.778}(l_{fus})^{0.383}(N_{pax})^{0.455} \tag{12.26}$$

where $P_{max}, l_{fus}, N_{pax}$ are fuselage length, maximum perimeter of the fuselage and number of passengers, respectively. For this method, the pilot (and any crew members) is included in the number of passengers. Both formulas are used to compute the weight of the fuselage and the average is taken, to account for both high rear wing and low front wing of configuration. The vertical stabiliser weight is calculated the following formula [104]:

$$W_v = \frac{1.68(W_{TO})^{0.567}(S_v)^{1.249}(AR_v)^{0.482}}{639.95(t_{r_v})^{0.747}(cos(\Lambda_{1/4}))^{0.882}} \tag{12.27}$$

Using the above listed formulas and the relevant values results in Table 12.6. These values were obtained

Table 12.6: Component weight fractions for the Wigeon.

	Mass [kg]	% of OEM	% of MTOM
Front wing	174.9	12.2	6.3
Back wing	174.9	12.2	6.3
Fuselage	210.6	14.7	7.5
Vertical tail	14.9	1.0	0.5
Passengers	440.0	0.0	15.8
Furnishings	98.4	6.9	3.5
Electronics	131.6	9.2	4.7
Cargo	35.0	0.0	1.2
Battery	886.2	0.0	31.8
Landing gear	121.0	8.5	4.3
Propulsion	502.6	35.2	18.0
Total Mass		1428.9 kg	2790.1 kg

at the end of the optimisation iteration. Moreover, including a contingency of 10% with every iteration, the MTOM becomes 3024 kg, about 7.7% higher than the initially predicted weight. The structural weight roughly equates to 696.3 kg, taken from Table 12.6. Referring back to the requirement stating that the structural weight shall be at most half of the OEM, VTOL-STS-1-STR-3, the Wigeon complies with it.

12.10. Verification & Validation

In order to make reasonable design claims with the analysis outlined above, verification and validation must be performed. This section outlines the methods used to verify and validate the models constructed.

12.10.1. Verification

Verification is an important process, as it confirms that a method is implemented as intended. This is usually done by comparing a simulation result to an analytical solution of a simple case of a problem, or by performing unit tests for each part of a method.

Loads & Stresses

In order to verify whether the computation of the loads and stresses are valid, a simple case is used with a cantilever beam with a uniform distributed load. The computations were also performed analytically and the internal loads were compared. Considering the wing is modelled very similarly to a cantilever beam in bending due to a distributed load, and that the loads and deflections obtained corresponded exactly to those modelled to six decimal places, this is considered to be verified. The stress calculations were verified using analytical calculations of shear flows in one region of the box that was the simplest. By doing so it also yielded the same result. Finally, the normal and Von Mises stress calculations are verified in code as they are relatively simple formulas.

Fatigue

In order to verify the model used to calculate the fatigue life of the structure, several tests were conducted. Firstly, to verify whether the ground air ground cycle is the one that is expected, the period is calculated separately (once the ground-air-ground cycle is already calculated) and their equivalence is asserted. Thereafter, the minimum and maximum stresses are also computed separately and their equivalence to the minimum and maximum stresses of the model is asserted. The random noise generated to simulate stochastic loads are not tested, but the maximum and minimum values mentioned includes those and their deviation is visually assessed by means of the graph. For variable amplitude loading, the Miner's Rule computation is verified using Figure 10.4 on page 301 of Schijve [112].

The Basquin's Law was also verified with that as the stress amplitudes were also given along with their fatigue lives, which could be checked with their corresponding SN-curve. As Schijve [112] performed aluminium computations with the alloy Aluminium 2024-T3 the same was done for verification, although a different alloy (Aluminium 7075-T6) was used for the analysis. The Paris Law was verified using the values presented in Table 8.2 of page 241 of Schijve [112].

Finally, for the lug analysis, the stress concentration coefficients of the lug were checked against lug a5 in [64] in which the analysis was performed. The discrepancies for k1, k2 and reference area are non existent.

Buckling & Crippling

Buckling and crippling was verified in means of comparison of numerical model with the analytical model in combination with unit tests. The unit tests passed if the critical buckling stress magnitude retrieved from the numerical functions was 'almost equal' to the one retrieved from the analytical example. Analytical examples were taken from the course 'Structural Analysis & Design' [81].

12.10.2. Validation

Validation is essential for any model as it determines whether or not the assumptions correspond to reality. However, as data on this subject is scarce validation is not always possible.

Loads & Stresses

The computation of the loads and deflections was done using the standard uniform cantilever beam. Finite Element data was found by Tuan Ya et al [88] with the intention of training an artificial neural network with it. While the purpose is somewhat irrelevant, the data used to train their model was used in order to validate the deflections, and therefore loads applied on a uniform cantilever beam. This is because the deflections were computed from the loads. Therefore, as all the results of the numerical model corresponded exactly to those in the finite element model, this model is considered to be validated. Methods used to compute stresses from the given loads, however, are yet to be validated.

Fatigue

As fatigue is a concept difficult to validate, and is not done during this phase of the design. The uncertainties encountered therein pertain to three main areas [112]: the load spectrum, fatigue properties of the structure and the reliability of the predictions.

The tests used to validate the fatigue life must use the same geometry of the joint or connection in which fatigue is expected. In order to test an unnotched specimen, it must be produced with as few defects as possible in order to avoid scatter. The first test shall start at a stress of 400 MPa which is slightly below the yield strength of Aluminium 7075-T6. Then the load can be decreased to stress amplitude during cruise - 200 MPa. Then the stress amplitude versus number of cycles can be graphed at which point the SN curve constants can be determined and compared to the one currently being used. The crack growth test can be performed in a similar manner but with automating the detection of the crack. This can be done using the procedure outlined in [130], which used mechanoluminescence film to detect invisible cracks.

Finally in order to validate the lug analysis, the stresses of the lug were checked against lug a5 in [64]. In the paper a finite element analysis was performed on the reference lug in which the error on the stress was less than 1.6% (10 vs 9.8 MPa) and another on aluminium a5 was performed in which a result of 8.7 was obtained resulting in an error of -33%. This is seen on page 44 Table 6.3 of the paper in which their analytical methods performed comparably to this one, although better (error of -26%) for this case. However, considering the methods are varied the order of the discrepency makes sense.

Buckling & Crippling

Validation of buckling can prove to be difficult as the exact geometry is needed. Therefore, for validation it may not be possible to find an already existing experiment that exactly replicates the desired scenario, but rather an own experiment should be conducted. This either involves a computational experiment using a well validated and proven FEM software, or a real life set-up where the exact wingbox can get tested. Although the loads are most times simulated with point loads rather than distributed loads, a physical experiment is as close to the real situation as one can get. Such an experiment most often consists of a wing bending test with simulated ultimate loads applied.

13 Integration and Optimisation

This chapter addresses the procedure followed to arrive to a converged design. Section 13.1 covers the procedure followed to integrate the methodologies from the individual departments into one program used to design the Wigeon. The result of this integrated program is the configuration that has been analysed throughout the report. Section 13.2 covers the procedure followed to then optimise the integrated design. It is very important to note that the result of this optimisation is only presented in this chapter. The information in the report only concerns the integrated (but non-optimised) design. Lastly, Section 13.3 contains three-view drawings of both configurations for visual reference and comparison.

13.1. Integration

In order to reach a consistent and converged design, the work from every department was integrated together. Since most departments depend on outputs from all the others, no clear order could be constructed to run the code of all the departments. To mitigate this, iterations had to be performed until all the aircraft variables converged to fixed values. A flow chart of the high-level structure of the design code is shown in Figure 13.1. In this chart, it can be seen that first the most important aircraft parts were sized based on the input parameters. Afterwards, it was checked whether the aircraft was not too unstable, and if it was controllable. If it was not, the relative wing size or aspect ratio were changed manually. The resulting design is shown in Figure 13.3

To allow for an optimisation algorithm to be used in a later stage, the integrated design program was made such that it produced a convergent design based on several fixed aircraft parameters used as an input. These mainly concerned the wings of the aircraft, and included the aspect ratio of both wings, the taper ratio, the positioning of both wings and the ratio of their surface areas, but also the cruising altitude. Apart from some fixed parameters, some initial guesses had to be made to start up the iteration. Estimated variables were the cruise speed, the maximum take-off mass, the maximum power, the maximum lift coefficient, the vertical tail area, the downwash of the front wing, the stall speed, the propeller radius, and the maximum thrust propellers can provide during stall.

Since the aircraft mass is likely to change in a later design stage, a 10 % contingency was added to the weight. This is done in order to be sure that in case of an unforeseen mass increase during the design, the aircraft and its subsystems are still capable of performing the mission and meeting the requirements. This means that the aircraft is in fact designed for a heavier mass, which translates into bigger wings, more powerful engines and a heavier battery. Note that this is not optimal for the design without contingencies. If later on it is found out that the mass estimation was too conservative, these contingencies have to be removed, and the wings will have to be sized again.

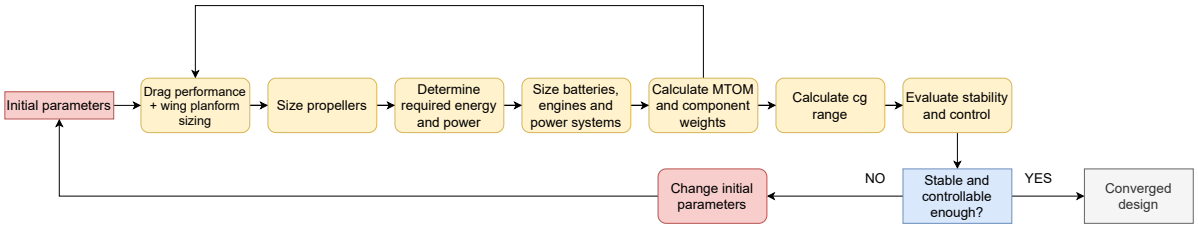

Figure 13.1: Flow chart of the integrated design program

13.2. Optimisation

After having obtained a converged design, an optimisation was started. The procedure used to do this is explained in Section 13.2.1. The design resulting from this optimisation is presented in Section 13.2.2. Note that the aircraft that is analysed in the rest of the report is that resulting from the integrated program,

without running an optimisation. The optimised aircraft design is only presented here as a next step in the design procedure.

13.2.1. Procedure

The optimisation was conducted using the integrated framework presented in Section 13.1. For this, a local optimiser in OpenMDAO[1] was used, utilising the COBYLA algorithm. This algorithm was used because it is easy to implement, and because it allows to set constraints on certain parameters. Since the optimised aircraft could not differ too much from the concept analysed earlier, such that all models and assumptions used still apply, a local search was preferred. The optimisation goal was to minimise the energy consumption, as optimising for this variable is beneficial for a lot of other aircraft parameters, such as the mass. It also helps with sustainability, due to the lower energy consumption; and for operational costs, due to lower energy costs. Furthermore, a low energy consumption means that less time is needed to charge the Wigeon, reducing turnaround times. To obtain a low energy consumption, good aerodynamic performance, a low weight and efficient engines are required.

To set up the iterations, a slightly modified version of the program presented in Section 13.1 was used. Instead of manually checking whether the aircraft was stable and controllable, C_{m_α} and the difference between the most forward cg and the cg limit for controllability were calculated inside the main program and constrained to meet the requirements. This modified program was used in the main optimisation code, where for every optimisation iteration a convergent design was reached through subiterations of the integrated code. A flowchart of the optimisation program is shown in Figure 13.2.

In order to allow fast convergence and keep the similarity between the first converged design and the optimised design high enough, the number of design variables was kept low. In particular, the design variables were the aspect ratio of both wings, the relative size of the wings, the position of the rear wing, and the centre of gravity of the batteries. The reason why the area ratio was used and not the area itself, is that the required total wing area is sized based on the stall requirement inside the integrated program. Moreover, only the position of the rear wing was modified because the position of the front wing is positioned in such a way that it allows for enough space for its wingbox, (part of) the batteries, the wing rotation mechanism, and and the front landing gear, which are all placed in the nosecone, and thus, its position is fixed. In order to ensure that the position of the rear wing stayed within the fuselage limits, the length of the tailcone was also varied as a function of the wing position. This resulted in a longer tailcone (and hence fuselage), translating into more separation between the wings, which is beneficial in terms of aerodynamic performance, stability and drag, as the upsweep angle of the tailcone is reduced.

To keep the aircraft parameters within the range of validity of the models used, constraints were applied to all design variables. A list of all design variables and their constraints can be found in Table 13.1. Additional constraints were applied to other parameters, such as the MTOM and the wing span, to keep the design within all requirements.

Table 13.1: Design variables used, and their respective constraints

Variable	Lower bound	Upper bound
AR_1	5	15
AR_2	5	15
S_2/S_1	0.01	-
$x_{mac,2}$	-	8 m
$x_{battery}$	0.5 m	2.5 m

Table 13.2: Design variables used, and their respective constraints

Variable	Lower bound	Upper bound
C_{m_α}	-	0.12
$x_{cg,front} - x_{cg,ctrl}$	0	-0.1
S_2/S_1	0.01	-
$x_{mac,2}$	-	8 m
$x_{battery}$	0.5 m	2.5 m

[1] https://openmdao.org/ [cited 29 June 2021]

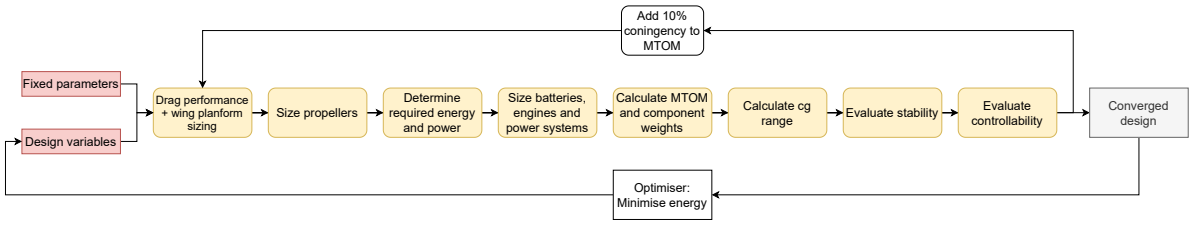

Figure 13.2: Flow chart of the optimisation procedure

13.2.2. Results

Table 13.3 presents the resulting parameters of the optimised aircraft. It can be seen that the mass has decreased significantly, coming from 2790 kg. This is mainly achieved by increasing the aspect ratio of the wings to decrease drag. The reduction in drag leads to a reduction in energy consumption, and thus in battery mass. This in turn, results in lower power required from the engines to hover, which reduces the necessary engine size (and therefore mass) and necessary power from the battery. Due to the lower mass, the size of the wings also becomes smaller. This starts a snowball effect that results in a significant reduction in energy consumption and mass. Furthermore, the aircraft is now marginally statically unstable with $C_{m_\alpha} = 0.12$, but this can easily be dealt with using a controller similar to the one designed in Section 11.4. In Table 13.4, the changes to some important performance and finance related properties can be found.

Table 13.3: Parameters of the Wigeon after optimisation

Parameter	Value
MTOM	2124 kg
S_1	6.34 m^2
S_2	7.66 m^2
AR_1	9.51 [-]
AR_2	9.98 [-]
b_1	7.76 m
b_2	8.47 m
$x_{mac,1}$	0.50 m
$x_{mac,2}$	7.38 m
l_{fus}	8.61 m
$x_{battery}$	2.49 m

Table 13.4: Changes in the most relevant aircraft parameters after the optimisation.

Parameter	Value	Change
Energy consumption	571 MJ	-35 %
Cruise speed	65.9 m/s	-8.5 %
Flight time (300 km)	1 h 25 min	+19 %
Cost	792461 $	-30%

13.3. Three View Drawings

In order to visualise the results of the integrated design and the optimised design, three-view drawings of both versions of the Wigeon can be seen in Figure 13.3 and Figure 13.4, respectively. These images also allow to visualise the differences in wing planform and positioning, and they include a human for reference.

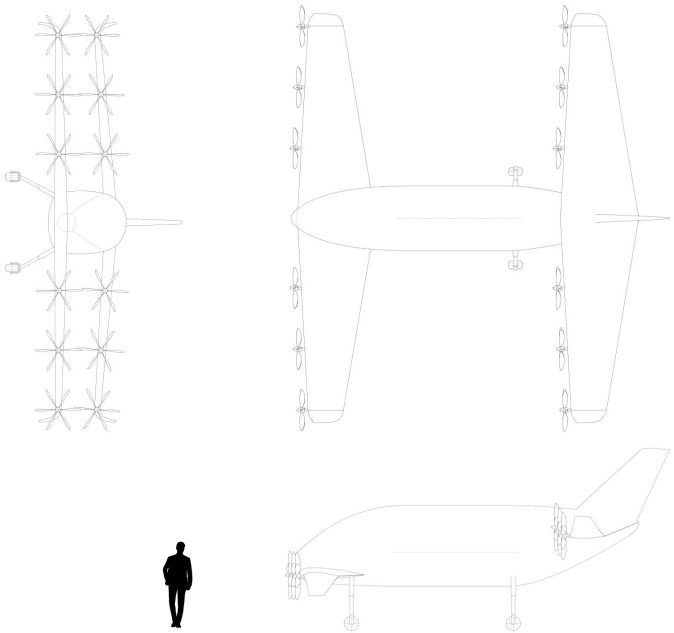

Figure 13.3: 3 view drawing of the integrated design.

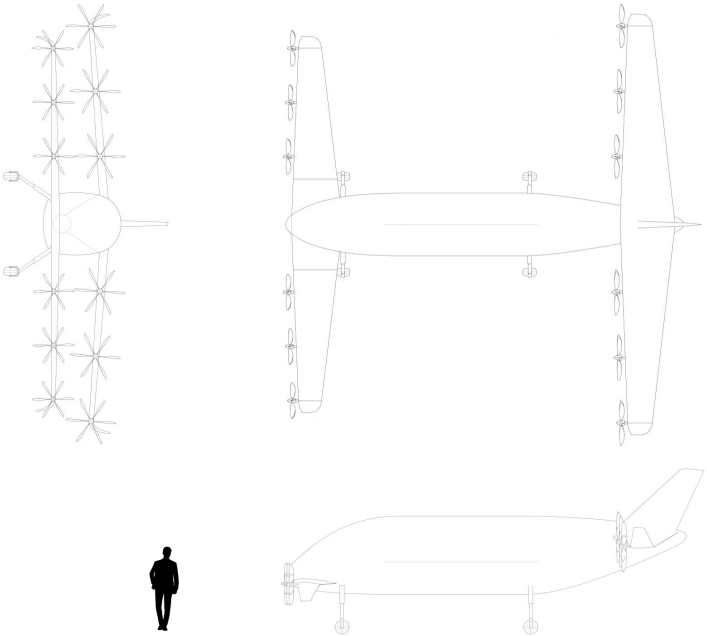

Figure 13.4: 3 view drawing of the optimised design.

14 Resource Allocation and Budget Breakdown

Since the eVTOL market is only starting to emerge and little data is available on previous vehicles, accurately predicting many parameters such as mass, cost and power in the conceptual design stage is challenging. This introduces uncertainties a into the design, which result in risks, e.g. not meeting the range and lift requirements (RT.1, RT.2 in Chapter 6). If the mass increases beyond its design value, it can trigger the so-called "snowball effect" where the mass spirals out of control due to larger wings, engines and batteries being required. Such risks are managed using a process called Technical Performance Management (TPM) [49]. In this process, the compliance with technical objectives is demonstrated for the current design and anticipated for the future.

To simplify the certification process, the mass of the Wigeon should be limited to a maximum of 3175 kg [119] (VTOL-MAS-1). With the current best estimates, an optimised design could achieve far lower masses. However, to avoid the "snowball effect" and ensure that the vehicle remains within the mass, thrust, power and energy budgets, the aircraft subsystems are sized for an empty mass (OEM) 10% higher than the best prediction. This results in a design with an MTOM of 2790 kg, according to the current mass prediction methods. While this is heavier than the optimal design, it allows for a contingency margin: the lift, power, and thrust subsystems can remain unchanged even if the MTOM increases to 3025 kg during the preliminary or detailed design stages.

This margin does not only allow for contingencies in terms of MTOM. Since the thrust, lift, and power subsystems are designed to tolerate a higher mass of the vehicle, they have a margin if the mass remains below 3025 kg. This way of applying margins has the advantage that the largest margins will be present for the performance parameters with the highest sensitivity to mass. Table 14.1 shows the margins on energy capacity, maximum thrust, and maximum power. Since the energy for a 300 km mission is very sensitive to mass, a 10% empty mass margin results in a large margin on energy. The sensitivity of thrust and power to mass is smaller, so the margins flowing down from the mass margin are also less.

Table 14.1: Margins on energy, maximum thrust and maximum power that flow down from a 10% margin on the OEM. These margins apply if the predicted MTOM of 2790 kg is achieved.

	MTOM	**Energy**	**Maximum thrust**	**Maximum power**
Maximum capability	3025 kg	1084 MJ	34.31 kN	1.809 MW
Required for 2794 kg MTOM	2794 kg	880.7 MJ	32.88 kN	1.707 MW
Margin	8.268%	23.08%	4.349%	5.975%

Another important resource budget is cost, which is a vital figure for the economic success of the project. As for the technical parameters, there is much uncertainty in the estimation methods since the eVTOL market is only starting to gain traction. In order to account for this, conservative parameters were chosen in the estimation of operating cost and unit cost. Growth and sales numbers were capped after 2035 because of the difficulty to predict so far into the future. Production cost was scaled up by 20% for the first units to be sold until a nominal production rate of 200 aircraft per year was achieved to allow for some margin for other unexpected and unforeseen costs. For more information on the financial plan of the project, see Chapter 4.

15 Sustainability Approach

Sustainability is defined as meeting the needs of the present without compromising the needs of the future [101].

15.1. The 3 Pillars

In sustainability there are 3 most fundamental aspects that are considered, namely the social, economic and environmental sustainability, which are defined in this section.The metrics used to define sustainability include energy consumption, impact on consumer and bystander wellbeing, and contribution to product value (and return on investment). The CO2 emissions will not contribute to the sustainability analysis due to it being fully electric which (presupposing the electricity is produced in a sustainable manner) results in 0 emissions. Environmental sustainability involves the protection of natural capital in order to preserve the state of the environment.

Economic sustainability is the objective to encourage economic development and an increase in quality of life. This makes the position of the vehicle positively contributing to the economy, which in the aerospace industry (and other closely related industries) contributes to the gross domestic product. In order to ensure that the project is economically sustainable in the long term, the product must address a market need that will grow in the future. Electric VTOLs will be desirable to enable faster door-to-door travel times, and can also be a part of the restructuring of urban transport. There is a growing public interest in reducing the number of private cars, and eVTOLs could provide a solution for this scenario [107]. However, the depletion of other resources (especially for battery manufacturing) may affect eVTOLs.

Social sustainability is the aim to increase the quality of life of those around Wigeon. Specifically, it pertains to the contribution to social quality, including aspects such as human rights and equality. In the context of this project, especially the impact of eVTOLs on modern day living and culture is investigated. One of the major challenges for urban air mobility is the acceptance by the general public. This is in part related to the noise produced by VTOL vehicles with rotors. This is why ICAO noise regulations is taken into account in the design. This is achieved by optimising disk loading of the propellers.

15.2. Lean Manufacturing

Lean manufacturing is a dynamic, knowledge-driven, customer-focused process, through which all people in a defined enterprise continuously eliminate waste with the goal of creating value [60]. The use of lean manufacturing plays a central role in the sustainable development of any tangible product. Therefore, the 5S principle is used in order to eliminate waste, which is defined as something that does not add value despite consuming resources [60]. The 5S principle consists of the actions sort, simplify, scrub, standardise and sustain. Performing these steps makes the manufacturing process more sustainable and more efficient, which results in lower costs. There are different types of waste to reduce, including material waste, unnecessary transportation as well as the underutilisation of workers. Line production is to be used to minimise waste, but also improves social and environmental sustainability.

15.3. Influences on Design

The impact that sustainability has on the design of the different disciplines is now discussed.

15.3.1. Aerodynamics

Over the course of the design phase, several steps are taken in order to aerodynamically optimise the design. This plays a significant role in sustainability not only because aerodynamically efficient designs result in less drag which in turn saves energy, but also because resources have to be utilised in order to design the aircraft in such a manner. This drives environmental sustainability to a certain extent, which is explicated below.

One example of this is the use of resources in testing the airfoil, which constitutes a small but significant part of the costs. This is because wind tunnels require a significant amount of power (up to 5000 hp) and lab equipment in order to run [39]. Therefore, in order to ensure that the testing is sustainable, they are only conducted in order to validate preexisting models, such as those involving CFD. This ensures that the least amount of energy is consumed to run the wind tunnel facility, while permitting the empirical validation of any models used in the design process.

As a relatively novel airfoil is used, this will also be a driving factor for environmental sustainability. This is because manufacturing a wing with few defects and an acceptable geometry is difficult enough, but due to the novelty in the design, this will result in even more waste in terms of raw material, as well as time of the workers. Due to the principle of lean manufacturing, this is to be minimised as much as possible by training workers beforehand to avoid under-utilising them and to prevent the production of an unacceptable wing geometry. The novel airfoil geometry is selected for its high efficiency, which is meant to compensate for its novelty in terms of manufacturing, as mentioned above. This will in turn increase the metric of value due to its efficiency but may not contribute to the wellbeing of workers.

15.3.2. Control & Stability

The stability of an aircraft is paramount for a sustainable design as it directly impacts the comfort, and more importantly, safety of its passengers. For a pilot to be capable of controlling the vehicle, they must first undergo a normally extensive training for conventional vehicles. However, this being rather unconventional means that they must undergo an even more specialised training module. Therefore, the controllability of the aircraft is essential so that training can be completed by most capable human beings without necessitating the development of arduous or redundant skills and abilities.

This also has an impact on social sustainability due to the safety of an aircraft, especially on its influence as an urban air mobility vehicle. The manoeuvres that the aircraft is able to perform has a direct link to the perception of safety of the aircraft. This is particularly true for those on the ground, who are forcibly exposed thereto. Due to its low altitude, the perception of their safety may be distorted by the seemingly dangerous manoeuvres being performed. This may also result in the agitation of mental disorders such as stress induced psychosis or post traumatic stress disorder in a certain percentage of the population. Such effects were observed in vivo by Gouwelous et al wherein 42% of those involved in a plane crash developed post traumatic stress disorder [51]. Therefore, the stability subsystem strongly contributes to the wellbeing of the consumers and bystanders, consumes little energy and adds a moderate amount of value making it highly sustainable.

15.3.3. Propulsion & Power

The propulsion & power subsystem has a great impact on social and environmental sustainability due to its use of energy. Like many other aspects of the Wigeon, this susbsytem is optimised for efficiency in order to reduce the weight, and therefore the power used as much as possible. In this manner, the costs reduce, and the long term environmental sustainability of the vehicle drastically increases even with a small increase in propulsive performance.

With the above in mind, the battery selected uses cobalt, which unfortunately is not socially sustainable, due to its source. As the majority cobalt is mined in the Democratic Republic of the Congo, it is often associated with child labour and several other human rights violations [98]. In spite of this, its use remains widespread and in the trade off, it still was the most efficient battery, which is why it was selected despite its

questionable impact on social sustainability. However, as the release year of Wigeon is in 2031, other equally well-performing batteries without cobalt might become available, in which case they would be the preferred option for the vehicle. However, until then, the design is continued (due to a lack of current options that are as suitable energy-wise) using the battery that consists of cobalt. Furthermore, this strongly and negatively impacts the wellbeing of bystanders, but allows the plane to fly which makes it somewhat unsustainable at the moment but the latter cannot be overlooked.

Another impact that the system has on social sustainability is its noise emissions, which are minimised whenever possible. This is to prevent citizens from being disturbed and to thereby permit it to be used as an urban air mobility vehicle. The system is designed to adhere to the regulations as set by ICAO, making the compliant design relatively socially sustainable in this regard. However, the noise emissions will overall negatively impact the wellbeing of bystanders, especially if it is used as an urban air mobility vehicle.

An impact this system has on environmental sustainability, aside from the battery efficiency, is the testing of the engines. As engine testing is a highly resource consuming activity, due to its high power consumption and lab equipment, it is seldom used aside from the verification of preexisting models. This minimises the use of scarce resources resulting from engine tests because most of the research and development is conducted using models based on theory, which are subsequently verified using the aforementioned tests. However, due to the engine's high consumption of electricity in and out of tests, it is regarded as relatively unsustainable despite its positive impact on profits and generally positive impact on consumers.

15.3.4. Structures & Materials

The structure of an aircraft is one of the most significant factors that determines its sustainability. Creating the most weight-optimised structure is beneficial in almost every aspect of design, not just sustainability, but sometimes this is at a large cost.

The main decision that impacts environmental sustainability is that of materials. Materials that are used are displayed in Figure 12.17 in the material selection section of this report. Most of the load bearing structure as well as the skin of the aircraft is made of aluminium. This is beneficial for environmental sustainability because with modern technology, aluminium can be recycled while retaining its original strength. In fact, new aluminium is recycled at a rate of 100% [124]. It has relatively safe and well known manufacturing techniques due to its long history of use in the aerospace and automotive industry and it can be ingested without adverse effects. This makes it socially sustainable for workers, especially considering the manufacturing techniques used are well documented [10]. This makes it highly sustainable due to it being good to manufacture for workers which increases their well being, consumes relatively little energy in production and can be recycled and retain most of its energy. Furthermore, its material properties contribute value to the vehicle.

That being said, not all components are made of aluminium. Composites are challenging to recycle due to the cost and quality of recycling, given the current technology [133]. Because of this, composites are used sparingly in the design of Wigeon. The technical details regarding this decision can be found in Section 12.4. Furthermore, composites are known to be potent toxins [109], making their manufacturing not only difficult and strenuous for the workers but also hazardous. As a result, composites are considered unsustainable in terms of the wellbeing metric, unsustainable in terms of the energy metric and marginally more sustainable in terms of value. Therefore, it is usually traded off in favour of a more sustainable material such as aluminium.

Finally, textiles can readily be recycled as well, making the soft parts of the cabin environmentally sustainable too [122]. In the case of Wigeon, most of the material used in structural components can be recycled, making it an environmentally sustainable design. However, the scheme used to recycle varies based on the material used. For aluminium, the alloy can be melted and reused, maintaining 95% of its energy [124]. For commercial aircraft, 15% of the aircraft ends up in landfills by mass, and most of this is due to the interior of the cabin [11]. This can be applicable to Wigeon as well, considering the vast majority of the vehicle is composed of aluminium, (much like conventional aircraft) it is likely to be as sustainable in this regard. In order to increase the sustainability metrics even more, the use of composites should be reduced even further.

16 Production Plan

Production and design are heavily interrelated phases of the aircraft life, as one heavily influences the other. This chapter conveys the production of Wigeon. Section 16.1 demonstrates arguments and choices for different manufacturing techniques and Section 16.2 talks about the assembly of the Wigeon.

16.1. Manufacturing Methods

First and foremost, different materials require different manufacturing techniques. Each manufacturing technique has a cost attached to it due to the facilities and machinery required.

Thermoplastics can be extensively used inside the cabin, for instance the furnishings, and even on the body of the aircraft. Manufacturing technique for thermoplastic components comes down to two choices: compression moulding versus injection moulding. While injection moulding is not a labour heavy process and can achieve high detail designs, the equipment and energy costs are high. Compression moulding does not allow for such high detail, although sufficient amount of detail can still be achieved with lower energy costs [60]. However, compression moulding is less automated and requires more human assistance. Considering that parts of the skin can be made from thermoplastics, and these involve large doubly-curved parts, compression moulding is beneficial in this case. Furnishings, on the other hand, can be made through injection moulding through outsourcing third-party manufacturers that can produce these in large batches. This way no equipment has to be purchased, saving a lot of cost as injection moulding machines can cost up to several million euros[1]. As a matter of fact, outsourcing is generally cost saving, as staff, equipment, software, insurance costs are cut, which is substantial. Big companies like Boeing outsource most components of the aircraft, leaving anything to do with assemblies at their own facilities[2].

Wings, namely the wingbox, vertical tail, fuselage frame is mostly made out of **aluminium**, specifically Aluminium 7075-T6 as these are the integral load bearing structures and thus must have sufficient strength and stiffness. The parts of such structures are typically single-curved, like ribs and stiffeners, with some double-curved parts, like fuselage frames and longerons. Rubber forming is the best choice of manufacturing in this case. The method is cheap, and the rubber beds allow for a wide range of geometries to be made. On the other hand, the soft rubber beds do wear off and require replacement in the long run and rubber forming normally involves long cycle times of several minutes [60]. Taking into account the goal of producing 1000 aircraft in the first 5 years of production, as mentioned in Chapter 4, which equates to roughly 17 aircraft per month, long cycle time is not a major drawback.

For the **skin**, it is largely made out of aluminium once more. Large sheets of aluminium can be plastically formed by bending or stretch-forming. On top of that, achieving the right temperatures, aluminium becomes superplastic, allowing for more freedom in geometry with less energy required to form the sheet. Although energy is still required to heat up the material, overall energy is still generally lower than that of regular bending [60].

For **attachment brackets**, such as the wing-fuselage attachment discussed in Section 12.3.3, or vertical tail-fuselage attachments, forging would present itself as the best manufacturing choice. The foundation of this lies in the fact that only a few of such brackets have to be manufactured per aircraft, and that they must be safe-life due to the sheer importance of the part. Forging introduces fibrous grain structure into the part, which highly benefits the strength and the fatigue life of such brackets and attachments [60]. Although being a generally expensive process, forging of small number of parts of simple geometry that are critical to the structure is justified.

[1] https://www.msi-mold.com/injection-molding-cost/ [cited on June 14th 2021]
[2] http://www.b737.org.uk/production.htm [cited on June 14th 2021]

Another point important to make is the growing use of **additive manufacturing** in aircraft [69]. Binder jetting is popular additive manufacturing techniques in aerospace as it allows to 3D print shapes of unlimited sizes. In the future, complex designs of the frames or control surface deployment mechanisms created using topology optimisation can be 3D printed using the binder jetting technology. Having a relatively small number of units when compared to car manufacturers is beneficial for additive manufacturing as the price per part is then lower. This is demonstrated in Figure 16.1.

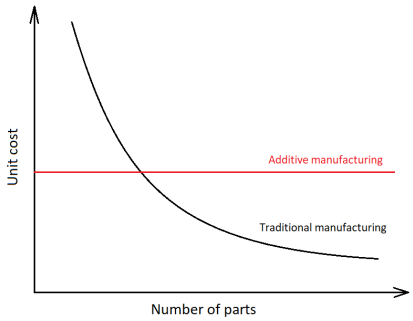

Figure 16.1: Additive manufacturing vs. Traditional manufacturing [76].

16.2. Assembly

The decision to assemble the aircraft rather than building it all in one might seem like a trivial one, however there are a couple of important reasons on why it is today's industry standard. Some of these are: production efficiency reasons, structural reasons, political or economical reasons, and maintenance and operations reasons.

16.2.1. Divisons

Special attention is paid to structural, maintenance and operational reasons. These divide the assembly into manufacturing and mounting divisions, with manufacturing divisions relating to components that use different manufacturing techniques or are too large and require several stations, and mounting divisions relating to components that might have to be detached to perform maintenance and repairs, or even replacement. The following text will describe sub-assembly divisions.

- The fuselage, namely being made out of aluminium, can be divided into 3 manufacturing divisions: the central cabin section and the 2 conical sections of the nose and tail cones, all of which are manufactured by bending thin sheets and attaching them to longerons and frames. Those assemblies are connected by overlapping skin joints and fixed with rivets. Additionally, the two cones have rubber-formed sphere sections on the tips, attached to the cone sections with rivets.
- Front and rear wings can be split into their own divisions as well. These include the wingbox assemblies for both, with ribs, stringers, and spars, as well as the hydraulic and mechanical systems for the control surfaces and wing-tilt mechanisms. The pre-formed airfoil skin is then fit over the wingbox and fastened with rivets.
- Then, the landing gear can be considered a separate mounting division. This also includes the hydraulic dampers and the deployment mechanism.
- Then, the vertical tail has to be attached to the fuselage and thus entails another manufacturing division. Its production process is similar to that of the wings, and the spars of the tail are mounted to the fuselage's frames.
- Lastly, the propulsion system, including engine, propellers, nacelles and attachment brackets, can be considered as a mounting division. Although not all of the propulsion is a mounting division, for instance the attachment bracket will not have to be dismounted, but since sub-assembly divisions are considered, propulsion group will be regarded as one division in its entirety.

16.2.2. Assembly line

Once again, considering the rate of production of 17 aircraft per month, a hybrid between dock and a moving line assembly is utilised, which is common in the aircraft industry today. This hybrid essentially involves a very slow moving production line. As an example, Boeing 737 using a 5 cm/min moving line with a delivery rate ranging from 26 to 52 aircraft per month[3]. Roughly halving the speed of the line brings it to 2.5 cm/min, or 1 inch/min. Needless to say, Boeing 737 MTOM is about 20 times larger than that of Wigeon, resulting in a much larger structure and longer throughput time, but the amount of workforce is large.

A conceptual design of such production line is presented in Figure 16.2. Sub-assemblies are represented with green arrows, with their most significant components with white arrows. The main production line is represented by the red arrow.

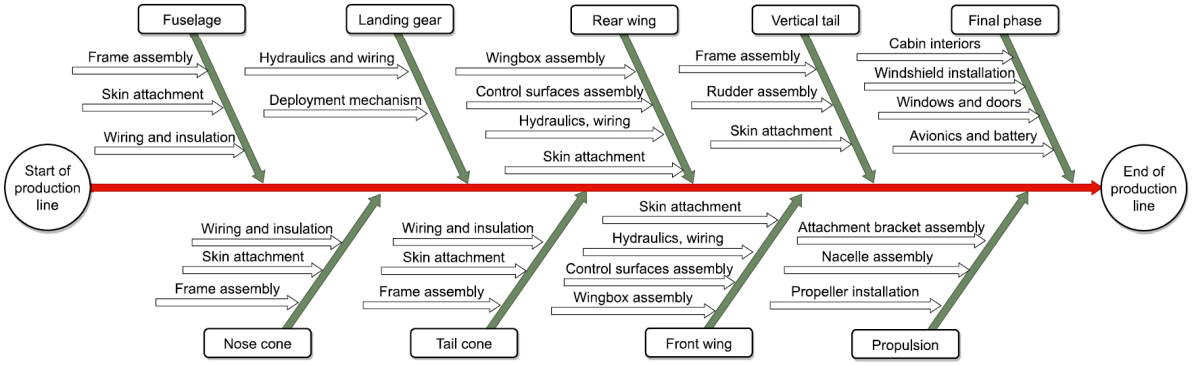

Figure 16.2: Production flow of Wigeon.

Since it is difficult to estimate the throughput time of each sub-assembly being incorporated into the main production line, Figure 16.2 is only sequential. The order is similar to commercial aircraft, however the time that each stage would take differs. Having a large number of engines increases the assembly and the installation time substantially, even though the engines are fractional in size compared to those of large passenger aircraft. Moreover, having a fully electric propulsion system would increase the time taken by the installation of the electrics.

Looking at the Figure 16.2 once again, the *Final phase* of assembly consists of fitting of windows, doors, windshield, interiors as well as avionics and batteries. These were placed in the final phase deliberately, as sensitive structures and components are best to be fit in the end. This reduces the risk of these sustaining any damage, as otherwise such components would have to be replaced. Overall, auxiliary systems of the sub-assemblies are integrated during the assembly of these sub-assemblies to avoid any potential issues with accessibility and damage.

Another general aerospace manufacturing practice is to perform continuous checks and quality control, the so called process focused quality control. This does increase the throughput time slightly once again, but is an essential sacrifice as the global system is extremely complex, backtracking or scrapping the product is extremely costly both in terms of time and funds.

[3]http://www.b737.org.uk/production.htm [cited on June 14th 2021]

17 Operations and Logistics

During the design and optimisation phase of a project, one must not forget about the operational and logistical aspects of the mission. An aircraft that's very inconvenient to operate is not going to attract many customers. Now that the design has been formed into a detailed, measurable shape, its operational and logistical advantages and disadvantages can be discussed in more detail and some improvements to the design can be suggested.

17.1. Detailed Description

The analysis of the design from the point of view of operations and logistics includes identifying the actions related to the use and support of the system, and confirming that the system allows for performing those actions, preferably in a quick and convenient manner. First, storage and standby operations are considered for all three concepts. Then, operation of the vehicle is described briefly, such as the flight mission itself, loading and unloading of passengers and more. After that, the actions related to the use and support of the system are be identified. The actions to be considered are: inspection, replacing and charging batteries, replacing and repairing damaged parts. Last but not least, the end-of-life logistics are discussed. The flowchart of the aircraft's operations, which guides the structure of this section, can be seen in figure 17.1.

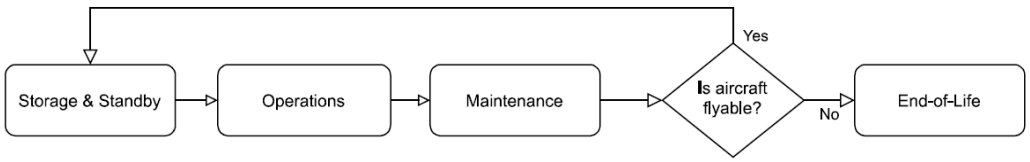

Figure 17.1: Generalised Operations and Logistics flow block diagram.

Starting off with ***Storage & Standby***, the main concern is the wingspan. As opposed to aerodynamic efficiency, for sideways clearance on taxiing or hangar storage, a small wingspan is beneficial. As the aim of the project is to design a personal air-transport vehicle, a large wingspan may require extra infrastructure to facilitate the vehicle. The final design does satisfy the requirement of maximum wingspan, so a regular helipad sized space is sufficient to store the vehicle, making it possible for private owners to store the vehicle on their properties, and for transport companies to efficiently store their vehicles in a hangar.

Operations involves mainly the mission itself and ground operations. In essence, the nominal mission is simply transportation of passengers between two locations, including taxiing and performing flight. The mission is very similar to a conventional passenger aircraft, with a few differences such as the ability to hover, which removes the need for taxiing on some missions. Additionally, as opposed to conventional aircraft, landing and take-off do not require a runway, reducing the infrastructure required substantially. Communications between the pilot and Air Traffic Control still remain a necessity throughout the mission, so the aircraft includes standard radio equipment and a transponder. Communications between the pilot and the passengers is done through a simple intercom as the cabin's sound isolation is good enough to eliminate a need for in-flight headsets, greatly improving passenger comfort. Finally, pilot training will be longer than for a Private Pilot Licence, because the set of skills required to operate the aircraft includes all of the conventional flight techniques, with the added complexity of hover flight.

Another important aspect of operations is the accessibility to the cabin during ground operations. The cabin layout, described in section 2.2, has four seats in a rectangular pattern behind the cockpit, two of which point backwards and the other two point forwards, allowing for a single door on either side of the passenger cabin. With the wings at the extreme front and back locations and the door in the middle, the walking path from the outside to the door is straight and easy. With a distance of 5.8 m between the wings, there is more

than enough space to walk to the door comfortably, which also reduces the risk of damaging one of the front propellers with a suitcase. Additionally, the cargo compartment is behind the cabin, closer to the rear wing. With the rear propellers higher than 2 m above the ground in landing configuration, the cargo compartment door can be reached just as easily as the cabin door. Lastly, the pilot is provided with a separate door to the cockpit at the left side of the fuselage, just behind the front wing. The door opens backwards to prevent it from hitting the front propellers when opened, and the pilot, as a responsible person, is trusted to not damage the front propellers with his belongings or body.

The other aspect of ground operations is the turnaround time, which depends on loading and unloading the payload, described above, and charging the batteries, Assuming that the latter is the rate-limiting step, the minimum turnaround time is 25 minutes, from section 9.2. For easy charger connection, the cables leading to all batteries will connect into just one inlet implemented in the skin of the fuselage behind an aerodynamic cover. The inlet is located on the right side of the fuselage to make flight preparation easier, since the pilot door and the luggage compartment access are already on the left side.

Moving onto ***Maintenance***, general inspection techniques can be used on all aircraft, like performing visual, mechanical, electrical and power checks. A full maintenance of the aircraft should have a reasonable length, requiring the inspection of 2 wing-rotation mechanisms, 12 open propellers, 3 landing gears, all the smaller actuation mechanisms and all skin surfaces. A frequent task during maintenance will be replacing the batteries. Because of their convenient placement between the cockpit and the cabin

After the aircraft's safe life span passes and main structural components are at a risk of failing in fatigue, the aircraft moves on to the ***End-of-Life*** operations, which largely involve dismantling the aircraft with the aim to either repurpose the parts, recycle or discard them if not recyclable. After the dismantling, the parts would be analysed and either reused in the aircraft currently on the production line, recycled or discarded. As most of the aircraft is made of aluminum, only a small fraction of parts need to be discarded, and the rest can be reused for production or recycled.

The current design performs reasonably well in all the operations and logistics categories, because storage, operations, maintenance and the end of the life cycle were implemented into the design decisions in the early design stage. Therefore, no critical design changes are necessary.

17.2. RAMS

In order to save costs of failures, as well as minimise their occurrences, the reliability, availability, maintainability and safety characterises of any design must be considered. These are key to designs in the aerospace industry as there is a large cost associated with designs that are not maintainable (i.e. are unable to fulfil requirements after a certain duration or failure) and not highly available (i.e. are unable to be operational for a large percentage of its design life), as well as unreliable and / or unsafe [6]. Firstly, availability will be briefly defined and discussed.

Availability can be defined by the ratio of the expected uptime to the nominal mission duration [13]. Design aspects that impact availability include turnover time, endurance, loiter time as well as other extraneous factors. Therefore, the power subsystem is designed as such to support the high range, and to have high energy density. Since the design is optimised for range and not endurance, which in a way hinders availability, but to a degree that compromises the mission. That being said, the turnover time (that is primarily dependant on battery recharging) is kept low, ensuring an available system. On the whole, as availability is a key factor in the design of an urban air mobility vehicle, which was accounted for during the design, the design is considered to be highly available.

Safety is an important characteristic of design, which is mainly discussed by the crashworthiness. Safety is essentially the lack of the propensity for a system to fail. To attenuate the impact of failure, it is mostly a question of structural integrity. That is why the landing gear and relevant crashing materials were analysed in depth to accommodate for this in Section 12.7. The other safety critical functions pertain to avionics, radio navigation, engine control and life support. A key aspect of design is not only the measured safety but also the passenger's perception thereof. There have been numerous surveys [105] where passengers'

perception of cabin safety was recorded. It was mentioned that despite most passengers being relatively unenthusiastic about the briefings themselves, they were fairly confident with the cabin safety equipment itself. Therefore, the most important aspect of this is to demonstrate the use of cabin safety equipment itself, which significantly boosts the impression of safety. Overall, the design is made to be safe, however, this has yet to be validated in real life tests.

Maintainability is the ability for a system to be continuously improved and kept in its original condition. This includes replacement of parts and disassembling, but also involves its ability to meet novel requirements, should they appear [13]. For this reason, parts or assemblies that are relatively modern are those that hinder maintainability despite being innovative. That being said, considering the technology currently makes this design unfeasible, (while not to a large extent), more modern parts must be used. However, by doing so, maintainability is compromised. An example of this is the tilting wing mechanism, which is one of the key aspects of this aircraft. The tilting wing is a highly complex and new mechanism, which likely cannot be replaced or improved in any significant manner without enduring high costs. In addition, the battery placement in the cabin within the division between the pilot and passengers, allows easy access thereto. This facilitates the periodic or ad-hoc inspection and replacement of the batteries.

Reliability entails the probability that the system will perform its required function under given conditions for a stated time interval [13]. It furthermore decreases as a function of system complexity. This is because, the more complex the system is, the more difficult it is to predict points of failures and therefore decreases the mean time between failures (MTTF). Hence, high complexity of the design is not preferred, similarly to maintainability. Reliability also depends on extrinsic factors such as the operating condition and the mission profile [13]. That being said, as the phenomena involved in the flight of Wigeon are complex, the required design must be commensurately complex. Therefore, many mechanisms compromise on reliability for the sake of functionality and efficiency. The impact on reliability is yet to be quantified. These mechanisms include the rotating wing, the wing mounted engines, and all moving or static parts that increase the complexity of the design. Furthermore, it is evident in the means of compliance that small category VTOL carry less risk compared to large category and therefore must adhere to less stringent requirements. This is explained in more detail in Chapter 18.

All in all, it is clear that in every engineering design RAMS characteristics are always considered to some extent to minimise failures and costs associated. Many characteristics pertaining to RAMS are unquantifiable, making them rather abstract. However, several operational measures are planned in order to mitigate failures or minimise costs associated thereto, as explained in Section 17.1. With these measures in place, and the adherence to the regulations, the RAMS characteristics can be beneficial to the continuous operation of Wigeon.

18 Requirements Compliance

This chapter contains a compliance matrix with the requirements of the Wigeon project. A more detailed description of the requirements can be found on [5].

The compliance matrix can be found in Table 18.1. For each requirement in the table, there is a reference to the section where the requirement was addressed, except if the requirement could not be addressed within the scope of the DSE, in which case it is marked with a *TBD*. Each cell is also marked with a colour to represent the compliance with the requirement. On the one hand, green means that the requirement is met, either with enough margin or with contingencies in the calculations. On the other hand, certain detailed requirements that concern subsystems or characteristics of the aircraft which have not been designed or analysed within the scope of the DSE, in which case the requirement compliance is marked with a grey box. Please note that even if some requirements could not be verified in the DSE (marked as grey), they might still have a reference to a section. This is because such section addresses the requirement explaining why it was not verified, or proposing how to address it in the future. Lastly, NA means that the requirement is no longer applicable. This concerns the original noise requirements, which were updated (as discussed below), and the requirements about cabin pressurisation, since the cabin is not pressurised.

18.1. Compliance with the Mass Requirement

One particularly stringent requirement is that of the MTOM being within 3175 kg. This is because, out of all the technical budgets, mass is an aspect of design which affects nearly all the others. In fact, the mass of a design can make or break the feasibility of the design, which is why this is considered in more detail.

The requirement for mass is derived from the EASA Special Condition VTOL proposed Means of Compliance. This is meant for aircraft which hold under 9 passengers, such as Wigeon, and the requirement for maximum mass is 3175 kg. This is because the nature and risk of operating such a vehicle is defined to be lower than that of large rotorcraft. Furthermore, as aircraft above 3175 kg do not adhere to the CS-27 small rotorcraft category, the means of compliance proposes they adhere to another set of requirements. That being said, the large category vehicles must adhere to more stringent policies in contrast to their smaller counterparts, such as having to continue flying to the original intended destination or an alternate vertiport in the event of a failure. However, for small aircraft, only the requirements of controlled emergency landing must be met, which is described by EASA as similar to a controlled glide or autorotation. The requirements are outlined, as mentioned above, due to the magnitude and nature of the risk that larger aircraft pose in comparison to their lighter versions, which make it imperative that they function more reliably.

On the whole, the complexity of the system also increases as the mass of the aircraft increases, making the reliability more difficult to ensure, with the requirement therefore being even more stringent. This makes the requirement even more difficult to achieve, as a result of the snowball effect. That is why overall, due to the number of passengers carried, it is highly beneficial to have the aircraft be as lightweight as possible and under the limit of 3175 kg for the purpose of effective certification and high reliability characteristics.

18.2. Change in Requirements

Some of the requirements in [5] still featured a TBD value instead of a specific value for the requirement. In such requirements for which a specific value was not yet selected in [5], the new requirement value is also mentioned in the relevant section in which the requirement is addressed.

During the final phase of the project it was found that requirement *VTOL-NOI-1*, and its subsystem requirements *VTOL-NOI-1-LFT-1* and *VTOL-NOI-1-PRP-1*, were worded in such a way that makes them a killer requirement. This is because no procedure for measurement or distance at which the noise level has to be met was specified. Taking a distance of 0 metres would make it a killer requirement. After discussing it with

Table 18.1: Compliance matrix, containing the requirement ID, its level of compliance, and the section in which more information can be found. Green means compliant, grey means not yet verified.

ID	Further information	ID	Further information	ID	Further information
VTOL-STK-1	Section 2.2	VTOL-LFT-5	Section 10.4.2	VTOL-CTL-4	Section 11.5
VTOL-STK-2	Section 10.4.2	VTOL-LFT-6	Section 7.1	VTOL-CTL-4-CTR-1	Section 11.5
VTOL-STK-3	Section 10.4.2	VTOL-LFT-7	Section 10.4.2	VTOL-CTL-4-CTR-2	Section 11.5
VTOL-STK-4	Section 8.5.1	VTOL-LFT-8	Section 8.5.1	VTOL-MFA-1	Section 11.5
VTOL-STK-5	Section 8.5.1	VTOL-PLD-1	*TBD*	VTOL-MFA-2	Section 11.5
VTOL-STK-6	*TBD*	VTOL-PLD-1-CAB-1	*TBD*	VTOL-MFA-2-CTR-1	Section 11.5
VTOL-STK-7	Section 11.5	VTOL-PLD-1-CAB-2	*TBD*	VTOL-MFA-3	Section 11.5
VTOL-STK-8	Section 12.5	VTOL-PLD-2	Section 12.9	VTOL-MFA-3-CTR-1	Section 11.5
VTOL-STK-9	Section 4.1	VTOL-PLD-2-STR-1	Section 12.3.1	VTOL-MFA-3-CTR-2	Section 11.5
VTOL-STK-10	*TBD*	VTOL-PLD-3	Section 9.7	VTOL-MFA-4	Section 11.5
VTOL-STK-11	*TBD*	VTOL-PLD-3-POW-1	Section 9.7	VTOL-MFA-5	Section 11.5
VTOL-STK-12	Section 9.7	VTOL-PLD-4	*NA*	VTOL-MFA-6	Section 11.5
VTOL-STK-13	Section 11.5	VTOL-PLD-4-STR-1	*NA*	VTOL-MFA-7	Section 9.7
VTOL-STK-14	Section 10.4.2	VTOL-PLD-5	Section 2.2	VTOL-MAS-1	Chapter 14
VTOL-STK-15	Section 2.2	VTOL-PLD-5-CAB-1	Section 2.2	VTOL-SAF-1	Section 2.2
VTOL-STK-16	*TBD*	VTOL-PLD-6	Section 2.2	VTOL-SAF-2	Section 12.7
VTOL-STK-17	Section 10.4.2	VTOL-PLD-6-CAB-1	Section 2.2	VTOL-SAF-3	Section 11.5
VTOL-STK-18	*TBD*	VTOL-PLD-6-CAB-2	Section 2.2	VTOL-SAF-4	Section 11.5
VTOL-STK-19	Section 2.2	VTOL-MTN-1	*TBD*	VTOL-SAF-5	Section 11.5
VTOL-STK-20	Section 2.2	VTOL-MTN-2	*TBD*	VTOL-SAF-6	Section 9.7
VTOL-STK-21	Section 11.5	VTOL-MTN-3	*TBD*	VTOL-SAF-6-POW-1	Section 9.7
VTOL-STK-22	Section 11.5	VTOL-GND-1	Section 7.1	VTOL-EFG-1	Section 9.7
VTOL-STK-23	Section 11.5	VTOL-GND-2	Section 7.1	VTOL-EFG-1-POW-1	Section 9.7
VTOL-THR-1	Section 8.5.1	VTOL-GND-3	Section 2.2	VTOL-OPL-1	*Section 12.6*
VTOL-STS-1	Section 12.2.4	VTOL-PRF-1	Section 10.4.2	VTOL-OPL-2	*TBD*
VTOL-STS-1-STR-1	Section 12.2.4	VTOL-PRF-2	Section 10.4.2	VTOL-COS-1	*Section 4.1*
VTOL-STS-1-STR-2	Section 12.5	VTOL-PRF-3	Section 10.4.2	VTOL-COS-2	*Section 4.3*
VTOL-STS-1-STR-3	Section 12.9	VTOL-PRF-3-POW-1	*Section 9.7*	VTOL-COS-3	Section 4.1
VTOL-STS-2	Section 12.2.4	VTOL-PRF-4	*Section 9.7*	VTOL-COS-4	*TBD*
VTOL-STS-2-STR-1	Section 12.2.4	VTOL-PRF-5	Section 10.4.2	VTOL-SOC-1	*Section 2.2*
VTOL-STS-2-STR-2	Section 12.2.4	VTOL-PRF-5-PRP-1	Section 8.5.1	VTOL-ENV-1	Section 9.7
VTOL-STS-2-STR-3	*TBD*	VTOL-PRF-6	*TBD*	VTOL-ENV-2	Section 9.7
VTOL-STS-2-STR-4	Section 12.1.1	VTOL-PRF-6-PRP-1	*TBD*	VTOL-ENV-3	Section 10.4.2
VTOL-VIB-1	Section 12.8.1	VTOL-PRF-7	*Section 10.4.2*	VTOL-EAS-1 to -18	*TBD*
VTOL-VIB-2	Section 12.8.2	VTOL-PRF-7-POW-1	Section 9.7	VTOL-NOI-1	*NA*
VTOL-VIB-2-STR-1	*TBD*	VTOL-PRF-7-PRP-1	Section 8.5.1	VTOL-NOI-1-LIF-1	*NA*
VTOL-LFT-1	Section 8.5.1	VTOL-CTL-1	Section 2.2	VTOL-NOI-1-PRP-1	*NA*
VTOL-LFT-2	Section 10.4.2	VTOL-CTL-1-CTR-1	*TBD*	VTOL-CRE-1	Section 11.5
VTOL-LFT-3	Section 10.4.2	VTOL-CTL-2	Section 11.5	VTOL-NOI-2	*TBD*
VTOL-LFT-4	Section 8.5.1	VTOL-CTL-3	Section 11.5	VTOL-NOI-3	*TBD*

the tutor, it was agreed to substitute these requirements by more accurate ones, based on ICAO Annex 16 Vol. I noise regulations [58].

- **VTOL-NOI-2**: The noise level of the aircraft in cruise condition should comply with the maximum noise level described in 10.4 b) in chapter 10 of ICAO Annex 16 Vol. I on noise regulations.
- **VTOL-NOI-3**: The noise level of the aircraft in hover configuration should comply with the maximum noise level described in 11.4.2 in chapter 11 of ICAO Annex 16 Vol. I on noise regulations.

These requirements should be verified following a specific measurement procedure laid down in ICAO Annex 16 Vol. I noise regulations [58], and thus cannot be verified within the scope of the DSE. The same applies to requirement VTOL-STK-11, which is the stakeholder requirement from which VTOL-NOI-2 and -3 flow.

18.3. Recommendations on Unverified Requirements

Some of the requirements in Table 18.1 are not yet verified, as explained before. This section addressed the reason for this and proposes how to address them in the future.

Requirement VTOL-STK-6, which restricts the ground turnaround time of the Wigeon with respect to that of its main competitors, could not be addressed since relevant data for competitors could not be found. However, due to the fast charge of the batteries, it can be said that the turnaround time of the Wigeon is low enough, even though the requirement could not be formally verified.

VTOL-STK-10 and its system requirements VTOL-EAS-1 to -18 are the requirements concerning the compliance with EASA regulations. The compliance with these requirements will be formally verified during the

certification phase of the aircraft (see Section 4.4.1 for more information on this phase).

Requirements VTOL-STK-16, VTOL-STK-18, and VTOL-PLD-1 and its susbsystem requirements, all concern the detailed design of the cabin interior. Since this has not been done within the DSE (aside from cabin configuration and sizing), these requirement will only be verified once the detailed design of the passenger cabin is performed. On a similar manner, VTOL-CTL-1-CTR-1 concerns the maximum distance between the controls in the cockpit to the pilot's seat. This requirement can thus only be verified once the cockpit is designed in detail.

Requirements VTOL-MTN-1 and -2, and VTOL-OPL-2 concern maintenance aspects of the design and part replaceability. In order to properly verify these requirements, a more detailed design of the aircraft needs to be performed. However, it can be said at this stage that critical parts such as the batteries and engines are located in places in which easy access can be granted easily, thus paving the way for the compliance with these requirements. Moreover, VTOL-MTN-3 concerns the training of maintenance personnel, which does not fall within the scope of the DSE.

Requirement VTOL-PRF-6 constrains the minimum acceleration needed from stall to cruise speed. This requirement is not verified because it has not been possible to set a strict number on this requirement yet.

Lastly, the end-of-life costs could not be calculated yet at this stage, among other reasons because of the fact that this phase of the project will only come in over two and a half decades, if the expected timeline is followed (see Section 4.4.2 for the project timeline)

19 Conclusion & Recommendations

This chapter outlines the main findings and conclusions of the design process performed by the team. The conclusion itself is laid out in Section 19.1 and recommendations are presented in Section 19.2.

19.1. Conclusion

Like any other industry, the aviation industry thrives on innovation. With personal sustainable transport gaining popularity, a gap is opening in personal and emission-free air travel. An opportunity to breach this gap presents itself as the design of an innovative air-vehicle with a goal of fulfilling the following mission need statement:

Provide sustainable, personal aerial transportation for inter-city travel that is competitive with the current transportation methods while requiring minimal infrastructure.

After an extensive conceptual and preliminary design process, the team was able to devise a solution. After multiple iterations and an optimisation procedure, the solution consists of the parameters shown in Table 19.1. More detailed and in-depth parameters can be found in the respective chapters. The design is also depicted in Figure 19.1, that is a tandem wing configuration with equally sized wings and distributed propulsion placed on tilt wings.

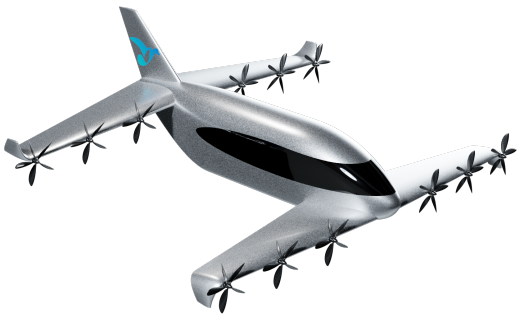

Figure 19.1: The Wigeon.

Table 19.1: Final design parameters of Wigeon

Parameter	Value	Parameter	Value
MTOM [kg]	2 790.1	Wing span [m]	8.2
OEM [kg]	1 428.9	Total wing area [m^2]	19.8
Range [km]	400	Fuselage length [m]	7.3
Cruise speed [m/s]	72.2	Lift to Drag ratio [-]	16.3
Stall speed [m/s]	40	No. of engines [-]	12
Battery capacity [kWh]	301.1	Maximum Thrust [kN]	2 859.3
Battery recharge time [min]	25	Payload mass [kg]	475
No. passengers and pilot [-]	5	Cost [€]	938 700

19.2. Recommendations

The goal of the project itself was to produce an ingenuitive and innovative design. Moreover, the goal had to be achieved in a time constraint of 10 weeks. Therefore, a detailed design would be simply unfeasible during this time frame, giving rise to many possible future recommendations and developments. This section is dedicated to the major design methods and possibilities that were left out of the process due to the time constraint.

As for the structures department, a detailed design of the fuselage structure and an optimised wing rotation mechanism should still be created. A logical next step is to create a detailed CAD model consisting of individual structural parts, as opposed to only outside surfaces. The model can then be used for FEM analysis. This way a more precise mass estimation can be done too along with an improved material selection process.

The stability and control department, on the other hand, can proceed to improving the aerodynamic interactions in the analytical models, mainly including the effect of the front wing's downwash on the back wing's flow. Later, focus could be put on the dynamics of control during transition, which would be analysed using Simulink with the help of a sophisticated CFD simulation. Finally, the preliminary analytical model to determine stability derivatives should be validated and the dynamic model should be model matched with the use of CFD simulations.

When it comes to propulsion, having a better understanding of the propeller interactions, both regarding propeller-propeller and propeller-wing interactions, would improve the propeller design substantially, which again requires the use of accurate CFD analysis.

Furthermore, the batteries could be modelled more accurately as resistance of an individual cell was deemed to be negligible during the design process. In reality, having such a large battery would most definitely add to the resistance of the electric system, resulting in less electrical power supplied to the systems, mainly the engines. Thermal management of batteries has also not been investigated and most often is an important part of an electric power system, again provided the size of the batteries.

Finally, the performance of the final design should at some point be validated using a small scale flying model.

References

[1] S. Addarkaoui et al. *Graduate Team Aircraft Design Competition: Electric Vertical Takeoff and Landing (E-VTOL) Aircraft Mistral Air Taxi Faculty members*. 2019.

[2] C.N. Adkins and R.H. Liebeck. "Design of optimum propellers". In: *Journal of Propulsion and Power* 10.5 (May 1994), pp. 676–682. ISSN: 07484658. URL: https://doi.org/10.2514/3.23779.

[3] Airbus. *Civil Helicopters*. 2021. URL: https://www.airbus.com/helicopters/civil-helicopters.html (visited on 04/25/2021).

[4] Airbus. *Global Market Forecast: Cities, Airports and Aircrtaft. 2019-2038*. 2019.

[5] J. Alba Maestre et al. *Baseline Report - Multi-Disciplinary Design and Optimisation of Long-Range eVTOL Aircraft*. 2021.

[6] "An overview on reliability, availability, maintainability and supportability (RAMS) engineering". In: *International Journal of Quality and Reliability Management* 25 (3 2008), pp. 330–344. ISSN: 0265671X. DOI: 10.1108/02656710810854313.

[7] J.D. Anderson. *Fundamentals of Aerodynamics*. 6th international ed. New York, United States: McGraw Hill Education, 2017.

[8] M.F. Ashby, H. Shercliff, and D. Cebon. *Materials: engineering, science, processing and designs*. 3rd ed. Oxford, United Kingdom: Butterworth-Heinemann, 2014.

[9] ASM. "ASM handbook Volume 2 - Properties and selection: Nonferrous alloys and special-purpose materials". In: *ASM Metals Handbook* 2 (1993). ISSN: 08170379.

[10] Atsdr. *Public Health Statement Aluminum CAS 7429-90-5 Division of Toxicology and Environmental Medicine*. 2008. URL: www.atsdr.cdc.gov/.

[11] "Aviation industry under pressure to reduce landfill waste from scrapped airliners | News | Flight Global". In: (). URL: https://www.flightglobal.com/aviation-industry-under-pressure-to-reduce-landfill-waste-from-scrapped-airliners/97762.article.

[12] A. Betz. *Screw Propellers with Minimum Energy Loss*. Technical translation. NRC, Division of Mechanical Engineering, 1958. URL: https://books.google.nl/books?id=QvVyNAEACAAJ.

[13] A. Birolini. *Basic Concepts, Quality & Reliability (RAMS) Assurance of Complex Equipment & Systems*. Springer Berlin Heidelberg, 2017, pp. 1–24. DOI: 10.1007/978-3-662-54209-5_1.

[14] BIS Research. *EVTOL Market To Hit 1.9bn By 2035 As Urban Congestion Rises*. 2019. URL: https://industryeurope.com/sectors/aerospace-defence/evtol-market-to-hit-1-9bn-by-2035-as-urban-congestion-rises/.

[15] BIS Research. *Global Electric VTOL (eVTOL) Aircraft Market to Reach 1.9 Billion by 2035*. 2020. URL: https://www.prnewswire.com/news-releases/global-electric-vtol-evtol-aircraft-market-to-reach-1-9-billion-by-2035--300984170.html.

[16] J. Boling and G. C. Zha. "Numerical investigation of longitudinal static stability of a high-speed tandem-wing vtol vehicle using coflow jet airfoil". In: *AIAA Scitech 2021 Forum*. American Institute of Aeronautics and Astronautics Inc, AIAA, 2021, pp. 1–22. ISBN: 9781624106095. DOI: 10.2514/6.2021-1732.

[17] T. Bouquet and R. Vos. "Modeling the propeller slipstream effect on lift and pitching moment". In: American Institute of Aeronautics and Astronautics Inc., 2017. ISBN: 9781624104473. DOI: 10.2514/6.2017-0236.

[18] R. V. Brulle. "Engineering the Space Age". In: *Air University Press* (2008). URL: https://media.defense.gov/2017/Apr/05/2001727358/-1/-1/0/B_0113_BRULLE_ENGINEERING_SPACE_AGE.PDF.

[19] Business Set Free. *4 Stages of the Small Business Product Life Cycle*. URL: https://businesssetfree.com/small-business-product-life-cycle.

[20] Lai C. H. and N Kamaruddin. "Effect of fuselage diameter on aerodynamic characteristics for straight wing at low and high aspect ratio". In: *IOP Conference Series: Materials Science and Engineering* 370 (May 2018), p. 012055. DOI: 10.1088/1757-899X/370/1/012055.

[21] D. A. Caughey. *Introduction to Aircraft Stability and Control Course Notes for AE5070*. 2011.

[22] A. Cawez et al. *DUCKAMPUS Autonomous Electric Vertical TakeOff and Landing Aircraft*. 2019.

[23] *Certification Specifications and Acceptable Means of Compliance for Small Rotorcraft CS-27*. 2020. URL: https://www.easa.europa.eu/sites/default/files/dfu/cs-27_amendment_7.pdf.

[24] A. Cervone. *AE2230-II Propulsion and Power Lecture Notes EPS2*. 2021.

[25] S. S. Chauhan and J. R.R.A. Martins. "Tilt-wing eVTOL takeoff trajectory optimization". In: *Journal of Aircraft* 57 (1 2020), pp. 93–112. ISSN: 15333868. DOI: 10.2514/1.C035476.

[26] H. Chen. *Effectiveness of Thrust Vectoring Control for Longitudinal Trim of a Blended Wing Body Aircraft*. Tech. rep. 2015. URL: http://resolver.tudelft.nl/uuid:de4a4261-0948-45e9-9525-b78e2a664af2.

[27] H. Cheng and H. Wang. "Prediction of lift coefficient for tandem wing configuration or multiple-lifting-surface system using prandtl's lifting-line theory". In: *International Journal of Aerospace Engineering* 2018 (2018). ISSN: 16875974. DOI: 10.1155/2018/3104902.

[28] E. Chesmar et al. *Care and Repair of Advanced Composites*. July 2019. DOI: 10.4271/9780768084320.

[29] Circuitlab. *Online circuit simulator & schematic editor - CircuitLab*. 2021. URL: www.circuitlab.com.

[30] *Cities in the World: A new perspective on urbanization*. OECD, June 2020. ISBN: 9789264519718. DOI: 10.1787/d0efcbda-en.

[31] "Combined Corrosion and Wear of Aluminium Alloy 7075-T6". In: *Journal of Bio- and Tribo-Corrosion* 2 (2 June 2016). ISSN: 21984239. DOI: 10.1007/s40735-016-0042-3.

[32] "Commercial airplane applications of superplastically formed AA5083 aluminum sheet". In: *Journal of Materials Engineering and Performance* 16 (2 Apr. 2007), pp. 136–141. ISSN: 10599495. DOI: 10.1007/s11665-007-9023-5.

[33] H. D. Curtis. R. D Irwin, 1996. ISBN: 978-0256192605.

[34] Guang Xun D. et al. "Controllability analysis for multirotor helicopter rotor degradation and failure". In: *Journal of Guidance, Control, and Dynamics* 38.5 (Jan. 2015), pp. 978–984. ISSN: 15333884. DOI: 10.2514/1.G000731. arXiv: 1403.5986.

[35] Guang-Xun D. and Quan Q. *A Matlab Toolbox for Calculating an Available Control Authority Index of Multicopters*. Mar. 2016. URL: http://rfly.buaa.edu.cn/resources.

[36] Scholz D. *Aircraft Design*. Tech. rep. Hamburg Open Online University (HOOU), 2017.

[37] Glaister D. H. "Human tolerance to impact acceleration". In: *Injury* 9.3 (1978), pp. 191–198. ISSN: 0020-1383. DOI: https://doi.org/10.1016/0020-1383(78)90006-2. URL: https://www.sciencedirect.com/science/article/pii/0020138378900062.

[38] J. P. Dear et al. "Energy Absorbing Ability of Sandwich Composite Structures". In: *Fracture of Nano and Engineering Materials and Structures*. Ed. by E. E. Gdoutos. Dordrecht: Springer Netherlands, 2006, pp. 1263–1264. ISBN: 978-1-4020-4972-9.

[39] D. DeFelice. "NASA - Flying on the Ground". In: ().

[40] Deloitte. *A bumpy ride ahead. Cash & working capital insights into the airline sector*. 2019. URL: https://www2.deloitte.com/content/dam/Deloitte/uk/Documents/corporate-finance/deloitte-uk-a-bumpy-ride-ahead-airline-sector.pdf.

[41] Deloitte. *Advanced air mobility*. 2021. URL: https://www2.deloitte.com/us/en/insights/industry/aerospace-defense/advanced-air-mobility.html.

[42] J. DeYoung and C. W. Harper. "Theoretical symmetric span loading at subsonic speeds for wings having arbitrary plan form". In: *Span* (921 1948).

[43] R. Domingo. *AC 43-4B - Corrosion Control for Aircraft*.

[44] Senkans E. et al. "A First-Principle Power and Energy Model for eVTOL Vehicles". In: (2020). DOI: 10.2514/6.2020-1008.c1.

[45] Eurocode. *Table of design properties for metric hexagonal bolts M5 to M39*. 2021. URL: https://eurocodeapplied.com/design/en1993/bolt-design-properties.

[46] R.. Farrington and J. Rugh. *Impact of Vehicle Air-Conditioning on Fuel Economy, Tailpipe Emissions, and Electric Vehicle Range Preprint Impact of Vehicle Air-Conditioning on Fuel Economy, Tailpipe Emissions, and Electric Vehicle Range*. 2000. URL: http://www.doe.gov/bridgeonlineordering:http://www.ntis.gov/ordering.htm.

[47] Federal Aviation Administration. *Airworthiness certification*. 2021. URL: https://www.faa.gov/aircraft/air_cert/airworthiness_certification/#:~:text=The%5C%20certification%5C%20was%5C%20completed%5C%20in,between%5C%205%5C%20and%5C%209%5C%20years..

[48] S. J. Findlay and N. D. Harrison. *Why Aircraft Fail*. Materials Today, Nov. 2002.

[49] Eberhard G. *Lecture 1 - Course Organization & Systems Engineering - AE3211-I Systems Engineering & Aerospace Design (2020/21 Q3)*. URL: https://brightspace.tudelft.nl/d2l/le/content/293146/viewContent/1909569/View (visited on 04/27/2021).

[50] H. Glauert. "Airplane Propellers". In: *Aerodynamic Theory: A General Review of Progress Under a Grant of the Guggenheim Fund for the Promotion of Aeronautics*. Berlin, Heidelberg: Springer Berlin Heidelberg, 1935, pp. 169–360. DOI: 10.1007/978-3-642-91487-4_3.

[51] Juul Gouweloos et al. "The risk of PTSD and depression after an airplane crash and its potential association with physical injury: A longitudinal study". In: *Injury* 47 (1 Jan. 2016), pp. 250–256. ISSN: 18790267. DOI: 10.1016/j.injury.2015.07.005.

[52] Grand View Research. *Commercial Helicopter Market Size, Share & Trends Analysis Report By Type (Light, Medium, Heavy), By Application (Medical Services, Law Enforcement & Public Safety), By Region, And Segment Forecasts, 2019 - 2025*. 2018. URL: https://www.grandviewresearch.com/industry-analysis/commercial-helicopters-market.

[53] S. Gudmundsson. *General Aviation Aircraft Design: Applied Methods and Procedures*. 2013. DOI: 10.1016/C2011-0-06824-2.

[54] Kinjo H. *Mitsui & Co. Global Strategic Studies Institute Monthly Report Development Trends and Prospects for eVTOL: A New Mode of Air Mobility*. Mitsui & Co, 2018.

[55] Booz Allen Hamilton. *UAM Market Study - technical out brief*. NASA, 2018. URL: https://www.nasa.gov/aam-studies-reports/.

[56] N. Hashemnia and B. Asaei. "Comparative study of using different electric motors in the electric vehicles". In: 2008. DOI: 10.1109/ICELMACH.2008.4800157.

[57] *HexWeb® A1 and A10 High strength aramid honeycomb Product Data*. 2007. URL: https://www.hexcel.com/user_area/content_media/raw/A1A10_eu.pdf.

[58] ICAO. *Environmental Protection Annex 16 to the Convention on International Civil Aviation International Civil Aviation Organization International Standards and Recommended Practices Fifth Edition*. Tech. rep. 2008.

[59] IDTechEx. *Air Taxis: Electric Vertical Take-Off and Landing Aircraft 2021-2041*. 2021. URL: http://www.idtechex.com/en/research-report/air-taxis-electric-vertical-take-off-and-landing-aircraft-2021-2041/804.

[60] Sinke J. *Production of Aerospace Systems (Reader)*. 2021.

[61] How J. P. *Aircraft Lateral Autopilots*. Tech. rep. Massachusetts Institute of Technology, 2004. URL: https://ocw.mit.edu/courses/aeronautics-and-astronautics/16-333-aircraft-stability-and-control-fall-2004/lecture-notes/lecture_12.pdf.

[62] J.A. Mulder, W.H.J.J van Staveren, J.C. van der Vaart, E. de Weerdt, C.C. de Visser, A.C. in 't Veld & E. Mooij. *AE3202 Flight Dynamics Lecture Notes*. Delft, The Netherlands: Delft University of Technology, 2013.

[63] Jetex. *8 Types of private jets*. URL: https://www.jetex.com/types-of-private-jets/#:~:text=Small (visited on 04/25/2021).

[64] R C Kuipers. *Methodology for Prediction of the Fatigue Life for Lug Joints Sub-jected to Combined In-Plane and Out-of-Plane Loading*.

[65] Traub L. W. "Analytic drag prediction for cambered wings with partial leading-edge suction". In: *Journal of Aircraft* 46 (1 2009), pp. 312–317. ISSN: 15333868. DOI: 10.2514/1.38558.

[66] E. E. Larrabee. "Practical Design of Minimum Induced Loss Propellers". In: *SAE Transactions* 88 (1979), pp. 2053–2062. URL: http://www.jstor.org/stable/44690041.

[67] S.E. Larsson. *The Development of a Calculation Method for the Fatigue Strength of Lugs and a Study of Test Results for Lugs of Aluminium*. Elsevier, 1969, pp. 309–342. DOI: 10.1016/b978-0-08-011697-6.50017-5.

[68] William A. Lies et al. "Low SWaP-C Radar for Urban Air Mobility". In: *2020 IEEE/ION Position, Location and Navigation Symposium, PLANS 2020*. Institute of Electrical and Electronics Engineers Inc., Apr. 2020, pp. 74–80. ISBN: 9781728102443. DOI: 10.1109/PLANS46316.2020.9110148.

[69] Schwartz M. *3D Printing Aerospace | How 3D Printing is Transforming the Industry*. 2017. URL: https://blog.trimech.com/3d-printing-transforming-aerospace-industry.

[70] Yildirim M., Polat M., and Kurum H. "A survey on comparison of electric motor types and drives used for electric vehicles". In: Institute of Electrical and Electronics Engineers Inc., Dec. 2014, pp. 218–223. DOI: 10.1109/EPEPEMC.2014.6980715.

[71] J. A. Maestre et al. *Midterm Report Multi-Disciplinary Design and Optimisation of a Long-Range eVTOL Aircraft*. 2021.

[72] C. Mair, D. Rezgui, and B. Titurus. "Nonlinear stability analysis of whirl flutter in a rotor-nacelle system". In: *Nonlinear Dynamics* 94 (3 Nov. 2018), pp. 2013–2032. ISSN: 1573269X. DOI: 10.1007/s11071-018-4472-y.

[73] Markets and Markets. *eVTOL Aircraft Market*. 2019. URL: https://www.marketsandmarkets.com/Market-Reports/evtol-aircraft-market-28054110.html.

[74] Markets and Markets. *eVTOL Aircraft Market*. 2020. URL: https://aerospacedefenseland.wordpress.com/2020/01/06/key-emerging-trends-in-evtol-aircraft-market-global-forecast-to-2030/.

[75] J. E. Marte and D. W. Kurtz. *A Review of Aerodynamic Noise From Propellers, Rotors, and Lift Fans*. 1970. URL: https://ntrs.nasa.gov/citations/19700005920.

[76] K. Masania. *Additive Manufacturing of Bioinspired Composites - AE3211-II Production of Aerospace Systems*. 2021. URL: https://brightspace.tudelft.nl/d2l/le/content/293147/viewContent/2100064/View.

[77] T. Mayor and J. Anderson. *Getting Mobility off the ground*. KPMG, 2019.

[78] McKinsey&Company. *Urban Air Mobility (UAM) Market Study*. NASA, 2018. URL: https://www.nasa.gov/aam-studies-reports/.

[79] *Means of Compliance with the Special Condition VTOL*. Tech. rep. European Union Aviation Safety Agency, 2021. URL: https://www.easa.europa.eu/sites/default/files/dfu/moc_sc_vtol_issue_2_12-may-2021_shaded_0.pdf.

[80] T.H.G. Megson. *Materials: engineering, science, processing and designs*. 6th ed. Oxford, United Kingdom: Butterworth-Heinemann, 2017.

[81] J. Melkert and C. Rans. *Lecture on Buckling - AE2135-I Structural Analysis & Design*. 2019. URL: https://brightspace.tudelft.nl/d2l/le/content/213463/viewContent/1472842/View.

[82] J A Mulder et al. *Lecture Notes AE3202 Flight Dynamics*. 2013.

[83] M. M. Munk. *General Biplane Theory*. 1923.

[84] Polaczyk N. et al. *A review of current technology and research in urban on-demand air mobility applications*. 2019, pp. 333–343.

[85] R. Nederlof. *Improved modeling of propeller-wing interactions with a lifting-line approach Investigation of a suitable correction method to account for the enite slipstream height*. Tech. rep. 2020. URL: https://repository.tudelft.nl/islandora/object/uuid%5C%3Ad952665d-475f-483d-94f5-2b929ea6e713.

[86] F. Nicolosi et al. "Fuselage aerodynamic prediction methods". In: *Aerospace Science and Technology* 55 (Aug. 2016), pp. 332–343. ISSN: 12709638. DOI: 10.1016/j.ast.2016.06.012.

[87] M. Nita and D. Scholz. *Estimating the Oswald Factor from Basic Aircraft Geometrical Parameters*. 2012.

[88] "Nonlinear stability analysis of whirl flutter in a rotor-nacelle system". In: *Nonlinear Dynamics* 94 (3 Nov. 2018), pp. 2013–2032. ISSN: 1573269X. DOI: 10.1007/s11071-018-4472-y.

[89] Al-Shamma O., Ali R., and Hasan H. S. *An Educational Rudder Sizing Algorithm for Utilization in Aircraft Design Software*. Tech. rep. 10. 2018, pp. 7889–7894. URL: http://www.ripublication.com.

[90] Al-Shamma O., Ali R., and Hasan H. S. "An instructive algorithm for aircraft elevator sizing to be used in preliminary aircraft design software". In: 4 (2017), pp. 489–494. DOI: 10.5937/jaes15-14829.

[91] F. Oliviero. "AE2111-II Systems Design: AircraftDesign-2_2019 BS- Lift & Drag Estimation (1)". In: ().

[92] F. Oliviero. "Aircraft aerodynamic analysis – Mobile surfaces on the wing". In: (2019).

[93] F. Oliviero. *Lecture 4 - Requirement Analysis and Design principles for A/C stability & control (Part 1) - AE3211-I Systems Engineering and Aerospace Design (2020/21 Q3)*. Delft, The Netherlands, 2021.

[94] F. Oliviero. *Lecture 9 - Design for Lateral-directional aspects and design for ground operations - AE3211-I Systems Engineering and Aerospace Design (2020/21 Q3)*. Delft, The Netherlands, 2021.

[95] F. Oliviero. *Requirement Analysis and Design Principles for AC Stability and Control (Part 1)*. Feb. 2021.

[96] B. N. Popov. *Stress Corrosion Cracking*. Elsevier, Jan. 2015, pp. 365–450. DOI: 10.1016/B978-0-444-62722-3.00009-4. URL: https://linkinghub.elsevier.com/retrieve/pii/B9780444627223000094.

[97] F S Pranoto, A Wirawan, and D A Purnamasari. "Electrical Power Budgeting Analysis for LSA-02 UAV Technology Demonstrator". In: *IOP Conference Series: Material Science and Engineering* 160 (1 2016). DOI: 10.1088/1757-899X/160/1/012088.

[98] *Profits and loss: Mining and human rights in Katanga, Democratic Republic of the Congo - Amnesty International*. URL: https://www.amnesty.nl/actueel/profits-and-loss-mining-and-human-rights-in-katanga-democratic-republic-of-the-congo.

[99] Frick R. and Grimm B. *Long-distance Mobility: Current Trends and Future Perspectives*. Institute of Mobility Research, 2014. URL: www.nit-kiel.de.

[100] Vos R., Melkert J. A., and Zandbergen B.T.C. *Aerospace Design and Systems Engineering Elements AE1222 II A/C Preliminary Sizing (class I weight estimation method)*.

[101] A. Raj and Samir K. Srivastava. "Sustainability performance assessment of an aircraft manufacturing firm". In: *Benchmarking: An International Journal* 25.5 (Jan. 2018). Publisher: Emerald Publishing Limited, pp. 1500–1527. ISSN: 1463-5771. DOI: 10.1108/BIJ-01-2017-0001. (Visited on 04/27/2021).

[102] D. P. Raymer. *Aircraft Design: A Conceptual Approach*. 1992.

[103] Reports and Data. *Urban Air Mobility Market To Reach USD 7.9 Billion By 2030 Reports And Data*. 2019. URL: https://www.globenewswire.com/news-release/2019/03/18/1756495/0/en/Urban-Air-Mobility-Market-To-Reach-USD-7-9-Billion-By-2030-Reports-And-Data.html.

[104] J. Roskam. *Airplane design Part V: Component Weight Estimation*. DARcorporation, 1986. ISBN: 9781884885501.

[105] R. Ruenruoy, P. A. Craig, and W. S. Beckman. *Passengers' Perception of the Safety Demonstration on Board an Aircraft*. 2015.

[106] J. J. Ruijgrok. *Elements of Airplane Performance*. 2nd ed. Delft, the Netherlands, 2009, pp. 175–199. ISBN: 978-90-6562-203-7.

[107] T. Rye and R. Hrelja. "Policies for reducing car traffic and their problematisation. Lessons from the mobility strategies of British, Dutch, German and Swedish Cities". In: *Sustainability (Switzerland)* 12 (19 Oct. 2020). ISSN: 20711050. DOI: 10.3390/su12198170.

[108] Gudmundsson S. "Miscellaneous Design Notes". In: *General Aviation Aircraft Design*. Elsevier, Jan. 2014, pp. 947–983. DOI: 10.1016/b978-0-12-397308-5.00023-4.

[109] Gupta S. et al. *Release and toxicity of dental resin composite*. Sept. 2012. DOI: 10.4103/0971-6580.103652.

[110] M. Sadraey. *Aircraft Design: A Systems Engineering Approach*. 2012. ISBN: 381,0000.191.

[111] G. M. Scamans, N. Birbilis, and R. G. Buchheit. *Corrosion of aluminum and its alloys*. Elsevier, Jan. 2010, pp. 1974–2010. DOI: 10.1016/B978-044452787-5.00095-0.

[112] "Designing against Fatigue of Structures". In: *Fatigue of Structures and Materials*. Ed. by J. Schijve. Dordrecht: Springer Netherlands, 2009, pp. 559–586. DOI: 10.1007/978-1-4020-6808-9_20.

[113] D. Schiktanz. "Conceptual Design of a Medium Range Box Wing Aircraft". In: (July 2011).

[114] D. Schiktanz and D. Scholz. *Box Wing Fundamentals - An Aircraft Design Perspective*. 2011.

[115] D. Scholz. *Aerospace Europe 6th CEAS Conference Definition and Discussion of the Intrinsic Efficiency of Winglets*. 2017.

[116] Omran Al-Shamma, Rashid Ali, and Haitham S. Hasan. "Programmable Aileron Sizing Algorithm for use in Preliminary Aircraft Design Software". In: *Journal of Engineering and Applied Sciences 13* (2018). ISSN: 1816-949X. URL: http://docsdrive.com/pdfs/medwelljournals/jeasci/2018/3458-3462.pdf.

[117] T. Sinnige et al. "Wingtip-Mounted Propellers: Aerodynamic Analysis of Interaction Effects and Comparison with Conventional Layout". In: *Journal of Aircraft* 56.1 (2019), pp. 295–312. DOI: 10.2514/1.C034978.

[118] The Vertical Flight Society. *eVTOL Aircraft Directory*. 2021. URL: https://evtol.news/aircraft.

[119] *Special Condition for small-category VTOL aircraft Statement of Issue*. Tech. rep. European Union Aviation Safety Agency, 2019. URL: https://www.easa.europa.eu/sites/default/files/dfu/SC-VTOL-01.pdf.

[120] Statista. *Electricity prices for households in Germany from 2010 to 2020, semi-annually*. URL: https://www.statista.com/statistics/418078/electricity-prices-for-households-in-germany/.

[121] Stokkermans T. C. A. et al. "Aerodynamic Interaction Effects Between Propellers in Typical eVTOL Vehicle Configurations". In: (2021). DOI: 10.2514/1.C035814.

[122] *The Basics of Textile Recycling*. URL: https://www.thebalancesmb.com/the-basics-of-recycling-clothing-and-other-textiles-2877780.

[123] T. Theodorsen. *Theory of propellers*. 1st ed. New York: McGraw-Hill Book Co., 1948.

[124] *UK Aluminium Industry Fact Sheet 5 : Aluminium Recycling*. URL: www.alfed.org.uk.

[125] Valuates Reports. *eVTOL Aircraft Market Size USD 87640 Million By 2026 At CAGR 11.1%*. 2020. URL: https://www.prnewswire.com/news-releases/evtol-aircraft-market-size-usd-87640-million-by-2026-at-cagr-11-1---valuates-reports-301180461.html.

[126] R. Vos. "Design of the fuselage (Lecture Slides Aerospace Design and System Engineering Elements I)". In:

[127] J. Weissinger. *The Lift Distribution of Swept-Back Wings*. 1947.

[128] Marino108LFS in Wikimedia Commons. *Propeller blade BET*. 2020. URL: https://commons.wikimedia.org/wiki/File:Propeller_blade_BET.svg (visited on 06/19/2021).

[129] Yang X. et al. "Crashworthy design and energy absorption mechanisms for helicopter structures: A systematic literature review". In: *Progress in Aerospace Sciences* 114 (Apr. 2020), p. 100618. ISSN: 03760421. DOI: 10.1016/j.paerosci.2020.100618.

[130] Fujio Y. et al. "Invisible crack visualization and depth analysis by mechanoluminescence film". In: *Journal of Alloys and Compounds* 832 (Aug. 2020), p. 154900. ISSN: 09258388. DOI: 10.1016/j.jallcom.2020.154900.

[131] Karamian Y. et al. "Spricho, an on demand energy efficient eVTOL Airtaxi". In: (2019).

[132] Luhan Y., Xin L., and Paulson J. A. "A dynamic stability design strategy for lithium metal solid state batteries Check for updates". In: *218 Nature* 593 (2021). DOI: 10.1038/s41586-021-03486-3.

[133] Yang Y. et al. "Recycling of composite materials". In: *Chemical Engineering and Processing: Process Intensification* 51 (Jan. 2012), pp. 53–68. ISSN: 02552701. DOI: 10.1016/j.cep.2011.09.007.

[134] Ahmad Z. *Selection of materials for corrosive environment*. Elsevier, Jan. 2006, pp. 479–549. DOI: 10.1016/b978-075065924-6/50010-6.